HIGH PERFORMANCE READOUT AND CONTROL ELECTRONICS FOR MEMS GYROSCOPES

A THESIS SUBMITTED TO
THE GRADUATE SCHOOL OF NATURAL AND APPLIED SCIENCE
OF
MIDDLE EAST TECHNICAL UNIVERSITY

BY

EMRE ŞAHİN

IN PARTIAL FULLFILMENT OF THE REQUIREMENTS
FOR
THE DEGREE OF THE MASTER OF SCIENCE
IN
ELECTRICAL AND ELECTRONICS ENGINEERING

FEBRUARY 2009

Approval of this thesis:

HIGH PERFORMANCE READOUT AND CONTROL ELECTRONICS FOR MEMS GYROSCOPES

submitted by **EMRE ŞAHİN** in partial fulfillment of the requirements for the degree of **Master of Science in Electrical and Electronics Engineering Department, Middle East Technical University** by,

Prof. Dr. Canan Özgen _____
Dean, Graduate School of **Natural and Applied Sciences**

Prof. Dr. İsmet Erkmen _____
Head of Department, **Electrical and Electronics Engineering**

Prof. Dr. Tayfun Akın _____
Supervisor, **Electrical and Electronics Engineering Dept.**

Examining Committee Members:

Prof. Dr. Murat Aşkar _____
Electrical and Electronics Engineering Dept., METU

Prof. Dr. Tayfun Akın _____
Electrical and Electronics Engineering Dept., METU

Prof. Dr. Cengiz Beşikçi _____
Electrical and Electronics Engineering Dept., METU

Assoc. Prof. Dr. Haluk Külah _____
Electrical and Electronics Engineering Dept., METU

Dr. Said Emre Alper _____
Technical Vocational School of Higher Education, METU

Date: 13.02.2009

I hereby declare that all information in this document has been obtained and presented in accordance with academic rules and ethical conduct. I also declare that, as required by these rules and conduct, I have fully cited and referenced all material and results that are not original to this work.

Name, Last name : Emre Şahin

Signature :

ABSTRACT

HIGH PERFORMANCE REDAOUT AND CONTROL ELECTRONICS FOR MEMS GYROSCOPE

Şahin, Emre
M.Sc., Department of Electrical-Electronics Engineering
Supervisor: Prof. Dr. Tayfun Akın

February 2009, 179 pages

This thesis reports the development of various high performance readout and control electronics for implementing angular rate sensing systems using MEMS gyroscopes developed at METU. First, three systems with open loop sensing mechanisms are implemented, where each system has a different drive-mode automatic gain controlled (AGC) self-oscillation loop approach, including (i) square wave driving signal with DC off-set named as OLS_SquD, (ii) sinusoidal driving signal with DC off-set named as OLS_SineD, and iii) off-resonance driving signal named as OLS_OffD. A forth system is also constructed with a closed loop sensing mechanism where the drive mode automatic gain controlled (AGC) self-oscillation loop approach with square wave driving signal with DC off-set named as CLS_SquD. Sense and drive mode electronics employ transimpedance and transresistance amplifiers as readout electronics, respectively. Each of the systems is implemented with commercial discrete components on a dedicated PCB. Then, the angular rate sensing systems are tested with SOG (Silicon-on-Glass) gyroscopes that are adjusted to have two different mechanical bandwidths, more specially 100 Hz and 30 Hz. Test results of all of these cases verify the high performance of the systems.

For the 100 Hz bandwidth, the OLS_SquD system shows a bias instability of 4.67 ˚/hr, an angle random walk (ARW) 0.080 ˚/√hr, and a scale factor of -22.6 mV/(˚/sec). For the 30 Hz bandwidth, the OLS_SquD system shows a bias instability of 5.12 ˚/hr, an ARW better than 0.017 ˚/√hr, and a scale factor of -49.8 mV/(˚/sec).

For the 100 Hz bandwidth, the OLS_SineD system shows a bias instability of 6.92 ˚/hr, an ARW of 0.049 ˚/√hr, and a scale factor of -17.97 mV/(˚/sec). For the 30 Hz bandwidth, the OLS_SineD system shows a bias instability of 4.51 ˚/hr, an ARW of 0.030 ˚/√hr, and a scale factor of -43.24 mV/(˚/sec).

For the 100 Hz bandwidth, the OLS_OffD system shows a bias instability of 8.43 ˚/hr, an ARW of 0.086 ˚/√hr, and a scale factor of -20.97 mV/(˚/sec). For the 30 Hz bandwidth, the OLS_OffD system shows a bias instability of 5.72 ˚/hr, an ARW of 0.046 ˚/√hr, and a scale factor of -47.26 mV/(˚/sec).

For the 100 Hz bandwidth, the CLS_SquD system shows a bias instability of 6.32 ˚/hr, an ARW of 0.055 ˚/√hr, and a scale factor of -1.79 mV/(˚/sec). For the 30 Hz bandwidth, the CLS_SquD system shows a bias instability of 5.42 ˚/hr, an ARW of 0.057 ˚/√hr, and a scale factor of -1.98 mV/(˚/sec).

For the 100 Hz bandwidth, the R^2 nonlinearities of the measured scale factors of all systems are between 0.0001% and 0.0003% in the ±100 ˚/sec measurement range, while for the 30 Hz bandwidth the R^2 nonlinearities are between 0.0002% and 0.0062% in the ±80˚/sec measurement range.

These performance results are the best results obtained at METU, satisfying the tactical-grade performances, and the measured bias instabilities and ARWs are comparable to the best results in the literature for a silicon micromachined vibratory gyroscope.

Keywords: MEMS Gyroscope, Gyroscope Electronics, Control Electronics, Interface Circuit, Amplitude-Controlled Oscillation, Closed-loop Angular Rate Sensing, Microelectromechanical Systems (MEMS)

ÖZ

MEMS DÖNÜÖLÇERLER İÇİN YÜKSEK PERFORMANSLI OKUMA VE KONTROL ELEKTRONİĞİ

Şahin, Emre

Yüksek Lisans, Elektrik-Elektronik Mühensdiliği Bölümü

Tez Yöneticisi: Prof. Dr. Tayfun Akın

Şubat 2009, 179 sayfa

Bu tez ODTÜ'de geliştirilmiş MEMS dönü ölçerler kullanarak açısal dönü algılama sistemleri uygulamak için çeşitli yüksek performanslı okuma ve kontrol elektroniğinin geliştirilmesini anlatmaktadır. İlk olarak, açık döngü algılama mekanizmalı üç sistem uygulanmıştır, bu sistemlerin her biri (i) OLS_SquD olarak adlandırılan DA bağıl konumlu kare dalga sürüş sinyali (ii) OLS_SineD olarak adlandırılan DA bağıl konumlu sinüs sürüş sinyali ve (iii) OLS_OffD olarak adlandırılan rezonans frekansında olmayan sürüş sinyalini içeren farklı sürüş-modu otomatik kazanç kontrollü (OKK) kendinden salınım döngü yaklaşımlarına sahiptir. Dördüncü bir sistemse CLS_SquD olarak adlandırılan DA bağıl konumlu kare dalga sürüş sinyalli otomatik kazanç kontrollü (OKK) kendinden salınım döngü yaklaşımının olduğu kapalı döngü algılama mekanizmasıyla yapılmıştır. Algılama ve sürüş modu elektroniği sırasıyla geçiş-empedansı ve geçiş-direnci yükselticilerini okuma elektroniği olarak kullanmaktadır. Her bir sistem ticari ayrık devre elemanlarıyla baskı devre üzerinde uygulanmıştır. Daha sonra, açısal dönü ölçme sistemleri, iki farklı mekanik bant genişliğine sahip olacak şekilde, 100 Hz ve 30 Hz,

ayarlanan SOG (Cam-üstü-Silikon) dönü ölçerlerle test edilmiştir. Bütün durumlarda elde edilen test sonuçları sistemlerin yüksek performansını doğrulamaktadır.

100 Hz bant genişliği için, OLS_SquD sistemi 4,67 °/saat sabit kayma karasızlığı, 0,080 °/√saat açısal rastgele kayması (ARK) ve -22,6 mV (°/sn) orantı katsayısına sahiptir. 30 Hz bant genişliği için, OLS_SquD sistemi 5,12 °/saat sabit kayma karasızlığı, 0,017 °/√saat'ten iyi ARK ve -49,8 mV (°/sn) orantı katsayısına sahiptir.

100 Hz bant genişliği için, OLS_SineD sistemi 6,92 °/saat sabit kayma karasızlığı, 0,049 °/√saat ARK ve -17,97 mV (°/sn) orantı katsayısına sahiptir. 30 Hz bant genişliği için, OLS_SineD sistemi 4,51 °/saat sabit kayma karasızlığı, 0,030 °/√saat ARK ve -43,24 mV (°/sn) orantı katsayısına sahiptir.

100 Hz bant genişliği için, OLS_OffD sistemi 8,43 °/saat sabit kayma karasızlığı, 0,086 °/√saat ARK ve -20,97 mV (°/sn) orantı katsayısına sahiptir. 30 Hz bant genişliği için, OLS_OffD sistemi 5,72 °/saat sabit kayma karasızlığı, 0,046 °/√saat ARK ve -47,26 mV (°/sn) orantı katsayısına sahiptir.

100 Hz bant genişliği için, CLS_SquD sistemi 6,32 °/saat sabit kayma karasızlığı, 0,055 °/√saat ARK ve -1,79 mV (°/sn) orantı katsayısına sahiptir. 30 Hz bant genişliği için, CLS_SquD sistemi 5,42 °/saat sabit kayma karasızlığı, 0,057 °/√saat ARK ve -1,98 mV (°/sn) orantı katsayısına sahiptir.

!00 Hz bant genişliği için, ölçülmüş orantı katsayısının R^2 doğrusallığından sapması ±100°/sn ölçüm aralığında %0,0001 ve %0,0003 arasındadır. 30 Hz bant genişliği için, ölçülmüş orantı katsayısının R^2 doğrusallığından sapması ±80°/sn ölçüm aralığında %0,0002 ve %0,0062 arasındadır.

Bu performans sonuçları ODTÜ'de elde edilen en iyi sonuçlardır, taktiksel-seviye performansları sağlamaktadır ve ölçülen sabit kayma kararsızlığı ve ARK, literatürdeki silikon mikroişlenmiş dönü ölçerler için en iyi sonuçlarla kıyaslanabilmektedir.

Anahtar Kelimeler: MEMS Dönü ölçer, Dönü ölçer Elektroniği, Kontrol Elektroniği, Arabirim Devreleri, Genlik Kontrollü Salınım, Kapalı Döngü Açısal Dönü Algılama, Mikroelektromekanik Sistemler (MEMS)

To My Family

ACKNOWLEDGEMENTS

I would like to express my appreciation and gratitude to my advisor Prof. Dr. Tayfun Akın for his guidance, support, encouragement, and help throughout my graduate studies and the development of this work. It is a great opportunity for me to work with him.

I also would like to thank to Dr. Said Emre Alper for his guidance, patience, and friendly attitude. The work would be insignificant without his superb gyroscopes.

I am particularly grateful to Yüksel Temiz for the discussions on the gyroscope electronics; it is a great chance for me to start my engineering carrier near an excellent colleague like him. I also thank to the other inertial sensor group members Korhan Şahin and Kıvanç Azgın for sharing their knowledge and experience on the design and test of the gyroscope. Moreover, I am very grateful to all my friends at METU-MEMS VLSI Research group for providing a nice research environment and for their invaluable friendships.

I would like to express my particular gratitude to Yunus Sarp Yıldırım, Yakup Erdoğan, Serdar Tuğcu, Mutlu Ertürk, Serdar Orcan, Sadık Topal, Alperen Yeşil, Mustafa Karakaya, Kutlu Şahin, and İlker Şahin for their friendships throughout my undergraduate and graduate studentships.

I would like to thank TÜBİTAK for their support of my M.Sc. studies with their scholarship.

Last but not least, I am very grateful to my family, especially my parents for their invaluable support, patience, encouragement, efforts, and dedication throughout my life.

TABLE OF CONTENTS

LIST OF TABLES

TABLES

LIST OF FIGURES

FIGURES

CHAPTER 1

INTRODUCTION

At the beginning of the 20th century, the vacuum tube was used to amplify, switch and create electrical signals that lead to the development of innovative devices such as radio, television, radar, sound reduction, large telephone networks, analog and digital computers, and industrial process controller. However, the vacuum tube based technology is limited due to the large size, high power consumption, large economical cost, unreliable and inefficient operation of vacuum tube circuits [1]. Fortunately, the invention of the transistor and improvement in IC (Integrated Circuit) technology in 1950s have removed the limitations and initiated a new approach to the cutting edge technologies: development of more sophisticated and complex systems employing electronical circuits in miniature size. Today's highly developed IC fabrication technology enables not only the realization of such systems but also the fabrication of micro-scale mechanical systems integrated with electrical components which are promising due to their high performance and low cost. Such systems have dimensions in the order of micrometers and these systems are called Micro Electro-Mechanical Systems (MEMS). Vast variety of sensors and actuators has been developed thanks to MEMS technology, and these devices have been used in many fields involving military, industrial, medical, and consumer applications in the past few decades [2].

The MEMS technology has been commonly employed in the development of inertial sensors. These sensors monitor the linear and angular motions to obtain the exact position and orientation of the moving objects. Such sensors are employed in application areas like automotive industry for tracking control, handheld camera stabilization, airplane and submarine navigation, and high-g munitions where the overall size and weight of the sensors are required to be small and light [3-5]. The MEMS inertial sensors can be categorized in to two groups; (i) accelerometers which

monitor the linear acceleration of the center of the mass of the body, (ii) gyroscopes which sense angular rate of the inertial frame. Micromachined accelerometers have been used in automotive industry in mass production. Recently, micromachined accelerometers have been started to be used in military applications where inertial grade acceleration sensing is required due to their capability of sensing micro-g level acceleration inputs [2]. On the other hand, development of micromachined gyroscopes and therefore their use in industry have taken more time compared to accelerometers, as they require more elaborated electrical circuitry and advanced micromachined fabrication techniques. The performance of the today's micromachined gyroscopes is adequate for automotive applications but still not sufficient enough to provide the requirements of the navigation systems. Therefore, in many applications, especially in military applications conventional mechanical and optic gyroscopes are widely used. However, the promising properties of the MEMS gyroscopes, especially their small size, boost the research on improving the performance of the MEMS gyroscopes to a level competitive to conventional gyroscopes even for military applications. Moreover, MEMS manufacturers are willing to increase the volume of MEMS gyroscope in defense and automotive industry, mainly in IMUs (Inertial Measurement Unit), and it is estimated that market share of the micromachined gyroscope will be reached around 800 million dollar in 2010 [6].

The performance of the gyroscope is classified into three groups according to a number of performance criteria such as rate noise density, bias drift full scale range, scale factor, g-survivability, and input bandwidth: rate-grade, tactical-grade, and inertial-grarde. The definitions of the gyroscope performance criteria and the requirements of the performance grades can be found in [7] and summarized in Section 1.1. By the way, the MEMS gyroscope researches focus on the advanced mechanical design, improved and optimized fabrication techniques, high performance readout and control electronics, and high quality packaging in order to satisfy the high performance requirements of military applications. Among these, readout and external electronics are the most promising issues since the acquired experience during the past half century in IC technology and advanced IC components render possible the design and implementation of different novel

solutions to improve the performance of the MEMS gyroscope. The readout electronics is employed to convert the extremely small displacement due to angular rate input to voltage output, while the control electronics provides proper operation condition for gyroscopes. Analog [8-12] or mixed signal [13-22] electronics are commonly used in the design of the readout and control electronics, and the designs are implemented with ASICs (Application Specific Integrated Circuit), or commercial discrete components. Since the structures implemented with analog electronics are fixed and limited, resent researches generally employ digital and mixed signal electronics in order to develop novel approaches for control electronics. As a result of the ongoing researches, angular rate sensing systems satisfying the performance requirement of tactical-grade are reported [5, 20-23]. Similar to the researches in the literature, various mechanical structures are developed and fabricated with various processes to improve the performance and robustness of the micromachined gyroscopes at Middle East Technical University (METU) [24-34]. Besides, relatively little work is performed on gyroscope electronics [35, 36]. AC-bridge preamplifier [35], UGBs (unity gain buffer) [24, 35, 36], and transimpedance amplifiers [36] type readout electronics are designed and implemented with ASICs. However, due to the structural and process related problems, the implemented readout electronics do not provide the requirement of the high performance operation. Hence, transimpedance amplifiers implemented with discrete components are used as readout electronics in previous works [36]. In addition, control electronics employing manual and automatic control of the gyroscope operations are also developed and implemented with commercial discrete components [36]. Open-loop angular rate sensing systems are constructed with gyroscopes developed at METU, and the performance tests show that the systems demonstrate performances close to the tactical-grade performance levels [36]. This thesis reports development and analysis of high performance electronic circuits to improve the performance of the MEMS gyroscope developed at METU. In this research, the previously developed readout and control electronics are modified for the recently developed double-mass gyroscopes at METU and different approaches for control electronics are proposed. Open-loop and closed loop angular rate sensing systems employing these control electronics are designed, and the electronics are implemented with

discrete components in order to determine the best approach for high performance. The proposed angular rate sensing systems are tested for similar operation conditions, and their effects on the gyroscope performance and how to improve the performance of the angular rate systems further are discussed. It is verified that with the advanced electronics, the angular rate sensing systems are capable to demonstrate performances satisfying the requirement of tactical-grade applications, and the results are very close to the best performance reported in the literature.

The organization of this chapter is as follows; Section 1.1 presents a brief introduction to vibratory micromachined gyroscopes with their basic operation principle. Section 1.2 gives an overview of vibratory micromachined gyroscopes in the literature. Then Section 1.3 summarizes the complementary electronics designed for vibratory micromachined gyroscopes. Section 1.4 gives the gyroscope electronics developed at METU, Section 1.5 provides the readout and control electronics developed in this thesis and Section 1.6 presents the research objectives and thesis organization.

1.1 Vibratory Micromachined Gyroscope

Figure 1.1 illustrates the simplified view of a single proof-mass micromachined vibratory gyroscope having two degree-of-freedom (2-DOF). The proof-mass is oscillated in the drive-axis, and if the oscillating proof-mass is rotated along sensitive axis, which is perpendicular to both drive and sense axis, some of the stored oscillation energy is transformed to the sense-axis which is called Coriolis coupling. Then, the transformed energy generates so called Coriolis-induced oscillation along sense axis. Fortunately, the amplitude of the vibration along sense axis is a function of Coriolis coupling, hence, the applied angular rate, the oscillation amplitude and frequency along drive-axis, and gyroscope parameters. Therefore, if the Coriolis-induced oscillation is monitored and the parameters creating Coriolis coupling except for rate input are kept constant, the angular rotation information can be extracted from the monitored raw output. It can be concluded that two conditions should be

satisfied to use a vibratory gyroscope to measure angular motion of the proof-mass: (i) constant amplitude vibration of the proof mass along the drive axis, (ii) sensing of the Coriolis-Induced Oscillation along sense-axis.

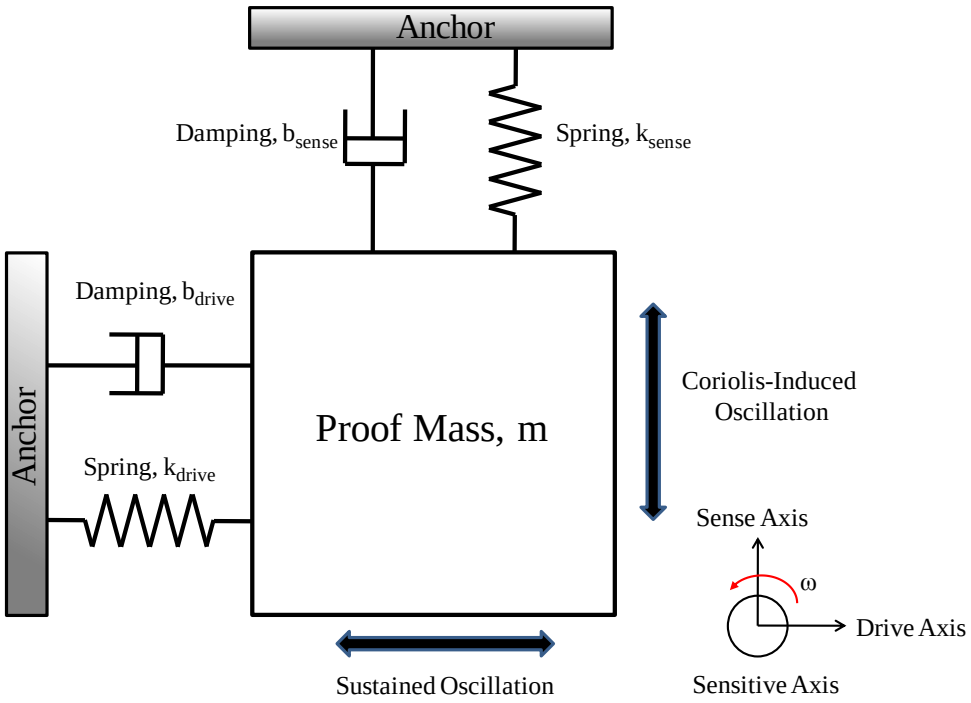

Figure 1.1: Simplified view of a single proof-mass micromachined vibratory gyroscope structure having two degree-of-freedom (2-DOF).

Special actuating and sensing mechanisms are employed to operate vibratory micromachined gyroscope properly. The sustained oscillation along drive axis may be generated using electrostatic, electromagnetic, or piezoelectric type actuators, while Coriolis-Induced oscillation is generally monitored by using capacitive, piezoelectric, piezoresistive or optical detector mechanism [2]. Among these actuation and sensing mechanisms, electrostatic actuation and capacitive sensing are widely used thanks to their easy fabrication steps. Moreover, capacitive sensing provides high sensitivity and robustness against temperature variations [37]. Accordingly, the vibratory MEMS gyroscopes developed at METU employ electrostatic actuation and capacitive sensing mechanism to obtain high performance operation.

As mentioned above, various gyroscopes are developed by using different mechanical design and electrical approaches, and their performance is determined according to a number of criteria and these criteria can be defined as [7]:

Rate Noise Density: It is the white noise generated by gyroscope mechanical structure, readout and control electronics that determines the minimum detectable rate input, hence the resolution of the gyroscope. The rate density is expressed in (deg/sec)/√Hz. Besides angle random walk (deg/√Hz) ,which describes the average error introduce by white noise with time, also defines the resolution of the overall angular rate sensing system.

Bias Drift: The rate sensor output has a non-zero output in the absence of zero rate input (ZRO), and this bias drifts due to a number of random sources in time. It is critical in gyroscope performance since the bias is the only reference for the gyroscopes' output and is expressed in (deg/hr)

Full Scale Range: It is maximum angular rate input which the gyroscope responses properly. It is expressed in ±deg/sec.

Scale Factor: It is the change in output voltage as response to unit angular rate input change and is expressed in V(deg/sec).

G-survivability: It is maximum g-shock applied that the gyroscope tolerates.

Input Bandwidth: It is the maximum frequency of time-varying rate input which gyroscope response. In other word, it also is defined as the frequency of the time-varying rate input which gyroscope's scale factor for time-invariant rate inputs drops to its 1/√2.

Regarding these performance criteria, the gyroscope can be classified into three main categories; rate grade, tactical grade, inertial grade. Table 1.1 summarizes the performance grades of gyroscope and corresponding performance criteria requirements [2].

Table 1.1: Performance requirements for three different classes of gyroscopes [2]

Parameter	Rate Grade	Tactical Grade	Inertial Grade
Angle Random Walk (deg/√hr)	>0.5	0.5-0.05	<0.001
Bias Drift (deg/hr)	10-1000	0.1-10	<0.01
Scale Factor Accuracy (%)	0.1-1	0.01-0.1	<0.001
Full Scale Range (°/sec)	50-1000	>500	>400
Max.Schock in 1 msec (g)	103	103-104	103
Bandwidth (Hz)	>70	~100	~100

1.2 Overview of Micromachined Vibratory Gyroscope

After the demonstration of the micromachined vibratory gyroscopes in the early 1980's, a vast diverse of vibrating micromachined gyroscopes have been reported, which vary owing to their operation principle, process materials, mechanical designs, fabrication processes and external circuitries. The first demonstrated gyroscopes were micromachined piezoelectric quartz gyroscopes and their batch processing is not compatible with IC fabrication techniques [2]. In addition, the success of the batch-fabricated silicon micromachined accelerometers have pushed the researches on silicon micromachined vibratory gyroscopes [2]. Eventually, the first batch-fabricated silicon micromachined gyroscope having double gamble structure was demonstrated by The Charles Stark Draper Laboratory in 1991 [8]. Unfortunately, the gyroscope exhibited an angular rate resolution of 4°/sec in a 1 Hz bandwidth due to high mechanical cross-talk between modes associated with its structure. Later, a tuning-fork gyroscope fabricated by silicon-on-glass (SOG) micromachining technology was reported by Draper Laboratory in 1993 [38]. The gyroscope has superior performance compared to the latter one and can be considered as one of the breakthroughs of that time. It has a resolution of 0.02°/sec in 1 Hz bandwidth (equivalently 0.72°/√Hz angle random walk) and bias drift of 50°/hr when operated at vacuum.

The sensitivity of a tuning fork gyroscope is increased if the resonance frequencies of gyroscope's drive and sense modes are equal. The ring structured micromachined vibratory gyroscope introduced by the University of Michigan allows easy matching of the two modes, owing to inherent symmetry of the drive and sense modes. Moreover, the structure provides electrostatic control of stiffness and mass imbalances resulting from fabrication tolerances [9]. Figure 1.2 shows SEM view of the ring gyroscope produced by The University of Michigan. The gyroscope demonstrates a resolution of 0.5 °/sec in 25 Hz bandwidth. The improved versions of the micromachined ring gyroscope which has a 150 μm thick single-crystal silicon structure was reported to demonstrate a resolution better than 11°/hr in 1 Hz bandwidth [39].

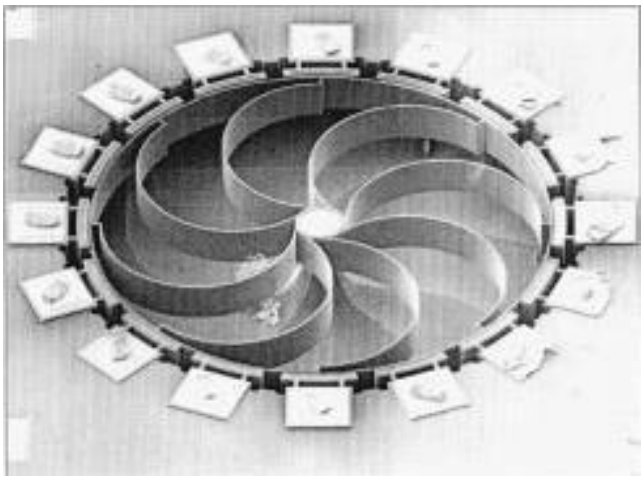

Figure 1.2: SEM view of the vibrating ring gyroscope produced by The University of Michigan [9].

As mentioned previously, the micromachined vibratory gyroscopes sense the Coriolis induced force in the sense-axis. However, the operation principle causes the gyroscope to be responsive not only to Coriolis induced force due to the angular rate input but also to other parameters like induced linear accelerations along sense axis and process variations, causing false output in the sense output. This problem can be eliminated by employing more than one proof mass as sensing element in a gyroscope. For example, Draper Laboratory [38] and Bosch Gmbh [40] reported

double mass tuning fork gyroscopes where linear acceleration sensitivity reduced. Figure 1.3 illustrates the mechanical model of the double proof-mass tuning fork gyroscope structure reported by Bosch Gmbh [40]. In this structure, the two proof masses are forced to resonate at same resonance frequencies but at opposite directions. Therefore, an applied angular rate input generates similar Coriolis induced forces at opposite direction on the proof masses whereas the linear acceleration acts on two proof masses in same direction. As a result, the difference of the distinct sense output inherently filters the linear acceleration.

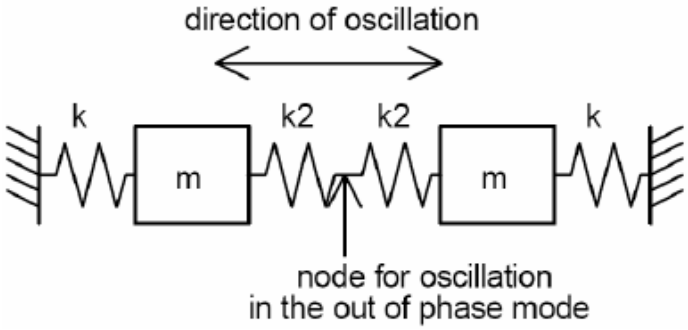

Figure 1.3: Mechanical model of the double proof-mass tuning fork gyro reported by Bosch Gmbh [40].

In addition to multi-mass structures, tuning fork gyroscopes having multi-degree-of-freedom (DOF) sense-modes were introduced by University of California Irvine in order to increase the structural robustness to environmental drifts. Figure 1.4 illustrates the schematic view of multi-degree of freedom tuning fork gyroscope produced by University of California Irvine. This structure consists of 2-DOF sense-modes and 1-DOF drive-mode in each double mass with an operation bandwidth larger than 500 Hz. These 2-DOF sense-mode forms a flat gain region which provides immunity to environmental changes and process variations [41].

The monolithic gyroscope approach, i.e. integrating CMOS circuits with mechanical structure on the same die, is another approach to increase performance of the micromachined gyroscopes by minimizing the effect of interconnection parasitic. Carnegie Mellon University developed a micromachined vibratory gyroscope by

post-processing a CMOS substrate containing gyroscope electronics [42]. The structure demonstrated a resolution of 0.5 °/sec in 1 Hz bandwidth [43]. University of Berkeley introduced another monolithic gyroscope whose operation principle based on the rotational resonance of the rotation disk [44]. Figure 1.5 shows the photograph of monolithic dual-axis gyroscope developed by University of Berkeley. The gyroscope is fabricated with Analog Devices' surface micromachining process and demonstrated angle random walk as low as 10 °/√hr.

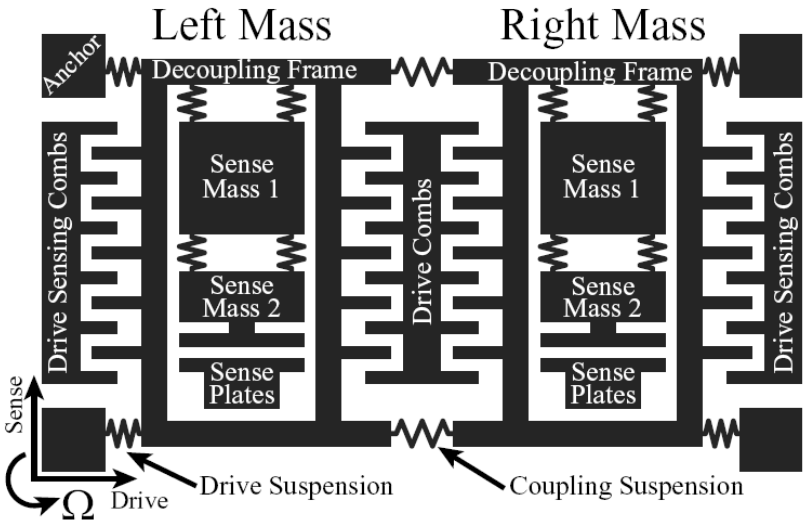

Figure 1.4: Schematic view of multi-degree of freedom tuning fork gyroscope produced by University of California Irvine [41].

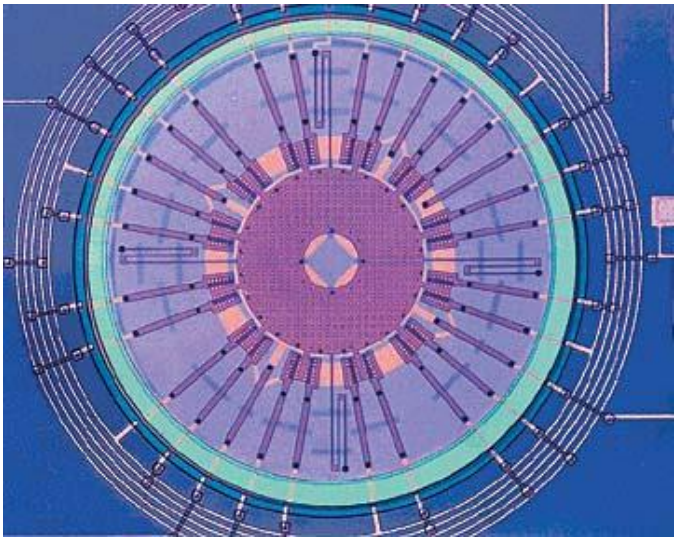

Figure 1.5: Photograph of monolithic dual-axis gyroscope developed by University of Berkeley [44]

Moreover, Analog Devices reported a surface micromachined monolithic gyroscope in 2002, using their state-of-art iMEMS process, which is an intra-CMOS micromachining process based on the BiCMOS fabrication technology [13]. Figure 1.6 demonstrates the die view of Analog Devices' iMEMS ADXRS gyroscope [13]. The angular rate sensing system consists of a tuning fork mechanical structure and on-chip signal processing electronics. The reported bias stability of iMEMS ADXRS is 50 °/hr owing to its superior dedicated electronic design. The gyroscopes are in batch-fabrication and available for consumer, automotive and industrial applications.

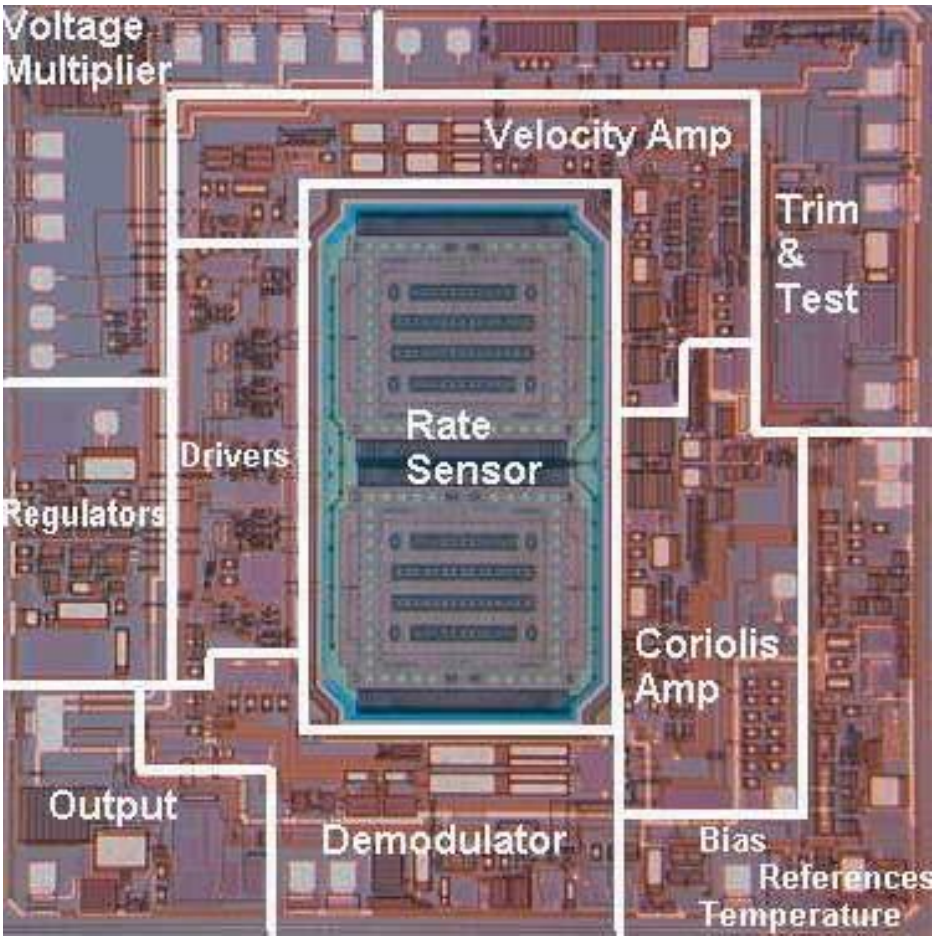

Figure 1.6: Die view of Analog Devices' iMEMS ADXRS gyroscope [13]

The researches on micromachined vibratory gyroscope at METU have been carried on by METU MEMS research group since 1998. The researches have mainly

focused on development of symmetric and decoupled gyroscopes. Various mechanical structures have been reported and these structures have been processed by using various micro machining techniques, including the dissolved wafer process (DWP) [24, 25], silicon-on-insulator (SOI) [26, 27], nickel electroforming [24, 28, 29] and silicon-on-glass (SOG) [24, 30-32] processes. The symmetric and decoupled structure minimizes the dependence of gyroscope response to thermal variations and mechanical crosstalk between sense and drive modes. Figure 1.7 illustrates the perspective view and SEM picture of the SOG fabricated advanced symmetric and decoupled structure developed at METU in 2005 [24]. The structure enables large vibrations in the drive axis thanks to varying overlap area type capacitive fingers, while it allows electrostatic frequency tuning of drive and sense modes by using high sensitive varying gap type capacitive fingers in sense-mode. The fabricated gyroscope demonstrated 15°/sec uncompensated quadrature error at 50 mTorr vacuum level.

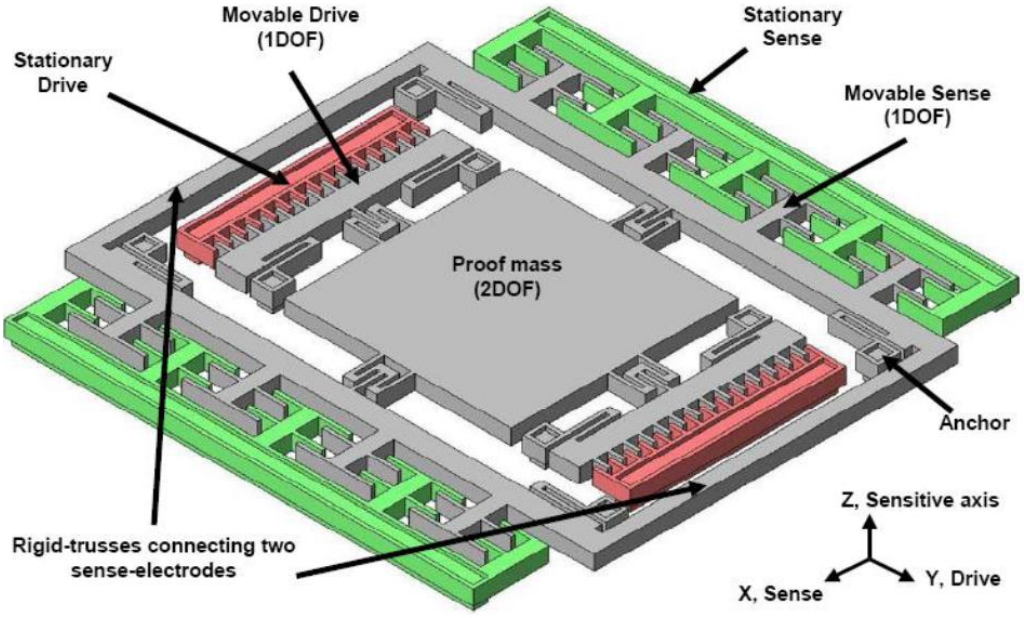

(a)

Figure 1.7: SOG fabricated advanced single-mass symmetric and decoupled gyroscope structure developed at METU in 2005: a) Perspective view of and b) SEM picture of [24]

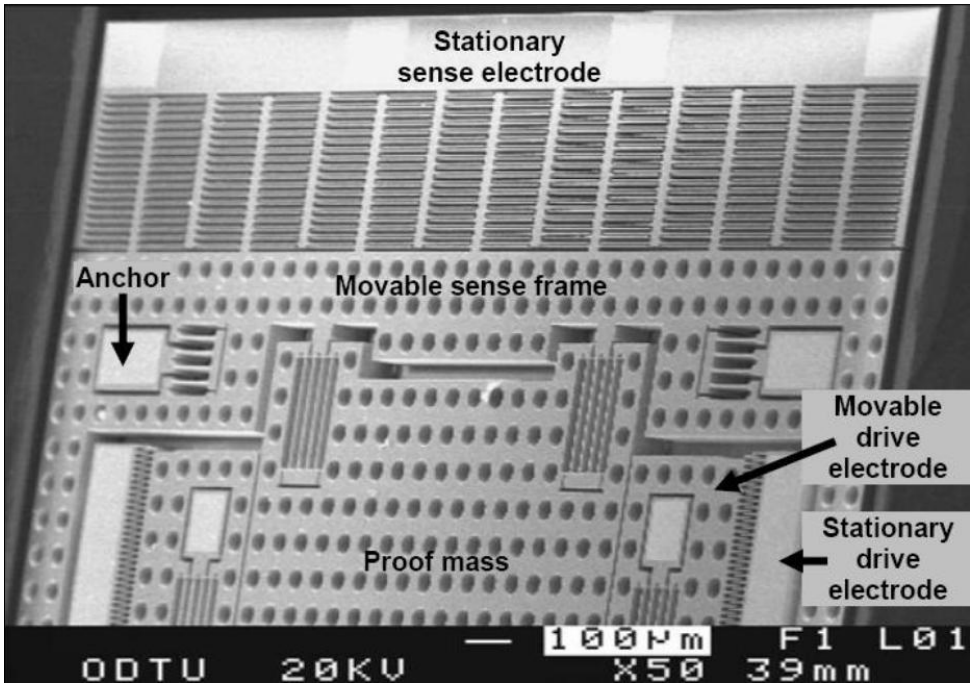

(b)

Figure 1.7 contn'd: SOG fabricated advanced single-mass symmetric and decoupled gyroscope structure developed at METU in 2005: a) Perspective view of and b) SEM picture of [24]

To decrease the acceleration sensitivity of the single-mass gyroscope structure, multi-mass gyroscope structure providing low g-sensitivity have been designed and developed at METU. Figure 1.8 shows the first multi-mass gyroscope developed at METU in 2007 [27]. The structure consists of two identical tuning fork gyroscopes mechanically coupled with a linear and symmetrically anchored ring spring. The ring spring enables the two identical gyroscopes' drive-modes to oscillate in opposite direction. Hence, the gyroscope sense any rate input as differential input whereas any linear acceleration along sense-axis is sensed as a common input. As a result, if the sense responses of the identical gyroscopes are differentiated, the effect of the linear acceleration on the gyroscope response is eliminated. The dual-mass tuning fork gyroscope was fabricated with the SOI-MUMPS process technology of MEMSCAP®, which involves double-sided DRIE (deep reactive ion etching) of an SOI waver with 25 μm epitaxial thickness and 400 μm substrate thickness, and the g-sensitivity of the gyroscope was measured as 9.3 (°/hr)/g [27].

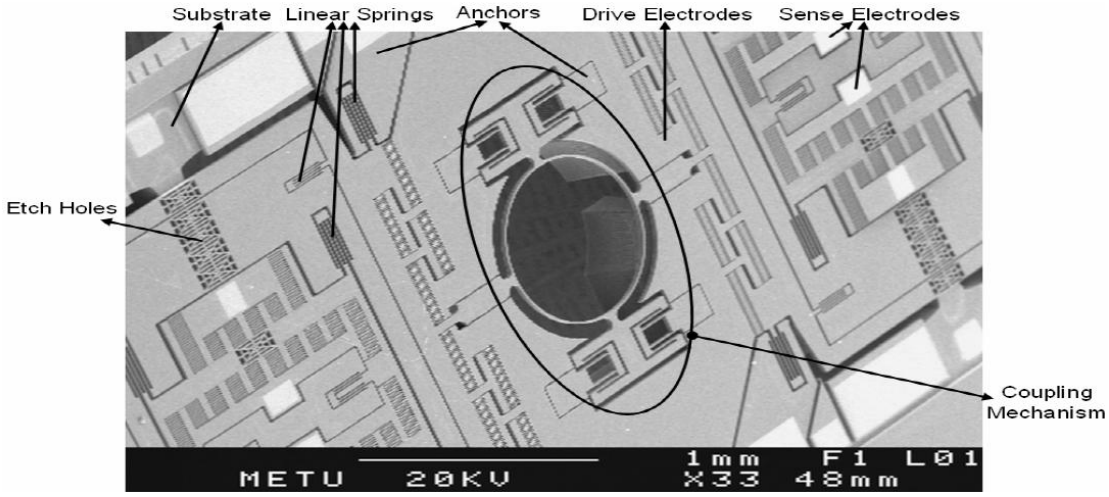

Figure 1.8: SEM view of dual-mass tuning fork gyroscope developed at METU and fabricated with SOI-MUMPS process technology of MEMSCAP® [27]

Another dual-mass gyroscope structure developed at METU was fabricated using the dissolved wafer process (DWP) and Silicon-on-Glass (SOG) processes. Figure 1.9 demonstrates the layout view and 3D view of dual-mass gyroscope developed and processed with SOG micromachining technology at METU [31]. Similar to the previous dual-mass gyroscope, the structure consists of two identical gyroscopes, that are improved versions of single mass symmetric and decoupled structure developed in 2005, and these gyroscopes are mechanically coupled with two folded beams. The gyroscope has differential actuation and single-ended sense electrodes in the drive mode while the sense-mode has differential outputs. Moreover, the force-feedback electrodes in this design render possible closed-loop angular rate sensing in the sense-mode.

To improve robustness of the gyroscope mechanical structure, there have been researches on the development of multi-degree-of freedom sense-mode gyroscopes. Figure 1.10 shows SEM picture of DOF sense-mode gyroscope fabricated with METU-SOG process [31]. The variation in the scale factor of the developed gyroscope is measured to be less than 0.38% when the vacuum level was varied between 40-500 mTorr [32].

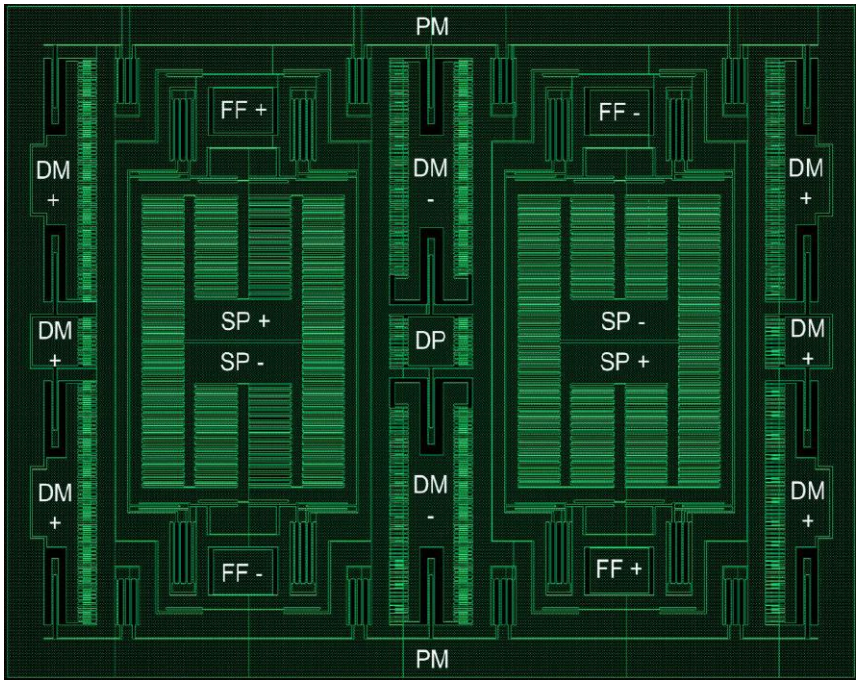

(a)

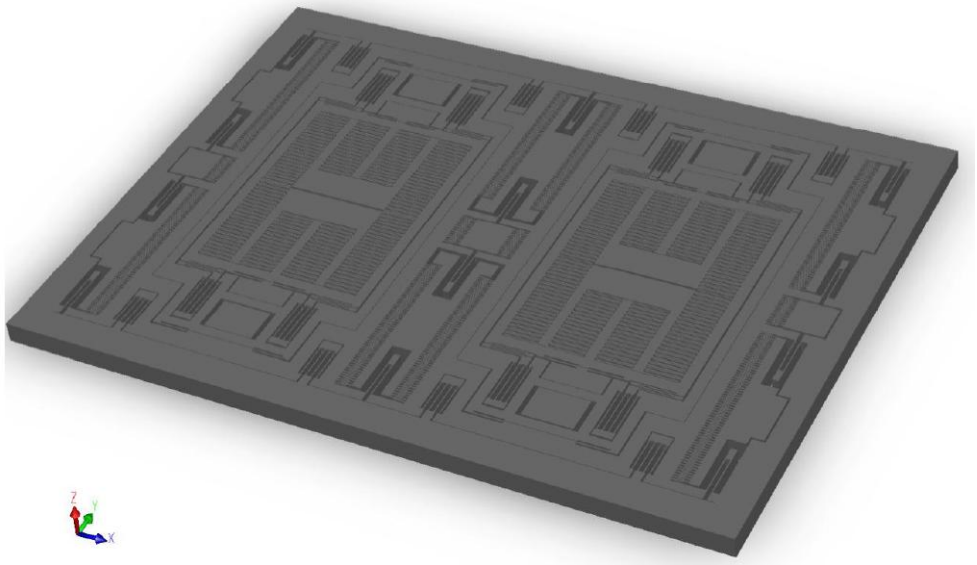

(b)

Figure 1.9: The dual-mass gyroscope developed and processed with SOG micromachining technology at METU: a) Layout view of and b) 3D view of [31]

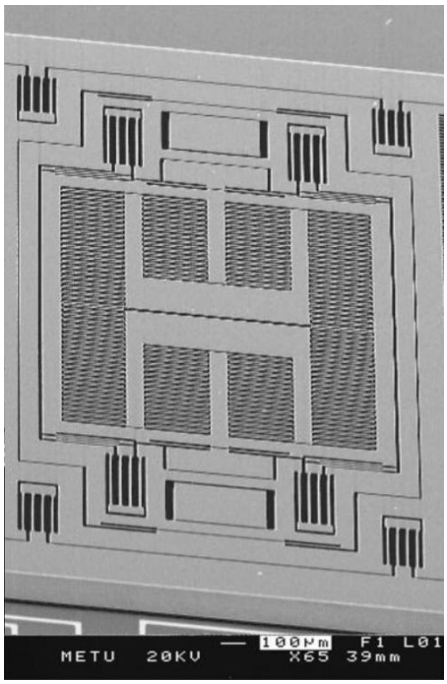

Figure 1.10: SEM picture of one half of 2 DOF sense-mode gyroscope fabricated with SOG process [31]

As it can be seen, there has been a number of works to achieve high performance micromachined gyroscopes at METU, and various fabrication techniques, and various mechanical structures. However, a similar big effort is necessary in development of high performance drive and sense mode electronics to improve the final performance of these gyroscopes, and the study presented in this thesis is a part of these efforts. Section 1.3 will first provide an overview of readout and control electronics for micromachined gyroscopes in literature, and then Section 1.4 will summarize the gyroscope electronics developed at METU. Section 1.5 will summarizes the readout electronics developed within this thesis.

1.3 Overview of Readout and Control Electronics for Micromachined Vibratory Gyroscopes

The readout and control electronics of the vibratory micromachined gyroscopes can be classified into three main parts: interface electronics, control electronics, and

sense-mode demodulation electronics. The interface electronics convert the displacement-induced capacitance changes in the mechanical structure to electrical signals. Then, the output of the interface electronics are processed by the control electronics to perform five main tasks; 1) resonating the drive-mode at its resonance frequency, 2) sustaining constant amplitude vibrations in the drive-mode, 3) canceling the quadrature error in the sense-mode output due to the mechanical cross-talk between the drive and sense modes, 4) driving the sense-mode displacement to zero in the force-feedback mode, and 5) matching the frequencies of the drive and sense modes. Finally, the sense-mode demodulation electronics extract the angular rate input related baseband signal by processing either the sense-mode interface output (in open-loop rate sensing systems) or the driving signal of the force feedback mode (in closed loop rate sensing systems).

To begin with, in case of capacitive-based micromachined gyroscopes, the capacitances and capacitance variations are very small, usualy the stationary capacitance of the sensor is order of a few hundred femto-farads ($1fF=10^{-15}$ F). Moreover, the displacement of sense-mode as a response to angular rate input is a fraction of the diameter of a silicon atom which results capacitance changes in the order of zetto-farads ($1\ zF=10^{-21}$ F). Therefore, the interface electronics should provide low-noise and parasitic capacitances to detect such small capacitance variations in high performance capacitive gyroscopes. In literature various capacitive interface circuits have been reported [9, 13, 14, 37, 45], however the most popular interface types are ac-bridge with voltage amplifiers [10, 37, 46], transimpedance amplifiers [11-13, 15, 47], switched-capacitor circuits [16, 47] and unity-gain buffers [9, 45].

Figure 1.11 shows the simplified view of ac-bridge preamplifier [46]. In this structure, a reference capacitor is connected to high impedance output of the sensor output and to the sensor and reference capacitor anti-phase clock signals are applied. The capacitance change of the sensor is monitored through voltage division. Although the structure is simple, the SNR (signal-to-noise ratio) may be affected by parasitic capacitances at the input of the voltage amplifier that decreases the minimum detectable capacitance change [14]. Therefore, this type of preamplifiers

is usually used in monolithic type capacitive sensors where parasitic capacitance due to interconnection is minimized [2].

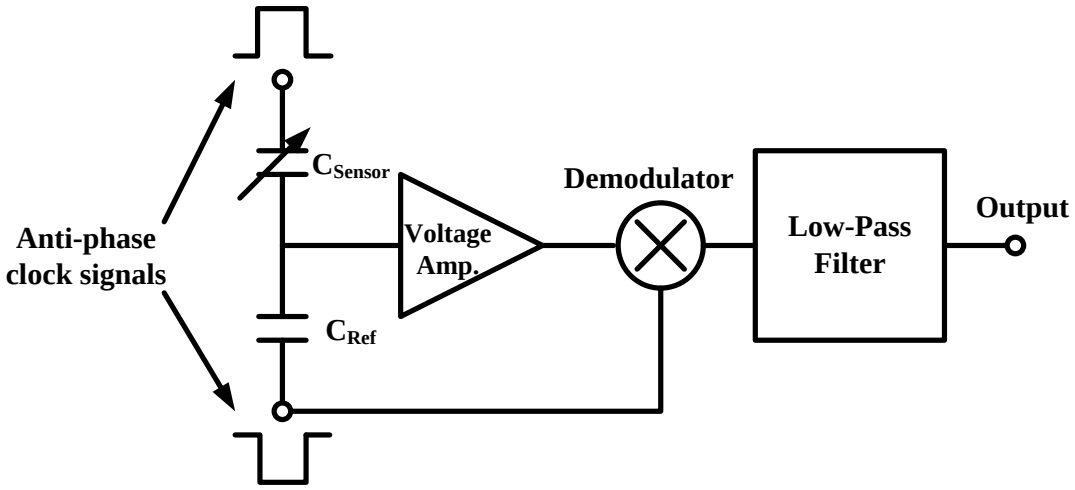

Figure 1.11: Simplified view of ac-bridge preamplifier [46]

In the transimpedance type interface, the sensor capacitor is biased to a DC voltage via an opamp and the charge pumped by the sensor is converted to voltage by impedance in the feedback path of the opamp. The impedance is usually introduced by a resistor, or capacitor, or even both. In fully differential interfaces, the high impedance outputs of the sensor are biased by the common mode feedback (CMFB) mechanism with feedback resistors. The advantage of the transimpedance amplifiers is their inherit insensitivity to parasitic capacitances at the interface input. Figure 1.12 gives the circuit schematic of fully differential transimpedance amplifier designed by Analog Devices [13]. The controlled impedance structure using matching of similar width size FETs with significantly different lengths provides an effective biasing resistance of 2.5 GΩ when the long MOSFET's on resistance is set to 50 MΩ and the current in the wide MOSFET is bypassed with a 1/50 duty cycle [13]. The minimum detectable capacitance change has been reported to be 12 zF [13].

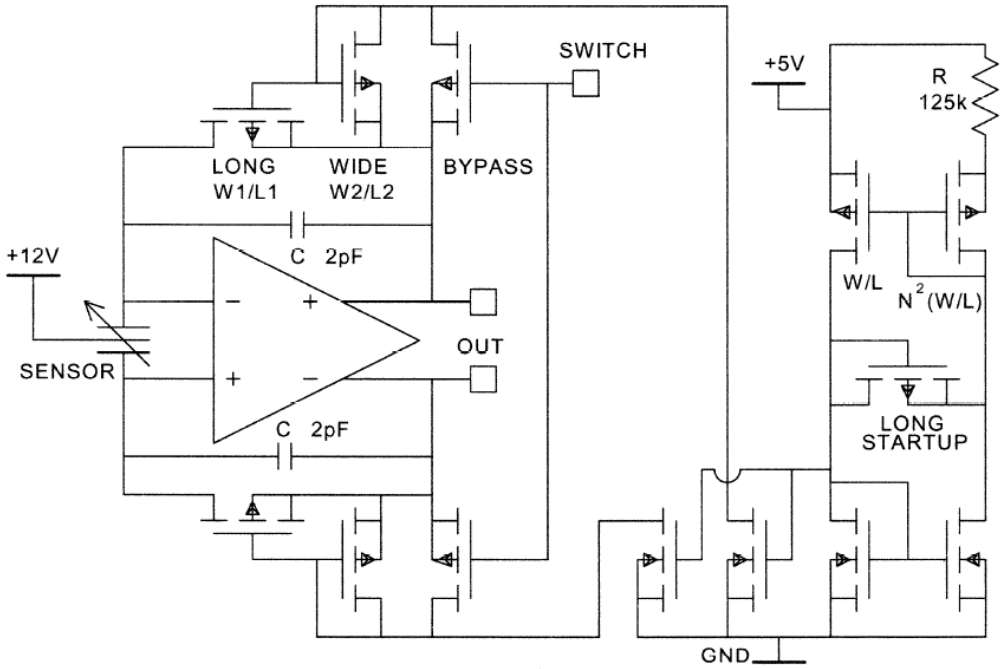

Figure 1.12: Circuit schematic of fully differential transimpedance amplifier designed by Analog Devices [13]

Moreover, in the switched capacitor type interfaces, the current pumped by sensor capacitance is integrated through a feedback capacitor and the capacitor is reset after each integration step. A sensitivity of 10 aF has been reported to be achieved by employing fully differential version of this structure [48].

Unity gain buffer (UGB) type interfaces are also commonly used in micromachined gyroscopes. The current pumped by sensor is converted voltage on the input impedance of the buffer. Moreover, the low input capacitance of the buffer provides high current-to-voltage conversion, resulting in a high SNR. In addition, the input parasitic capacitances can be minimized by using bootstrapping method in UGB [9, 35, 45]. However, the biasing of the high impedance output of the sensor in case of low input capacitance for high sensitivity requires high biasing resistor values, which may not be possible to be realized in practical applications.

In addition to interface electronics, control electronics provide proper operation conditions for vibratory gyroscopes and are generally employed to improve gyroscope performances. In most of the angular rate systems, control electronics

vibrate the drive-mode at its resonance frequency to obtain large displacement and the displacement of the vibration is sustained a predetermined value as monitoring the vibration amplitude [9, 12, 17, 49-51]. The drive-mode can be driven at its resonance frequency by constructing either PLL (phase-locked loop)-based loop [12, 18] or self-resonance loop [9, 12, 49, 51]. Figure 1.13 illustrates the self resonance loop with automatic gain control (AGC) [49]. In this loop, the drive-mode displacement is converted to electrical signal by transresistance amplifiers and the signal is shifted to baseband to extract the magnitude of the vibration. Then, the PI controller adjusts the gain of the VGA (variable gain amplifier) to satisfy the oscillation criteria and set the vibration amplitude to a value determined by V_{ref}. Instead of analog controllers, similar AGC self resonance loop structures have been reported to be constructed by using digital controllers [17, 18, 52].

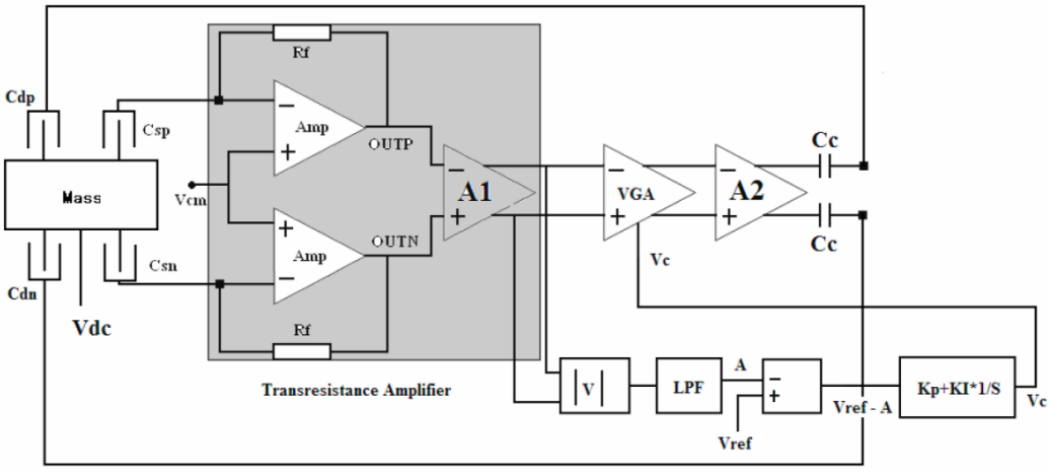

Figure 1.13: Self-resonance loop with automatic gain control (AGC) [49]

The sense-mode interface output is composed of amplitude-modulated rate signal and quadrature error both at the drive-mode resonance frequency with a 90° phase difference. Hence, a phase sensitive AM demodulation can be used to process the raw sense-mode output to obtain a baseband angular rate input in open-loop rate sensing systems. Figure 1.14 shows the complementary electronics designed for micromachined gyroscopes developed at Georgia Institute of Technology [18]. In this structure the drive-mode is sustained constant-amplitude vibration at its

resonance frequency by a PLL-based AGC loop. In addition, the differential sense-mode outputs are converted to a single-ended output, and the AM signal is transferred to baseband by a demodulator composed of a multiplier, after which a low-pass filter (LPF) extracts the rate output.

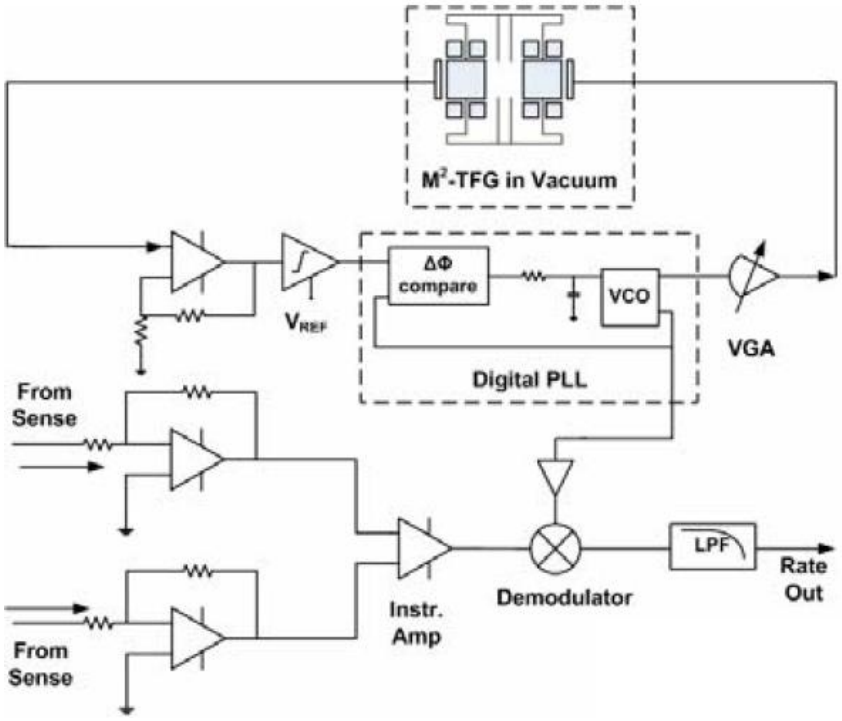

Figure 1.14: Simplified block diagram of the drive-mode PLL-based drive loop and sense-mode open-loop rate sensing designed for micromachined gyroscopes developed at Georgia Institute of Technology [18].

Moreover, in closed-loop rate sensing systems, the sense-mode displacement due to angular rate input is driven to zero by applying voltage to force-feedback electrodes in the sense-mode [9, 17, 19-21, 53]. Figure 1.15 gives the AGC analog force-feedback loop developed by Seoul National University [54]. In this structure the velocity of the sense-mode, which is the result of the superposition of Coriolis-induced and quadrature displacement, is monitored by rectifier and LPF and compared with reference signal, which is usually ground level. Then, the controller processes the error signal in order to drive the sense-mode displacement to zero and controller output is multiplied by a sinusoidal wave signal having a unit amplitude at

sense-mode output signal frequency. Besides, since the phase of multiplier signal is determined by Coriolis signal and quadrature error signal, the resultant multiplied signal, hence the force-feedback signal inherits components in phase with both Coriolis-signal and quadrature error signals. As a result, the force-feedback signal is an AM signal and when it is demodulated phase sensitively, an output voltage related to angular rate input is obtained. It has been reported that the closed loop system has a resolution of 5 °/hr in 1 Hz bandwidth and increases the operation bandwidth of the system around 70 Hz [54]. Another approach of analog AGC force-feedback loop is to construct two different loops to drive displacement due to Coriolis force and quadrature error to zero separately [9, 22]. In these structures, the output of two loops are added and applied to the force feedback electrodes, therefore feedback loop not only eliminates the quadrature error, but also allows to implement electrically tunable mechanical structures minimizing the crosstalk between sense and drive modes are also possible [22].

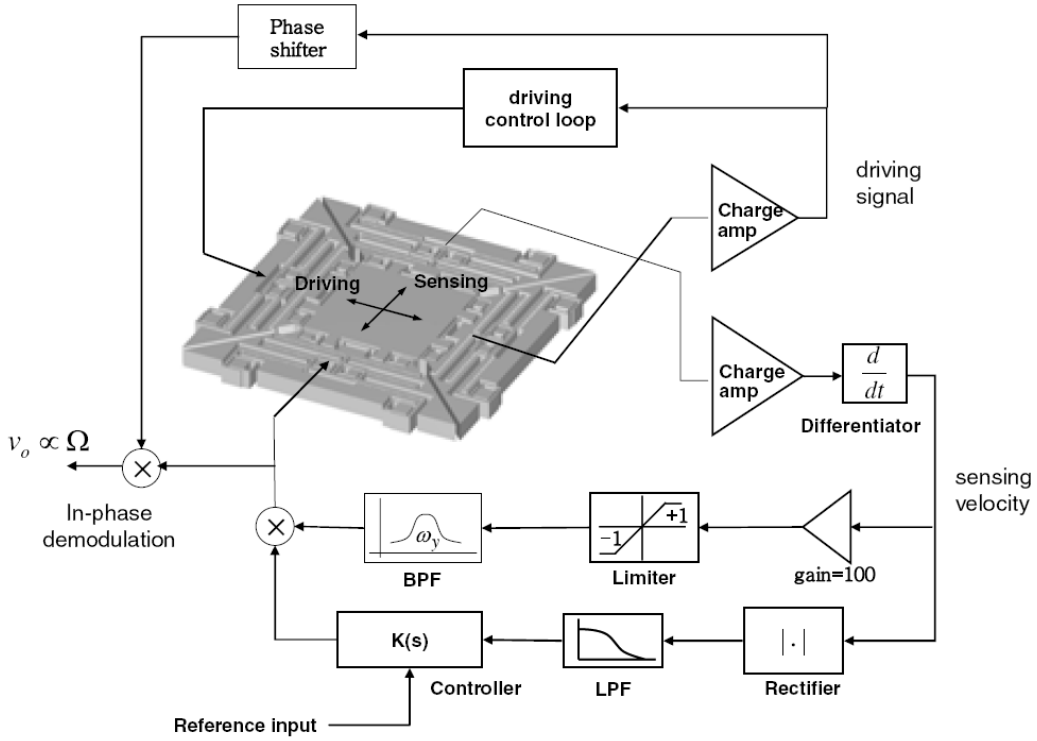

Figure 1.15: AGC analog force-feedback loop developed by Seoul National University [22].

The closed-loop rate sensing systems can also be realized by digital control electronics [20, 21, 53]. ∑Δ (delta sigma) based interface and/or ∑Δ modulators are used to convert the gyroscope oscillations to the digital domain with high resolution. The digitalized signal enables complex control algorithms to be realized in order to improve the gyroscope performance and minimize the low frequency noise source [21]. Figure 1.16 demonstrates the system-level overview of the digital closed-loop rate sensing system developed in [53]. The performance measurement of this architecture gives a resolution of 0.055 °/s/√Hz. Moreover, the ∑Δ based digital controlled MEMS gyroscope developed by Imego AB has been reported to have a 0.003 °/s/√Hz resolution and 3.2 °/hr bias instability [21].

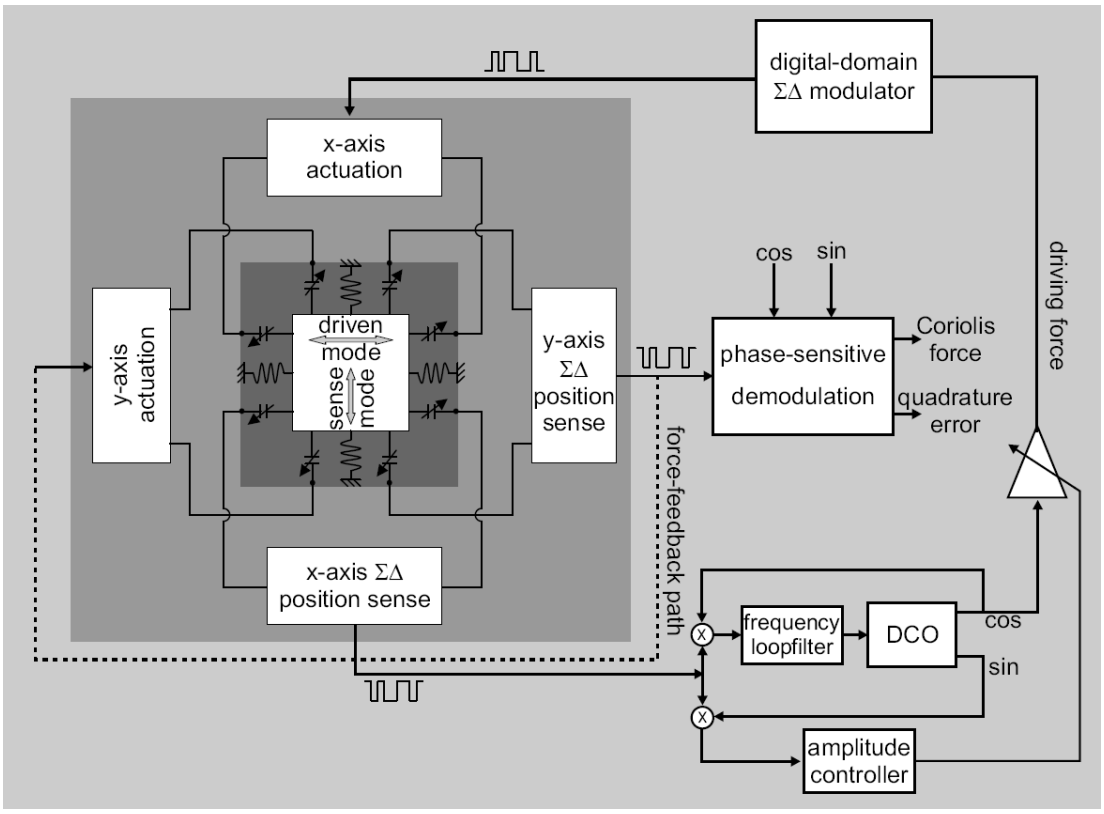

Figure 1.16: System-level overview of digital closed-loop rate sensing system based on ∑Δ modulation [53]

As mentioned previously, matching of drive and sense modes' resonance frequencies boost the mechanical gain of the angular rate sensing mechanism. The researchers at

Georgia Institute of Technology reported a mode-matched gyroscope which demonstrates a bias instability as low as 0.15 °/hr with a 0.003°/√hr angle random walk [23]. The gyroscope monitors the quadrature error, and adjusts the voltage applied to the proof mass by employing a digital controller. However, the bandwidth of the developed gyroscope is less than 10 Hz. Another mode-matched gyroscope developed by Northrop Grumman that has both closed-loop rate sensing and electrically tunable quadrature cancellation mechanism, has an angle random walk less than 0.4 °/h, and a bias stability smaller than 5 °/h with a operation bandwidth larger than 500 Hz [22].

In conclusion, different interface architecture, control electronics and sense-mode electronics have been proposed to improve the performance of the gyroscopes. The control electronics are mainly constructed by using classical control theory approach. In addition, more complex control approaches such as adaptive control [55, 56] and H∞ [57] algorithms are also introduced. The adaptive control extracts the system variables and updates the system controllers during operation, hence it does not require the exact gyroscope parameters, while H∞ is applicable to problems involving multivariable systems, which is the case in the gyroscope and minimizes the output and control inputs for proper operation. However, these algorithms are beyond the scope of the thesis.

1.4 Gyroscopes Electronics Developed at METU

Various interface electronics have been designed and implemented at METU. Closed-loop AC-bridge with correlated double sampling (CDS) mechanism is the first capacitive type interface developed at METU [33]. The test result verifies the proposed architecture has a 45 mV/fF capacitance change to voltage sensitivity. However, the interface couldn't be tested with a MEMS gyroscope. Following interface developed at METU is capacitive UGB (unity gain buffer) which biases the high impedance output of the gyroscope with a MOS transistor operating in cut-off region [24, 44]. Although the structure promises owing to its low input capacitances,

the biasing mechanism doesn't bias the high impedance not properly that leads instabilities in the gyroscope operation.

The next generation interface electronics developed at METU is single ended and differential source follower circuits biased with a subthreshold transistor [35]. Figure 1.17 illustrates the schematic of the single-ended source follower biased with subthreshold NMOS transistor. The floating voltage source connected between gate and source of the biasing transistor enables the channel resistance of the transistor to be controlled. The performed noise test of the proposed interface structure verify that the structure capable of sensing 58.3 zF capacitance change in 1 Hz bandwidth. Moreover, it has been reported that the interface hybrid connected to SOG single mass gyroscope developed at METU has been reported to have 2.158 °/√hr angle random walk and 124.7 °/hr bias instability. However, the proposed structure has some drawbacks. To begin with, the DC voltage drop on the input transistor of the source follower should be compensated by adjusting the voltage value of the voltage source connected to source of the biasing transistor manually. Furthermore, the channel resistance is process dependent and the structure has a low PSRR (power supply rejection ratio).

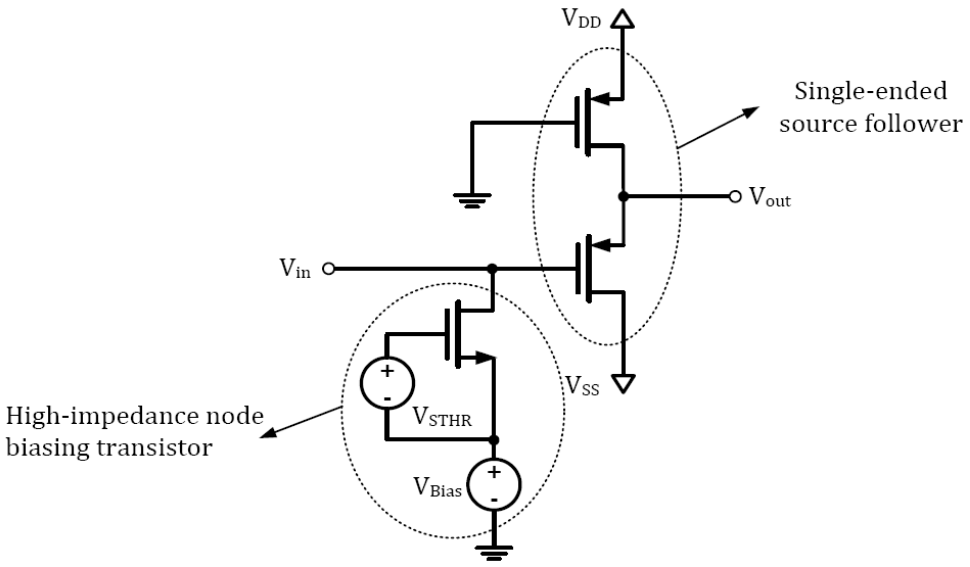

Figure 1.17: Single-ended source follower biased with subthreshold NMOS transistor [35]

There also have been researches on improving the previously introduced interface structures reported in [24, 36, 45, 58]. Figure 1.18 shows the schematic view of a modified UGB [36]. This modified UGB has a 2.71 fF input capacitance according to simulation results. The structure is used to introduce resistive and capacitive type UGB. In resistive UGB, a 200 kΩ interface resistor ,which is implemented with low-doped polysilicon, biases the high impedance node of the gyroscope whereas subthreshold PMOS and NMOS type transistors each having 800 MΩ effective biasing resistance are employed to bias the high-impedance node of the gyroscope in capacitive UGB considering 10 kHz operation frequency. Both interface types demonstrate unity gain with a phase error less than 1° and a thermal noise level around 60 nV/√Hz. However, an unpredicted DC offset error is observed at the output of both UGB resistive and UGB capacitive type interfaces due to the process variations and transistor mismatches. Nevertheless the performance of interfaces hasn't been tested with a MEMS gyroscope.

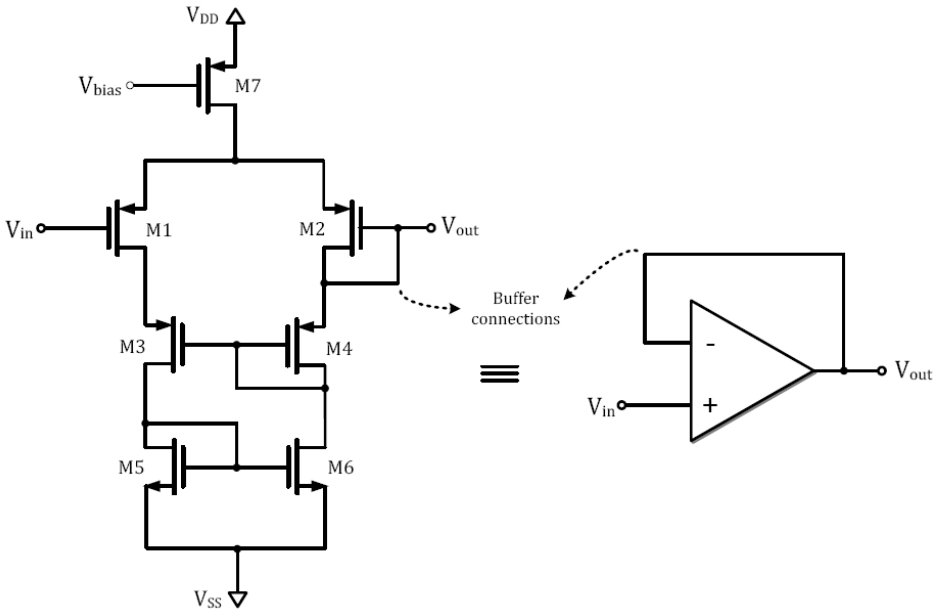

Figure 1.18: The schematic view of modified UGB [36]

Transresistance and transcapacitive type CMOS interfaces have been also developed [36]. Although the transresistance type interface biases the high-impedance node,

the interface also has output offset problem at its output. Moreover, the transcapacitance type interface can't operate properly since the interface output cannot be biased to a DC value. In this structure a MOSFET operating in threshold region is employed to bias the output node of the opamp. The channel resistance of MOSFET in subtreshold region is highly dependent to the process, and the test results of the transcapaccitance type interface show that the channel resistance of the MOSFET is much larger than the designed value, thus it is concluded that such a large resistance cannot bias the output of the interface opamp.

In addition to interface electronics, control electronics and sense-mode rate sensing electronics are also developed at METU. Figure 1.19 demonstrates the circuit view of self-resonance loop with manual amplitude control [36]. In this circuit, the drive-mode oscillation is sensed by a capacitive interface and to satisfy self-oscillation criteria the signal 90° phase shifted by a differentiator. Then, the phase-shifted signal converted a square wave and the amplitude of the actuating signal is manually adjusted by an attenuator stage in order to sustain the vibration amplitude to a desired value. The circuit was implemented with discrete components and was tested with single-mass SOG [24] and SOI MUMPS [34] gyroscopes. In these tests open-loop rate sensing which is a simple AM demodulation was used as sense-mode electronics and 124.7 °/hr, 106 °/hr bias instability and 2.16 °/√hr, 4.8 °/√hr angle random walk were reported as best performances for SOG and SOI MUMPS gyroscopes respectively [36].

The self-resonance loop is improved by introducing a controller to sustain constant vibration automatically. Figure 1.20 shows the circuit schematic of drive loop with automatic amplitude control and open-loop rate sensing system developed at METU [36]. In this circuit transresistance type interface converts the drive-mode oscillation to voltage and the interface output is amplified by a controllable VGA (variable gain amplifier). Then the amplified signal is applied to drive-mode actuators. The tests of this circuit with single mass SOG gyroscope demonstrate superior performance compared to previous gyroscope systems. The bias instability and angle random walk of the gyroscope system were measured to be as low as 12.2°/hr and 0.126 °/√hr when the mechanical bandwidth is around 10 Hz. The same approach is

adjusted to vibrate differential input and output double-mass SOI gyroscope [27] and the bias instability and angle random walk were found as 102.4 °/hr and 2.19 °/√hr.

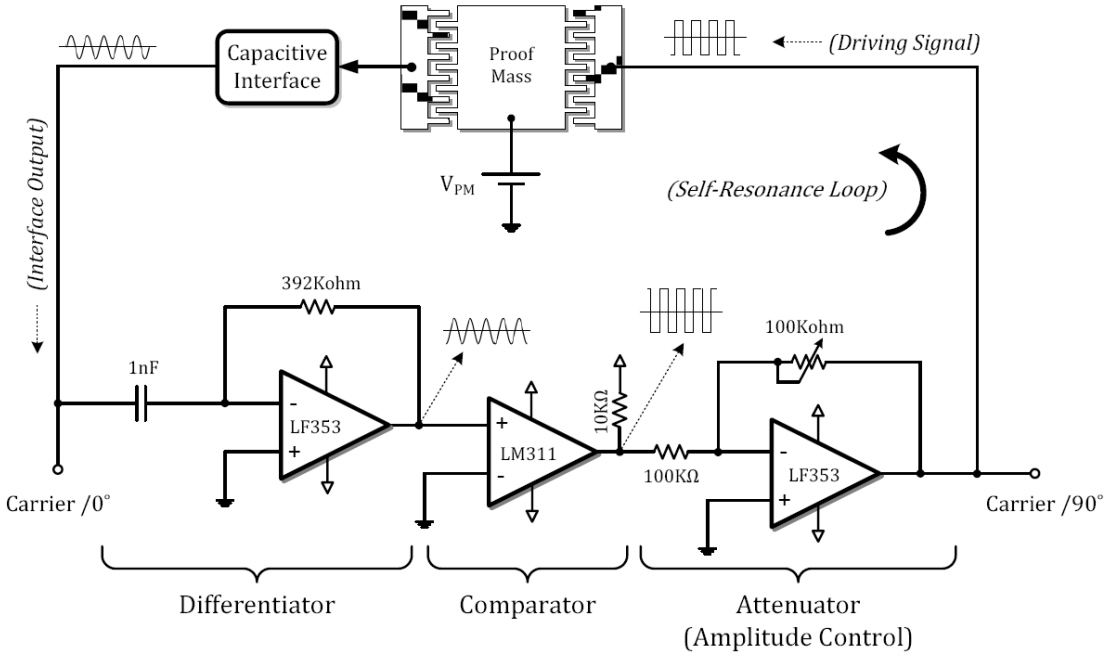

Figure 1.19: Circuit view of self-resonance loop with manual amplitude control [36].

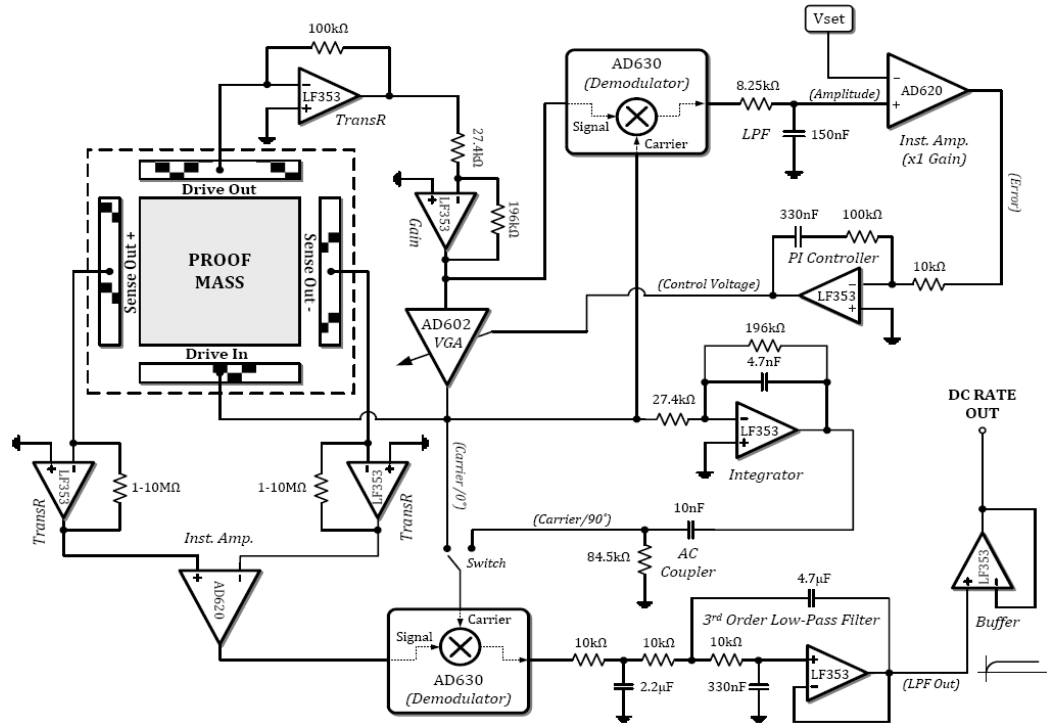

Figure 1.20: Circuit schematic of automatic amplitude control drive loop and open-loop rate sensing developed at METU [36].

In summary, researches have been carried on to develop the interface and control electronics at METU. Although the interface electronics processed with CMOS technology haven't provided satisfactory performance, the research on control and sense-mode electronics show that the gyroscope performance is closely related to gyroscope electronics and superior gyroscope performance can be obtained by employing advanced electronics. The previous works employed square and sinusoidal wave signals at drive-mode mechanical resonance frequency to oscillate the drive-mode. However, since the center frequency of the sense-mode output signal is also at the drive-mode resonance frequency, the coupling of the electrical signals at this frequency to the sense-mode output introduce error in the demodulation of the raw sense-mode output. Moreover, any variation in these electrical signals, such as noise and bias drift, is added to the variations in the sense-mode, and hence degrades the performance of the angular rate sensing systems. Therefore, in this thesis, a new approach employing an off resonance frequency, which inherits no electrical signal at resonance frequency, is proposed to oscillate the drive-mode at resonance and self-oscillation loop of the proposed driving approach is designed. In addition the control electronics in previous work is updated for the double-mass gyroscopes developed at METU and the performance of the all approaches is tested in order to investigate their effects on the performance of the angular rate sensing systems. Besides, in previous work only open-loop angular rate sensing systems are designed and implemented. In this work, a closed-loop angular rate sensing system is proposed in order to improve the robustness of the system against mechanical structure and ambient variations. The previous section will give the details of the readout and control electronics in this thesis in more detail.

1.5 Gyroscope Electronics Developed in This Thesis

The work presented in this thesis reports the development of the high performance readout and control electronics. Transresistance and transimpedance type interfaces are designed and implemented with discrete components as readout electronics for SOG gyroscopes developed at METU, and four different AGC (automatic gain

control) loops for the drive-mode are developed with three different driving approaches: (i) the square-wave driving signal at the drive-mode mechanical resonance frequency, (ii) the sinusoidal-wave driving signal at the drive-mode mechanical resonance frequency, and (iii) the off-resonance frequency driving signal. Then, open-loop and closed-loop sense-mode electronics are designed, and four different open-loop rate sensing systems, and one closed-loop rate sensing system are constructed with four different AGC loops, and square-wave driving signal AGC loop, respectively. The first phase in this research is the development of the readout electronics. In the previous works, transresistance type interfaces are developed and implemented with discrete components [36]. The previously developed transresistance type interfaces employ an opamp to DC bias the high impedance output of the gyroscope for a proper capacitive sensing mechanism, and a resistive negative feedback to convert the induced current in the capacitive sensing mechanism to a voltage output. However, a high resistance for high responsivity leads to instability, and hence oscillation, in the interface network. In this work, the reason of this instability is investigated, and it is found out that the feedback resistor together with capacitance introduced at the inverting input of the interface opamp creates a zero degrading the stability, hence a capacitance is added to parallel to the feedback resistor to compensate the unwanted zero. Moreover, transimpedance type interfaces having a capacitive feedback are also designed and implemented. The readout electronics are tested with SOG gyroscopes developed at METU, and the test results are used to construct the mathematical model of the gyroscope.

In the second phase, four different AGC self-oscillation loops are designed for drive-mode. To begin with, in previous work, the square-wave is employed to construct self-oscillation loops to oscillate the drive-mode at its resonance frequency; however, these loops do not include automatic amplitude control [24, 36]. In [31], it is shown that if the drive-mode displacement amplitude is not controlled automatically, the displacement amplitude is changed by the angular rate input, which is not acceptable for high performance applications. Therefore, an automatic amplitude controller is added to the previous approach, and a square-wave driving signal AGC loop is designed. Secondly, sinusoidal-wave driving signal AGC loop is designed and tested with single-mass SOG gyroscopes developed at METU in [36]. Although the AGC

loop provides automatically controlled sustained oscillation, the controller design of this loop does not investigate the start up condition, and the self-oscillation loop make an overshoot larger than 30 %, which may lead structural deformation and malfunction in the gyroscope operation. Hence, in this work, the start-up condition of the loop is investigated and a controller design approach including the start-up response of the system is proposed. Moreover, the self-oscillation loop is updated for double-mass SOG gyroscopes, and the test results show that the proposed controller provides an overshoot less than 13%. Finally, an off-resonance frequency driving signal having no frequency component at the drive-mode mechanical resonance frequency is proposed to oscillate the drive-mode at its resonance frequency. Since, the center frequency of the sense-mode output is also at the drive-mode resonance frequency, the proposed driving approach eliminates the performance degradation due to the electrical coupling between the sense-mode electrode and electrical signals at the drive-mode resonance frequency. The off-resonance frequency is constructed by modulating the DC biased sinusoidal signal at resonance frequency by a carrier signal at half of the resonance frequency. Two different AGC self-oscillation loops, which control the magnitude of either the DC bias, or the sinusoidal signal, are constructed by using this off-resonance frequency driving approach. The simulation and test results verify that the proposed self-oscillation loops oscillate the drive-mode at its resonance frequency.

In third phase, open-loop and closed-loop sense-mode electronics are designed. The open-loop electronic is similar to the previous work [24, 36], which is an AM demodulation circuit. On the other hand, the closed-loop sense-mode electronic is similar to the square-wave driving signal AGC loop, however, the loop is a negative feedback loop and the loop tries to null the sense-mode displacement in this case.

Finally, four open-loop angular rate sensing systems are constructed with open-loop sense-mode electronics and the four proposed AGC loops, while a closed loop rate sensing system is constructed with the closed-loop sense-mode electronics and square-wave driving signal AGC loop. Then, performance tests of the all systems are done in order to determine the scale factor, the scale factor nonlinearity, zero rate output, angle random walk and bias instability of the systems. The test results show

that all open-loop rate sensing systems provide the bandwidth, the angle random walk and the bias instability requirements of the tactical-grade applications whereas the angle random walk and bias instability of the closed-loop angular rate sensing system is sufficient enough for tactical-grade applications, however the bandwidth of the system could not be tested due to the set up incapability. The obtained test results are the best results obtained at METU, and comparable with the best results reported in the literature.

1.6 Research Objectives and Thesis Organization

The goal of this research is to develop and analyze high performance readout and control electronics for MEMS gyroscopes developed at METU. These electronics consist of different types of sensor interfaces, different self-oscillation control electronics, open-loop and closed-loop angular rate sensing systems implemented with the commercial discrete components. The specific objectives of this study are as follows:

1. Analysis of the double-mass SOG MEMS vibratory gyroscopes and development of the mathematical model of the electromechanical conversion of the capacitive actuating and sensing mechanism. This model of the actuating mechanism should enable the calculation of the generated electrostatic force on the moving part of the vibratory gyroscope when the electrical signals having different waveforms applied to the capacitive actuators of the gyroscope. Moreover, the overall gyroscope should be modeled for simulations of the readout and control electronics

2. Design and implementation of different fully-functional open-loop angular rate sensing systems for double-mass SOG gyroscopes with discrete components. The systems include single-ended transresistance type interface for drive-modes and transimpadence type interface for sense-modes. The advanced control electronics should process the single-ended output of the

drive-mode transresistance amplifier and generate differential driving signals to provide self-triggered, sustained self-oscillations at frequency close to the resonance frequency in the drive-mode robust against the sensor parameters and ambient conditions. Control electronics oscillating the drive-mode at resonance frequency by applying driving signals at resonance frequency and off-resonance frequency should be investigated theoretically and designed. The sense-mode electronics should convert the modulated sense-mode output to the baseband signal which is proportional to the applied angular rate input. The systems should be implemented on compact and well-designed PCBs and should be characterized in terms of scale factor, the scale factor linearity, zero-rate output, angle random walk and bias instability.

3. Development of a fully-functional closed-loop angular rate sensing system for double-mass SOG gyroscopes. The closed-loop angular rate sensing system should be similar to one of the open-loop angular rate sensing systems except for sense-mode electronics in order to examine the effects of closed-loop rate sensing on system performance. In addition, the control electronics in the sense-mode should nullify the induced Coriolis acceleration on the proof-mass by generating differential signals which are applied to the force feedback electrodes. Moreover, the amplitude of these differential signals, thus output of the angular rate sensing system should be proportional to the applied angular rate input.

The organization of the thesis and the contents of the following chapters are summarized as follows:

Chapter 2 briefly gives the theory of the vibratory gyroscopes and introduces the governing equations of gyroscope operation and transduction mechanism. Then, it provides the electrical and mathematical model of the mechanical sensor constructed by the equations introduced. The theory behind the gyroscope interfaces and the criteria and principles of the sense-mode and drive-mode electronics are also given in this chapter.

Chapter 3 explains the design details of readout and complementary electronics of double-mass SOG vibratory gyroscopes developed at METU and gives the simulation results of designed electronics with mathematical model of the gyroscope. The chapter starts with the description of transresistance and transimpedance type interfaces. Then, it describes four different drive-mode AGC (automatic gain control) loops implemented with the commercial discrete components and gives the modeling and controller design for these loops. Moreover, the operations of the proposed AGC loops are verified through system-level simulations in SIMULINK. Finally, the open-loop and closed-loop rate sensing mechanism designed for vibratory gyroscope are introduced and simulated.

Chapter 4 presents the results of tests performed with angular rate sensing systems developed in this research. First, the double-mass SOG gyroscopes developed at METU with discrete interfaces are characterized. Then, the operations of the proposed control electronics are verified by monitoring the actuation and sensing signals. Moreover, the performance characteristics of the proposed angular rate systems are given in terms of scale factor, scale factor linearity, zero-rate offset, angle random walk and bias instability.

Finally, Chapter 5 summarizes the research and provides the conclusion. Furthermore, suggestions for following research are given.

CHAPTER 2

VIBRATORY GYROSCOPE THEORY

This chapter introduces the vibratory gyroscope theory. Section 2.1 explains the basic theory of the vibratory gyroscopes and analyzes their drive-mode and sense-mode mechanism. Section 2.2 presents the actuation and sensing mechanism of the vibratory gyroscopes, gives the principles of the mechanical-electrical domain and electrical-mechanical domain conversions by using a parallel-plate capacitor. Section 2.3 gives overall mathematical model of the vibratory gyroscope and models the gyroscope in electrical domain by using analogy between electrical and mechanical domain. Section 2.4 describes the type of the interface electronics and presents the criteria and principles of the drive-mode and sense-mode electronics. Section 2.5 provides a summary for this chapter.

2.1 Basic Theory of Vibratory Gyroscope

The operation of a vibratory gyroscope is based on "the transfer of some energy of resonating drive-mode to the perpendicularly placed sense-mode due to the Coriolis acceleration" [31]. Transferred energy creates a displacement in sense-mode, and the amount of displacement is directly proportional to the angular rate of the rotation which is orthogonal to the resonating drive-mode plane. Hence, by sensing this displacement at the sense-mode electrodes, the magnitude of the angular rotation is converted to an electrical signal. The mechanical cross-talk from the drive-mode to the sense-mode due to the misalignments and fabrication imperfections results in a large output offset in this electrical signal although there is a zero rate input. This large output offset is called the quadrature error. The gyroscopes used in this study have fully-decoupled and balanced structures to minimize the mechanical cross-talk

between the vibrating drive-mode and sense-mode. To achieve the fully-decoupled structure, the drive and sense electrodes' motion are limited to one-degree-of-freedom (1-DOF), whereas the proof-mass has a two-degree-of freedom (2-DOF). In addition to the quadrature error, any acceleration input along the sense-mode causes undetermined errors at the sensor output (g-sensitivity) [34]. To suppress the g-sensitivity, the gyroscopes in this research have two identical masses, which are vibrated along the same drive axis with a 180 ° phase difference. Therefore, any rate input to the gyroscope results in equal magnitude but opposite directions displacements in the sense-modes of the two masses, whereas acceleration input along sense axis generates equal and same direction displacements. In other words, thanks to the this structure, the rate input is sensed as differential mode input, and the acceleration input is sensed as common mode input; so that the differentiation of the sense-mode outputs of two masses has only rate input data and a g-insensitive gyroscope is achieved. In the following subsections, the dynamics of mechanically decoupled and g-insensitive gyroscope are investigated.

2.1.1 Drive Mode Mechanics

The drive-mode of the gyroscope can be considered as a mechanical resonator and be modeled with a second-order mass-spring-damping system with flexible beams, 1-DOF drive-mode mass, and the viscous damping of the surrounding air. For such a single 1-DOF damped system, the relation between displacement and applied force can be expressed as

$$\frac{X_D(\mathrm{s})}{F_D(\mathrm{s})} = \frac{1}{m_D.s^2 + b_D.s + k_D} \qquad 2.1$$

where F_D is the force acting along the drive-mode axis, m_D is the mass, X_D is the displacement, b_D is the damping factor, and k_D is the spring constant of the drive-mode. Equation 2.1 can be defined in terms of the resonance frequency, ω_D, and quality factor of the system, Q_D, as

$$\frac{X_D(s)}{F_D(s)} = \frac{1/m_D}{s^2 + (\omega_D/Q_D).s + \omega_D^2} \quad 2.2$$

where

$$\omega_D = \sqrt{\frac{m_D}{k_D}} \quad 2.3$$

$$Q_D = \frac{\sqrt{k_D.m_D}}{b_D} \quad 2.4$$

The maximum displacement for the applied force is achieved when the applied force is at drive-mode resonance frequency, $s = j.\omega_D$ and for this case Equation 2.2 simplifies to

$$\frac{X_D(j.\omega_D)}{F_D(j.\omega_D)} = \frac{Q_D}{j.k_D} = \frac{\sqrt{m_D}}{j.b_D.\sqrt{k_D}} \quad 2.5$$

Equation 2.5 implies that to provide maximum energy efficiency for a fixed gyroscope structure, the damping factor, b_D, should be decreased. Since b_D is dominated by the air damping at the atmosphere, lower damping factor, b_D for a gyroscope is obtained by operating the gyroscope at vacuum ambient, where damping is dominated by the mechanical structure.

The equations above explain the dynamics of the drive mode of a single mass gyroscope; however, the gyroscope used in this research has a double-proof-mass structure. Therefore, the above equations should be extended in order to describe the double-proof-mass gyroscope. Figure 2.1 illustrates the spring-mass-damper model for double-proof-mass gyroscope. The gyroscope can be described as two single-mass-gyroscopes connected together via a spring. For out of the phase operation, the

overall structure has its own and single resonance frequency, and the interconnection spring behaves as two distinct springs connected together at a stationary reference point called "node". If the drive-modes of two single-mass gyroscopes are identical, the spring constant of these virtual springs are equal to each other and two times of that of the interconnection springs. The total spring constant associated to the drive-mode and drive-mode resonance frequency for double-proof-mass gyroscope are defined as [34],

$$k_D = k_{drive1} + k_{drive2,1} = k_{drive} + 2.k_{drive2} \tag{2.6}$$

$$\omega_D = \sqrt{\frac{m_D}{k_D}} = \sqrt{\frac{m_D}{k_{drive1} + 2.k_{drive2}}} \tag{2.7}$$

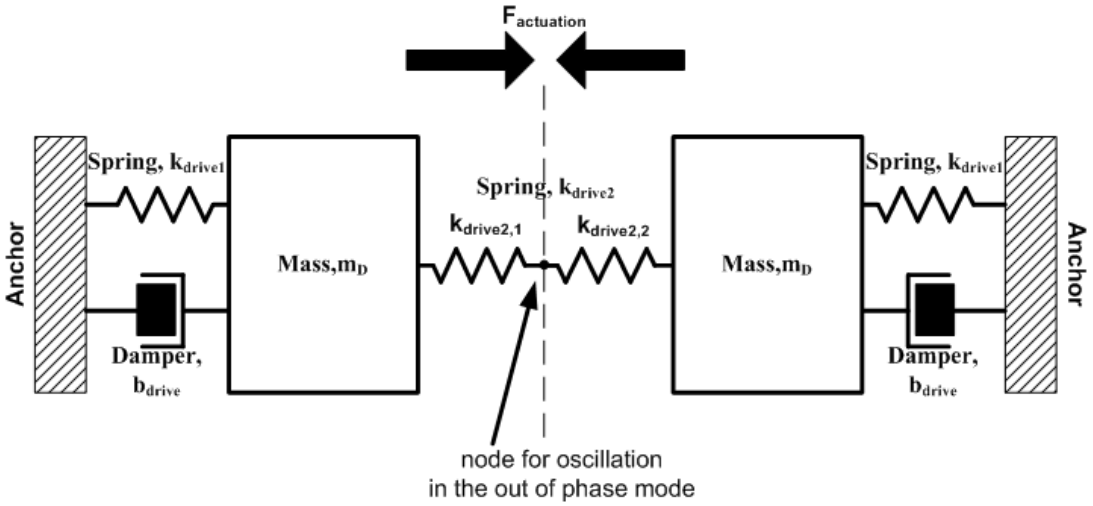

Figure 2.1: Spring-mass-damper model for describing of a double-proof-mass gyroscope structure.

Equations 2.6 and 2.7 are derived assuming that two structures are identical; however, in case of the mismatches in drive-mode masses, $m_{D,}$ and spring constants, k_{drive1}, the coupling spring compels the overall system to have only one resonance frequency adjusting its "node" position, thus the effective spring constants of virtual

springs, $k_{drive2,1}$ and $k_{drive2,2}$. The detailed analysis for such a system is beyond the scope of study, and in the following sections the gyroscope's drive-mode is considered as a single-mass system which has differential driving forces.

2.1.2 Coriolis Coupling and Mechanics of Sense-Mode Accelerometer

The sense-mode of the gyroscope is modeled as a second order mass-spring-damper system similar to the drive-mode. Since there isn't any mechanical coupling between two sense-mode of the gyroscopes used in this study, they behave as the sense-mode of the two distinct single-mass gyroscopes' sense-modes. Therefore, to model the sense-mode, the same Equations 2.2-2.6 are valid; however the values of mass, spring constant, and damping factor are replaced with that of the single mass sense-mode parameters. There are two driving forces acting on sense-mode: Coriolis force and the force generated by force-feedback electrodes. In the open-loop sense-mode systems, the Coriolis force deflects the sense-mode along the sense axis; whereas, in the closed-loop systems, the force generated by the applied electrical signal to force-feedback electrodes endeavors to neutralize the Coriolis force and to minimize the sense-mode deflection. The resultant sense-mode displacement is sensed by the sense-mode parallel plate capacitors. The overall force acting on the sense-mode, and the overall force and sense-mode displacement relation are expressed as

$$F_{overall}(s) = F_{Coriolis}(s) - F_{forcefeedback} \tag{2.8}$$

$$\frac{Y(s)}{F_{overall}(s)} = \frac{1}{m_s.s^2 + b_s.s + k_s} = \frac{1/m_s}{s^2 + (\omega_s/Q_s).s + \omega_s^2} \tag{2.9}$$

When the angular rate input about z-axis is applied to the proof-mass vibrated by the drive-mode along x-axis, the Coriolis force acting on the proof mass is given as [24]

$$F_{Coriolis,y}(t) = -2.m_{PM}.\Omega_z(t).\dot{x}(t) \tag{2.10}$$

where m_{PM} is mass of the proof-mass, $\Omega_z(t)$ is the rate input about z-axis, and $\dot{x}(t)$ is the velocity of the drive-mode oscillation. Equation 2.10 states that the Coriolis force, and thus the displacement of the sense mode, is the modulation of the angular rate input, $\Omega_z(t)$, by the drive-mode resonance frequency. Therefore, the resultant Coriolis force is an AM (amplitude modulated) force and has two frequency components which are separated equally from the drive-mode resonance frequency by the angular rate input frequency. For an open-loop sense-mode system, assuming the drive-mode is vibrating at its resonance frequency and inserting Equation 2.10 into Equation 2.9, the displacement of the proof-mass along sense axis due to these components are simplified to [24]:

$$Y(\omega_D + \omega_z) = \frac{\Omega_z \cdot X_D \cdot \frac{m_{PM}}{m_s} \cdot \left(\omega_D + \frac{\omega_z}{2}\right)}{(\omega_s^2 - (\omega_D + \omega_z)^2) + j \cdot (\omega_D + \omega_z) \cdot \frac{\omega_s}{Q_s}} \qquad 2.11$$

$$Y(\omega_D - \omega_z) = \frac{\Omega_z \cdot X_D \cdot \frac{m_{PM}}{m_s} \cdot \left(\omega_D - \frac{\omega_z}{2}\right)}{(\omega_s^2 - (\omega_D - \omega_z)^2) + j \cdot (\omega_D - \omega_z) \cdot \frac{\omega_s}{Q_s}} \qquad 2.12$$

where ω_z is the frequency rate input, and X_D is the magnitude of the drive-mode displacement. The above two equations indicate that the sense-mode displacement due to an angular rate input is based on the difference between the drive-mode and sense-mode resonance frequencies, assuming $\omega_z \ll \omega_D$ and $\omega_Z \ll \omega_s$, which is valid most of the practical applications. Hence, the sense-mode displacement, and thus sense-mode output, should be analyzed for two cases when the difference between sense-mode and drive-mode resonance frequencies is small, i.e., when $\omega_s \approx \omega_D$ (matched mode) and the resonance frequencies are apart from each other (mismatched mode). In the matched mode and mismatched mode operations Equations 2.11and 2.12 simplify to

$$Y_{matched}(s) \approx \frac{2 \cdot \Omega_z \cdot X_D \cdot Q_s}{\omega_D} \cdot \frac{m_{PM}}{m_s} \qquad 2.13$$

$$Y_{mismatched}(s) \approx j \cdot \frac{\Omega_z \cdot X_D}{(\omega_s - \omega_D)} \cdot \frac{m_{PM}}{m_s} \qquad 2.14$$

When the above equations compared, the maximum sense-mode vibration amplitude is achieved in the matched mode operation, and this vibration amplitude increases further as increasing the sense-mode quality factor, Q_s. However, the increase of the quality factor decreases the bandwidth of the gyroscope, i.e., for a sense-mode having 12 kHz resonance frequency, quality factors of 100 and 1000 yield bandwidth around 40 Hz and 4 Hz, respectively. Table 1.1 states that the bandwidth of the gyroscope is required to be larger than 70 Hz; hence the narrow bandwidth is undesirable for most of the practical applications. On the other hand, although in mismatched mode operation the sensitivity of the gyroscope decreases, the bandwidth increases considerably, and the sensitivity becomes less susceptible to the quality factor, thus to the vacuum level. Moreover, matching of the two modes is difficult owing to the process variations, accordingly it requires complicated mechanical and control electronics design. Therefore, in practice a slightly mismatched mode operation is preferred in order to have sufficient sensitivity and wider bandwidth [36].

2.2 Actuation and Sensing Mechanism in Capacitive Vibratory Gyroscopes

In capacitive vibratory gyroscopes, an electrical signal is applied to the actuation capacitances in order to generate actuation force, while the physical deflection of the masses is converted to an electrical signal at the sensing capacitances. Thus, the transduction mechanism of actuation and sensing capacitances should be taken into account in modeling the overall behavior of the gyroscope. This section analyses the electrostatic force generation and sensing mechanism in parallel plate capacitors, and

describes the electrostatic spring effect used in drive-mode and sense-mode resonance frequency matching.

2.2.1 Actuation Mechanism Using Parallel Plate Capacitor

Two charged and isolated conductive plates biased at different potential try to pull each other. If one of the plates is fixed and the other one is movable, the gap between two plates is decreased by the generated electrostatic force, and the stored electrostatic energy is dissipated by the physical movement of the movable conductive plate. This is the basic principle of the electrostatic actuation in capacitive gyroscope. Figure 2.2 shows the typical parallel plate capacitor configuration with parametric dimensions, which is commonly used in capacitive vibratory gyroscopes.

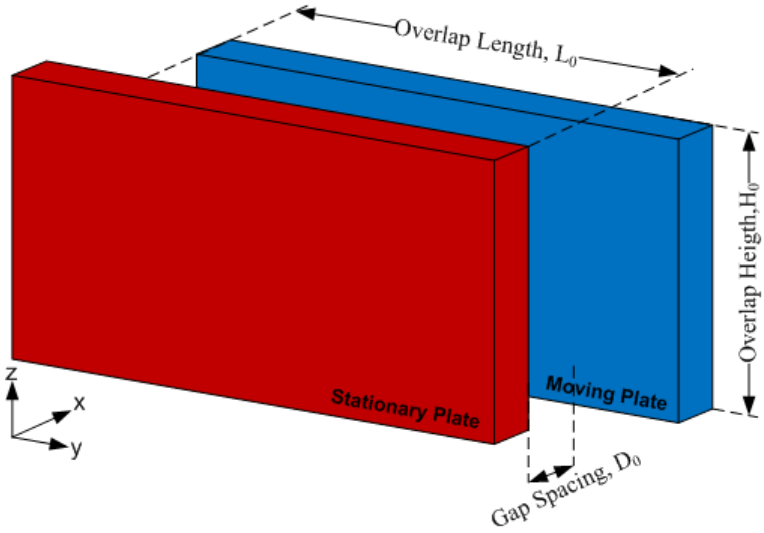

Figure 2.2: Parallel plate capacitor configuration with parametric dimensions, which is commonly used in capacitive vibratory gyroscopes.

The position dependent capacitance between two plates in Figure 2.1 can be expressed as

$$C = \alpha \cdot \varepsilon_0 \frac{L(y) \cdot H(z)}{D(x)} \quad 2.15$$

$$L(y) = L_0 + y \quad 2.16$$

$$H(z) = H_0 + z \quad 2.17$$

$$D(x) = D_0 + x \quad 2.18$$

where α is the fringing field correction factor, $\varepsilon_0$is the permittivity of air, $L(y)$ is the overlap length, $H(z)$ is the overlap height, $D(x)$ is the gap spacing between two plates and $L_0, H_0,$ and D_0 are the design parameters of the undisturbed actuation capacitor.

The force generated by a parallel plate capacitor is defined as the position gradient of the stored energy in the capacitor [24]. The stored energy in a capacitor is

$$E = \frac{1}{2} \cdot C \cdot V^2 \quad 2.19$$

where V is the potential energy difference between two plates. Taking the partial derivative of the result in Equation 2.19 with respect to x-y-z position vectors, the force acting on movable plate in this direction can be defined as [24]

$$F_x = \frac{\partial E}{\partial x} = \frac{1}{2} \cdot \frac{\partial C}{\partial D} \cdot \frac{\partial D(x)}{\partial x} \cdot V^2 = -\frac{1}{2} \cdot \alpha \cdot \varepsilon_0 \cdot \frac{H_0 \cdot L_0}{(D_0 - x)^2} \cdot V^2 \quad 2.20$$

$$F_y = \frac{\partial E}{\partial y} = \frac{1}{2} \cdot \frac{\partial C}{\partial L} \cdot \frac{\partial L(y)}{\partial y} \cdot V^2 = -\frac{1}{2} \cdot \alpha \cdot \varepsilon_0 \cdot \frac{H_0}{D_0} \cdot V^2 \quad 2.21$$

$$F_z = \frac{\partial E}{\partial z} = \frac{1}{2} \cdot \frac{\partial C}{\partial H} \cdot \frac{\partial H(z)}{\partial z} \cdot V^2 = -\frac{1}{2} \cdot \alpha \cdot \varepsilon_0 \cdot \frac{L_0}{D_0} \cdot V^2 \qquad 2.22$$

In Equations 2.20-2.22, it is assumed that the potential difference, *V*, does not change with the position. When the equations are studied carefully, F_y and F_z are constant regardless of the change in the position at those directions, while only the generated force along x direction, F_x, is a function of the displacement. Although F_x is a nonlinear function of the displacement, F_x is the largest force component among all of three, since L_0 and H_0 are usually designed larger than D_0 for typical micromachined structures [36].

In the drive-mode, the applied voltage should generate electrostatic force at the drive-mode resonance frequency to achieve maximum efficiency while the force-feedback actuation mechanism should generate force which has same frequency with the Coriolis force acting on the proof-mass. The Equations 2.19-2.22 indicate that, the resultant electrostatic force depends on and is a nonlinear function of the applied voltage difference, *V*. Therefore, to generate the required force in the actuation mechanisms, the nonlinearity of the voltage-force relation should be taken into account, and the relation should be linearized to complete the electromechanical model of the gyroscope. The applied voltage waveform and its fundamental frequency vary according to the trade-offs of the closed-loop circuit design; above all, the sinusoidal and the square-shaped waveforms at drive-mode resonance frequency are commonly used in transduction mechanism. The electrostatic force expressions for the purely sinusoidal and square waveform signals having amplitude of V_{ac} are calculated as:

$$F = \frac{\partial E}{\partial r} = \frac{1}{2} \cdot \frac{\partial C}{\partial r} \cdot \left(V_{ac} \cdot sin(\omega \cdot t)\right)^2 = \frac{\partial C}{\partial r} \cdot \left[\underbrace{\frac{V_{ac}^2}{4}}_{DC} - \underbrace{\frac{V_{ac}^2}{2} \cdot cos(2 \cdot \omega \cdot t)}_{AC\ at\ 2\omega}\right] \qquad 2.23$$

$$F = \frac{\partial E}{\partial r} = \frac{1}{2} \cdot \frac{\partial C}{\partial r} \cdot \left(\underbrace{\frac{4}{\pi} \cdot \sum_{n=1,3,5,..}^{\infty} \frac{V_{ac}}{n} \cdot sin(n \cdot \omega \cdot t)}_{\substack{Fourier\ series\ expansion \\ of\ square\ wave}} \right)^2 = \underbrace{\frac{\partial C}{\partial r} \cdot V_{ac}^2}_{DC} \qquad 2.24$$

respectively. It is observed that, a purely square waveform potential difference only generates a DC force that causes only static deflection, while the electrostatic force generated by the pure sinusoidal voltage difference has two frequency components, one of them DC and the other is AC at 2ω frequency. Hence, it is not possible to oscillate the mass by applying pure square wave, and the pure sinusoidal signal oscillates the drive-mode at its resonance frequency provided that the frequency of the voltage is half of the mechanical resonance frequency. Instead of applying pure square and sinusoidal voltage, a DC voltage can be added to the applied AC voltages to generate linear electrostatic force at the mechanical resonance frequency. Assuming DC voltage and AC signal are applied to the stationary and moving plates respectively, and rearranging Equation 2.23 and Equation 2.24 the generated electrostatic forces are calculated as

$$F = \frac{\partial E}{\partial r} = \frac{1}{2} \cdot \frac{\partial C}{\partial r} \cdot \left(V_{DC} - V_{ac} \cdot sin(\omega \cdot t) \right)^2$$

$$= \frac{1}{2} \cdot \frac{\partial C}{\partial r} \cdot \left\{ \left[\underbrace{V_{DC}^2 + \frac{V_{ac}^2}{2}}_{DC} \right] - \underbrace{2 \cdot V_{DC} \cdot V_{ac} \cdot sin(\omega \cdot t)}_{AC\ at\ \omega} + \underbrace{\frac{V_{ac}^2}{2} \cdot cos(2 \cdot \omega \cdot t)}_{AC\ at\ 2\omega} \right\} \qquad 2.25$$

$$F = \frac{\partial E}{\partial r} = \frac{1}{2} \cdot \frac{\partial C}{\partial r} \cdot \left(V_{DC} - \underbrace{\frac{4}{\pi} \cdot \sum_{n=1,3,5,..}^{\infty} \frac{V_{ac}}{n} \cdot sin(n \cdot \omega \cdot t)}_{\substack{Fourier\ series\ expansion \\ of\ square\ wave}} \right)^2 \qquad 2.26$$

$$= \frac{1}{2} \cdot \frac{\partial C}{\partial r} \cdot \left\{ \left[\underbrace{V_{DC}^2 + \frac{2 \cdot V_{ac}^2}{\pi}}_{DC} \right] - \underbrace{\frac{8}{\pi} \cdot V_{DC} \cdot V_{ac} \cdot sin(\omega \cdot t)}_{AC\ at\ \omega} + odd\ harmonics \right\}$$

for the applied sinusoidal and square wave voltage, respectively. It can be observed that if sinusoidal wave voltage or square wave voltage with DC biased is applied between stationary and movable electrodes, a sinusoidal force at ω is generated. As the sense-mode and drive-mode mechanical responses are considered high quality bandpass filter with center frequencies of ω_s and ω_D, respectively, if ω is closed to the resonance frequency of the mode to which voltage difference is applied, the DC and higher order force terms are filtered, and the transduction mechanism can be modeled as a gain stage whose gain is

$$n_{sine} = -\frac{\partial C}{\partial r} \cdot V_{DC} \qquad 2.27$$

$$n_{square} = -\frac{\partial C}{\partial r} \cdot \frac{4}{\pi} \cdot V_{DC} \qquad 2.28$$

Although, generating sinusoidal or square wave signals at drive-mode resonance frequency with DC offset is easy, the driving signal at resonance frequency leads errors at the sensing electrodes due to the electrical coupling between the driving and sensing electrodes. Hence, in some applications it is preferred to oscillate the drive-mode at its resonance frequency by applying an off-resonance frequency AC voltage difference to diminish the possible sensing errors. As indicated above, it is possible to generate force at frequency two times of the input by applying a pure sinusoidal

voltage difference. However, it is not esay to design a sinusoidal frequency divider. The frequency division of a square wave is rather easier, thus a sinusoidal signal at half frequency can be obtained by filtering the square waveform signal at half frequency; however, the filter shifts the phase of the signal, causing the system to oscillate at a different frequency than the mechanical resonance frequency. Although the phase shift can be compensated by using a phase compensation circuitry, the phase shift depends on the resonance frequency of the mechanical structure which varies due to the process variations, thus the compensator should be changed for every different mechanical structure. In addition, Equations 2.24 and 2.26 indicate that it is not possible to generate a force at resonance frequency by applying a square wave voltage difference at half of this frequency. An alternative approach is to apply a voltage difference which is the modulation of a DC biased sinusoidal voltage at resonance frequency by the half of the resonance frequency. Figure 2.3 illustrates the modulation of the DC biased sinusoidal voltage by a square wave at half of the resonance frequency in frequency domain. As it can be seen in Figure 2.3, the modulated signal, $V_{mod}(t)$, doesn't have any component at resonance frequency, this can also be verified by expressing the Fourier series expansion of the modulated signal. The Fourier series coefficient of the modulated signal is defined as

$$a_k = \frac{1}{T} \cdot \left[\int_0^T V_{mod}(t) \cdot e^{-j \cdot k \cdot \left(\frac{2 \cdot \pi}{T}\right) \cdot t} \cdot dt \right] \qquad 2.29$$

$$a_k = \frac{1}{T} \cdot \left\{ \int_0^{T/2} [V_{DC} + V_{AC} \cdot sin(\omega_D \cdot t)] \, . dt - \int_{T/2}^{T} [V_{DC} + V_{AC} \cdot \sin(\omega_D \cdot t)] \cdot dt \right\} \qquad 2.30$$

where T is the period of the modulated signal and equals to

$$T = \frac{4 \cdot \pi}{\omega_D} \qquad 2.31$$

Substituting Equation 2.31 into Equation 2.30 and calculating the integral terms, Equation 2.30 yields

$$a_k = \left[\begin{array}{c} \dfrac{V_{DC}}{-j \cdot 2 \cdot \pi \cdot k} \cdot \left(2 \cdot e^{-j \cdot \pi \cdot k} - 2\right) + \\ \dfrac{V_{AC}}{4 \cdot \pi \cdot (k-2)} \left(2 \cdot e^{-j \cdot \pi \cdot (k-2)} - 1 - e^{-j \cdot 2 \cdot \pi \cdot (k-2)}\right) + \\ \dfrac{V_{AC}}{4 \cdot \pi \cdot (k+2)} \left(2 \cdot e^{-j \cdot \pi \cdot (k+2)} - 1 - e^{-j \cdot 2 \cdot \pi \cdot (k+2)}\right) \end{array} \right] \qquad 2.32$$

The Equation 2.32 is always zero for all even harmonics. Although the equation results as "0/0" uncertainty for second harmonics ($k = \pm 2$), the limit of the equation is zero while k approaches to $k = \pm 2$. Hence, Equation 2.32 can be simplified to

$$a_k = \frac{2 \cdot V_{DC}}{j \cdot k \cdot \pi} - \frac{V_{AC}}{4 \cdot \pi} \left(\frac{16}{k^2 - 4}\right) \qquad k = \pm 1, \pm 3, \pm 5, \ldots \qquad 2.33$$

Then, the modulated voltage, V_{mod}, can be expressed by using the Fourier series expansion,

$$V_{mod}(t) = \sum_{k=1}^{\infty} \left\{ \frac{4 \cdot V_{DC}}{\pi \cdot k} \cdot \sin\left(k \cdot \frac{\omega_D}{2} \cdot t\right) - \frac{V_{AC}}{2 \cdot \pi} \cdot \left(\frac{16}{k^2 - 4}\right) \cdot \cos\left(k \cdot \frac{\omega_D}{2} \cdot t\right) \right\} \qquad 2.34$$

where $k = 1, 3, 5, \ldots$ It is obvious that the modulated signal doesn't include any harmonic at the mechanical resonance frequency. Then, by substituting Equation 2.34 into the electrostatic force expression, the force generated by the modulated voltage is found as

$$F = \frac{\partial E}{\partial r} = \frac{1}{2} \cdot \frac{\partial C}{\partial r} \cdot V_{mod}^2$$

$$= \frac{1}{2} \cdot \frac{\partial C}{\partial r} \cdot \left\{ \left[\underbrace{V_{DC}^2 + \frac{V_{AC}^2}{2}}_{DC} \right] + \underbrace{2 \cdot V_{DC} \cdot V_{AC} \cdot \sin(\omega_D \cdot t)}_{AC\ at\ \omega_D} - \underbrace{\frac{V_{AC}^2}{2} \cdot cos(2 \cdot \omega \cdot t)}_{AC\ at\ 2\omega} \right\} \quad 2.35$$

which is similar to the electrostatic force expression when a sinusoidal signal with a DC offset is applied to the paralel plate capacitor.

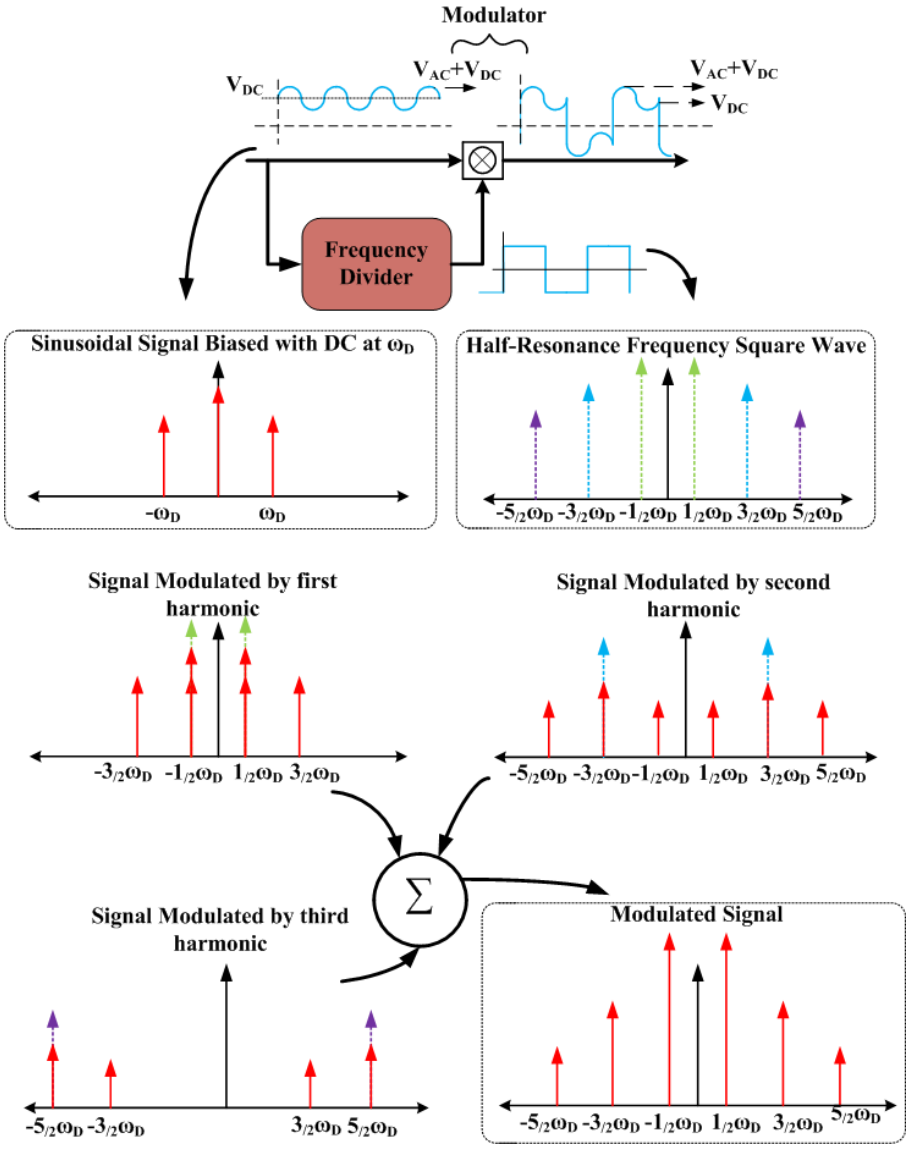

Figure 2.3: Modulation of the sinusoidal voltage with a DC biased by a square wave at half of the resonance frequency

Equation 2.35 indicates that the electrostatic force is generated at the mechanical resonance frequency when the modulated voltage difference, V_{mod}, is applied to the parallel-plate capacitor. This driving approach can be expanded on the modulation frequencies which are the 2^{-n} multiplies of the resonance frequency where n is an integer. Therefore, Equation 2.34 can be generalized as

$$V_{mod}(t) = \sum_{k=1}^{\infty} \left\{ \frac{4 \cdot V_{DC}}{\pi \cdot k} \cdot \sin\left(k \cdot \frac{\omega_D}{2^n} \cdot t\right) - \frac{V_{AC}}{2 \cdot \pi} \cdot \left(\frac{16}{k^2 - 2^n}\right) \cdot \cos\left(k \cdot \frac{\omega_D}{2} \cdot t\right) \right\} \quad 2.36$$

where $k = \pm 1, \pm 3, \pm 5, \ldots$ Besides, the generated force expression for these different modulated voltage difference is same as the expression in Equation 2.35. For this approach, the parallel plate transduction capacitor can be modeled as a gain stage as

$$n_{mod} = \frac{\partial C}{\partial r} \cdot V_{DC} \quad 2.37$$

In literature, there are two main parallel plate capacitor configurations which can be used in transduction mechanism in vibratory gyroscopes: varying-gap type capacitor and varying-overlap-area capacitor. Figure 2.4 shows the typical drive electrodes for varying-gap and varying-overlap-area actuation mechanism. In varying-gap type capacitor, the total force generated on the moving part is determined by the difference between the force applied by pairing finger, F_{x0}, and the force applied by anti-gap finger, F_{xa}. Adjusting Equation 2.20 for *N* number of fingers, [24]

$$F_{x,net} = N \cdot (F_{x0} - F_{xa}) = \frac{1}{2} \cdot N \cdot \alpha \cdot \varepsilon_0 \cdot H_0 \cdot L_0 \cdot \left[\frac{1}{(D_0 + x)^2} - \frac{1}{(D_a - x)^2}\right] \cdot V^2 \quad 2.38$$

where D_a is the spacing between two anti-gap fingers. Assuming the anti-gap spacing is much larger than gap spacing and the displacement is negligible compared to gap spacing, Equation 2.38 simplifies to

$$F_{x,net} = N \cdot (F_{x0} - F_{xa}) = \frac{1}{2} \cdot N \cdot \alpha \cdot \varepsilon_0 \cdot H_0 \cdot L_0 \cdot \left(\frac{1}{D_o^2} - \frac{1}{D_a^2}\right) \cdot V^2 \qquad 2.39$$

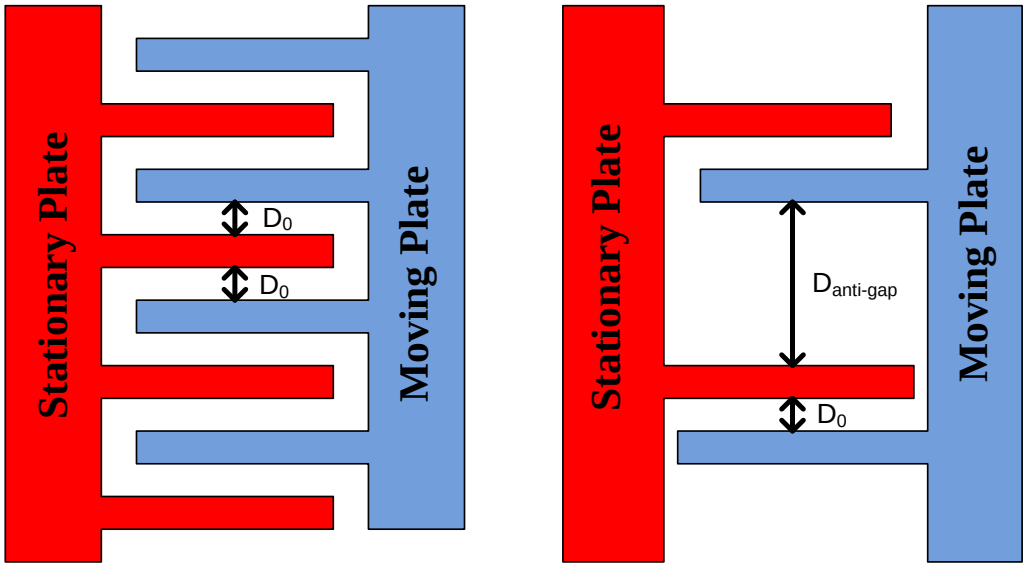

Figure 2.4: Drive electrodes for a) varying-gap and b) varying overlap area type actuation mechanism

For a varying-overlap-area type capacitor, the force applied by neighboring fingers cancel each other, there occurs a net force only along the oscillation direction, and this net force for *N* number of fingers is expressed as [24]

$$F_{y,total} \approx \frac{1}{2} \cdot N \cdot \alpha \cdot \varepsilon_0 \cdot \frac{H_0}{D_0} \cdot V^2 \qquad 2.40$$

Generally, D_0 is designed very narrow, and L_0 and H_0 are designed wide to increase the generated force. As a result, the electrostatic force generated by a varying-gap capacitor is larger than the electrostatic force generated by a varying-overlap-area capacitor for same dimensions [24]. However, as Equation 2.38 states, the force is a function of displacement, creating nonlinearity. In addition, the maximum displacement in a varying-gap type capacitors is limited by the gap, thus for the drive-mode actuation mechanism, which requires linearity and large displacement in oscillation, varying-gap capacitors are not feasible and varying-overlap-area capacitors are commonly used in the transduction mechanism.

2.2.2 Capacitive Sensing

The electrostatic actuation in the drive-mode and Coriolis coupling in the sense-mode create physical displacements, and the transduction mechanism of the capacitive vibratory gyroscope requires the conversion of these displacements in the mechanical domain to a meaningful data in the electrical domain. The data conversion is achieved by using capacitive sensing mechanism in capacitive vibratory gyroscopes. As the name implies, the capacitive sensing mechanism depends on the sensing the capacitance change in the transduction mechanism due to the physical displacement. The capacitance and charge-voltage relation of a capacitor are defined as

$$C = \frac{\varepsilon_0 \cdot A}{d} \tag{2.41}$$

$$Q = C \cdot V \tag{2.42}$$

where A is the overlapping area of the capacitor, and d is the distance between two capacitor plates. If one of the plates of the capacitor is kept stationary and the other

is moved, the movement results in a capacitance variation due to the change in the overlapping area, *A*, or the gap between two plates, *d*. It can be concluded from Equations 2.41 and 2.42 that, when the voltage difference between two plates is kept constant, the capacitance change due to the displacement injects charge in the capacitor. Hence, if the injected charge is converted voltage on impedance of the readout electronics connected in series to the sensing capacitor of the gyroscope, the displacement is monitored as a voltage [35]. Figure 2.5 demonstrates the basic electrical model for capacitive sensing [36]. The AC current source symbolizes the charge injection generated by the parallel plate capacitor biased with a constant DC source, C_0 is the stationary sensor capacitance and $Z_{readout}$ is the impedance of the readout electronics. To obtain a constant voltage difference between two parallel plates, the proof-mass of the gyroscope is biased to V_{PM} while the other plate is biased to ground by the readout circuitry. The sensing capacitance can be expressed as

$$C_s(t) = C_0 + \frac{\partial C}{\partial x} \cdot x(t) \tag{2.43}$$

where $x(t)$ is the time-varying displacement of sensing electrodes. The injected current generated in sensing electrodes can be calculated by taking the derivative of the total charge, Q_s, defined in Equation 2.42, and it is expressed as

$$i_0(t) = \frac{\partial Q_s}{\partial t} = \frac{\partial (C_s(t).V_o(t))}{\partial t} = V_0(t) \cdot \frac{\partial C_s(t)}{\partial t} + C_s(t) \cdot \frac{\partial V_o(t)}{\partial t} \tag{2.44}$$

Assuming V_{PM} is much larger than the AC output signal, and inserting Equation 2.43 into Equation 2.44, Equation 2.44 simplifies to

$$i_0(t) \approx V_{PM} \cdot \frac{\partial \left(C_0 + \frac{\partial C}{\partial x} \cdot x(t)\right)}{\partial t} = V_{PM} \cdot \frac{\partial C}{\partial x} \cdot \underbrace{\frac{\partial x(t)}{\partial t}}_{velocity} \tag{2.45}$$

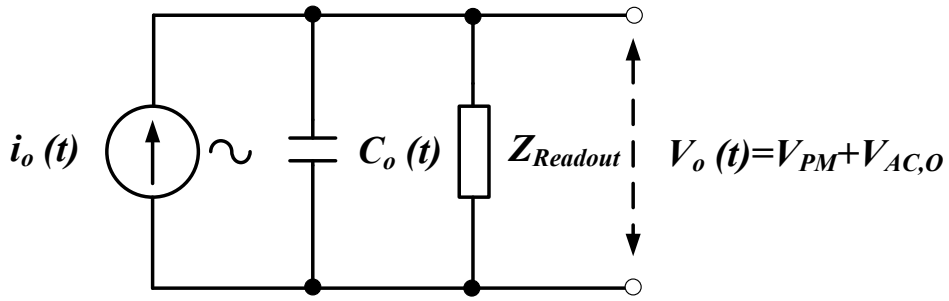

Figure 2.5: Basic electrical model of capacitive sensing [36]

Similar to the actuation capacitors, sensing capacitors can be modeled as gain stages, which amplifies the velocity of the proof-mass into the induced current. As indicated above, the injected current is converted to AC voltage by the impedance seen from the output node, which is the parallel of the readout impedance, $Z_{readout}$, and the stationary sensor capacitance, C_0 and the AC output voltage, $V_{AC,O}$, is formulated as

$$V_{AC,O}(s) = i_O(s) \cdot Z_{overall}(s) = V_{PM} \cdot \frac{\partial C}{\partial x} \cdot s \cdot X(s). \left(\frac{1}{s \cdot C_0} // Z_{readout}\right) \qquad 2.46$$

Equation 2.46 indicates that some of the generated current passes through the stationary capacitance, C_O, and the AC output is a function of mechanical and electrical parameters.

2.2.3 Electrostatic Spring Effect

As mentioned in Section 2.1.2, the sense-mode response due to the Coriolis coupling is boosted if the sense-mode and drive-mode resonance frequencies are close to each other (matched-mode operation). Although the resonance frequencies of the two modes are designed same, due to the process imperfections, a perfect matching of the modes are not possible. To match these modes, the gyroscopes used in study have varying-gap type electrodes, which act as an electrostatic spring in the sense-mode. The electrostatic spring constant of these electrodes is a function of the applied DC

voltage difference between two plates of electrodes, the electrostatic spring constant and the resonance frequency of the sense-mode are defined as [24]

$$\delta k = \frac{\partial F_x}{\partial x} \approx \alpha \cdot \varepsilon_0 \cdot \frac{H_0 \cdot L_0}{(D_0 - x)^3} \cdot V_{PM}^2 \qquad 2.47$$

$$\omega_s = \sqrt{\frac{k_s - \delta k}{m_s}} \qquad 2.48$$

The sense-mode of the gyroscopes used in the study is designed to have higher mechanical resonance frequency than of the drive-mode. The electrostatic spring effect of the sense-mode can also be employed to tune the gyroscope in the matched-mode or in the nearly mismatched-mode to test the performance of the gyroscope in these modes.

2.3 Modeling Capacitive Vibratory Gyroscope

The vibratory gyroscope electronics design requires both a mathematical and an electrical equivalent model of the gyroscope. In Sections 2.1 and 2.2 the mechanical structure, the actuation mechanism, and the sensing mechanism of the gyroscope are separately analyzed and modeled. To obtain the complete mathematical model, the drive-mode and sense-mode should be characterized by integrating these models into a single model. To obtain a drive-mode model, the relation between the applied voltage, $V_{in}(s)$, and the readout output voltage, $V_o(s)$ should be defined. Figure 2.6 shows the block diagram of the mechanical conversion algorithm for the drive-mode, according to algorithm the relation between $V_{in,D}(s)$ and $V_{o,D}(s)$ is

$$\frac{V_o(s)}{V_{in}(s)} = \frac{F_D(s)}{V_{in}(s)} \cdot \frac{X_D(s)}{F_D(s)} \cdot \frac{I_D(s)}{X_D(s)} \cdot \frac{V_o(s)}{I_D(s)} \qquad 2.49$$

Assuming a sinusoidal voltage difference with a constant DC biased, V_{PM}, is applied, and substituting Equations 2.2, 2.27, 2.45 and 2.46 into Equation 2.49, the mathematical model can be expressed as

$$\frac{V_{o,D}(s)}{V_{in,D}(s)} = \frac{\frac{1}{m_D} \cdot \frac{\partial C_{DM}}{\partial x} \cdot \frac{\partial C_{DP}}{\partial x} \cdot V_{PM}^2 \cdot \left(\frac{1}{s \cdot C_{0,D}} // Z_{interface,D}\right) \cdot s}{s^2 + (\omega_D / Q_D) \cdot s + \omega_D^2} \qquad 2.50$$

where *DM* denotes the dive-motor electrodes (actuation electrodes), *DP* is the drive-pick electrodes (sensing electrodes), and $C_{0,D}$is the stationary capacitance of the drive-pick electrodes. Then, for the input voltages at drive-mode mechanical resonance frequency, Equation 2.50 simplifies to

$$\frac{V_{o,D}(s)}{V_{in,D}(s)} = \frac{1}{m_D} \cdot \frac{\partial C_{DM}}{\partial x} \cdot \frac{\partial C_{DP}}{\partial x} \cdot V_{PM}^2 \cdot \left(\frac{1}{s \cdot C_{0,D}} // Z_{interface,D}\right) \cdot \frac{Q_D}{\omega_D} \qquad 2.51$$

As can be noted, the phase difference between input and output voltages is determined by the phase of the impedance seen by the induced current in sensing electrodes. Assuming that the readout circuitry impedance is much smaller than the impedence of the drive-pick electrodes, it can be concluded that the readout circuitry phase shift determines the phase of the output voltage.

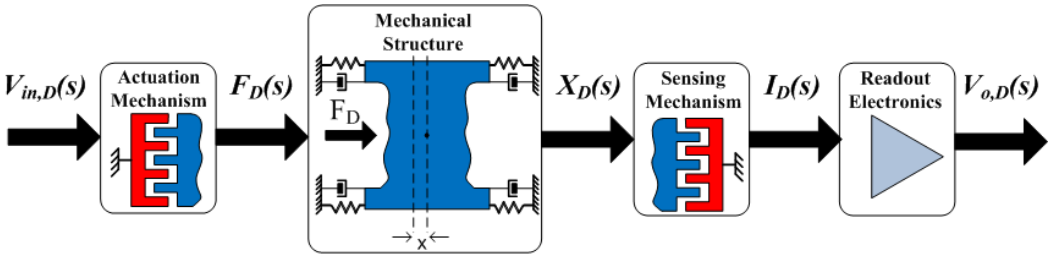

Figure 2.6: Block diagram of the electromechanical conversion of the drive-mode

The mathematical model can be derived for the sense-mode by using a similar approach. Figure 2.7 illustrates the algortihm which can be used to model sense-mode. Since subtraciton is a linear operation, the mathematical model for the force feedback actuation and Coriolis coupling are modeled seperately as

$$\frac{V_{o,S}(s)}{V_{in,FF}(s)} = -\frac{\frac{1}{m_S}\cdot\frac{\partial C_{FF}}{\partial x}\cdot\frac{\partial C_{SP}}{\partial x}\cdot V_{PM}^2\cdot\left(\frac{1}{s\cdot C_{0,S}}//Z_{interface,S}\right)\cdot s}{s^2+(\omega_S/Q_S)\cdot s+\omega_S^2} \qquad 2.52$$

$$\frac{V_{o,S}(s)}{F_{Coriolis}(s)} = \frac{\frac{\partial C_{SP}}{\partial x}\cdot V_{PM}\cdot\left(\frac{1}{s\cdot C_{0,S}}//Z_{interface,S}\right)\cdot s}{s^2+(\omega_S/Q_S)\cdot s+\omega_S^2} \qquad 2.53$$

respectively, where *FF*, and *SP* stand for the force feedback electrodes and the sense pick electrodes, respectively, and $C_{0,s}$ is the stationary capacitance of sense-pick electrodes. Substituting Coriolis description stated in Equation 2.10 into Equation 2.53 and assuming input rate frequency is much smaller than mechanical resonance frequencies of drive-mode and sense-mode, i.e. $\omega_Z \ll \omega_D, \omega_s$, the relation between sense-mode voltage output and drive-mode displacement can be written as

$$\frac{V_{o,S}(s)}{X_D(s)} = -\frac{2\cdot m_{PM}\cdot\Omega_Z\cdot\frac{\partial C_{SP}}{\partial x}\cdot V_{PM}\cdot\left(\frac{1}{s\cdot C_{0,S}}//Z_{interface,S}\right)\cdot s^2}{s^2+(\omega_S/Q_S)\cdot s+\omega_S^2} \qquad 2.54$$

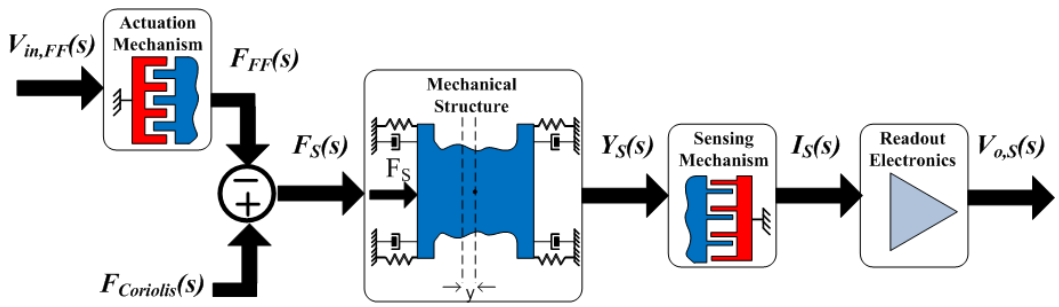

Figure 2.7: Block diagram of the electromechanical conversion of the sense-mode

Assuming that the drive-mode is resonated in its resonance frequency by the applied input, the displacement of the drive-mode can be expressed in terms of the applied voltage by arranging Equations 2.5 and 2.27 as

$$\frac{X_D(j \cdot \omega_D)}{V_{in}(j \cdot \omega_D)} = \frac{V_{PM} \cdot \frac{\partial C_{DM}}{\partial x} \cdot Q_D}{j \cdot k_D} \qquad 2.55$$

It is clear that if two modes are matched, then the phase difference between the drive-mode input and the sense-mode output is equal to 180° shifted of the readout electronics phas whereas in mismatched mode case the phase difference is 90° ($\omega_D \gg \omega_S$) or -90° ($\omega_S \ll \omega_D$) shifted compared to the readout electronics phase, owing to the mechanical response of the sense-mode. Hence, when designing the sense-mode electronics, it is critical to determine the mode of the operation, whether matched or mismatched, and the readout circuitry and sense-mode electronics should be designed carefully to have a minimum phase error.

The mathematical model derived above is valid for a single-ended drive and sense mechanism; as the gyroscopes used in study have differential driving in the drive-mode and differential sensing in the sense-mode, the right-hand side of Equations (2.49)-(2.55) should be multiplied by 2.

In addition to the mathematical model, the vibratory gyroscope should be modeled in electrical domain to simulate the gyroscope electronics in CAD tools. The electrical model of the gyroscope can be obtained by using the analogy between the mechanical mass-spring-damper system and the electrical domain. The mechanical structure of the gyroscope is modeled as a serially connected resistor-inductor-capacitor circuit (RLC). Table 2.1 demonstrates the electrical equivalent of the second order mass-spring-damper system [24]. Figure 2.8 shows the generalized model of the gyroscope used in this study. In the generalized model, the actuation and sensing mechanism are symbolized as a transformer and a current controlled current source, respectively, while the Coriolis coupling is symbolized as a current

controlled voltage source. The electromechanical coupling coefficients used in the model are [45]

$$n_{DM} = V_{PM} \cdot \frac{\partial C_{DM}}{\partial x} \quad 2.56$$

$$n_{FF} = V_{PM} \cdot \frac{\partial C_{FF}}{\partial x} \quad 2.57$$

$$n_{DP} = V_{PM} \cdot \frac{\partial C_{DP}}{\partial x} \quad 2.58$$

$$n_{SP} = V_{PM} \cdot \frac{\partial C_{SP}}{\partial x} \quad 2.59$$

$$n_{COR} = 2 \cdot m_{PM} \cdot \Omega_z \quad 2.60$$

Table 2.1: Electrical equivalent of the mechanical parameters of the second order mass-spring-damper system [24]

Mechanical Parameter	Electrical Equivalent
Mass (m)	Inductance (L)
Damping Coefficient (b)	Resistance (R)
Spring (k)	Capacitor (C)
Displacement (x)	Charge (Q)
Velocity (v)	Current (I)
Force (F)	Voltage (V)

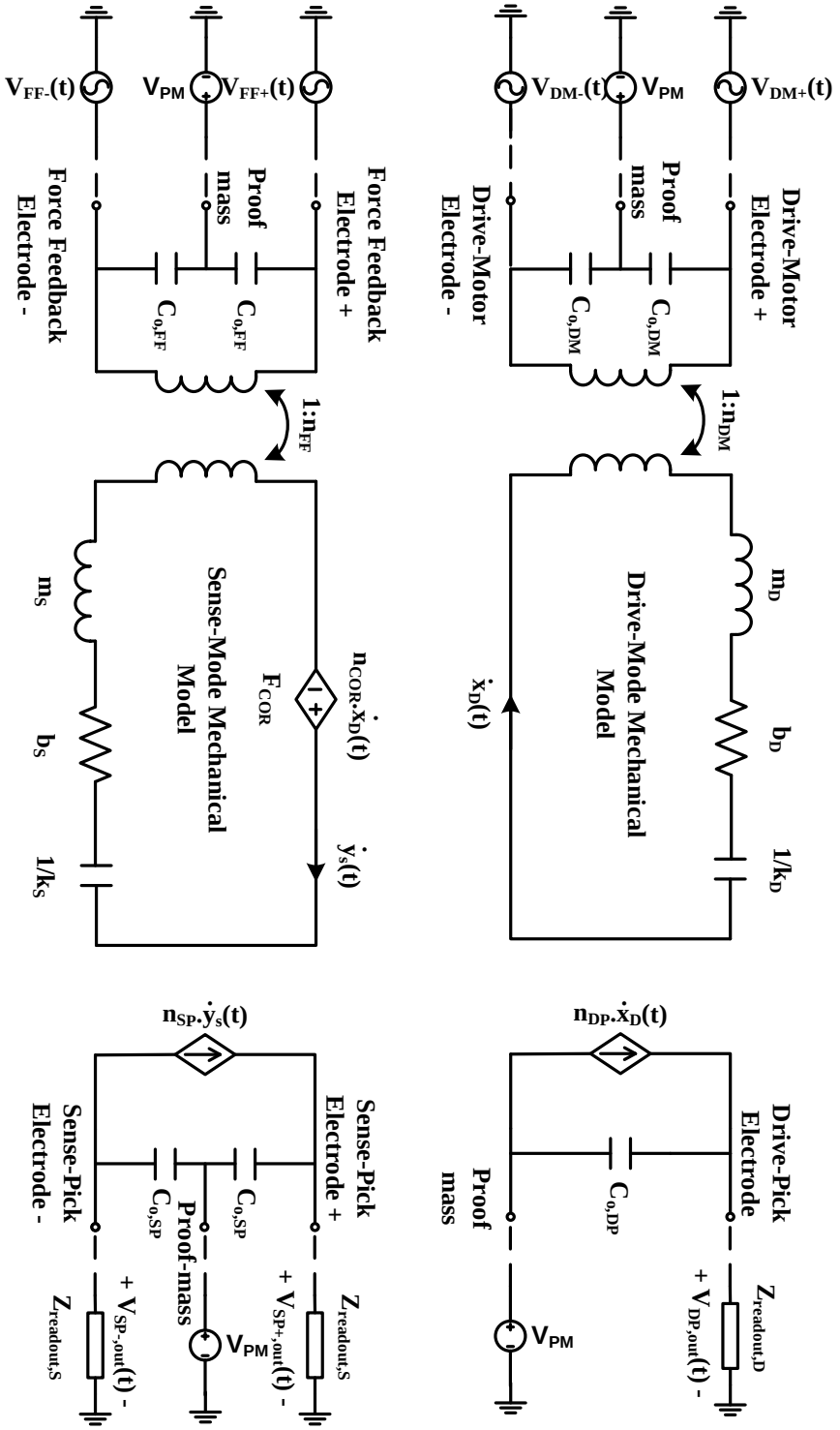

Figure 2.8: Generalized electrical model of the gyroscope used in the study

2.4 Vibratory Gyroscope Electronics

Vibratory gyroscope electronics includes: (i) interface electronics, which converts mechanical response of the gyroscope to electrical domain as a voltage, and (ii) external electronics, which process the output of the interface electronics for proper gyroscope operation. External electronics provide a constant amplitude vibration in the drive-mode and extract the rate input data out of the raw data of the sense-mode. This section analyzes the interface and external electronics of the vibratory gyroscope and describes the basic criteria for high performance and proper operations.

2.4.1 Interface Electronics of Vibratory Gyroscope

The vibratory gyroscope sensing mechanism provides the convertion of physical displacement in the mechanical domain to an induced current in the electrical domain. To process the output data due to the displacement in conventional circuitry, the induced current should be converted to a voltage. As indicated in Section 2.2.2 and modeled in Figure 2.8 , the gyroscope sensing mechanism as a high impedance node should be biased to a constant DC potential using a low impedance node interface. For a high performance gyroscope, the interface circuit must be stable, have very low noise, and introduce minimum phase error to the processed data. Figure 2.9 illustrates the generalized view of interface circuit. The output voltage $V_o(s)$ can be written in terms of the induced current $I_o(s)$ as

$$V_o(s) = A_v \cdot \left[I_o(s) \cdot \left(Z_{in} // \frac{1}{s \cdot C_s} // \frac{1}{s \cdot C_p} \right) \right] \qquad 2.61$$

where A_v is the amplifier gain, I_o is the induced current in the sensing capacitor, Z_{in} is the input impedance of the interface (readout) circuitry, C_s is the stationary capacitance of sensing capacitor, and C_p is the total of parasitic capacitance.

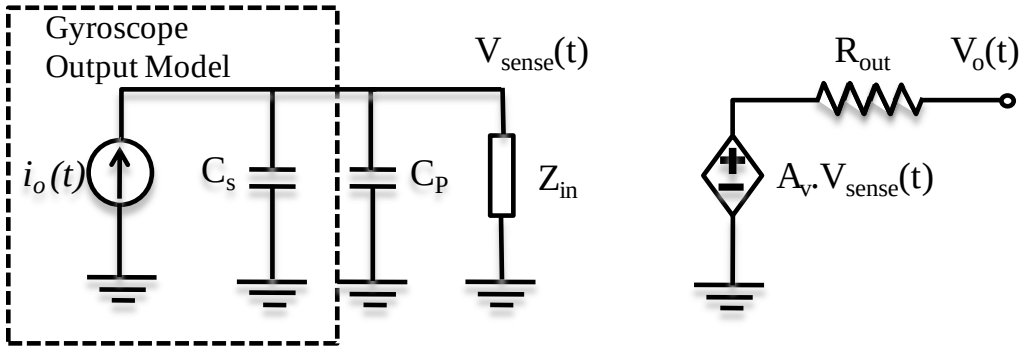

Figure 2.9: Generalized view of interface circuit

It is clear that the gyroscope output voltage is increased by increasing the input impedance, Z_{in}. The input impedance of the interface has resistive and capacitive parts, and generally, one of the parts is selected to be very large compared to the other, hence the input impedance shows the characteristics of the latter. According to the prominent impedance characteristics of the input impedance, the interface type is called resistive or capacitive interface, respectively. For a resistive interface type, the input resistance is much smaller than the input capacitor impedance in the gyroscope operation range, and in this case Equation 2.61 simplifies to

$$V_o(s) = A_v \cdot I_o(s) \cdot R_{in} \qquad 2.62$$

assuming $\left(s \cdot C_s + s \cdot C_p\right)^{-1} \gg R_{in}$. It is obvious that the phase of a resistive type is determined by the interface resistance and the total capacitance seen by this resistance. As mentioned above, for a proper interface circuitry, the phase shift of the interface circuitry should be small, around 0˚ for a resistive-type interface, hence one of the limiting factor of the interface resistance for a proper readout is the

stationary capacitance of the gyroscope and the parasitic capacitance of the interface circuit. Since the stationary capacitor is a design parameter which is fixed, the phase error introduced by these capacitances is lessened by decreasing either the parasitic capacitance or the input resistance. For the latter case, the amplifier gain should be increased in order to improve the resolution of the interface.

On the other hand, in capacitive-type interfaces, the input capacitor impedance for the operation range of the gyroscope is much smaller than the input resistance. In this type interfaces, the effective impedance is equal to the sum of the all capacitance introduced at the high impedance node, and the output voltage of the interface is defined as

$$V_o(s) = A_v \cdot I_o(s) \cdot \frac{1}{s \cdot \left(C_s + C_p + C_{in}\right)} \qquad 2.63$$

The interface behaves as a charge integrator and shifts the injected current 90˚. Although the maximum resolution is achieved for a minimum input capacitance, in order to bias the high impedance node to a DC value with minimum phase error, the input resistance value must be selected very large, which is usually an impractical value. Hence, several approaches like back-to back diodes, switched capacitors, and sub-threshold operating MOSFET are employed in capacitive-type interface circuitry to bias the output of the interface [36].

In this study, resistive-type and capacitive-type interfaces are used in the drive-mode and in the sense-mode, respectively, in order to eliminate the necessity of additional 90˚ phase shifters in the external electronics which is discussed in the following section.

2.4.2 External Electronics of Vibratory Gyroscopes

The external electronics of vibratory gyroscopes can be separated into two groups; the drive-mode electronics and sense-mode electronics. In the following subsections, the basic principles of the drive-mode and sense-mode electronics are explained separately.

2.4.2.1 Drive-Mode Electronics

The basic operation principle of the vibratory gyroscope is that the drive-mode mechanical structure should resonate to induce Coriolis coupling between the drive-mode and sense-mode. The drive-mode of the gyroscope as modeled in Equation 2.50 has one zero at $s = 0$ and two poles at

$$s_{1,2} = \frac{-\frac{\omega_D}{Q_D} \pm \sqrt{\left(\frac{\omega_D}{Q_D}\right)^2 - 4 \cdot \omega_D^2}}{2} \qquad 2.64$$

The poles of the drive-mode reside in left-hand-side of the imaginary axis which means the mechanical structure is stable and the poles should be shifted on imaginary axis or right-hand-side of the imaginary axis to obtain an instable system and to start oscillation. The instability is usually achieved by using a positive feedback loop design. "Barkhausen Criteria" states that a positive feedback loop system oscillates at a frequency, for which the total open loop gain is larger than or equal to unity and the total phase shift in the loop is integer multiple of 360˚. Figure 2.10 shows a basic positive feedback loop structure to oscillate the drive-mode where the K_D stands for the open-loop gain of the drive-mode with resistive-type interface and K_{loop} is the electrical gain introduced by the components in the loop. Providing that K_{loop} introduce no phase shift to the loop, the closed loop transfer function of the system is expressed as

$$\frac{V_{out}(s)}{V_{in}(s)} = \frac{\dfrac{K_D \cdot s}{s^2 + \left(\frac{\omega_D}{Q_D}\right) \cdot s + \omega_D^2}}{1 - \underbrace{\dfrac{K_D \cdot K_{loop} \cdot s}{s^2 + \left(\frac{\omega_D}{Q_D}\right) \cdot s + \omega_D^2}}_{open\ loop\ gain}} = \frac{K_D \cdot s}{s^2 + \left(\frac{\omega_D}{Q_D} - K_D \cdot K_{loop}\right) \cdot s + \omega_D^2} \qquad 2.65$$

The characteristic equation of the closed loop system can be extracted from Equation 2.65 as

$$s^2 + \left(\frac{\omega_D}{Q_D} - K_D \cdot K_{loop}\right) \cdot s + \omega_D^2 = 0 \qquad 2.66$$

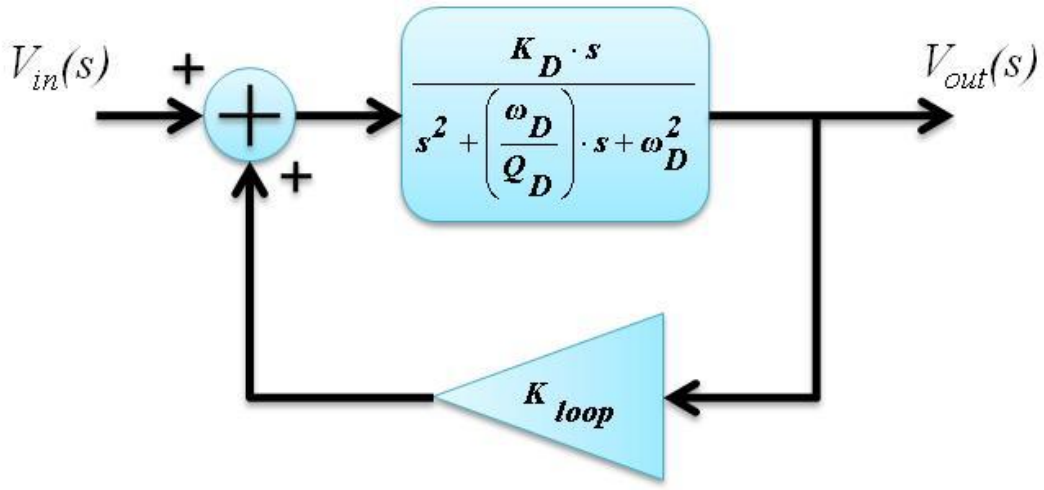

Figure 2.10: Schematic of a basic positive feedback loop to oscillate drive-mode

As indicated above, the drive-mode starts oscillation at its mechanical resonance frequency if the closed-loop poles lie on the imaginary axis or reside in the right-half plane, in other words characteristics equation's roots have positive real part. Figure 2.11 demonstrates the complementary root-locus of the basic positive feedback design. It is obvious that as K_{loop} increases the poles shifts towards the right-hand-side of the imaginary plane and after a K_{loop} value, the closed-loop system becomes

instable and starts to oscillate. The range of loop gain to start oscillation, K_{loop}, can be defined as

$$K_D \cdot K_{loop} \geq \frac{\omega_D}{Q_D} \quad 2.67$$

Or

$$K_{loop} \geq \frac{\omega_D}{Q_D . K_D} \quad 2.68$$

Equation set (2.65)-(2.68) express the closed-loop conditions to obtain oscillation at mechanical resonance frequency in the drive-mode. However, the closed-loop system hardly satisfies the necessary conditions to start up without triggering. The closed-loop system is usually triggered by noise; the noise input is shaped by the mechanical response of the drive-mode, and the output is fed to the actuation mechanism after amplified by the loop gain. If the loop gain is greater than unity, the output signal of the closed-loop system increases until it is saturated to the supply limit of the electronics unless there is a controller continuously adjusting the loop gain.

As stated in Equation 2.10, the Coriolis coupling is a function of both the velocity of the drive-mode and the rate input. Thus, the coupling should be only function of the rate input to extract the rate input from the Coriolis coupling; in other words the velocity of the drive mode should be kept constant. However, the vibration magnitude, and hence the velocity of the drive-mode, is susceptible to change due to the parameter variations in the mechanical structure and ambient conditions. The solution of this problem is to monitor the vibration magnitude of the drive-mode continuously and adjust the open loop gain as in to keep the magnitude at a constant value. Figure 2.12 shows the generalized schematic of the automatic gain control loop (AGC). The controller compares the vibration amplitude data with a reference voltage (or set voltage) and generates a control voltage, and hence the open loop gain according to error in order to adjust the amplitude of the oscillation to the reference value. Although the controller is illustrated as a regulating loop gain, K_{loop}, in the

figure, the control mechanism may also adjust the gain of the gyroscope, K_D, by changing V_{DC} in Equation 2.37.

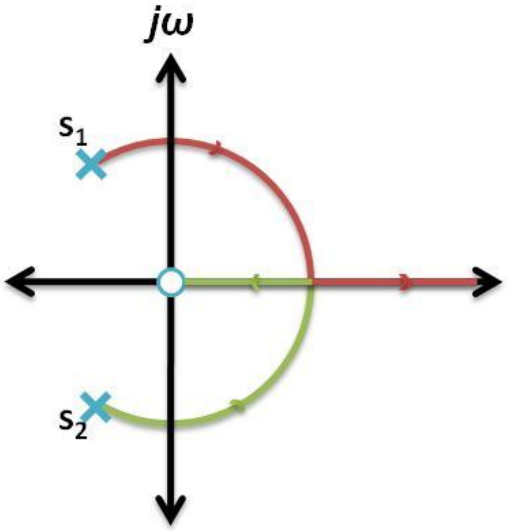

Figure 2.11: Complementary root-locus of basic positive feedback design

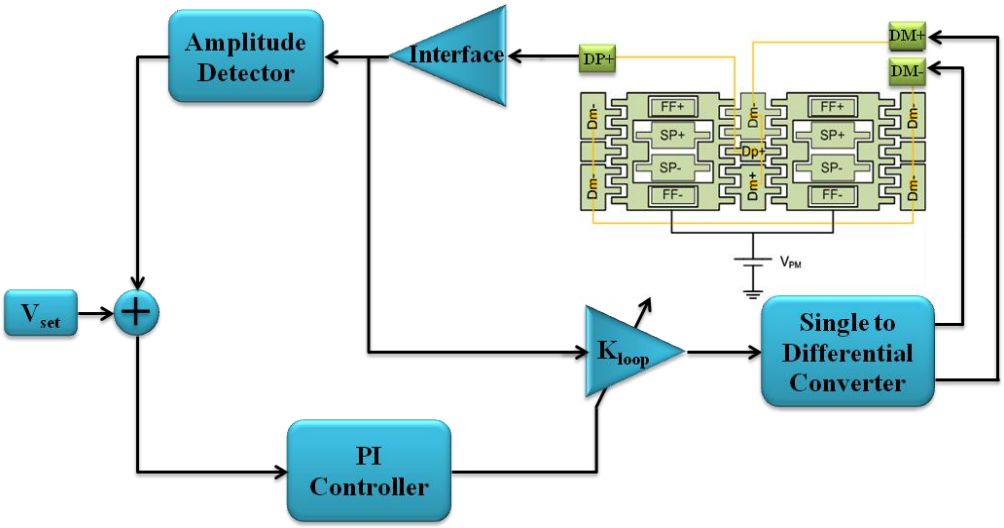

Figure 2.12: Generalized schematic of the automatic gain control loop

The closed-loop poles of the automatic gain control loop can be derived as

$$s_{1,2} = \frac{-\left(\frac{\omega_D}{Q_D} - K_D \cdot K_{loop}\right) \pm \sqrt{\left(\frac{\omega_D}{Q_D} - K_D \cdot K_{loop}\right)^2 - 4 \cdot \omega_D^2}}{2} \qquad 2.69$$

Figure 2.13 illustrates the pole placement from start-up to steady-state due to the open-loop gain adjustment. At the start-up, the controller increases the open loop gain and shifts the closed loop poles to RHP (right-half-plane). Thus, the system becomes instable, and the vibration amplitude of the gyroscope increases exponentially until it reaches the vibration amplitude limit defined by the reference voltage, V_{set}. At the steady-state, the automatic gain control loop adjusts itself as the closed loop poles lie on the imaginary axis where the open loop gain is unity. In addition, the controller provides the drive-mode to preserve its vibration amplitude at predetermined value in case of any change in the mechanical or ambient parameters, especially change in vacuum level.

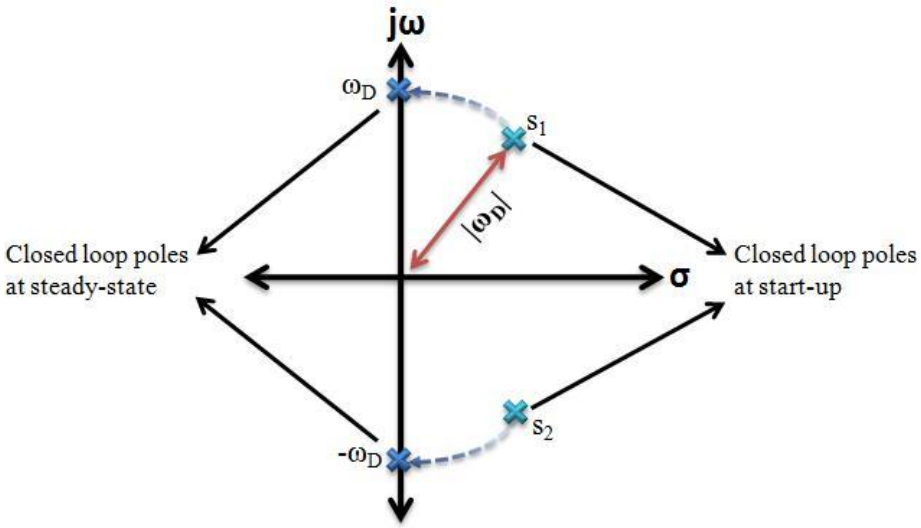

Figure 2.13: Closed loop pole diagram showing the pole placement from start-up to steady-state

Depending on the basics of the drive-mode automatic gain control loop, different topologies can be proposed and implemented. Regardless of the topology, a number of performance metrics should be taken in to account while designing the controller, including the performance metrics, such as stability of the loop, maximum overshoot of the vibration amplitude, settling time, and steady-state error. To design optimum controller, the performance metrics should be clearly defined, and the linear model of the automatic gain controller should be obtained.

2.4.2.2 Sense-Mode Electronics

In the presence of angular rate input to the vibratory gyroscope, the sense-mode output is an amplitude modulated (AM) signal, which is the modulation of the rate input at the oscillation frequency of the drive-mode. Assuming the velocity of the drive-mode is kept constant, the angular rate data is obtained by demodulating the AM signal to base-band and filtering through a LPF (low-pass filter). This approach is simply the open-loop rate sensing. The other approach is to use a closed-loop sensing, where the sense-mode displacement is damped to zero-displacement. In closed-loop sensing mechanism, the applied voltage to the force-feedback electrodes, which generates the force to eliminate Coriolis force acting on proof-mass, is monitored, and the rate data is obtained by extracting the envelope of the applied voltage. The subsections 2.4.2.2.1 and 2.4.2.2.2 describe these different approaches in more detail.

2.4.2.2.1 Open Loop Rate Sensing

The open-loop rate sensing is the convertion of the modulated signal at the sense-mode output to a base-band signal. Figure 2.14 shows the typical open-loop rate sensing circuit. Although the sense-mode and drive-mode are designed mechanically decoupled, due to the process imperfections the drive-mode vibration couples mechanically to sense-mode and a perpendicular signal, quadrature error, to rate signal is sensed at the output in addition to the rate signal. Thus, the sense-mode output can be expressed as

$$V_s(t) = \frac{A_s}{2} \cdot \{\cos[(\omega_D + \omega_Z) \cdot t + \varphi_s] + \cos[(\omega_D - \omega_Z) \cdot t + \varphi_s]\} + A_Q \cdot \cos(\omega_D \cdot t + 90 + \varphi_s) \quad 2.70$$

where A_s is the voltage amplitude of the rate signal, A_Q is the voltage amplitude of the quadrature signal, ω_D and ω_Z are drive-mode and rate input frequencies

respectively, and φ_s is the phase of the sense-mode output signal introduced by the interface. If the sense-mode output is demodulated with a carrier signal at mechanical resonance frequency of the drive-mode with phase φ_s, the demodulator output can be derived as

$$V_D(t) = \underbrace{\frac{A_s}{4}[\cos(\omega_z t + \varphi_s - \varphi_D) + \cos(-\omega_z t + \varphi_s - \varphi_D)]}_{baseband\ term}$$
$$\underbrace{+\frac{A_Q}{2}\cos(90 + \varphi_s - \varphi_D)}_{Quadrature\ Error} + \underbrace{\frac{A_Q}{2}\cos(2\omega_D t + 90 + \varphi_s - \varphi_D)}_{higher\ frequency\ terms} \quad 2.71$$
$$\underbrace{+\frac{A_s}{4}cos[(2\omega_D + \omega_z)t + \varphi_s + \varphi_D] + \frac{A_s}{4}cos[(2\omega_D - \omega_z)t + \varphi_s + \varphi_D]}_{higher\ frequency\ terms}$$

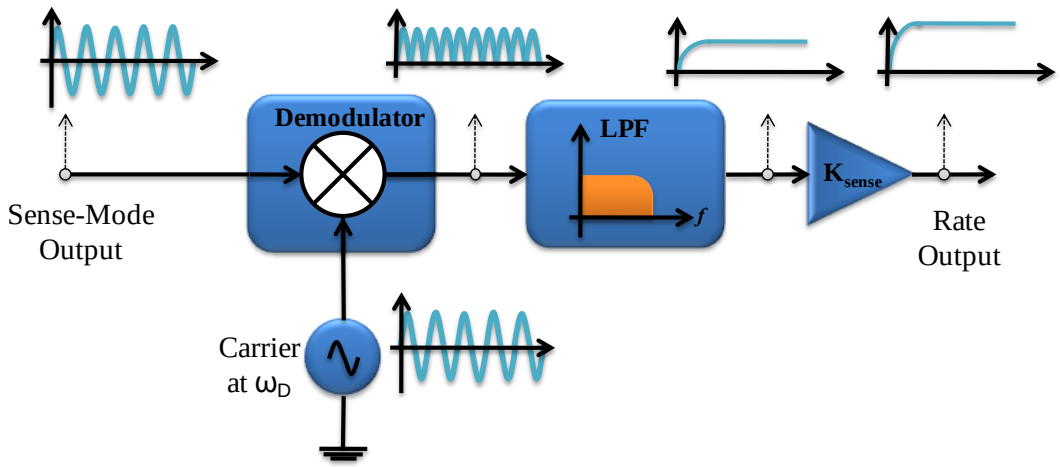

Figure 2.14: Typical open-loop rating circuit

The demodulator output is filtered through a LPF (low-pass filter) whose cut-off frequency is determined as rejecting the high frequency terms. The filtered signal includes both baseband rate voltage and quadrature error, and it is obvious that if the carrier signal and sense-mode output is in phase the quadrature error diminishes and only baseband rate voltage is obtained at the output of the open-loop rate sensing circuit. The carrier signal is usually generated by the drive-mode output signal;

hence to match these two phase, the phase difference between drive-mode output and sense-mode output should be taken into account and a phase shifter should be introduced between drive-mode output and demodulator carrier input if necessary. Table 2.2 provides a phase difference look-up reference depending on the frequency matching of the gyroscope and different interface-types [24].

Table 2.2: Look-up reference for determining the phase difference between drive and sense modes, the reference value is the drive-mode input signal [24]

Mode Matching	Interface Type	X_{drive}	$V_{drive,out}$	Y_{sense}	$V_{sense,out}$
Matched	Resistive	+90°	In-phase	±90°	0° or 180°
	Capacitive		+90°		±90°
Mismatched	Resistive		In-phase	0° or 180°	±90°
	Capacitive		+90°		0° or 180°

2.4.2.2.2 Closed-loop Rate Sensing

As the vacuum level increases, the quality factor of the sense-mode increases considerably, that decreases the bandwidth of the sense-mode into a few Hz. Although the sense-mode fingers have electrostatic spring constant effect that provides resonance frequency tuning, the matching of the sense-mode and drive-mode requires very precise tuning in vacuum ambient. Moreover, in matched-mode operation, the bandwidth of the rate sensing system is limited to a few Hz by the bandwidth of the sense-mode, which is not desirable for most of the practical applications. Operating the gyroscope in mismatched condition having a wide bandwidth is a plausible solution in most application; however, the low mechanical gain of sense-mode also limits the sensitivity of the gyroscope. In addition, the ambient parameter changes during operation (such as a change in the vacuum level) causes the scale factor of the gyroscope to change. Moreover, due to the process imperfection, the gyroscope sense-mode response may vary that causes different gyroscopes processed on same wafer to have different scale factors. To overcome

these problems, it is possible to use closed-loop rate sensing to widen the bandwidth of the sense-mode and to make the performance of the gyroscopes to be less susceptible to process variations. The closed-loop rate sensing employs electrostatic damping to increase the damping of the system, thus to decrease the bandwidth. As described in Section 2.1.2 the generated force by the force-feedback electrodes decreases the net force acting on sense-mode and decreases the sense-mode displacement. It should be noted here that, if the force-feedback electrodes simultaneously generate equal force to Coriolis coupling, the sense-mode vibration halts and the voltage applied to the force-feedback electrodes carry Coriolis coupling data. Therefore, the angular rate input can be extracted from the voltage applied to force-feedback inputs. At the steady-state condition, the force balance equation between Coriolis coupling and the generated force by force feedback actuator is given as

$$2 \cdot m_{PM} \cdot \Omega_z(t) \cdot \omega_D \cdot X_D \cdot \cos(\omega_D \cdot t) = V_{FF}(t) \cdot V_{PM} \cdot \frac{\partial C_{FF}}{\partial x} \qquad 2.72$$

where V_{FF} is the applied voltage to force feedback electrodes, X_D is the vibration magnitude of the drive-mode, and $\frac{\partial C_{FF}}{\partial x}$ is the force feedback electrodes capacitance gradient with respect to capacitive gap change. Then, the applied voltage can be defined in terms of angular rate input as

$$V_{FF}(t) = \frac{2 \cdot m_{PM} \cdot \Omega_z(t) \cdot \omega_D \cdot X_D \cdot \cos(\omega_D \cdot t)}{V_{PM} \cdot \frac{\partial C_{FF}}{\partial x}} \qquad 2.73$$

Equation 2.73 reveals that the amplitude of the voltage applied to the force feedback electrode is a linear function of the angular rate input at the steady state.

Figure 2.15 shows basic closed-loop rate sensing mechanism where $G_S(s)$ is the sense-mode mathematical model, $N(s)$ is the input referred noise, and $C(s)$ is a controller stage. The closed-loop transfer characteristics of the system becomes

$$\frac{F_{Coriolis}(s)}{F_{FF}} = \frac{G_s(s) \cdot C_s(s) \cdot V_{PM} \frac{\partial C_{FF}}{\partial x}}{1 + G_s(s) \cdot C_s(s) \cdot V_{PM} \frac{\partial C_{FF}}{\partial x}} \quad 2.74$$

If

$$G_s(s) \cdot C_s(s) \cdot V_{PM} \cdot \frac{\partial C_{FF}}{\partial x} \gg 1 \quad 2.75$$

in the desired new bandwidth, Equation 2.74 simplifies to

$$\frac{F_{Coriolis}(s)}{F_{FF}(s)} \approx 1 \quad 2.76$$

Then, Equation 2.73 becomes valid in the new bandwidth. To satisfy the condition stated in Equation 2.75, $C_s(s)$ could be a constant gain stage, a controllable gain stage, or a frequency dependent amplifier which provides high gain at the frequency range to which the bandwidth is to widen.

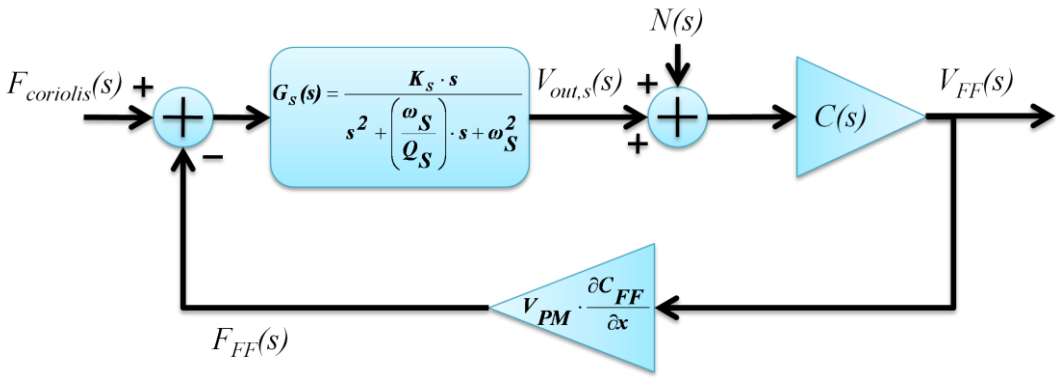

Figure 2.15: Basic closed-loop rate sensing mechanism

The applied voltage, $V_{FF}(t)$, is similar to Coriolis coupling, hence it is also an AM signal at the drive-mode vibration frequency, and the rate data can be extracted from applied voltage using same approach mentioned in Figure 2.14.

The closed-loop rate sensing reduces the effect of the fabrication and ambient variations on sense-mode performance fairly. However, the noise performance of the closed-loop system should be investigated, since the added $C_s(s)$ also amplifies the noise. The output referred noise, $N_o(s)$, in the closed loop system can be derived as

$$\frac{N_o(s)}{N(s)} = \frac{C_s(s)}{1 + G_s(s) \cdot C_s(s) \cdot V_{PM} \cdot \frac{\partial C_{FF}}{\partial x}} \qquad 2.77$$

If statement in Equation 2.75 holds, then Equation 2.77 simplifies to

$$\frac{N_o(s)}{N(s)} \approx \frac{C_s(s)}{G_s(s) \cdot C_s(s) \cdot V_{PM} \frac{\partial C_{FF}}{\partial x}} = \frac{1}{G_s(s) \cdot V_{PM} \cdot \frac{\partial C_{FF}}{\partial x}} \qquad 2.78$$

It is clear that the output noise of the closed-loop system is determined by the transfer characteristics between force-feedback and sense-pick electrodes. Since output referred noise, N_o, is shaped by the demodulation circuit, the noise out of the range between $(\omega_D - \omega_{c,LPF})$ and $(\omega_D + \omega_{c,LPF})$, where $\omega_{c,LPF}$ is the cut-off frequency of the LPF, is suppressed. Therefore, while the noise performance of the closed-loop rate sensing is discussed, the characteristic of Equation 2.78 in the range between $(\omega_D - \omega_{c,LPF})$ and $(\omega_D + \omega_{c,LPF})$ becomes critical. It can be concluded that if open-loop gain of the gyroscope between force-feedback and sense-pick electrodes is larger than one in the operation range, the output referred noise of the overall sense circuitry is decreased in magnitude. However, when noise performance of the angular rate sensing system is being analyzed, the output referred noise should be defined in terms of the angular rate. Hence, to determine the rate equivalent

output noise, the noise in magnitude should be converted to rate by dividing the noise to the scale factor of the system. The scale factors of the closed-loop and open-loop rate sensing systems for time-invariant angular rate inputs are expressed as:

$$Scale\ Factor_{Closed-loop} = \frac{V_{FF}(\omega_D)}{1\ rad/sec} = \frac{2 \cdot m_{PM} \cdot \omega_D \cdot X_D}{V_{PM} \cdot \frac{\partial C_{FF}}{\partial x}} \tag{2.79}$$

$$Scale\ Factor_{open-loop} = 2 \cdot m_{PM} \cdot \omega_D \cdot X_D \cdot |G(\omega_D)| \cdot |LPF| \tag{2.80}$$

where |LPF| is the gain of DC level extraction circuitry. Then, the rate equivalent of the output noise converted to baseband is calculated as:

$$\Omega_{n-Closed-loop} = \frac{N(\omega_D)}{|G(\omega_D)| \cdot 2 \cdot m_{PM} \cdot \omega_D \cdot X_D} \tag{2.81}$$

$$\begin{aligned} \Omega_{n-open-loop} &= \frac{N(\omega_D) \cdot |LPF|}{|G(\omega_D)| \cdot |LPF| \cdot 2 \cdot m_{PM} \cdot \omega_D \cdot X_D} \\ &= \frac{N(\omega_D)}{|G(\omega_D)| \cdot 2 \cdot m_{PM} \cdot \omega_D \cdot X_D} \end{aligned} \tag{2.82}$$

The Equations 2.81 and 2.82 show that although the closed-loop rate sensing affects the noise at the angular rate system in magnitude-wise, the rate equivalent noise at the output is the same for both the open-loop and the closed-loop rate sensing.

2.5 Summary

This chapter presents the basic theory of the MEMS vibrating capacitive gyroscopes and external electronics. First, the dynamics of the drive-mode and sense-mode are described by introducing force-displacement relations. Then, the actuation and sensing mechanism used in the capacitive vibratory gyroscope are investigated and different parallel plate capacitor configurations are analyzed. Thirdly, the electrical model and mathematical model of the gyroscope are obtained by combining the actuation-sensing mechanism and force-displacement relations. Next, the gyroscope external electronics theory and basics are introduced. The gyroscope electronics are separated as the drive-mode and sense-mode electronics. For drive-mode electronics, the oscillation criteria and automatic gain control loop basics are given. Finally, the open-loop and closed-loop rate sensing principles are discussed.

CHAPTER 3

READOUT AND CONTROL ELECTRONICS

This chapter represents the design details of the readout and complementary electronics of SOG (silicon-on-glass) vibratory gyroscopes developed at METU and gives simulation results of various control electronics. Section 3.1 describes transresistance and transimpedance types readout electronics designed and implemented in this study. Section 3.2 gives detailed design analysis of the drive and sense mode electronics. Moreover, this section proposes three different solutions for automatic gain control (AGC) loop design and describes modeling and controller design for these solutions. In addition, this section describes the open-loop and closed-loop rate sensing mechanism developed for the sense-mode of the vibratory gyroscopes. This section also gives simulation results which verify the operation of drive-mode and sense-mode electronics. Section 3.3 summaries the chapter.

3.1 Readout Electronics

The capacitance change due to the input angular rate is typically in the order of sub-attofarads ($1aF=10^{-18}F$) as the displacement of the micromachined gyroscope in the sense direction is smaller than a diameter of a silicon atom. Therefore, the induced current in the sensing electrode is very small and this current can be sensed only with dedicated readout electronics. Thus, the readout electronics have important role in determining the overall performance of the vibratory gyroscopes. A high performance gyroscope interface requires DC biasing of the high-impedance output of the gyroscope, low noise, low parasitic capacitance, and low drift. As mentioned in Section 2.4.1, there are two main interface types: resistive-type interface and capacitive-type interface. The discussion on the generalized interface in Figure 2.9

points out that the parasitic capacitance due to the interconnections limits the responsivity of the interface electronics. Hence, the effect of the parasitic capacitance should be eliminated by using a different topology. The effect of the parasitic capacitance is minimized with transimpedance amplifier (TIA) type interfaces [36], and they are preferred in this study. Figure 3.1 shows a TIA structure cascaded to a gyroscope, where i_o is the induced current in the sensing electrodes, C_s is the stationary capacitance of the gyroscope, C_P is the total of the parasitic capacitances coming from interconnections and opamp and $R_{interface}$ and $C_{interface}$ are the readout resistance and capacitance, respectively. The negative feedback configuration of the opamp compels the difference (or error) between inverting input and noninverting input to zero; if the opamp open loop gain is very large, the inverting input of the opamp is biased to the voltage applied to the noninverting input of the opamp. Hence, by connecting the noninverting input of TIA to the ground, the high impedance output of the gyroscope is biased to zero voltage, called as virtual ground, via the negative feedback resistor, $R_{interface}$. In addition to biasing the high impedance output of the gyroscope, the negative feedback resistance also biases the output of TIA to the zero DC voltage. Since the stationary capacitance of the gyroscope and overall parasitic capacitances are connected to ground in both ends in TIA, the effect of the capacitances between high impedance node and ground diminishes in the AC analysis. Thus, the induced current in the sensing parallel plate capacitor, i_o, passes through the interface impedance and is converted to output voltage which is expressed as

$$V_{out}(s) = -i_o(s) \cdot \left(R_{interface} // \frac{1}{s \cdot C_{interface}} \right) \tag{3.1}$$

As described in section 2.4.1, in the resistive type interfaces the resistance, the value of the interface resistor is smaller than the impedance value of the interface capacitor. In this case, Equation 3.1 simplifies to

$$V_{out}(s) = -I_o(s) \cdot R_{interface} \tag{3.2}$$

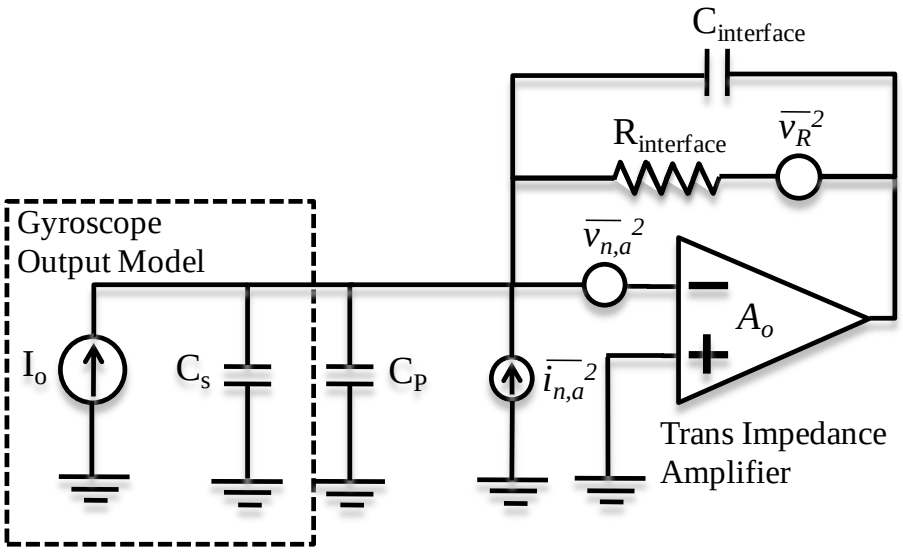

Figure 3.1: TIA structure cascaded to gyroscope output

The resistive type interface condition may be provided by using only the interface resistor in TIA, and it can be concluded that the interface resistance value is to be increased to obtain the maximum responsivity. However, the high resistance value of the feedback resistor may arise the stability problem in the TIA type readout electronics [58]. Figure 3.2 shows a generalized noise gain Bode plot for the TIA type interface. The net slope at the frequency where the open loop gain and noise gain intersects determines the stability of the amplifier. If the slope is equal to or less than 20 dB/decade, the amplifier satisfies the unconditional stability. The dashed line in the figure ($C_{interface}=0$) has a probability to intersect the line higher or equal to 20 dB/decade, therefore to a feedback capacitor, $C_{interface,}$ should be used in resistive-type interfaces compensate the gain [59]. The added capacitance value should be equal or larger than the capacitance between inverting input and AC ground [60]. Since the additional capacitor introduces a phase error, φ_{TRA}, the upper limit of the resistive value should be determined according to maximum allowable phase error, $\varphi_{TRA,max}$. The phase error of the transresistance amplifier (TRA) at mechanical resonance frequency of the drive-mode, φ_{TRA} is expressed as

$$\varphi_{TRA} = \tan^{-1}\left(\omega_D \cdot R_{interface} \cdot C_{interface}\right) \qquad 3.3$$

Then, for resistive interface the maximum interface resistance is found for unconditionally stability condition as

$$R_{interface,max} = \frac{\left|\tan\left(\varphi_{TRA,max}\right)\right|}{\omega_D \cdot C_{interface,stability}} \qquad 3.4$$

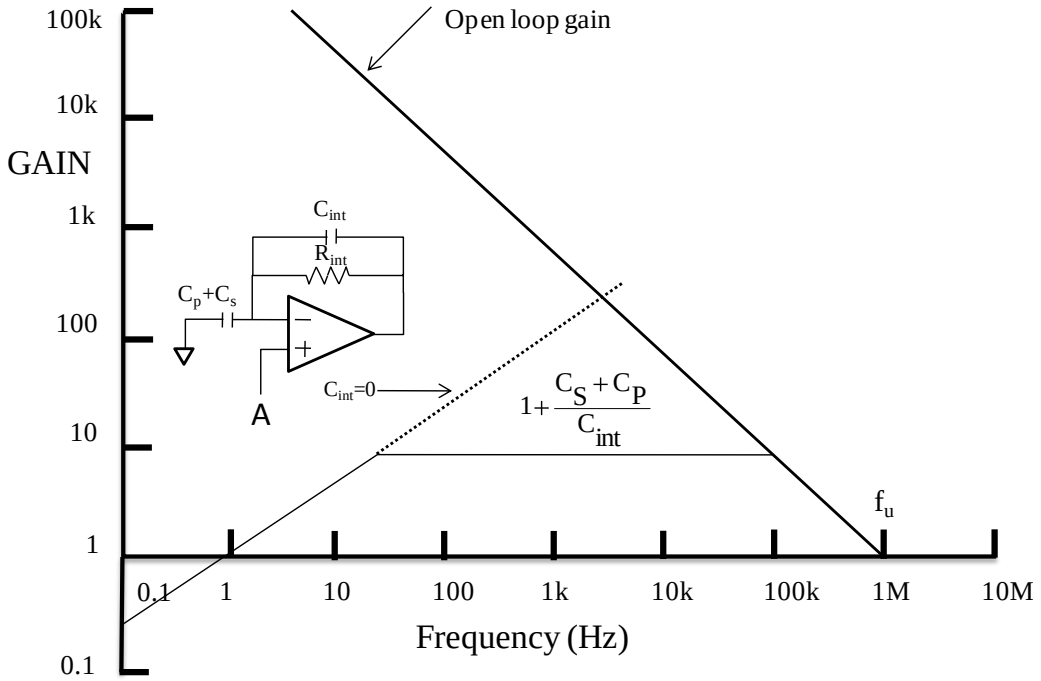

Figure 3.2: A generalized noise gain Bode plot for TIA type interface

As mentioned in Section 2.4.1, the capacitive type TIA interfaces are used in the sense-mode outputs to eliminate the requirement for a 90˚ phase shifter in mismatched operation. Capacitive TIA cannot be implemented by a single capacitive feedback, since it cannot bias the output of the TIA to DC zero value; hence, a resistive feedback parallel to the capacitor should be used for DC biasing the output. The resistive feedback used should be large enough to provide a small phase error at the output. However, the maximum available resistor value is limited by the process and the size of the resistor. Therefore, the minimum capacitor value is determined either by the maximum allowable phase error at the output. For the capacitive type interface, the capacitor value for the minimum allowable phase error is defined as

$$C_{interface,min} = \frac{\left|\tan\left(\varphi_{TIA,max}\right)\right|}{\omega_D \cdot R_{interface,max}} \quad 3.5$$

As mentioned above, the electronic noise contribution of the readout electronics has an important effect on the overall performance of the vibratory gyroscope. The total output referred electronic noise of the TIA can be derived as

$$Total\ RMS\ output\ referred\ noise = \int_{f_D - f_C}^{f_D + f_C} \overline{v_{o,rms}^2(f)} \cdot df \quad 3.6$$

where $\overline{v_{rms,o}^2(f)}$ is the output referred noise, f_D is the resonance frequency of the drive-mode and f_C is the cut-off frequency of the LPF described in Section 2.4.2.2.1. Assuming the opamp is ideal, $\overline{v_{o,rms}^2(f)}$ is expressed as

$$\overline{v_{o,rms}^2(f)} = \overline{\frac{v_R^2}{\left(s.R_{interface}.C_{interface} + 1\right)^2}} + \overline{v_{n,a}^2(f)} \cdot \beta(f)^2 + \overline{\iota_{n,a}^2(f)} \cdot Z_{interface}^2 \quad 3.7$$

where $\overline{v_R^2}$ thermal noise of the interface resistor, $\overline{v_{n,a}^2(f)}$ is the input-referred voltage noise of the OPAMP, $\overline{\iota_{n,a}^2(f)}$ is the input referred current noise of the OPAMP, $Z_{interface}$ is the impedance of the feedback network, and $\beta(f)$ is the voltage noise gain of the TIA interface. $\overline{v_R^2}$ and $\beta(f)$ are defined as

$$\overline{v_R^2} = 4 \cdot k \cdot T \cdot R_{interface} \quad 3.8$$

$$\beta(f) = 1 + \frac{j \cdot 2\pi f \cdot (C_s + C_P) \cdot R_{interface}}{1 + j \cdot 2\pi f \cdot C_{interface} \cdot R_{interface}} \qquad 3.9$$

and $\overline{v_{n,a}^2(f)}$ and $\overline{\iota_{n,a}^2(f)}$ are voltage and current noise values of the opamp. Moreover, input referred current noise of the TIA can be derived as

$$\overline{\iota_{n,rms}^2(f)} = \frac{\overline{v_R^2}}{R_{interface}^2} + \overline{v_n^2} \cdot \left[\frac{1}{Z_{interface}(f)} + 2\pi f \cdot (C_s + C_p)\right]^2 + \overline{\iota_{n,a}^2} \qquad 3.10$$

Equation 3.10 indicates that the noise contribution of the opamp should be minimized and $R_{interface}$ should be maximized in order to obtain low noise interface. Furthermore, the parasitic capacitance of the TIA should be decreased to lessen the effect of the voltage noise contribution of the opamp.

One of the critical design merits of high performance interfaces is the low offset and low drift; hence, the opamp used in the interface should have low offset voltage and low drift. Moreover, the interface resistor should have low thermal dependency in order to decrease thermal drift.

In this study, Analog Devices AD8608 OPAMPs are used [61], as these OPAMPs have low-DC offset (12 μV), low offset voltage drift (1 μV/°C), low input referred voltage noise (22 nV/√Hz), low input referred current noise (50 fA/√Hz) and high impedance (1.5 pF and CMOS input). As the interface resistance in the resistive type interfaces a 1 MΩ thick-film SMD resistor is used, and 1 pF interface capacitor is used for stability. In the capacitive TIA, a 470 MΩ resistor biases the output of the interface to DC ground, and a 1.8 pF capacitor converts the injected current to a voltage. The output referred voltage noise of the transimpedance amplifier is calculated approximately as 0.447 μV/√Hz, and the dominant noise source is the current noise of the amplifier.

3.2 Drive-Mode and Sense-Mode Electronics of Vibratory Gyroscope

As described in Section 2.4, external electronics oscillate the drive-mode at the mechanical resonance frequency with a sustained amplitude, while external electronics extract the angular rate input from the AM signal at the output of the sense-mode electrodes. The following subsections propose different solutions to achieve required operations in drive-mode and sense-mode.

3.2.1 Drive-Mode Electronics

Drive-Mode electronics aim to vibrate the drive-mode at its resonance frequency providing a closed loop positive feedback loop which satisfies "Barkhausen Criteria". Moreover, the magnitude of the drive-mode vibration is sustained to construct a high performance gyroscope. As analyzed in Section 2.4.1, AGC (automatic gain control) loop provides both oscillation at mechanical resonance frequency and controllable vibrating amplitude. The gyroscopes used in this study have differential drive (DM- and DM+) electrodes and single-ended sense electrode (DP) in drive-mode. Hence, the signal at the output of DP is to be amplified by a controller gain stage and converted to a differential signal in the closed-loop. In this study, three different AGC loop designs are proposed: (i) the square-wave driving signal AGC, (ii) the sinusoidal-wave driving signal AGC, and (iii) the off-resonance frequency driving signal AGC. In square wave and sinusoidal wave driving AGC loops, the applied voltage to DM+ electrodes should be in-phase with the DP electrode output whereas the DM- electrode is actuated by a voltage that has a 180 phase difference between the DP output. On the other hand, in the off-resonance frequency driving signal AGC loop DM- is in phase while DM+ is out of phase with DP output. The following subsection explains the loop operation principles and their controller designs.

3.2.1.1 Square-Wave Driving Signal AGC Loop

Remembering that a square-wave signal whose fundamental frequency at the drive-mode mechanical resonance frequency can generate a sinusoidal force at the resonance frequency, provided that the parallel plate capacitor is biased with a DC voltage difference [23]. Figure 3.3 shows a typical square-wave driving signal AGC loop structure. In this closed-loop, the amplitude of the signal at the drive-pick electrode is obtained by shifting the DP signal to baseband and filtering the high frequency components. Then, the amplitude is compared with a set voltage which corresponds to the desired vibration amplitude, and the error signal is amplified by a PI controller. The PI controller provides a controllable gain stage to satisfy the oscillation criteria and adjusts the open loop gain to set the vibration amplitude to the desired value. After the PI controller stage, the driving signal amplitude at DC is converted differential square-wave driving signal at the frequency of the DP signal. Provided that the phase introduced by interface and modulation circuitry is negligible, the loop oscillates at the drive-mode mechanical resonance frequency.

In order to design PI controller parameters, the overall loop is simplified to a second order system. Then, the first-order approximate model of the drive-mode resonator at resonance frequency can be expressed as [24]

$$TFD(s) = \frac{A_D}{1 + s \cdot t_{response}} \tag{3.11}$$

where A_D is the steady-state gain of the drive-mode between DM+ or DM- and DP at the resonance, and $t_{response}$ is the time lasted to reach 63% of the final vibration amplitude and is defined as

$$t_{response} = \frac{2 \cdot Q_D}{\omega_D} \tag{3.12}$$

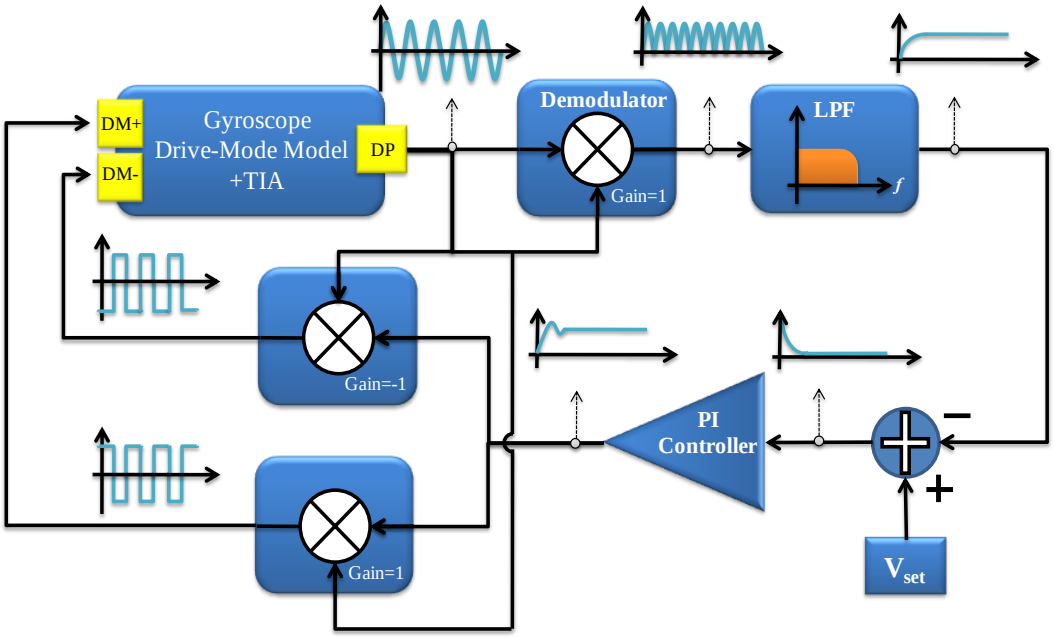

Figure 3.3: Typical structure of square-wave driving signal AGC loop

The frequency parameter s of *TFD* corresponds to the change of the vibration amplitude in the frequency domain. The characteristic equation of the simplified closed-loop system can be derived as

$$1 + Open\ loop\ gain = 0 \tag{3.13}$$

where open loop gain is

$$\underbrace{\frac{A_D}{1 + s \cdot t_{response}}}_{sensor} \cdot \underbrace{K_D}_{Demodulator} \cdot \underbrace{K_{LPF}}_{LPF} \cdot \underbrace{\frac{K_P \cdot s + K_I}{s}}_{PI\ Controller} \cdot \underbrace{K_M}_{Modulator} \cdot \underbrace{2}_{\substack{Differential \\ Drive}} \tag{3.14}$$

$K_{D,}$ K_M, and K_{LPF} are gain of the demodulator, modulator, and LPF stages, respectively, K_P is the proportional gain and K_I is the integral gain of the PI controller. Moreover, the loop gain is amplified by 2, since the drive-mode is

actuated differentially. The damping factor, ξ_D, and closed-loop resonance frequency of the characteristic equation given in Equation 3.13, ω_n, are calculated as

$$\omega_n = \sqrt{\frac{2 \cdot A_D \cdot K_D \cdot K_{LPF} \cdot K_M \cdot K_I}{t_{response}}} \quad 3.15$$

$$\xi_D = \frac{1}{2 \cdot \omega_n \cdot t_{response}} \cdot (1 + 2 \cdot A_D \cdot K_D \cdot K_{LPF} \cdot K_M \cdot K_P) \quad 3.16$$

The maximum overshoot and settling time of a second-order system, which is the time for the system to reach 99% of its final value, are defined in terms of damping factor and resonance frequency as [62]

$$Maximum\ overshoot = e^{-\xi_D \pi / \sqrt{1-\xi_D{}^2}} \quad 3.17$$

$$t_{settling}(1\%) = \frac{4.6}{\xi_D \cdot \omega_n} \quad 3.18$$

After specifying the maximum overshoot and settling time of a drive-mode for optimum operation, the PI controller parameters can be calculated by using equation set (3.15)-(3.18). The maximum overshoot value is critical as the large vibration displacement causes the movable parallel plate fingers to crash the stationary plate, which result in malfunction of the gyroscope. Moreover, the settling time determines the response of the drive-mode closed loop to change in the ambient, hence the settling time is to be chosen small; but fast enough to compensate the parameter changes.

Figure 3.4 shows the schematic of proposed square-wave driving AGC loop for SOG gyroscopes developed at METU. The resistive interface circuit converts the mechanical displacement of the drive-mode to a voltage, and this voltage is

transferred to the baseband using the demodulator configured AD630 [66], and the signal amplitude is extracted by a second-order LPF. Then, the vibration error is calculated by the instrumentation amplifier AD620 [67], and the PI controller processes the driving signal amplitude. The differential square-wave drive signals are constructed as modulating the driving signal amplitude by the DP output in the modulator configured AD 630.

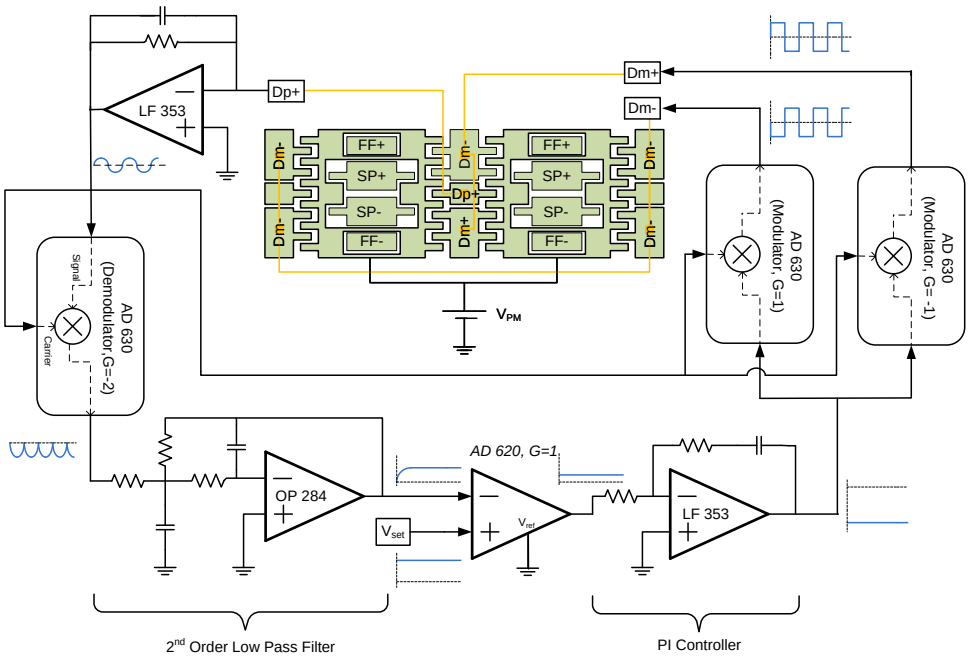

Figure 3.4: Circuit schematic of proposed square-wave driving signal AGC loop

Figure 3.5 shows SIMULINK transient simulation results of the interface output amplitude of the proposed AGC, hence the vibration amplitude change. The PI parameters are calculated using the equation set (3.15)-(3.18) to obtain a 5% overshoot and a 1 second settling time assuming that the quality factor of the system is 5000 and resonance frequency at 11.35 kHz with a 0.2 resonance gain. The full system SIMULINK simulation result shows that the overshoot and settling time values are slightly different than the calculated. Although the controller parameters are determined for a fixed vacuum level and quality factor, the ambient of the gyroscope may vary in time; therefore, the PI controller performance becomes critical in case of quality factor variations. Figure 3.6 shows the transient response

SIMULINK simulations of both the driving signal and the interface output. As increasing the quality factor higher than the value used in calculating PI parameters, i.e., Q=10000, the overshoot and settling time of the system increases. Decreasing the quality factor, i.e., Q=1000 increases the settling time. In addition, as the quality factor of the system decreases in time, the overshoot of the system at start-up is lower than the overshoot of the initial quality factor.

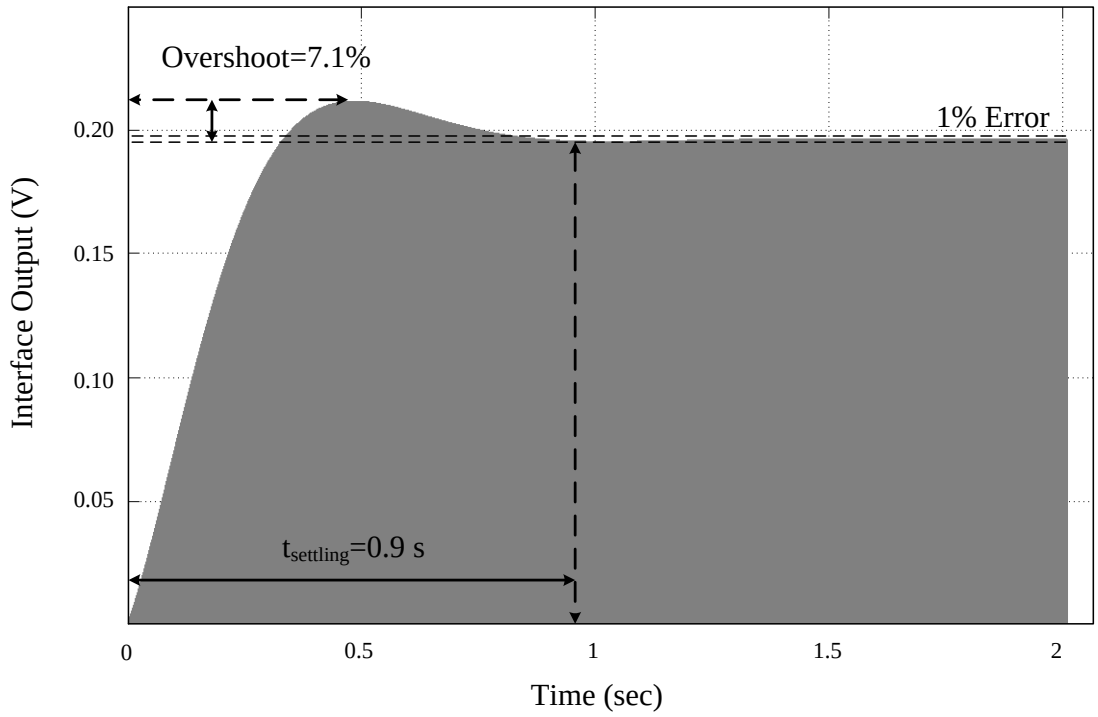

Figure 3.5: SIMULINK transient simulation of the interface output amplitude of the proposed square-wave driving signal AGC loop

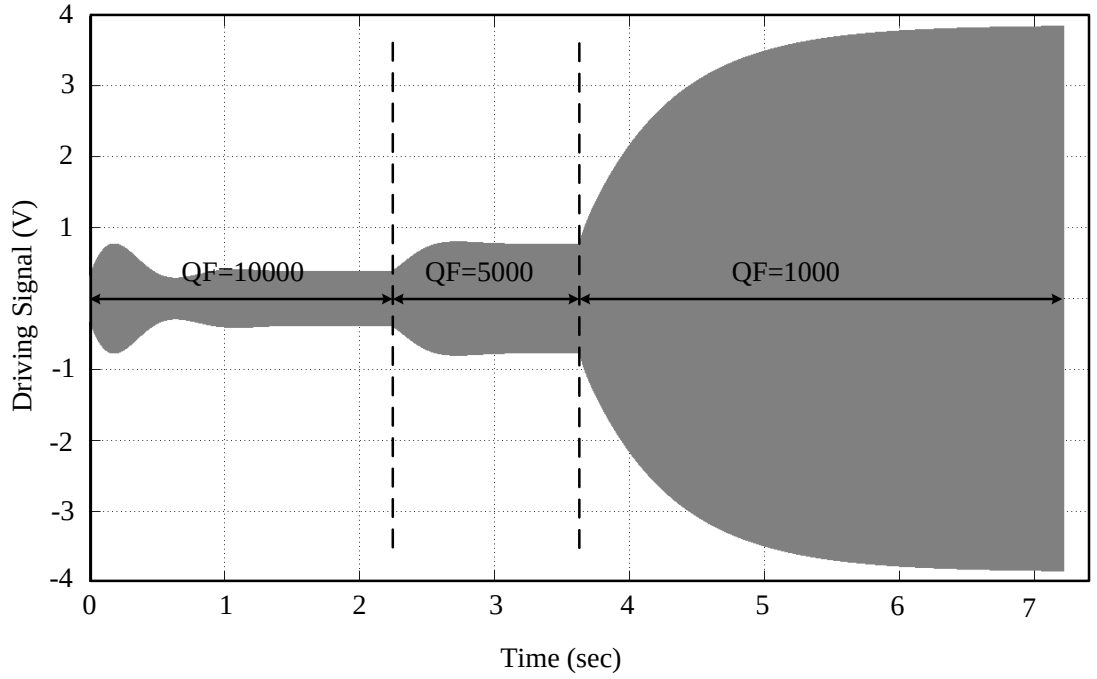

(a)

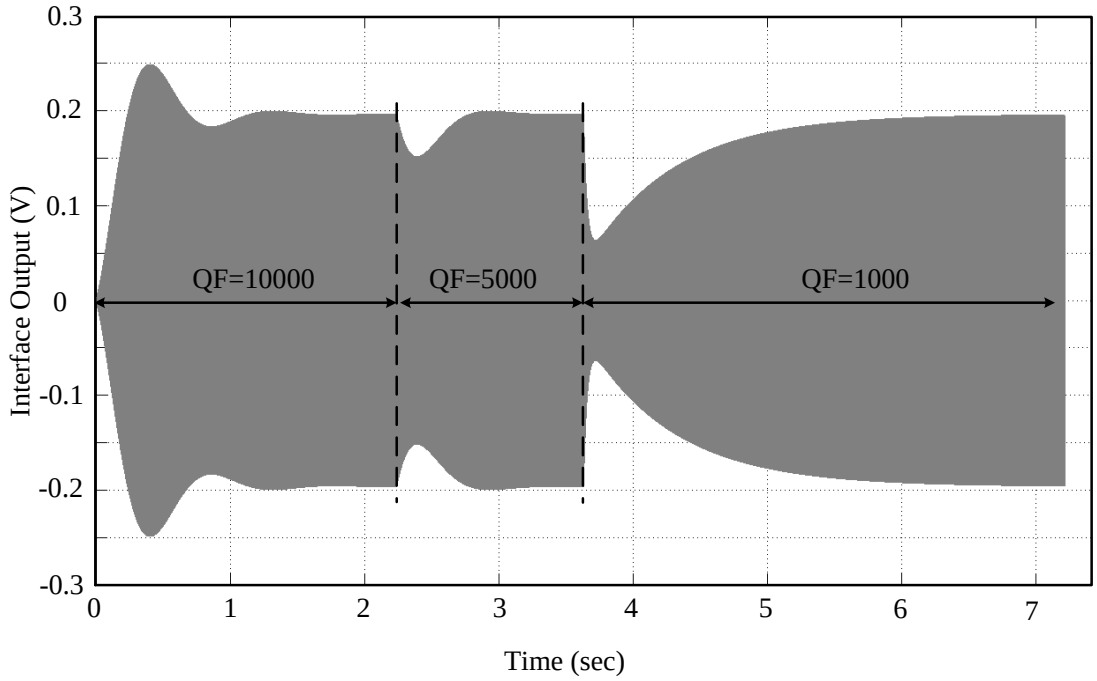

(b)

Figure 3.6: SIMULINK transient simulation for a) drive-pick interface output and b) driving square-wave signal as the quality factor (QF) of the system changes

In summary, in this section it is showed that the drive-mode of the gyroscope can be oscillated at resonance frequency by applying differential square wave driving signals, and if the amplitude of the driving signal is controlled by a PI controller, the displacement of the drive-mode can be set to the desired level. Besides, the controller design is given and it is verified that the controller provides sustained oscillation in case of the quality factor, and hence the ambient, changes.

3.2.1.2 Sinusoidal-Wave Driving Signal AGC Loop

Although the controller and loop design of the square-wave driving signal AGC loop are simple, the square-wave signal contains high frequency terms which results glitches in the circuit due to the electrical coupling and increases the mechanical noise since the higher order harmonics of the driving force should be dissipated by the mechanical structure. As the output signal of drive-mode output interface circuitry has a sinusoidal waveform, an AGC loop which amplifies the output signal to satisfy the oscillation criteria can be constructed [36]. Figure 3.7 illustrates a typical structure of a sinusoidal-wave driving signal AGC loop. In this loop, the vibration amplitude of the drive-mode electrodes is extracted by the amplitude detector circuitry which composes of demodulator and LPF, and the amplitude is subtracted from the required vibration amplitude. Then, the error is amplified by a PI controller which controls the gain of a VGA in order to fulfill the oscillation criteria and adjust the open loop gain unity at the steady-state operation. The output signal is multiplied by the gain of VGA, and the resultant voltage is converted to differential signals to oscillate the drive-mode mass.

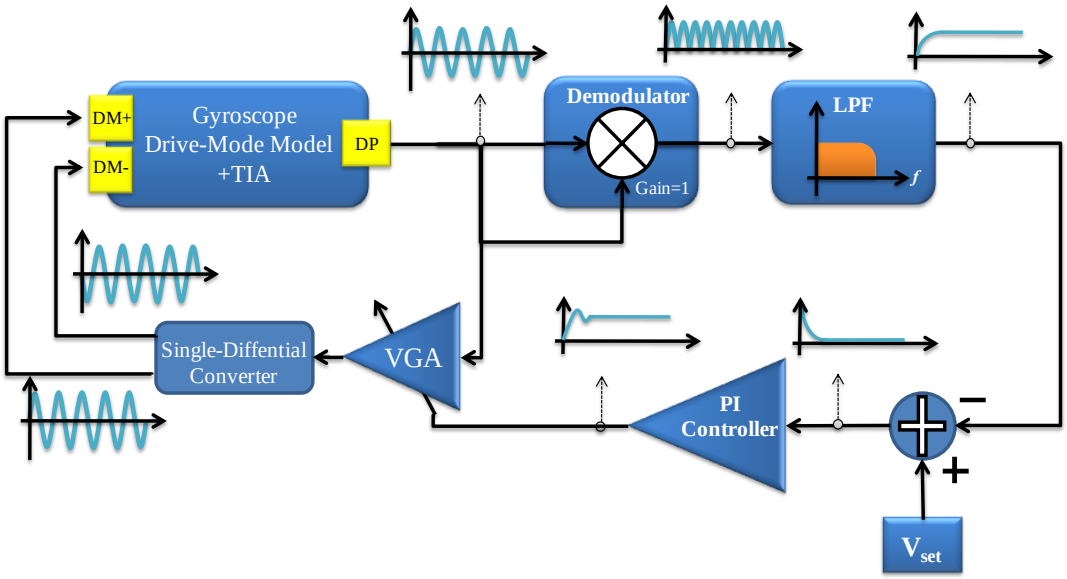

Figure 3.7: Typical structure of sinusoidal wave driving signal AGC loop

The proposed solution includes two nested loops, hence a generalized controller design is not easy. The loop should be linearized that requires reasonable assumptions. Therefore, it is better to design controller for the circuit implementation of the proposed method. Figure 3.8 gives the circuit schematic of the proposed solution. In this circuit, Analog Devices' variable gain amplifier AD600 is used as a controllable gain stage. The VGA provides dB linear gain between +30 dB and -10 dB, and the gain is controlled by applying signals between +0.625 V and -0.625 V. The control voltage higher than +0.625 V provides maximum gain which is +30 dB [65]. The gain characteristics of AD 600 VGA can be defined as

$$K_{VGA}(t) = 3.12 \cdot 10^{1.6 \cdot V_{control}(t)} \qquad 3.19$$

where $V_{control}$ is the gain control input of the VGA, which is equal to the output voltage of the PI controller, V_{PI}. The output voltage of PI controller can be defined as

$$V_{PI}(t) = K_P \cdot E(t) + K_I \cdot \int_0^t E(\acute{t}) \cdot d\acute{t} \qquad 3.20$$

where *E(t)* is difference between the reference voltage and the output of the amplitude detector circuit, in other words the interface output of the drive-mode. If the oscillation frequency is constant, the interface output of the closed-loop system, *A(t)*, can be defined as [65]

$$A(t) \approx A(t_0) \cdot \exp\left(-\frac{1}{2}\int_{t_0}^{t} b(t)\, dt\right) \qquad 3.21$$

where t_0 is the initial time, *b(t)* is the damping factor of the closed-loop system and is expressed as

$$b(t) = \frac{\omega_D}{Q_D} - K_{Drive} \cdot K_{VGA}(t) \qquad 3.22$$

K_{Drive} is the open-loop gain at resonance frequency excluding the VGA gain. It can be concluded that, if the closed-loop damping factor is kept constant at the start up, the vibration amplitude grows exponentially as a function of closed-loop damping factor. This can be achieved by applying a control voltage larger than 0.625 V. To provide the vibration amplitude to reach its desired value, V_{set}, the exponential growth given in Equation 3.21 is supposed to continue until t_1 ,when the vibration amplitude reaches the desired value, and the controller starts to sustain the vibration amplitude after t_1. Equating the interface output in Equation 3.21 to the reference voltage, t_1 can be calculated as

$$t_1 \approx \ln\left(\frac{V_{set}}{A(t_0)}\right) \cdot \left(-\frac{2}{b_{initial}}\right) \qquad 3.23$$

where $b_{initial}$ is damping factor of the closed-loop system when VGA has maximum gain. At time t_1 the error output, $E(t_1)$, becomes zero, then PI voltage is equal to the integration term of Equation 3.20. Then, substituting Equations 3.21-3.23 into Equation 3.20, the range of the PI parameter can be derived as

$$K_I \geq \frac{0.625}{[\ln(V_{set}) - ln\, A(t_0) - 1]} \cdot \frac{1}{V_{set}} \cdot \frac{K_{Drive} \cdot K_{VGA,max} - (\omega_D / Q_D)}{2} \qquad 3.24$$

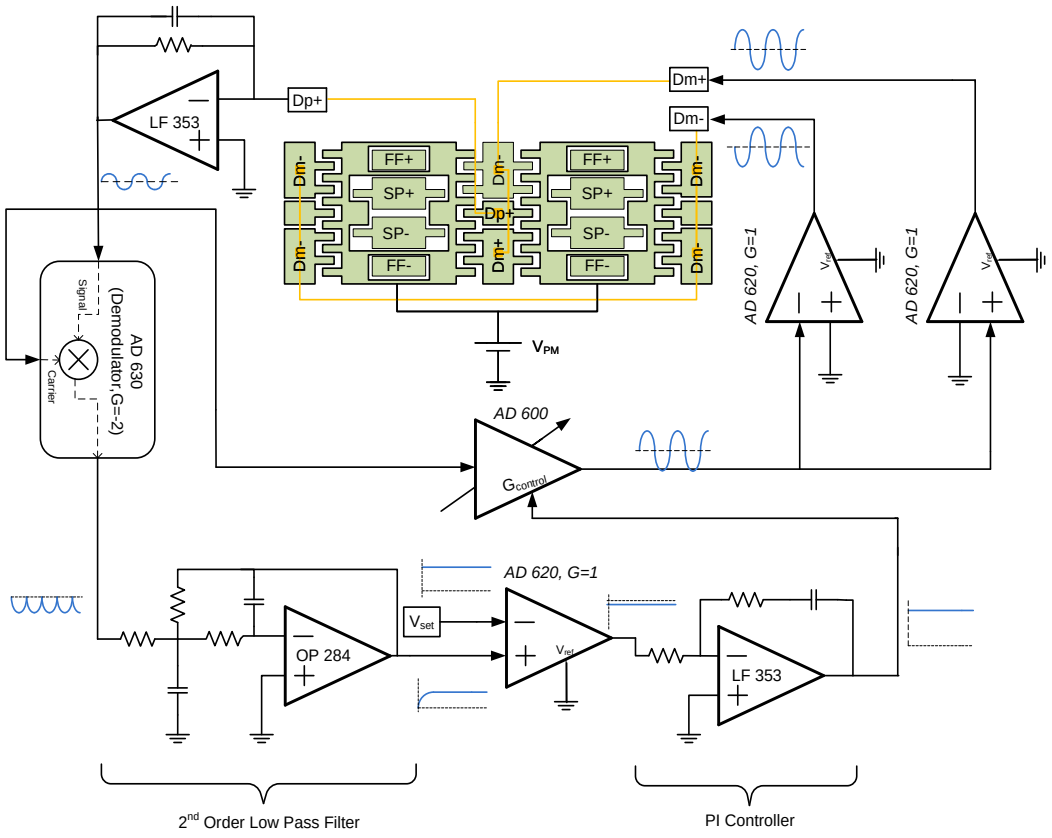

Figure 3.8: Circuit schematic of proposed sinusoidal-wave driving signal AGC loop

The above derivations satisfy the start-up of the closed-loop system and guarantee the vibration amplitude to reach around the desired level. Besides, the designed PI controller should control and limit the overshoot of the system. Therefore, in case of overshoot, the PI controller should attenuate the system vibration amplitude, which is

satisfied if the closed-loop damping factor of the closed-loop system is larger than zero. Then, the PI controller voltage to damp the signal is derived as

$$\frac{1}{1.6} \cdot log\left(\frac{\omega_D}{3.12 \cdot Q_D \cdot K_{Drive}}\right) > V_{PI} \qquad 3.25$$

Then, substituting Equation 3.20 into Equation 3.25 and assuming integration after t_1 is negligible and integration term is equal to 0.625 V (actually due to the overshoot the integrator starts to discharge and the integration term is less than 0.625 V, so in the actual case the overshoot is less than the case which the calculation is done according to this assumption), the proportional term of PI controller is defined as

$$K_P > \left[0.625 - \frac{1}{1.6} \cdot log\left(\frac{\omega_D}{3.12 \cdot Q_D \cdot K_{Drive}}\right)\right] \cdot \frac{1}{M \cdot V_{set}} \qquad 3.26$$

where M is the maximum overshoot percentage of the closed-loop system.

Figure 3.9 shows transient simulation of the interface output of the sinusoidal-wave driving signal AGC loop performed in SIMULINK. The loop controller parameter is calculated by using Equations 3.24 and 3.26 in order to keep the overshoot less than 10%. In the simulation, the mathematical model of the gyroscope in Section 3.2.1.1 is used. In addition, the reference voltage of the AGC loop is chosen as 0.2 V, and K_{Drive} is increased to 5.166. The simulation result verifies that the designed PI controller provides the closed-loop system to have overshot less than 10%. However, it should be noted that, if the cut-off frequency of the LPF in the amplitude detection mechanism is decreased, hence if the delay of the LPF increased; the exponential growth at the start-up last longer than the calculated value and PI controller interferes later than expected which causes the overshoot of the system to be larger than the calculated one.

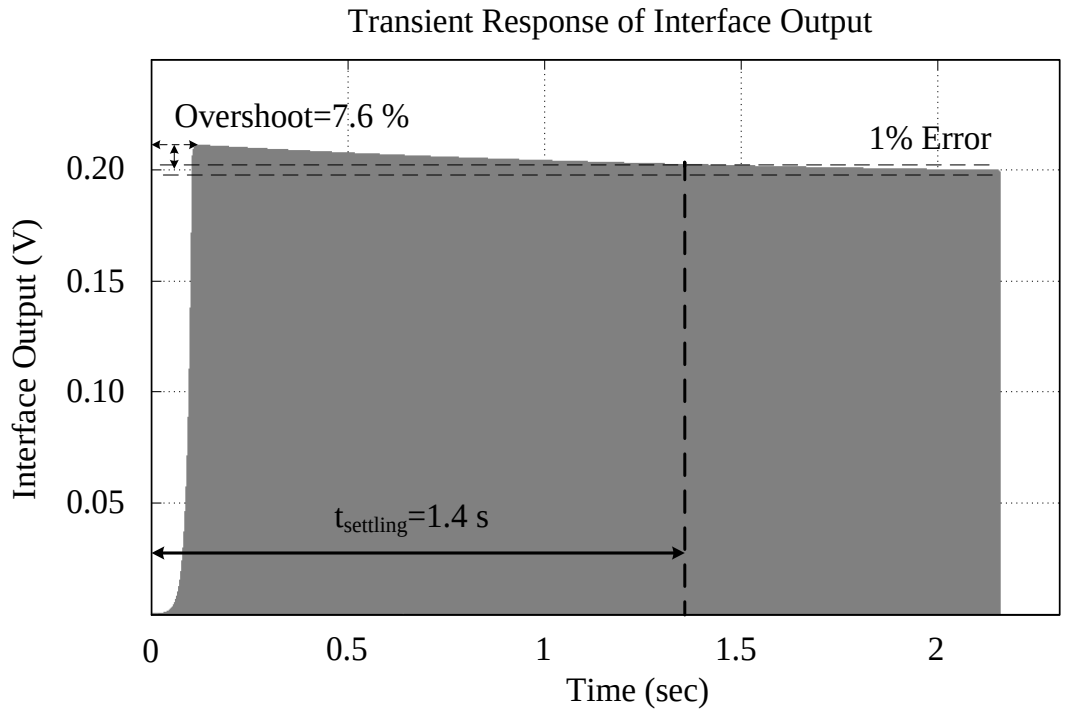

Figure 3.9: SIMULINK transient simulation of the interface output amplitude of the proposed sinusoidal-wave driving signal AGC loop

The PI controller design approach for sinusoidal-wave driving signal AGC investigates the closed-loop system performance at the start-up of the system. However, the ambient parameters change, especially with changing the vacuum level, which disturbs the closed-loop operation, hence the designed PI controller should compensate the disturbance and adjust the VGA gain to sustain the amplitude of the drive-mode vibration at the desired value. Figure 3.10 gives the linearized model of the sinusoidal-wave driving signal AGC loop which can be used to determine the performance of the closed-loop system at the presence of disturbance regardless of the used VGA [57]. This model is valid if the closed-loop damping factor, *b(t)*, is close to '0' and the vibration amplitude and damping factor relation can be defined as

$$A(t) \approx -\frac{A(t_i)}{2}\int_{t_i}^{t} b(t)\,dt \qquad 3.27$$

or equivalently

$$A(s) = -\frac{A_{t_i}}{2} \cdot \frac{b(s)}{s} \qquad 3.28$$

where t_i is the time when the system is disturbed and $A(t_i)$-is the vibration amplitude at time t_i which is equal to V_{set} in this discussion. The characteristic equation of the linearized model can be derived as

$$s^2 + \frac{A_{t_i} \cdot K_D \cdot K_p \cdot \alpha}{2} s + \frac{A_{t_i} \cdot K_D \cdot K_i \cdot \alpha}{2} = 0 \qquad 3.29$$

where α is the linearized relation between the PI controller voltage and VGA gain.

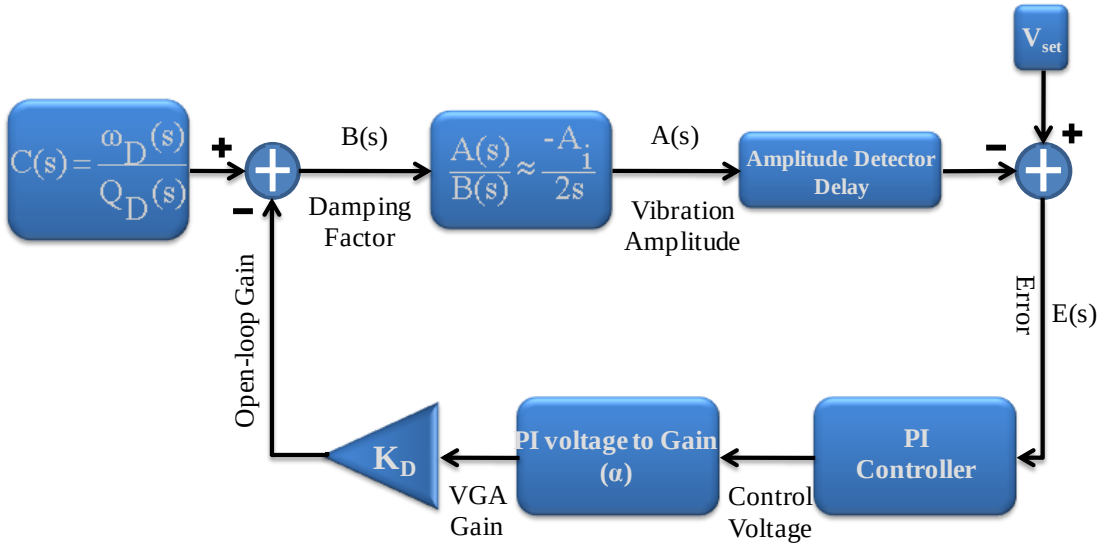

Figure 3.10: Linearized model for proposed sinusoidal-wave driving signal AGC loop

Figure 3.11 shows SIMULINK simulations of the transient response of the interface output and the driving signal amplitude as the quality factor of the system is decreased. When the PI parameters designed considering the start-up of the closed-loop system is substituted into Equation 3.29, the closed-loop system damping factor, ξ, is larger than one, the closed-loop system shows overdamped system

characteristics in presence of quality factor change at the steady-state operation. Hence, the system doesn't make an overshoot for these cases.

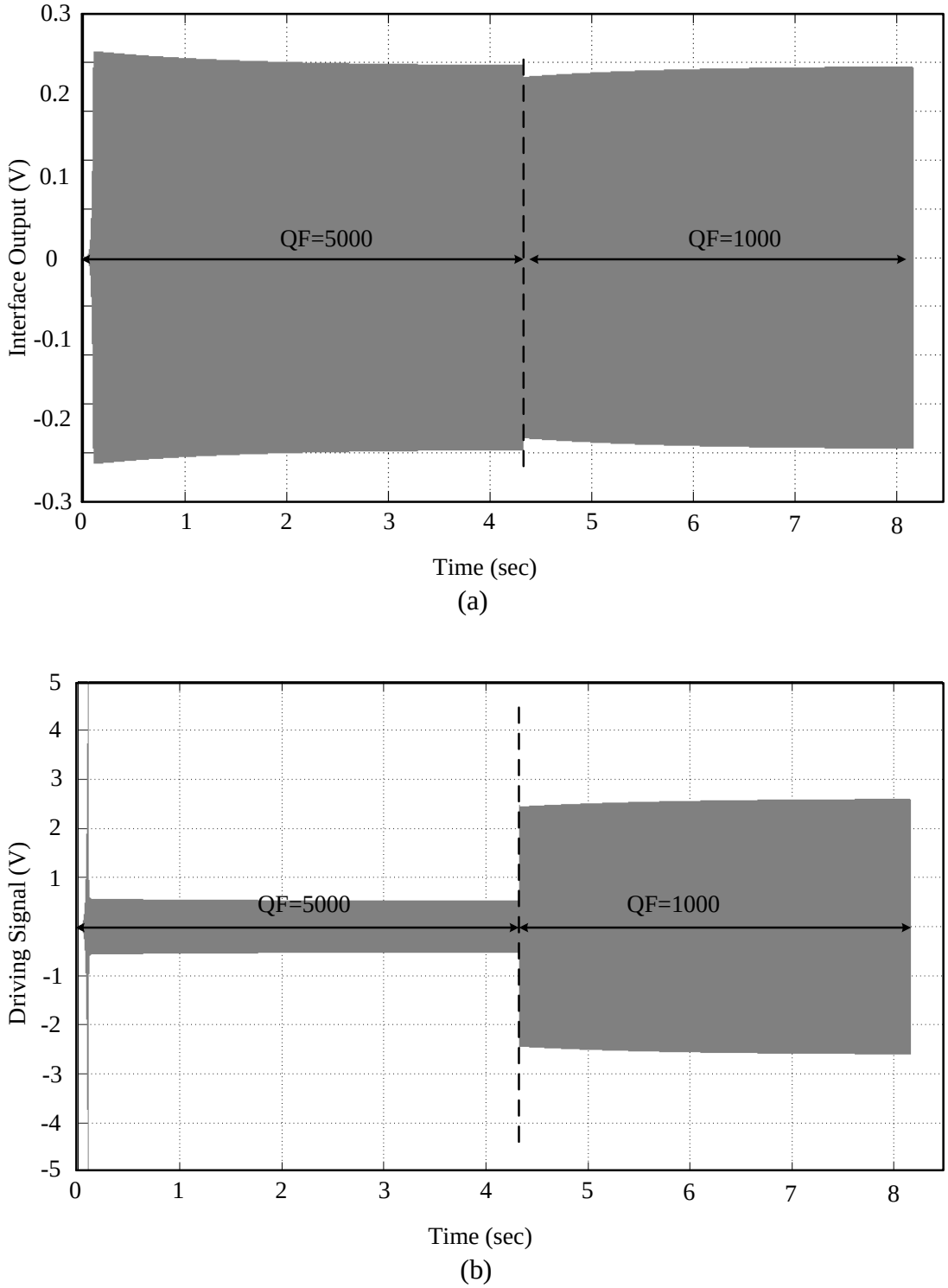

Figure 3.11: SIMULINK transient simulation for a) drive-pick interface output and b) driving sinusoidal-wave signal as the quality factor (QF) of the system changes

3.2.1.3 Off-Resonance Frequency Driving Signal AGC Loop

Both square-wave and sinusoidal-wave driving signal AGC loop actuate the drive mode at its mechanical resonance frequency by applying a time varying voltage whose fundamental frequency is equal to the drive-mode mechanical resonance frequency. Since the carrier frequency of the amplitude modulated signal at the sense-mode output electrodes is at drive-mode resonance frequency, the electrical coupling between the drive-mode driving electrodes and the sense-mode output electrodes may lead sensing errors. Moreover, the electrical noise of the driving signals and any change in the driving signals couple to the sense-mode output, degrading the vibratory gyroscope performance. Hence actuating the drive-mode at the mechanical resonance frequency by applying an actuating voltage which has no frequency component at the resonance frequency is a possible solution to eliminate sensing error and performance degradation due to electrical coupling. As discussed in Section 2.2.1, when a sinusoidal signal with DC offset is modulated at its half frequency, the resultant modulated signal has no component at the original signal frequency. Moreover, if the original signal frequency is at drive-mode mechanical resonance frequency, the modulated signal can oscillate the drive mode at its resonance frequency. The electromechanical conversion coefficient of this electrical to mechanical domain transformation is expressed in Equation 2.37. The generated force is a function of DC offset and sinusoidal signal. Therefore, an AGC drive loop can be constructed either controlling the DC offset or the sinusoidal wave amplitude of the driving signal generating the input signal of the modulators [51]. Figure 3.12 illustrates typical structures of half resonance frequency driving signal AGC loop with controlling a) DC offset b) sinusoidal signal amplitude of the driving signal generating the input signal of the demodulators. The approach illustrated in Figure 3.12 is valid in case of the carrier signal frequency is decreased to 1/4, 1/8 and 1/16 of the mechanical resonance frequency. In these loops the amplitude of the vibration is extracted from the output of the drive pick electrode and either the DC offset or the electrical open loop gain is adjusted by PI controller to adjust the vibration amplitude to the set level.

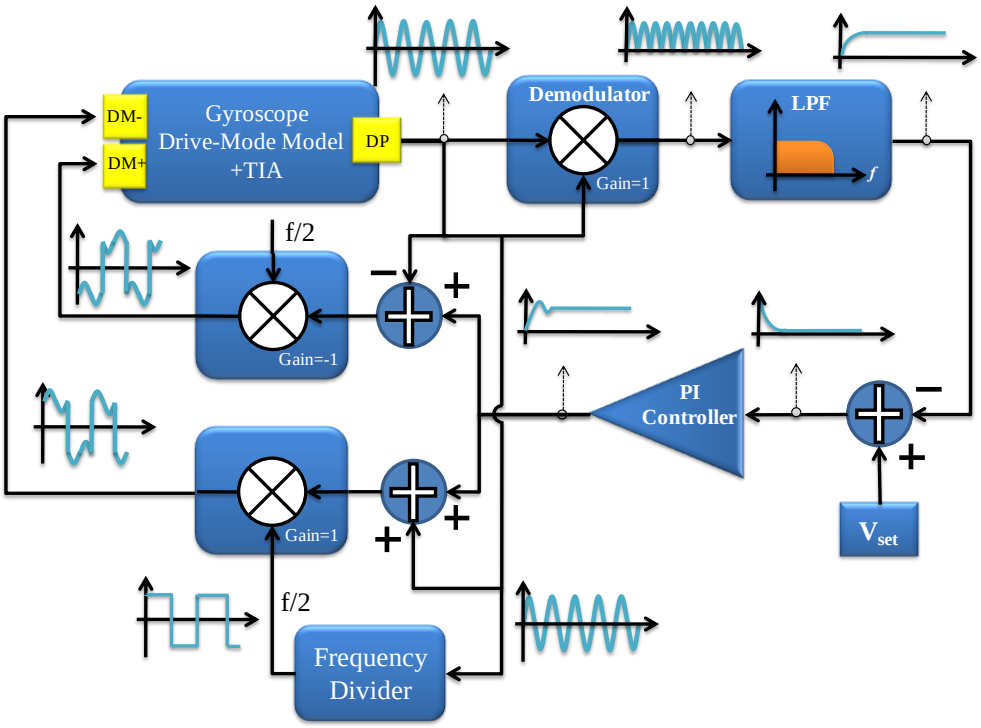

(a)

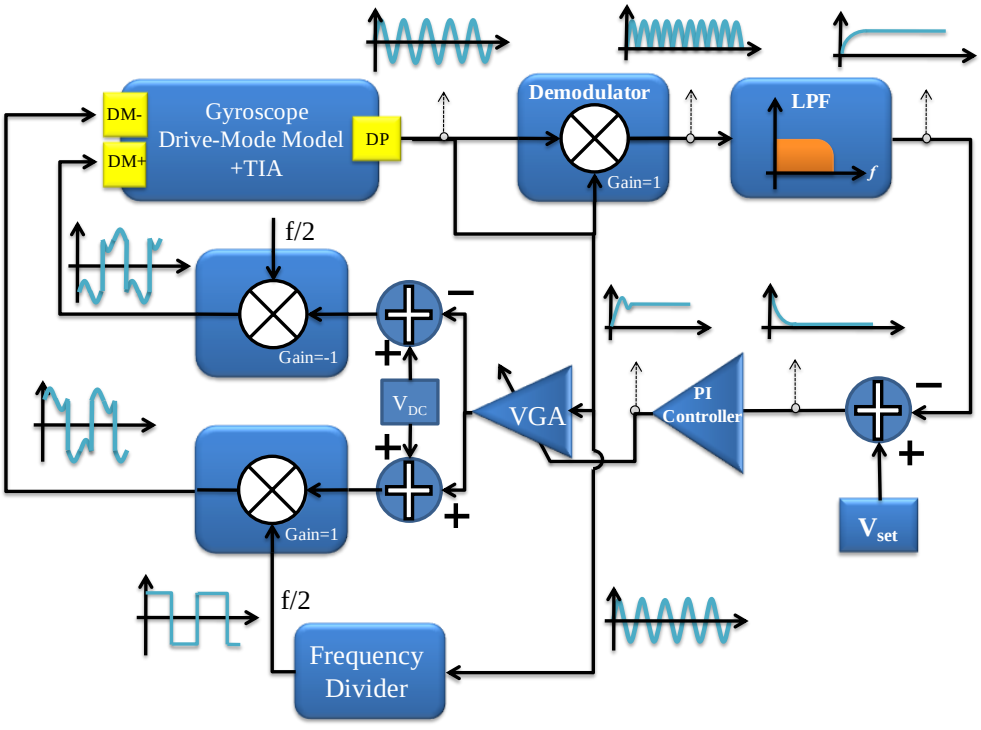

(b)

Figure 3.12: Typical structures of off-resonance frequency driving signal AGC with controlling a) DC offset and b) sinusoidal signal amplitude of the driving signal generating the input signal of the modulators

As expressed in Equation 2.35, the resultant electrostatic force is similar to the force generated by the sinusoidal wave driving signal, and the PI controller of the structure with VGA can be designed using the similar approach in the Section 3.2.1.2. Moreover, the maximum open-loop gain of the structure adjusting the DC offset is low in practice; hence, the system can be simplified to a second order expression in Equation 3.29, where α is 1 for this structure. Then, the PI controller parameters can be designed in order to provide the required system transient response performance.

Figure 3.13 gives the circuit implementation of the proposed solution in Figure 3.12 (a). The drive-pick output signal is processed to obtain the vibration amplitude in a similar fashion used in the previous circuit implementation of the proposed solutions. Then, the vibration amplitude is compared to a set value, and an error signal is created. To decrease the error, the PI controller adjusts the gain of the AD 602 (VGA), and the drive-pick output is amplified. Afterwards, the output sinusoidal signal is converted to differential signals by two instrumentation amplifiers, and a constant DC voltage is added to the differential sinusoidal signals in this step. Next, the differential sinusoidal signals with DC offset are modulated by a carrier signal whose fundamental frequency is half of the drive-pick output signal frequency. To generate electrostatic force at resonance frequency in the driving electrodes, the DC difference between driving signal and the proof mass should be zero; therefore, the modulated signals are coupled to the proof mass voltage before being applied to the drive-motor electrodes. The carrier signal used in modulator signal is generated by using digital frequency division approach. The sinusoidal signal is converted to a square wave signal and the square wave signal triggers a monostable multivibrator, whose response time is adjusted to be 2/3 of the mechanical resonance period, generating a square wave signal at mechanical resonance frequency with 66% duty cycle. The reason of using a monostable multivibrator is to eliminate the effect of the changes in the comparator circuit state due to the glitches in the drive-pick output signal during the transition of the driving signal. The monostable multivibrator output is used as a clock input of a 4-bit binary ripple counter IC. As a result, the every bit of the counter corresponds to division of the frequency to its 2^{-n} where n is the bit number of the counter, this way, the digital frequency division is achieved.

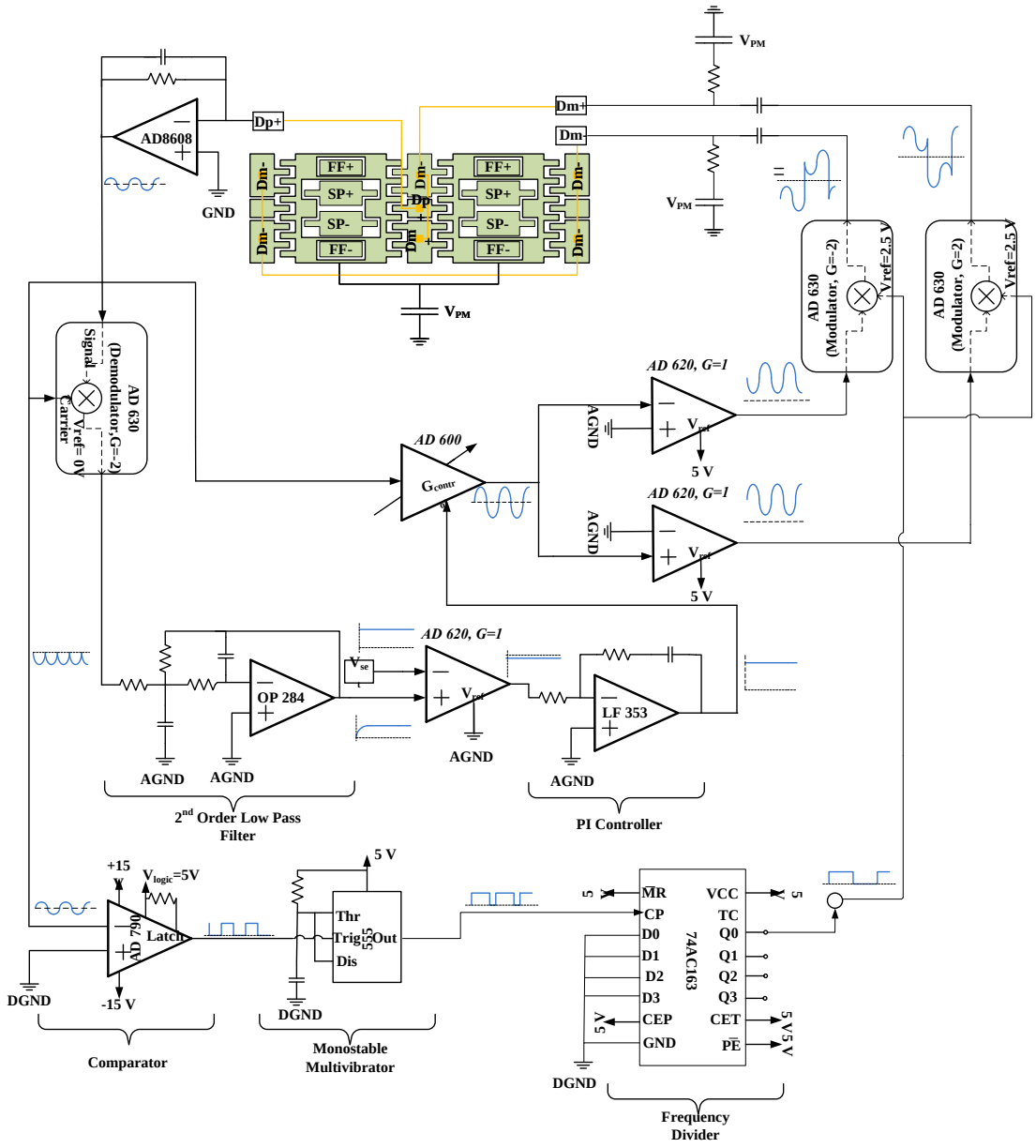

Figure 3.13: Circuit schematic of proposed off-resonance frequency driving signal AGC with VGA

As illustrated in Figure 3.12 (b), the loop can be constructed by controlling the DC offset, and the circuit implementation of this approach is shown in Figure 3.14. The proposed circuit is similar to the circuit described above except that the PI controller output is added to the drive-pick output as a DC offset. There is a constant AC gain in the loop to provide the PI controller to generate reasonable DC values in order to satisfy the Barkhausen criteria.

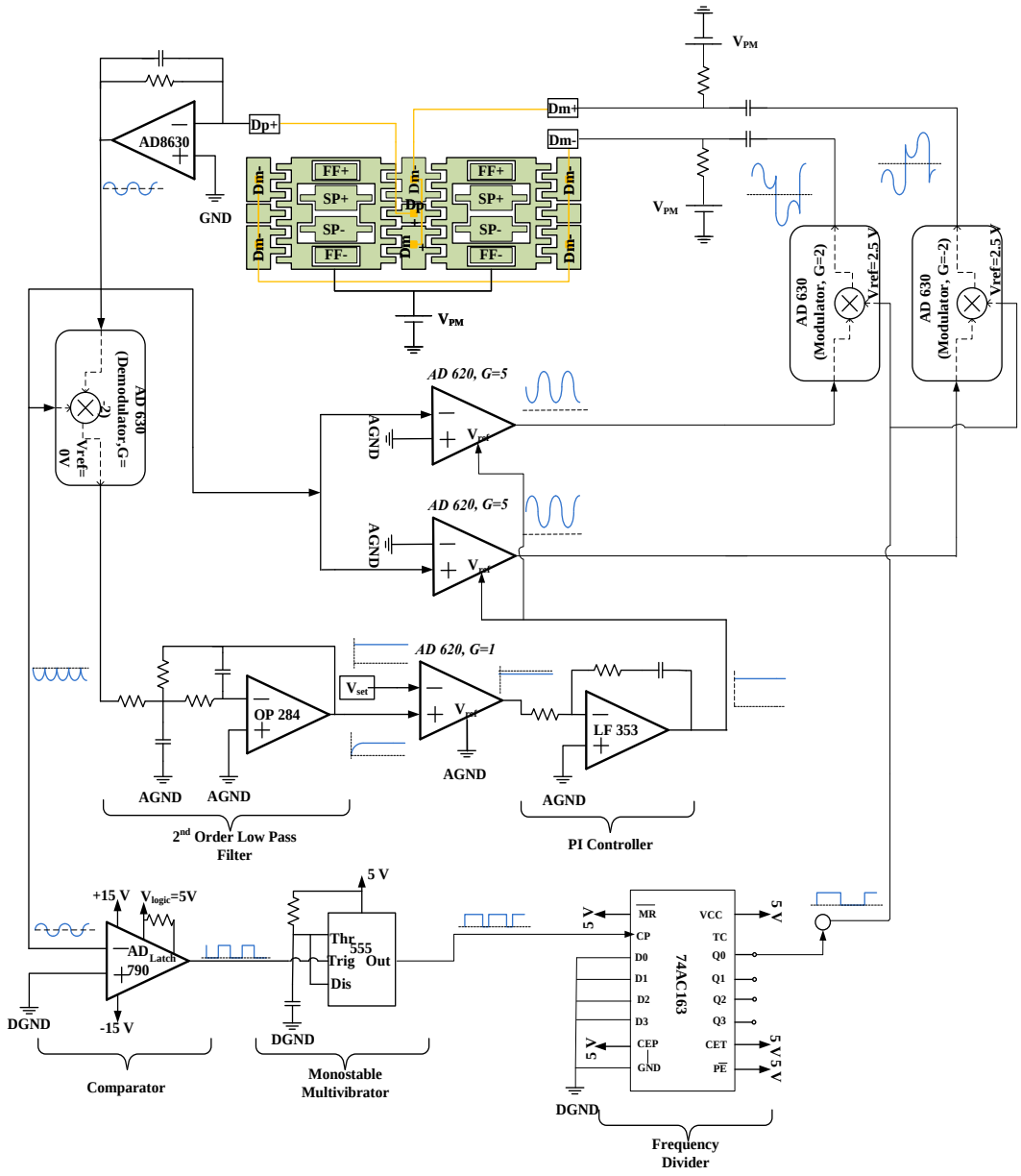

Figure 3.14 Circuit schematic of proposed half resonance frequency driving signal AGC with DC offset control

Figure 3.15 and Figure 3.16 give the simulation results of a) the drive-pick output, and the demodulator outputs of b) drive-motor+ and c) drive-motor- electrodes of the proposed circuit in Figure 3.13 and Figure 3.14 respectively when the set voltage is adjusted to 250 mV. The driving signals of the driving-motor electrodes are converted to force as described in the parallel-plate force generation expression in Equation 2.19, and then applied to the second-order model. Equation 2.35 indicates

that the generated force at the resonance frequency is equal to the multiplication of DC offset, $V_{DC,}$ and the magnitude of the modulated sinusoidal signal, V_{AC}, and $(\partial C/\partial x)$ of the drive-motor electrodes. Since the same gyroscope model is used in the simulations, the multiplication of the offset, $V_{DC,}$ and the magnitude of the modulated sinusoidal signal, V_{AC}, should be same to provide same drive-pick output, V_{DP}, which is provided in the simulations of the proposed circuits. Hereby, the simulation results verify that both circuitries are consistent with theoretical calculations and the proposed driving method can oscillate the drive-mode at its mechanical resonance frequency even though the driving signal doesn't have any component at mechanical resonance frequency. Besides, the above discussions are still valid when the drive-mode is driven by similarly generated driving signal whose fundamental frequency is at 2^{-n} of resonance frequency where n is a positive integer. Equation 2.35 states that the magnitude of the generated electrostatic force is independent of the fundamental frequency of the driving signal and is a function of DC offset, V_{DC}, and magnitude of the modulated sinusoidal signal, V_{AC}, and $(\partial C/\partial x)$ of the drive-motor electrodes. Therefore, since the DC offset of the modulated sinusoidal signal is same to the off-resonance frequency driving signal circuitry having a carrier frequency at the half of the resonance frequency, the amplitude of the modulated sinusoidal signal should be same. Figure 3.17 illustrates Simulink simulation results of the 1/4 resonance frequency driving signal AGC loop with VGA, verifying that the AC amplitude is same with the previous simulations, and the drive-mode oscillates at its resonance frequency. Without lost of generality, it can be concluded that using any output of 4-bit binary counter in the proposed circuitries as carrier signal, the proposed closed loops can oscillate the drive-mode at its resonance frequency.

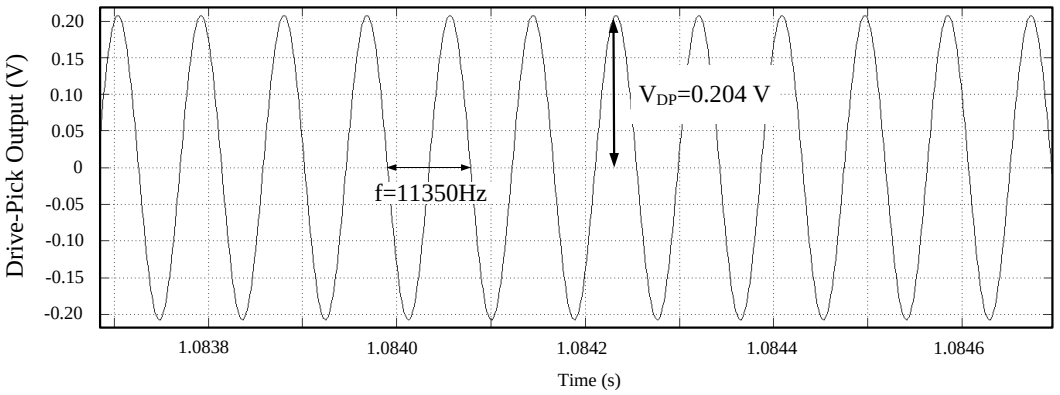

(a)

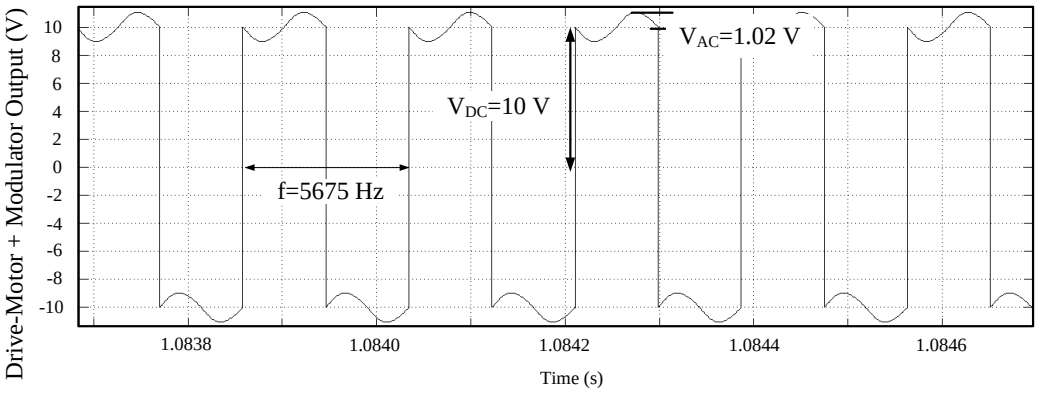

(b)

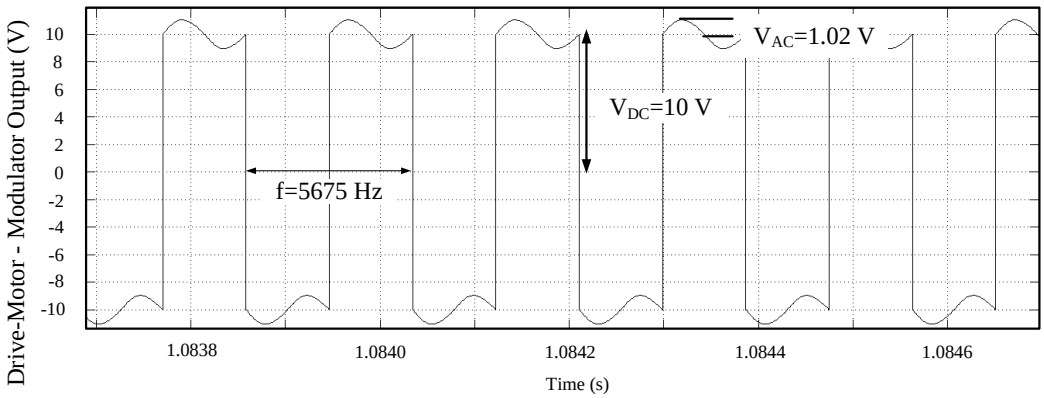

(c)

Figure 3.15: Simulation results of a) the drive-pick output, and the demodulator outputs of b) drive-motor+ and c) drive-motor- electrodes of the proposed circuit in Figure 3.13 when the set voltage is adjusted to 250 mV

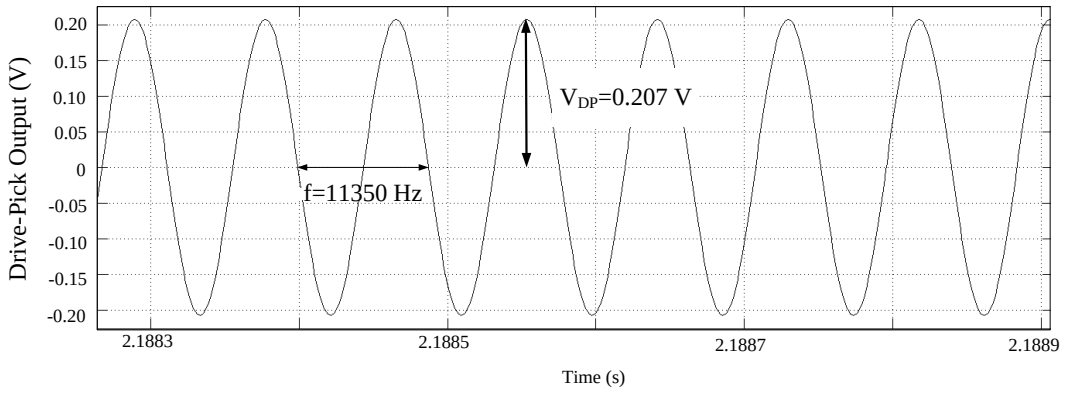

(a)

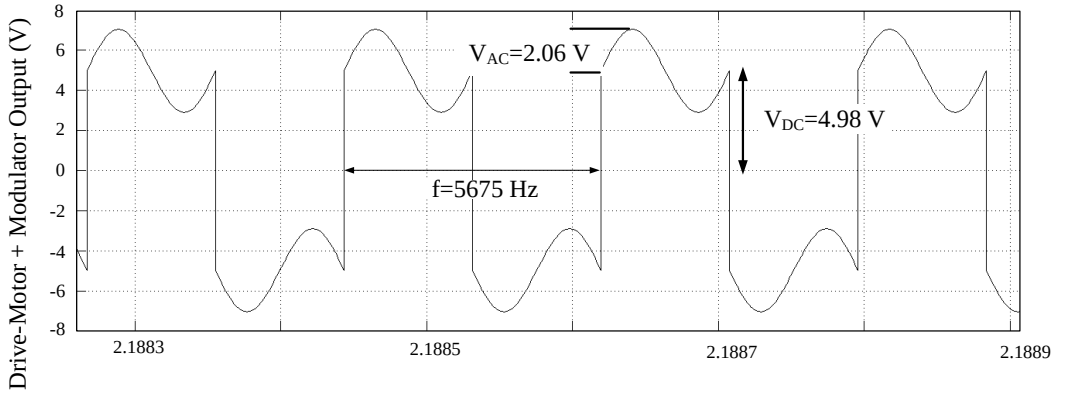

(b)

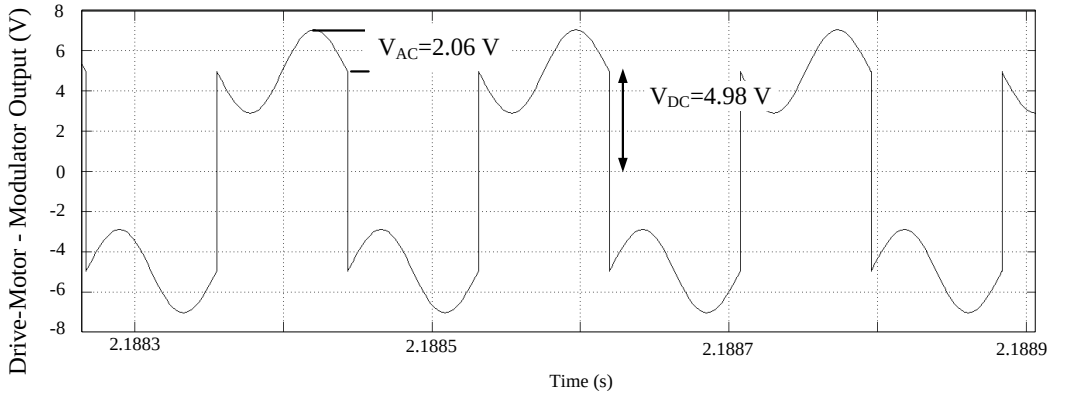

(c)

Figure 3.16: Simulation results of a) the drive-pick output, and the demodulator outputs of b) drive-motor+ and c) drive-motor- electrodes of the proposed circuit in Figure 3.14 when the set voltage is adjusted to 250 mV

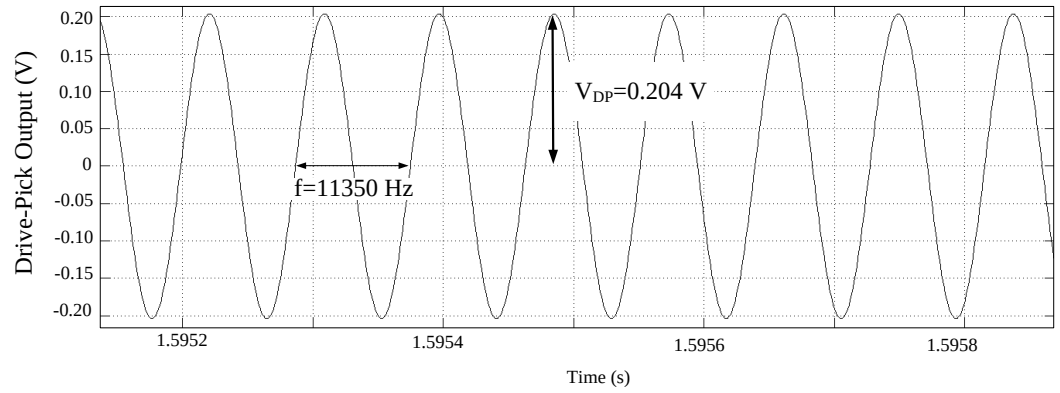

(a)

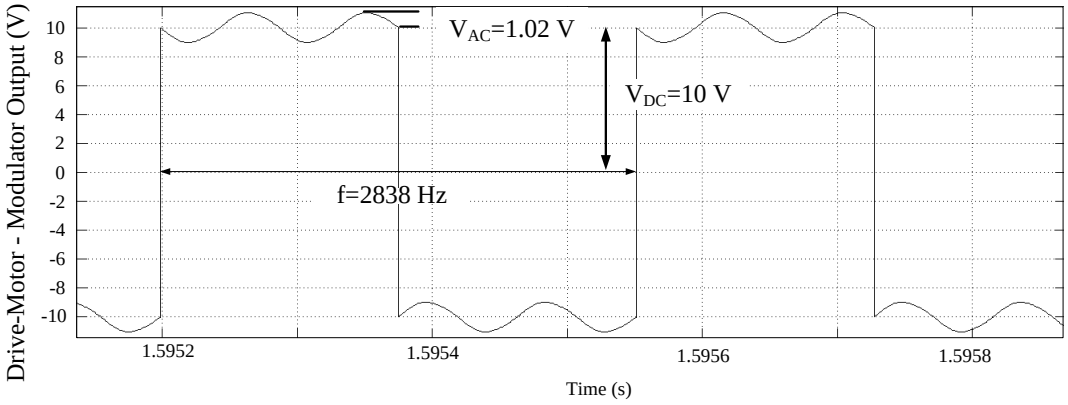

(b)

Figure 3.17: (a) Drive-mode output and the modulator output of the (b) drive-motor- of the 1/4 resonance frequency driving signal AGC loop proposed in Figure 3.13 the set voltage is adjusted to 250 mV

3.2.2 Sense-Mode Electronics

The output of the sense-mode in response to the rate input is an AM signal whose carrier frequency is the drive-mode oscillation frequency, and the amplitude is shaped by the angular rate input. As discussed in Section 2.4.2.2, two different approaches are used to obtain the rate input data from the sense-mode output: open-loop rate sensing and closed-loop rate sensing. Figure 3.18 gives the circuit schematic of the open-loop rate sensing. The output of the differential sense-pick electrodes are converted to a single-ended signal by using the Analog Devices AD620 instrumentation amplifier; then, the single-ended signal is transferred to baseband by a phase sensitive demodulator. Following the demodulation, the higher

frequency components are filtered by a second order filter, and the envelope, and hence the rate output, of the AM signal is obtained. The circuit in Figure 3.18 isconfigured for the mismatched operation, however for matched operation the drive-pick output should be 90° phase shifted for a proper operation.

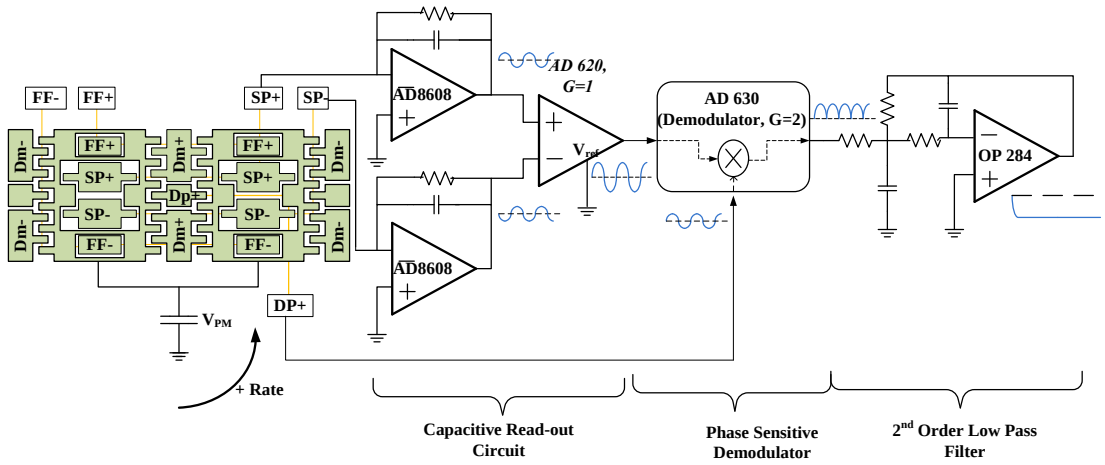

Figure 3.18: Circuit schematic of open loop rate sensing circuit to obtain the angular rate applied to system

As stated in Section 2.4.2.2.2, the closed-loop rate sensing is employed in order to improve the bandwidth of the sense-mode and make the gyroscope sense-mode output less susceptible to the ambient parameter changes as well as the process imperfections. The closed-loop rate sensing is obtained by introducing an electrical damping to the system. As illustrated in Figure 2.15, the electrical damping can be achieved by introducing a gain stage following the sense-mode output and applying the amplified signal to the force-feedback electrodes. Hence, similar AGC loop approaches used in the drive-mode can be employed in force feedback electrodes [9]; however, the closed-loop system has negative feedback and the oscillation amplitude is forced to be zero. In this research, a square-wave driving signal AGC is adjusted for closed-loop rate sensing. Figure 3.19 shows typical structure of the square-wave driving AGC loop for closed-loop rate sensing. In this structure, the vibration amplitude of the sense-mode is obtained, and PI controller adjusts the voltage amplitude applied to force-feedback electrodes to drive the vibration to become zero. As expressed in Table 2.2, the velocity of the drive-mode, and hence the Coriolis

force, is in-phase with the DP output signal in the mismatched operation. Therefore, the PI output signal is modulated by the DP output signal and the modulator outputs that are applied to force-feedback electrodes. Since the generated force in force-feedback electrodes is linearly dependent to applied voltage magnitude, the applied voltage magnitude, and hence the PI output corresponds to the rate output of the gyroscope.

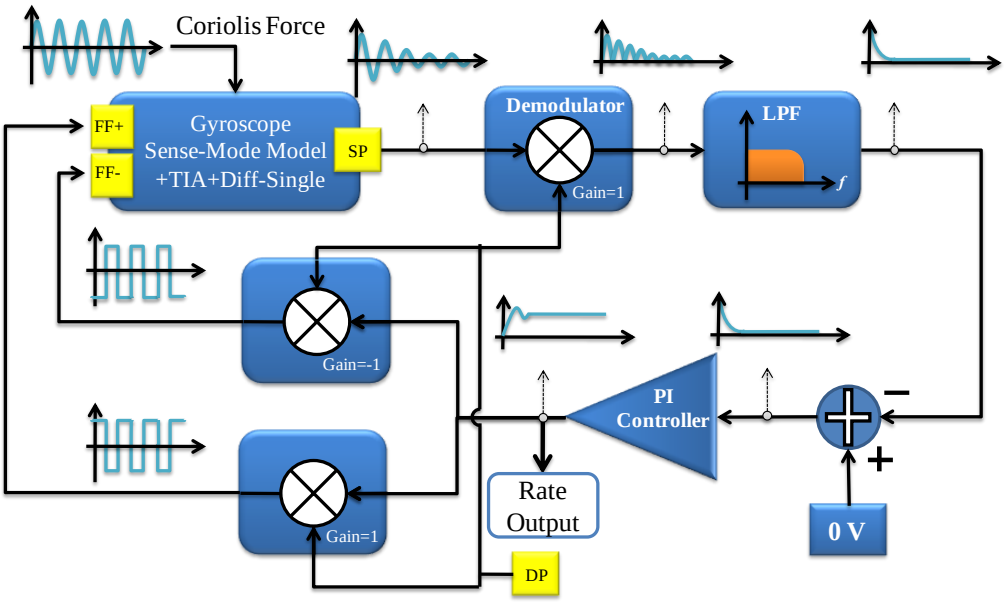

Figure 3.19: Typical structure of square-wave driving AGC loop for closed-loop rate sensing

Figure 3.20 illustrates circuit schematic of the proposed square-wave driving signal AGC loop for the closed-loop rate sensing. Since the sense-mode output of the gyroscope does not change instantaneously, the slowly varying envelope approximation given in Equation 3.11 can also be used for modeling the sense-mode [9]. It should be noted here that the PI controller parameters design approach discussed in Section 3.2.1.1 can be adapted for the square wave driving signal AGC loop for closed-loop rate sensing by substituting sense-mode parameters into Equations (3.11-3.18). By using these equations, the system response bandwidth can be set to the required value which is selected as 100 Hz in this research. Figure 3.21, Figure 3.22, Figure 3.23 and Figure 3.24 show SIMULINK simulation results of the proposed force feedback circuitry to time-invariant and time-varying rate inputs for

different sense-mode quality factors. The proportional and the integral parameters of the PI controller are designed as 0.25 and 3500, respectively, assuming that the sense-mode resonance frequency is 13 kHz with 13 dB gain at resonance for Q_s=500 while the drive-mode oscillates at its resonance frequency, 11350 Hz, with 8 µm maximum displacement. Figure 3.21 and Figure 3.22 indicate that the system has a 6.25 mV/° scale factor for two different quality factors, which verify that the proposed circuitry decreases the dependency of the sensor output to ambient pressure variations. Moreover, Figure 3.23 and Figure 3.24 shows that the scale factor of the system is simulated to change between 6.25 mV/° and 5.8 mV/° in a response to 0 to 100 Hz time-varying rate inputs for two different sense-mode quality factors, showing that the proposed system has a bandwidth larger than 100 Hz, as expected.

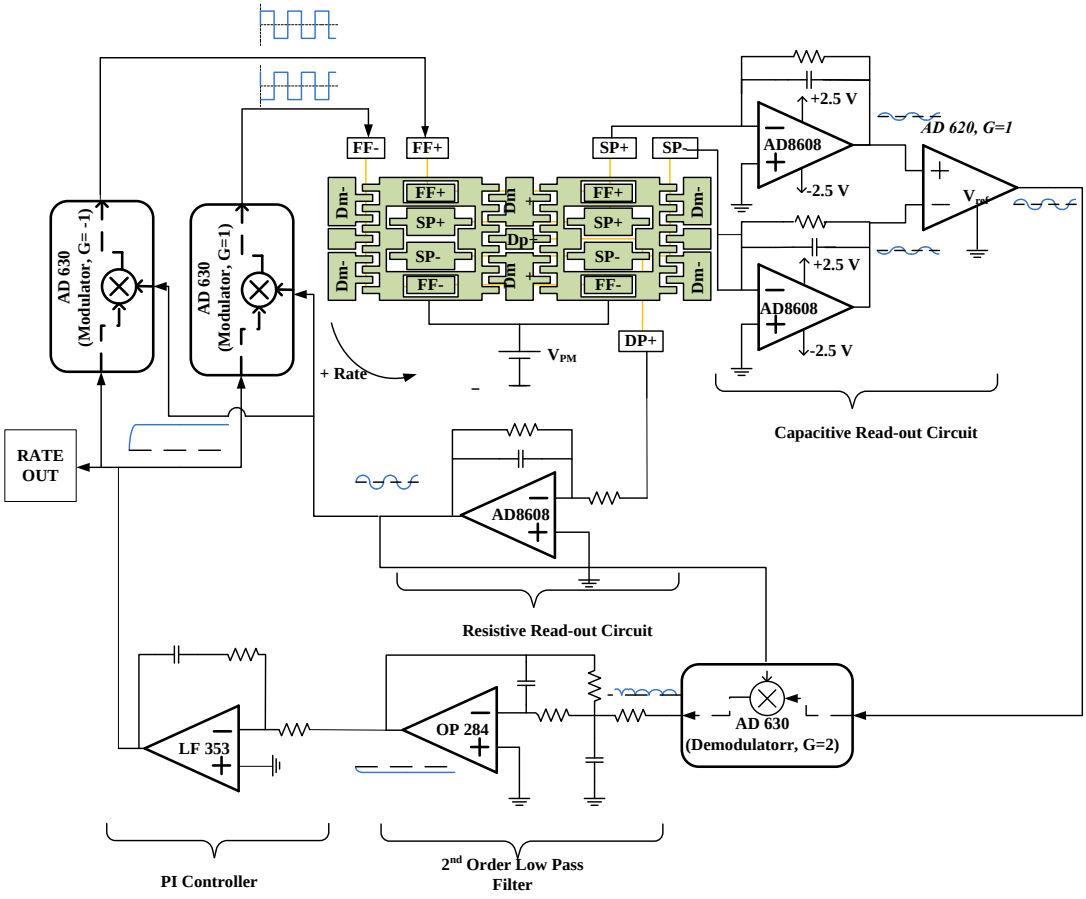

Figure 3.20: Circuit schematic of proposed square-wave driving signal AGC loop for closed-loop rate sensing

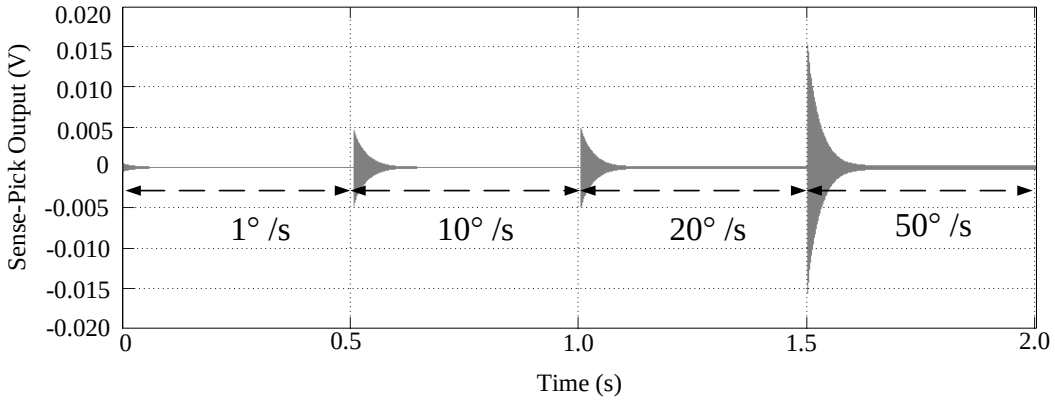

(a)

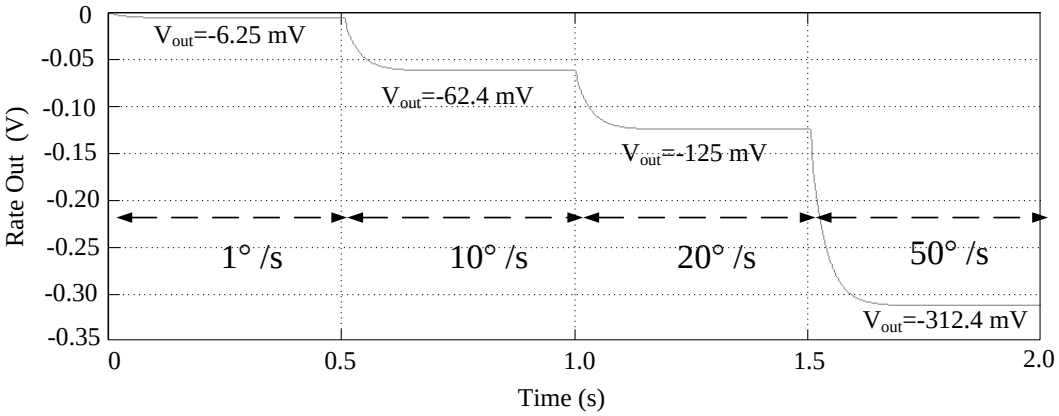

(b)

Figure 3.21: SIMULINK simulation results that shows the signals of (a) single ended- sense-pick output and (b) Rate output signals of the proposed force feedback circuitry for Q_s=1000 to different time invariant rate inputs

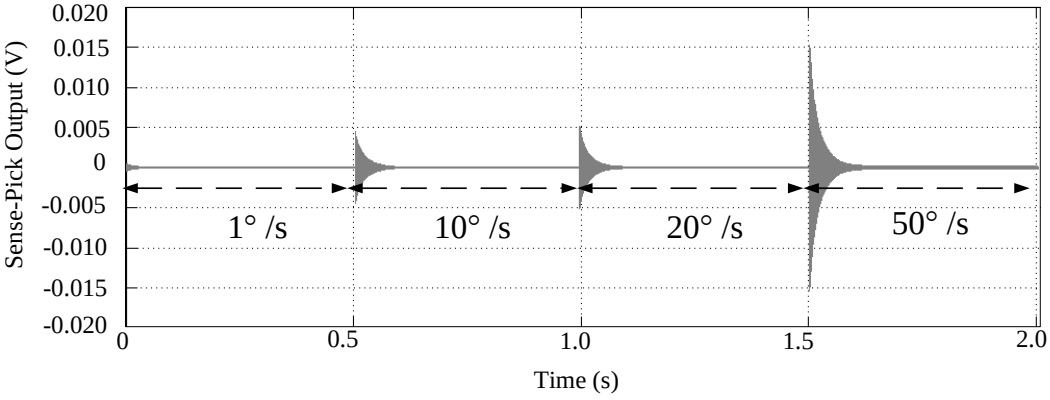

(a)

Figure 3.22: SIMULINK simulation results that shows the signals of (a) single ended-sense-pick output and (b) Rate output signals of the proposed force feedback circuitry for Q_s=500 to different time invariant rate inputs

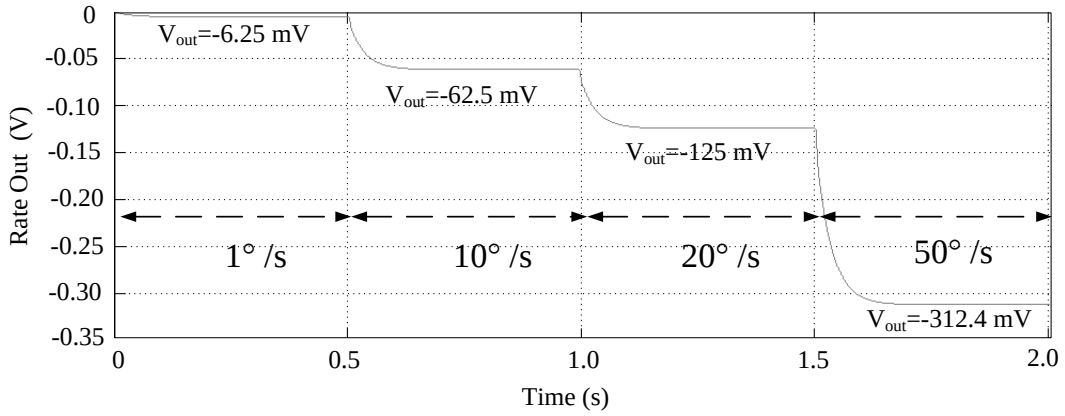

(b)

Figure 3.22 cont'd: SIMULINK simulation results that shows the signals of (a) single ended- sense-pick output and (b) Rate output signals of the proposed force feedback circuitry for Q_s=500 to different time invariant rate inputs

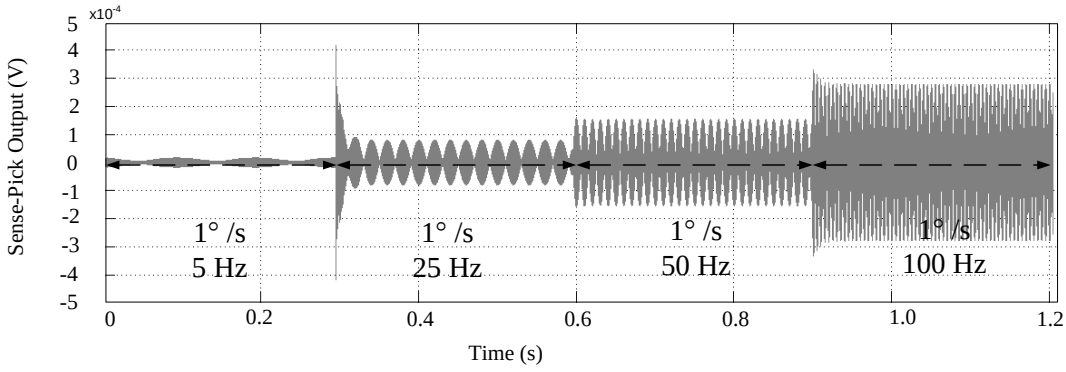

(a)

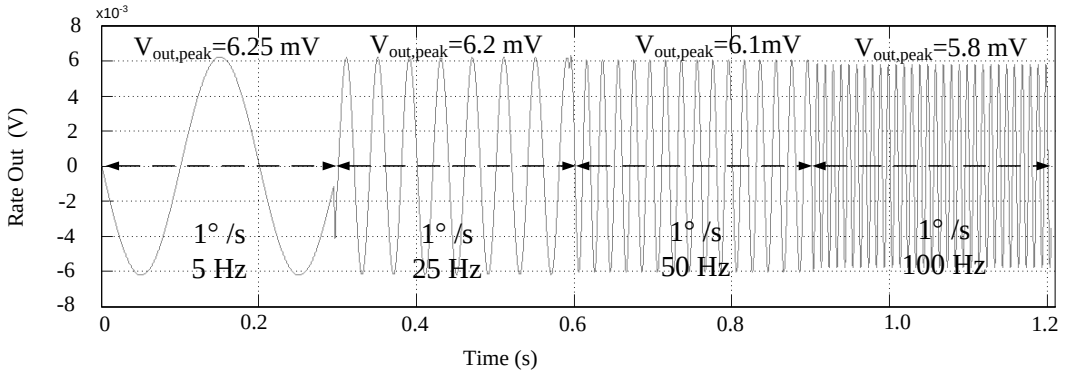

(b)

Figure 3.23: SIMULINK simulation results that shows the signals of (a) single ended-sense-pick output and (b) Rate output signals of the proposed force feedback circuitry for Q_s=1000 to different time-varying rate inputs

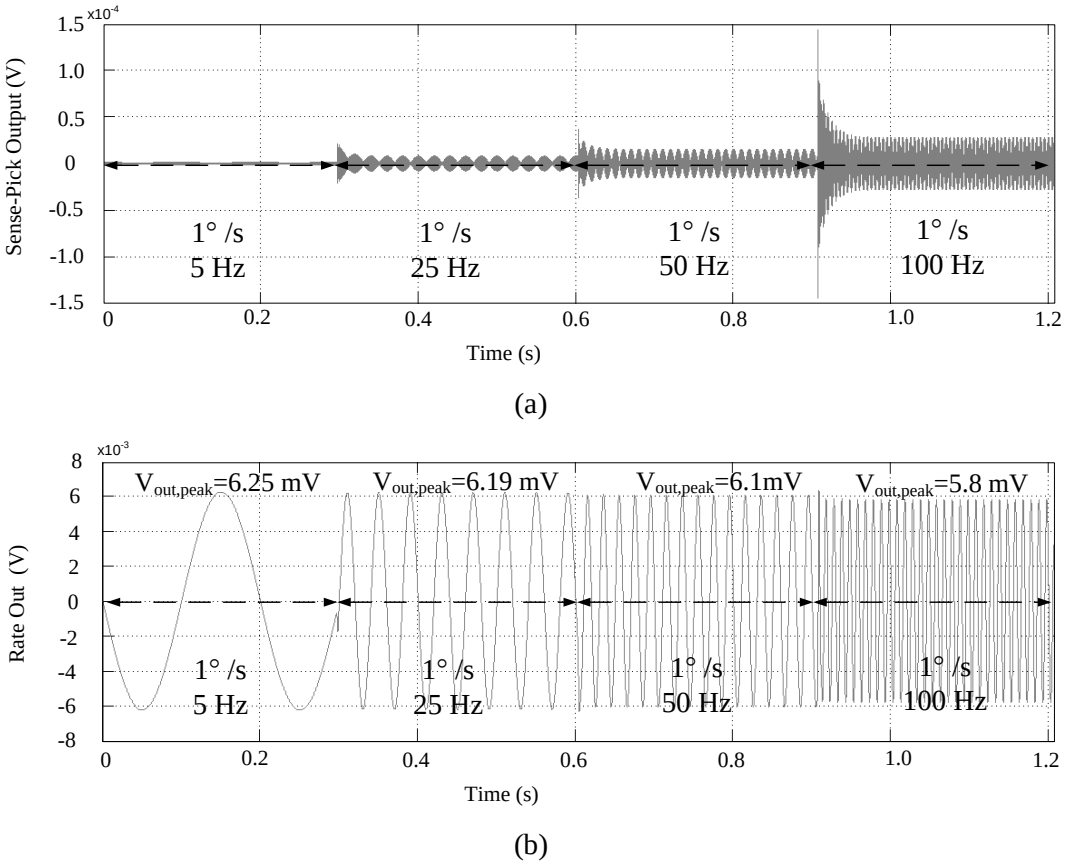

Figure 3.24: SIMULINK simulation results that shows the signals of (a) single ended-sense-pick output and (b) Rate output signals of the proposed force feedback circuitry for Q_s=500 to different time- varying rate inputs

As discussed above, the aim of the force feedback in sense-mode is to introduce an electrical damping to system and to decrease the sense-mode displacement due to the rate input. Although the decoupled design of drive and sense-modes, the drive-mode may still couple mechanically to sense-mode due to the process imperfection, resulting in a quadrautre error. In addition, a phase error in demodulation of the sense-mode output leads the loop to sense some of the quadrature error as a rate input. In such a case, the proposed force feedback generates force to stop the sensed quadrature error. Nevertheless, since there is 90° phase shift between the generated force and the quadrature error, the loop can't stop the quadrature error; on the contrary, it vibrates the sense-mode to null the electrical error signal, which leads to a DC offset at the rate output. As a result, the sense-mode has a residual vibration that causes nonlinearity in sense finger electrodes; the proposed closed-loop rate

sensing may not improve linearity of the sense-mode response for large quadrature errors.

In summary, the angular rate input can be sensed by employing open-loop and closed-loop angular rate sensing. Open angular rate sensing converts the AM signal at sense-mode output to the baseband signal and extract the angular rate input. The proposed closed-loop angular rate sensing mechanism generates square wave signals, and hence force, to null the Coriolis force acting on the sense-mode, and the amplitude of the generated signals is linearly dependent to the angular input rate. As a result, the angular rate input is sensed. The closed-loop angular rate sensing increases the bandwidth and improves the robustness of the system against the sense-mode frequency response variation.

3.3 Summary

This chapter provides detailed theoretical analysis of readout and complementary electronics of SOG (silicon-on-glass) vibratory gyroscopes developed at METU and gives simulation results of the control electronic circuitry. First transresistance and transimpedance interface types are discussed and performance criteria are introduced. Then, the drive-mode and sense-mode electronics are investigated. In the drive-mode electronics, three different solutions for automatic gain control (AGC) loop are proposed and their modeling and controller design are given. Moreover, the loops are simulated and the circuit operation is confirmed. Finally, as the sense-mode electronics for vibratory gyroscope, the open-loop and closed-loop rate sensing mechanisms are analyzed, and the closed-loop rate sensing is verified by the simulations performed in SIMULINK.

CHAPTER 4

TEST RESULTS

This chapter represents the tests results of readout and external electronics designed for the SOG gyroscopes developed at METU. Section 4.1 gives the results of the tests performed for characterizing and modeling the micromachined vibratory gyroscope. Then, Section 4.2 presents the performance test results of complete angular rate sensing systems proposed in Chapter 3. Finally, Section 4.3 summarizes and discusses the test results.

4.1 Characterization of Micromachined Gyroscope

The frequency responses of both the drive-mode and the sense-mode of the vibratory gyroscope should be characterized in order to design the external electronics for a proper and high performance operation. Firstly, gyroscopes are tested at atmosphere pressure ambient to determine whether they operate properly. Figure 4.1 shows the setup for the probe test. In this setup, the gyroscope to be tested is placed on to the Karl Suss micromanipulator probe station. The micromanipulator probes provide electrical connections to the mechanical structure's input and output pads. Then, the Agilent 4395A Network Analyzer is used to extract the frequency response of the gyroscope's drive-mode and sense-mode. The properly operating prototypes are hybrid connected to the preamplifiers mounted on a glass substrate which has thin gold paths and functions as a one-sided PCB (printed circuit board). Next, the glass substrate is fixed into a 16-pin hybrid package. Figure 4.2 shows the hybrid packaged gyroscope prototype.

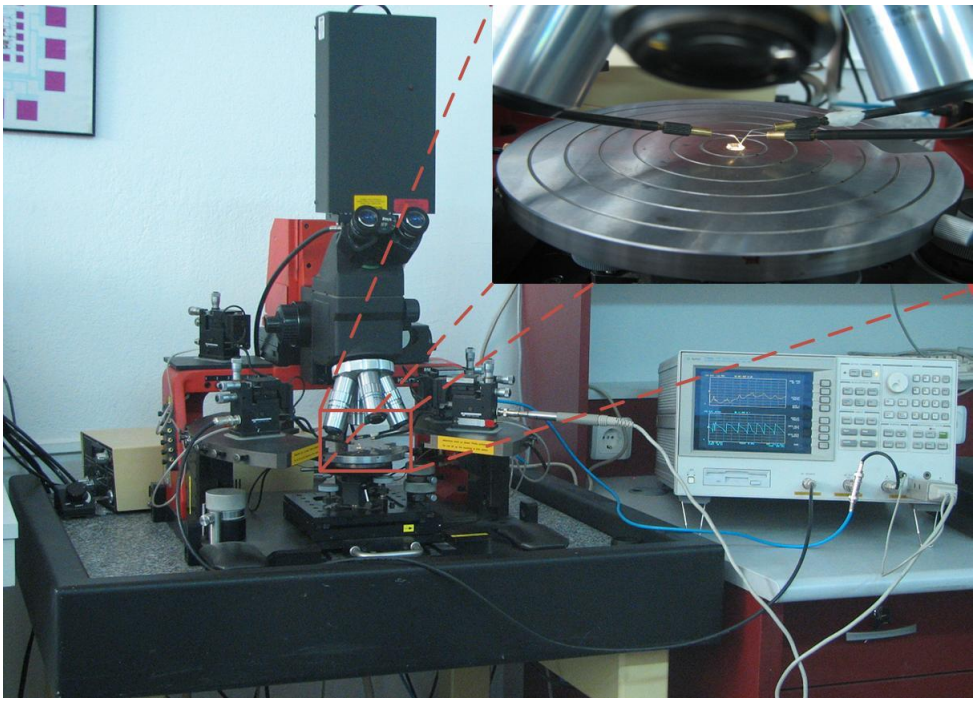

Figure 4.1: Setup for probe test of the gyroscope

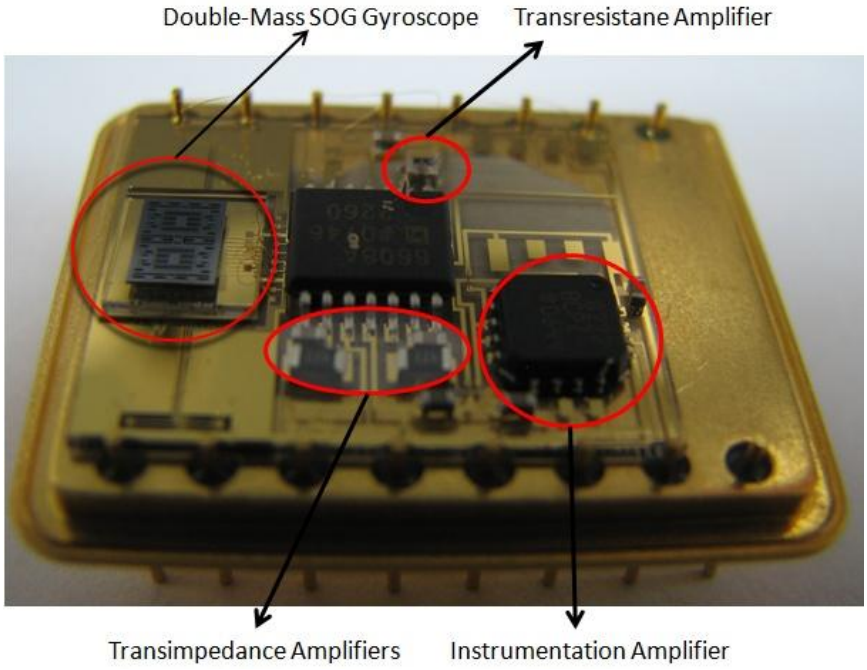

Figure 4.2: Hybrid packaged SOG gyroscope

The next step in characterization is to determine the resonance characteristics of the hybrid packaged SOG gyroscope's sense and drive modes at the atmospheric pressure and vacuum ambient. Firstly, the source output of Agilent DSA (Dynamic

Signal Analyzer) is converted to differential signal and applied to corresponding drive-motor pins (DM+ is in-phase and DM- is out of phase with DSA source signal) of the package, and the output of the transresistance amplifier (DP pin) is measured by the dynamic signal analyzer in order to determine the drive-mode resonance characteristics. Figure 4.3 gives the magnitude and phase frequency response of the hybrid packaged HSOGSNW#9-L10 gyroscope's drive-mode at atmosphere pressure as an example. As expected, the resonance frequency and quality factor of the drive-mode are measured to be independent of the applied proof-mass voltage, and they are equal to 10200Hz and 73, respectively. However, in a pure second order system with a transresistance amplifier, the phase response changes 90° to -90° at vicinity of the resonance frequency, and magnitude gain characteristics don't have zeros, which are not consistent with HSOGSNW#9-L10 frequency response. The inconsistency is occurred due to the stray capacitances between drive-motor electrodes and drive-pick electrode, in other words, the frequency characteristics monitored is the sum of the electrical coupling and drive-mode mechanical response of the gyroscope. Fortunately, at nearby of the resonance frequency, the mechanical response becomes dominant and the system can be modeled as a second order system.

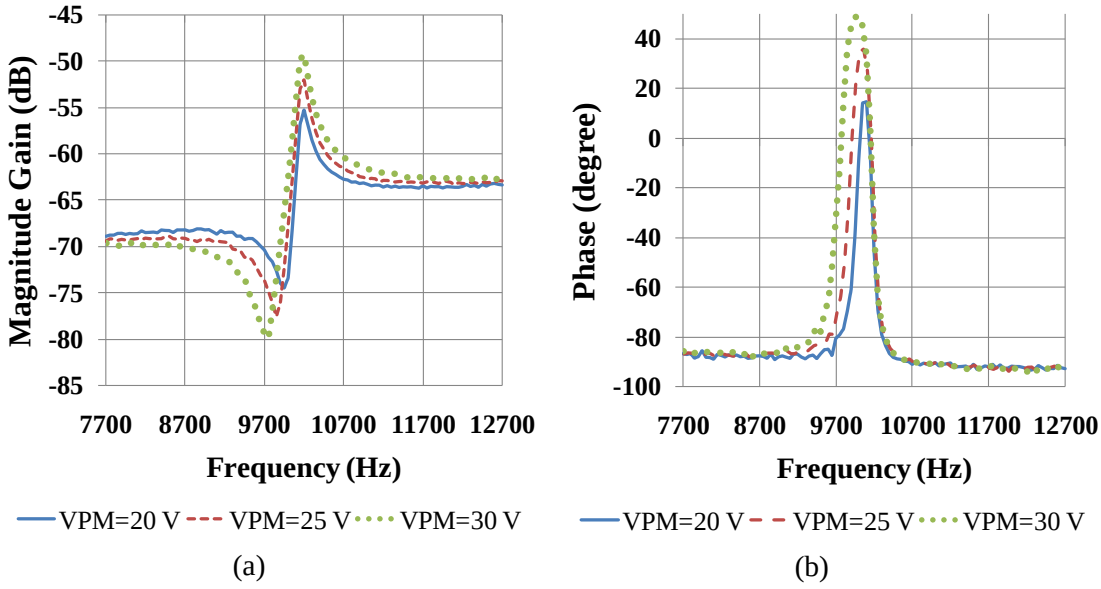

Figure 4.3: Drive-mode (a) magnitude and (b) phase frequency response of HSOGSNW#9-L10 gyroscope for different proof-mass voltages at atmosphere pressure

Similarly, sense-mode characteristics at atmospheric pressure ambient can be obtained by applying differential signal to force feedback electrodes and monitoring the difference of the sense-mode transimpedance amplifiers by the dynamic signal analyzer. Figure 4.4 illustrates the frequency response of HSOGSNW#9-L10 gyroscope's sense-mode. As the applied proof-mass voltage is increased 20V to 30V, the resonance frequency of the sense-mode decreases from 10300 Hz to 9100 Hz due to electrostatic spring effect of the varying-gap type fingers associated with the sense-mode. The resonance characteristics of the sense-mode is similar to a pure second order system since the mechanical gain of the sense-mode is larger compared to the drive-mode and complex zeros of the overall system is far away from the complex pole of the system.

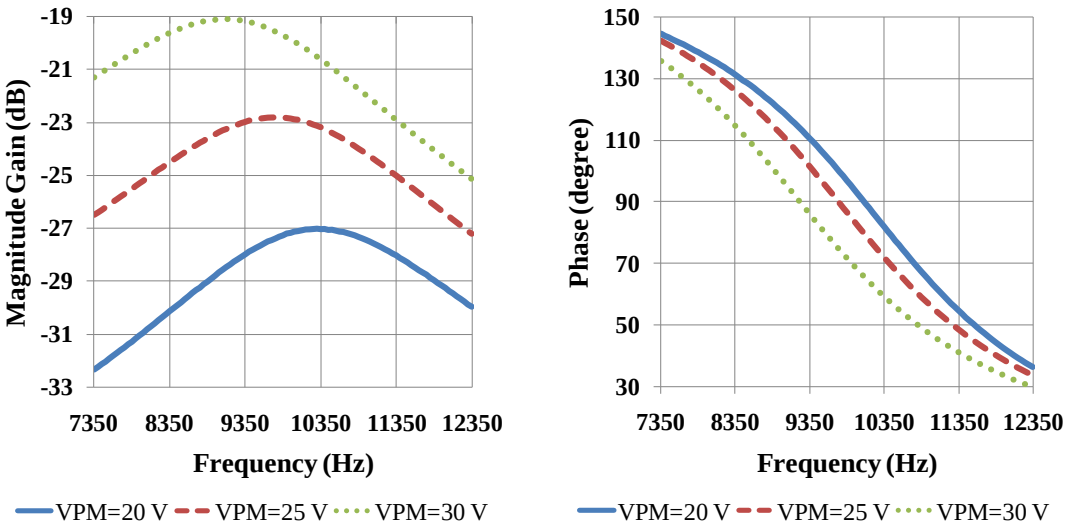

Figure 4.4: Sense-mode (a) magnitude and (b) phase frequency response of HSOGSNW#9-L10 gyroscope for different proof-mass voltages at atmosphere pressure

The tested hybrid packaged SOG gyroscopes prototypes are hermetically sealed at vacuum ambient at METU-MEMS Facility. Then, the sealed gyroscope prototypes are performed resonance tests, and the final mechanical model and operation modes of the gyroscope are obtained. Figure 4.5 shows the magnitude and phase frequency

response of HSOGSNW#9-L10 gyroscope's drive-mode at vacuum ambient tested for 10 mV sinusoidal input signal when 25 V is applied to the proof mass, as an example. The resonance frequency is measured to be 10163.83 Hz, and the phase error of the system at resonance is -7°. By the way, the gain of the mechanical structure at resonance is boosted to -4.64dB (-52 dB at atmosphere), and quality factor increases to 20327 (73 at atmosphere) at vacuum ambient. Moreover, the drive-mode behaves as a pure second order system around the resonance frequency, and it can be mathematically modeled as a second order system by obtained test results.

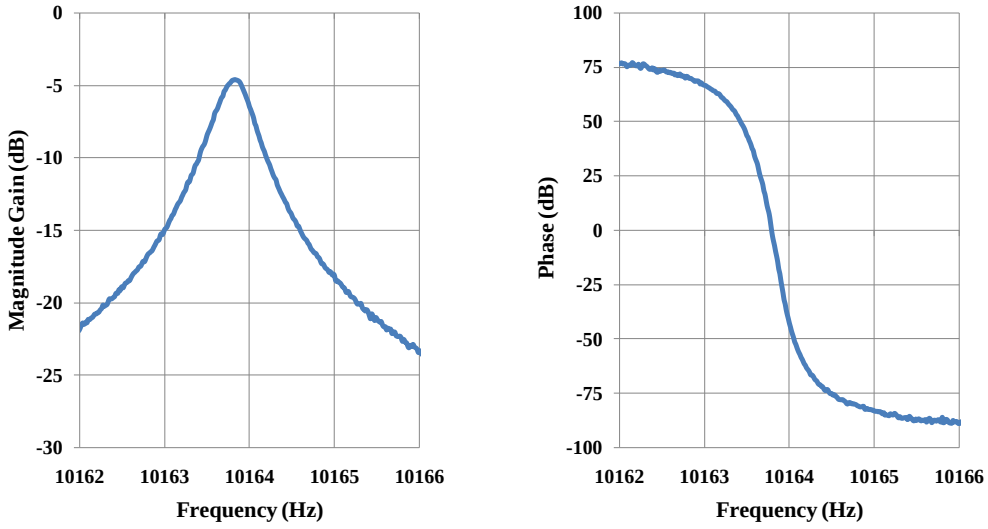

Figure 4.5: Drive-mode (a) magnitude and (b) phase frequency response of HSOGSNW#9-L10 gyroscope tested for 10 mV sinusoidal input signal when 25 V is applied proof-mass at vacuum ambient

As the input signal, and hence the driving force of the drive-mode, is increased, the mechanical structure response becomes nonlinear, and the magnitude gain of the system cannot be modeled as a second order system anymore. Figure 4.6 gives the magnitude gain and the phase response of the same SOG gyroscope package when 100 mV sinusoidal signal is applied as the test signal. The frequency response of the drive-mode deflects the ideal characteristics as the gain of the system increases and the maximum gain of the system is obtained at 10168 Hz, which is larger the resonance frequency given in the previous test result. Nevertheless, due to the

nonlinear characteristics of the drive-mode response the maximum gain frequency varies as the driving signal is changed. Fortunately, since the designed AGC (automatic gain control) loops lock the drive-mode oscillation frequency at which the phase shift of the SOG gyroscope package is zero degree, the closed loop system oscillates at the vicinity of the frequency where the maximum magnitude gain is obtained. It should be noted that if the phase error introduced by the external electronics of the drive-mode is larger than zero, the AGC loop tries to lock the system oscillation frequency to the frequency at which the phase shift of the gyroscope is negative. In this case, the mechanical gain of the gyroscope dramatically drops for large phase errors. Thus, if the open-loop gain is not large enough, the proposed closed-loop system may not start to oscillate due to the nonlinear behavior of the drive-mode. Therefore, the loop should be designed such that it should introduce a low phase error, and the AGC loop should provide large open loop gain, sufficient enough to satisfy the self oscillation criteria.

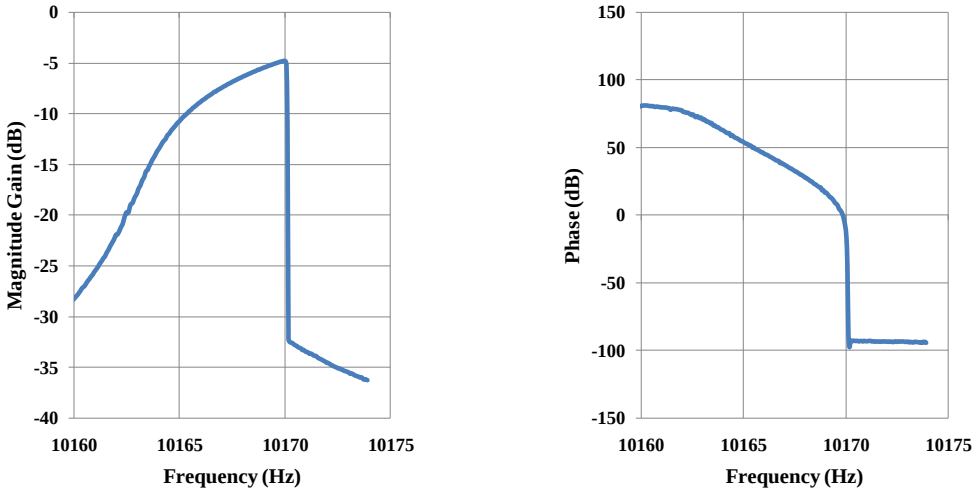

(a) (b)

Figure 4.6: Drive-mode (a) magnitude and (b) phase frequency response of HSOGSNW#9-L10 gyroscope tested for 100 mV sinusoidal input signal when 25 V is applied proof-mass at vacuum ambient

Figure 4.7 and Figure 4.8 give the sense-mode characteristics of two different gyroscopes, coded as HSOGSNW#9-L10 and HSOGSNW#13-I06. Since the sense-

modes of the double-mass gyroscopes are mechanically decoupled, the process imperfections may lead mismatches in the sense-modes' resonance frequencies. As a result, both of the gyroscopes have two different magnitude peaks in the sense-modes that is not observable in atmosphere pressure ambient. The difference of the peaks is not constant and depends on the process. Besides, similar to the drive-mode the quality factor and resonance gain of the sense-mode increases considerably at vacuum ambient and the phase difference is around 90˚ at resonance frequency as expected.

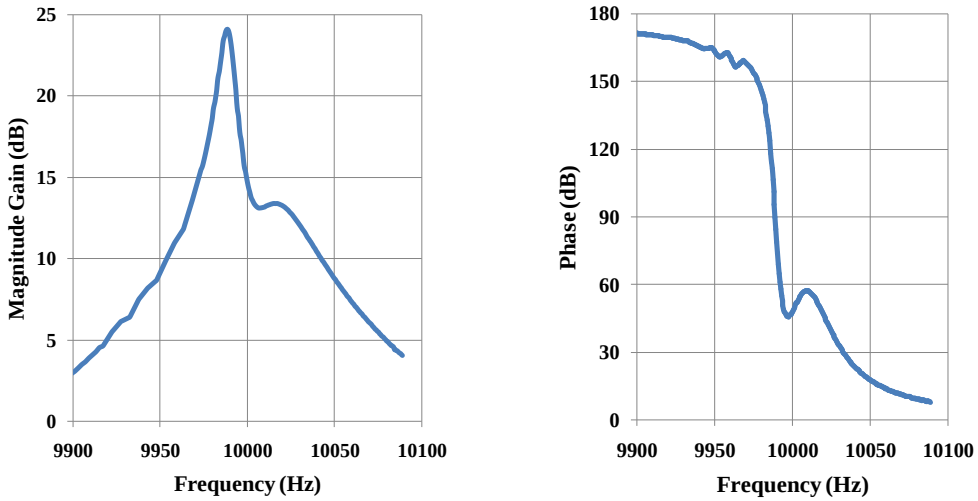

(a) (b)

Figure 4.7: Sense-mode a) magnitude and b) phase frequency response of HSOGSNW#9-L10 gyroscope when 25 V is applied proof-mass at vacuum ambient

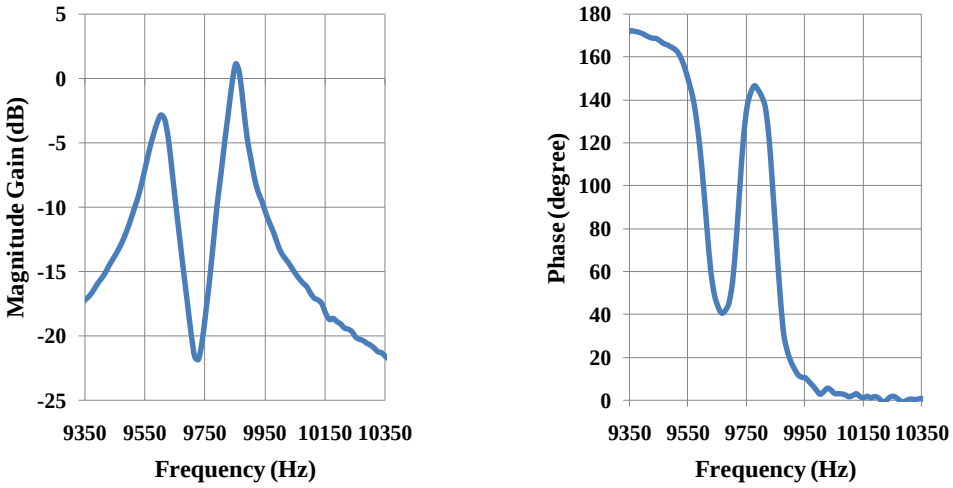

(a) (b)

Figure 4.8: Sense-mode (a) magnitude and (b) phase frequency response of HSOGSNW#13-I06 gyroscope when 25 V is applied proof-mass at vacuum ambient

As the Coriolis induced force acting on the proof-mass is the amplitude modulation of the angular rate input at the drive-mode frequency, the response of the sense-mode around the drive-mode frequency can be used to estimate the scale factor and mechanical bandwidth of the overall angular rate sensing system. Figure 4.9 illustrates the sense-mode frequency responses of the gyroscope coded as HSOGSNW#9-L10 at the vicinity of the drive-mode resonance frequency (10170 Hz) when different voltages are applied to the proof mass. The gyroscope has a 100 Hz mechanical bandwidth for the proof mass voltages 15 V and 28 V, while the bandwidth decreases to 30 Hz for 25 V. In all cases, the phase error is less than 4° in the operation bandwidth, allowing a phase sensitive AM demodulation with a little offset error. It should be noted that the magnitude gain obtained by resonance tests includes the electromechanical coupling gain of the force feedback electrodes expressed in Equation 2.57; hence, to compare of the scale factors of the gyroscope for different cases, the test results should be normalized by dividing the results with the applied proof mass voltages. Assuming that there is no phase error in the AM demodulation and same drive-mode displacement; and considering that the gains of the sense-mode obtained in the tests are normalized, the scale factor of the angular rate sensing system for 25 V and 28 V proof mass voltages are found to be 6.9 and 2.33 times of the scale factor for the 15 V proof mass voltage, respectively. The maximum scale factor is achieved when 25 V is applied to the proof mass since the system is closer to the matched-mode, and the gain is boosted, as expected. As mentioned before, the induced current, and hence scale factor, is a linear function of the voltage applied to the proof mass. Therefore, when scale factors for 15 V and 28 V are compared, the ratio of the scale factor is close to that of the proof mass voltage, and it can be concluded that the gain of the mechanical structure excluding the sensing mechanism is same for both cases. As a result, the comparison of the performance test obtained for 15 V and 28 V proof mass voltages provides important results about the effects of the gyroscope electronics on angular rate sensing system performance, as the mechanical characteristics are similar for these cases.

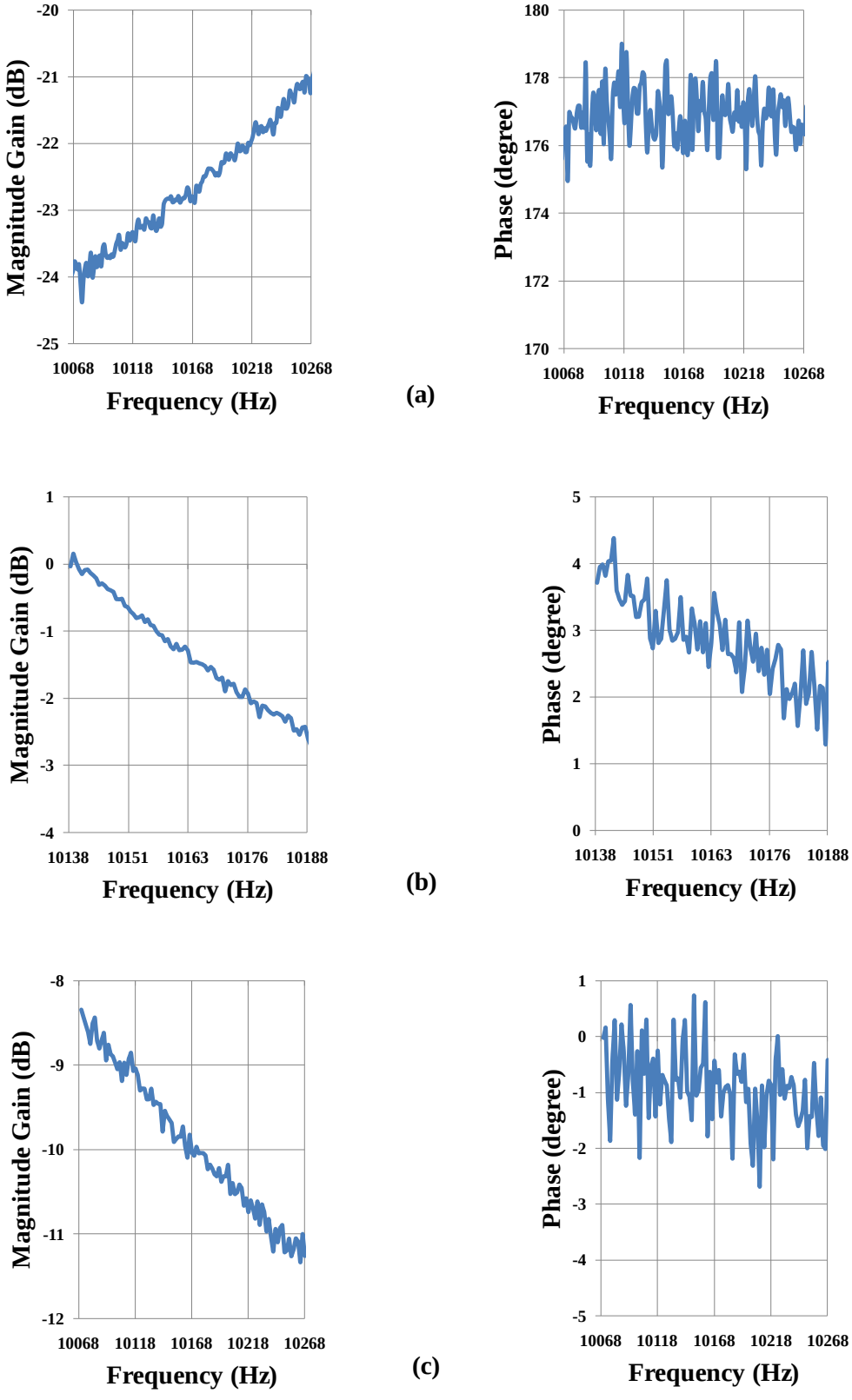

Figure 4.9: Measured sense-mode frequency response of HSOGSNW#9-L10 at the vicinity of the drive-mode resonance frequency (10168 Hz) when (a) 15 V (b) 25 V and (c) 28 V applied to the proof mass

After characterizing the gyroscope frequency response, the measured data is used to model the gyroscope mathematically. Although, the drive-mode frequency response characteristic diverges from the second-order system assumption for large driving signals, i.e., about 25 mV for HSOGSNW#9-L10, the drive-mode can still be modeled as a second-order system, since at the start-up the driving signal is small, and the critical point in the self-oscillation loop design is whether the drive-mode loop satisfies the criteria to start the oscillation. The mathematical model of the drive-mode is used to update the control parameters of the proposed AGC loops following the design procedure given in Section 3.2.1. In the tests performed with HSOGSNW#9-L10, the control parameters are designed according to the maximum overshoot and settling times used in the design and simulations of the AGC loops in Section 3.2.1.

4.2 Test Results of External Electronics

This section presents the test results of external electronics for open-loop and closed-loop rating systems. Section 4.2.1 explains the tests performed to assess the performance of the designed circuits. Then, Section 4.2.2 gives the test results of four open-loop angular rate sensing systems which have different drive-mode self-oscillation approaches. Finally, Section 4.2.3 presents the test result of the closed loop angular rate sensing system.

4.2.1 Performance Tests for Micromachined Vibratory Gyroscope

The performance tests for micromachined vibratory gyroscopes are performed to determine of the scale factor, scale factor nonlinearity, zero rate offset, angle random walk and bias instability. Figure 4.10 shows the test setup used for performance tests.

For scale factor tests, the angular rate sensing system is placed in the servo controlled Ideal Aerosmith 1280 single-axis rate table. Then angular rate applied to angular rate sensing system is swept from zero rate input to ±100 °/sec with 10 °/sec steps, and the output of the system is measured by the Agilent 34401 multimeter. The measured data is stored in a data acquisition PC by using HPVEE program and the stored data is used to construct the output voltage versus applied rate characteristics of the system. Finally, the constructed response curve is fitted to a straight line to obtain the scale factor, the R^2 nonlinearity of the scale factor, and the zero rate output of the system.

The bias instability and angle random walk values of an angular rate sensing system are determined by the Allan Variance analysis. The Allan Variance analysis requires acquiring drift data of rate sensing system for a time period when a zero rate input applied. The time period is determined according to required accuracy of the test results, typically a 2.5 hour-length test with 16 Hz sampling rate is estimated to provide determination of the performance of the system with an error less than 0.1 percent [66]. Figure 4.11 illustrates a sample Allan variance plot, $\sigma(\tau)$ (°/hr), versus sample time, τ (sec), where the plot is generated by the Allan Variance analysis [66]. To determine the Angle random walk value, a line having -1/2 slop is fitted to Allan Variance plot and the Allan variance value at τ=1 second on the fitted line gives the resolution of angular rate sensing system at 1 Hz [66]. Furthermore, the Angle random walk value of the sensor system is obtained by dividing the measured value by 60. Similarly, the bias instability of the angular rate sensing system is measured by fitting a line having zero slope to Allan variance plot and reading the value where the line intersect the Allan variance axis. To sum up, to obtain bias instability and the angle random walk of an angular rate sensing system, the system is fixed on a stationary platform, and the drift data of the system is collected for a period of 2.5 hours. Afterwards, the Allan variance plot of the system is generated; consequently, the bias instability and angle random walk values are measured by following the procedure described above.

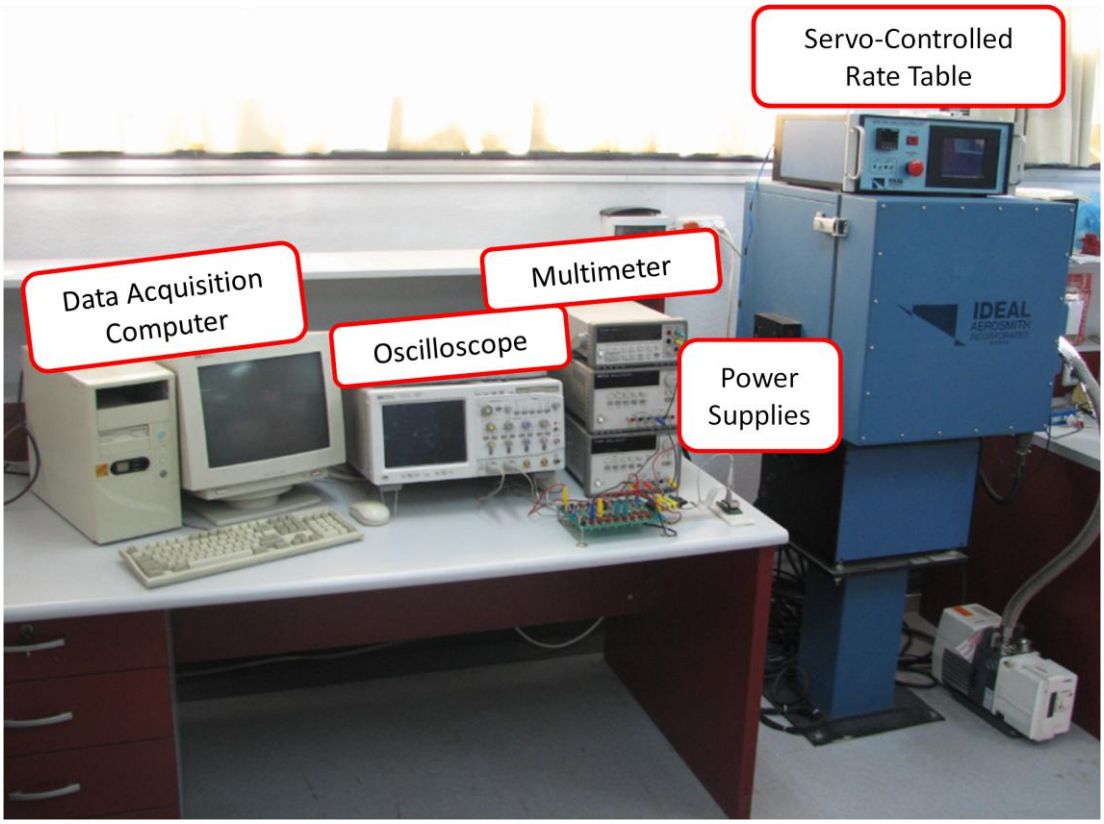

Figure 4.10: Test setup for performance tests

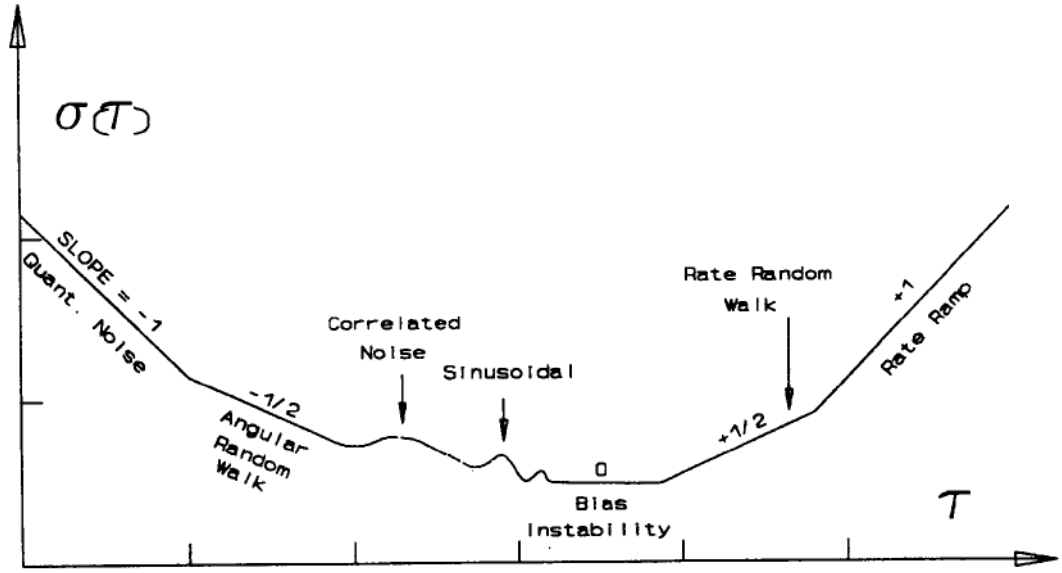

Figure 4.11: Sample plot generated by the Allan Variance analysis [66]

4.2.2 Test Results of the Open-Loop Angular Rate Sensing System with Square Wave Driving Signal AGC Loop

The section presents the tests results of the open-loop angular rate sensing system with square wave driving signal AGC loop, verifying its operation. The design details of the square wave driving signal AGC loop and open loop rate sensing circuitry are given in Sections 3.2.1.1 and 3.2.2, respectively, and will not be repeated here. Moreover, the tests are done using the hermetically sealed hybrid packaged HSOGSNW#9-L10 gyroscope, and as described in Section 3.2.1.1, the controller parameters are calculated according to resonance test results given in Section 4.1. Figure 4.12 shows the PCB of the open-loop angular rate sensing system. Figure 4.13 illustrates the drive-motor signals generated by the AGC loop and the drive-mode output signal of gyroscope when the proof mass voltage is 25 V and the amplitude set voltage is 250 mV. The oscillation frequency of the closed-loop system is measured to be 10171.7 Hz, and according to measured signals, the closed-loop system of the gyroscope at the closed-loop oscillation frequency (taking into account the first sinusoidal harmonic of the square wave) is -8.1 dB that is close to the frequency characteristics of the gyroscope given in Figure 4.6. 250 mV amplitude set voltage is supposed to adjust the drive-mode output to 98 mV. The drive-mode output signal is measured as 105 mV, which is slightly different the expected value. The difference occurs due to the gain and offset error in the LPF, and the demodulation error that shifts the amplitude of the drive-mode oscillation.

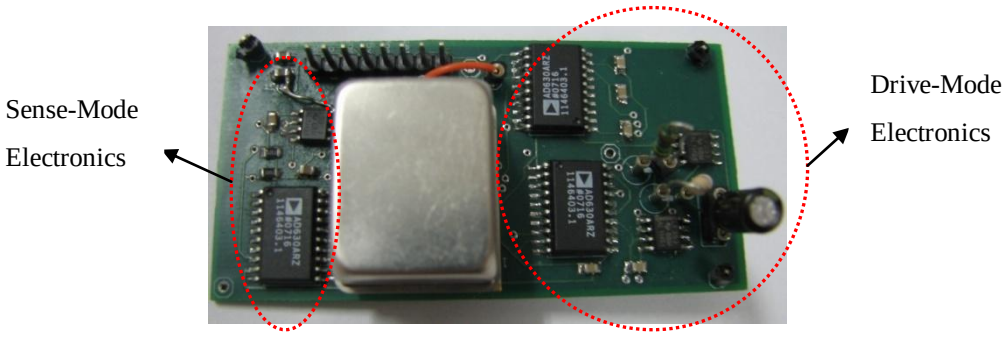

Figure 4.12: General view of the PCB of the open-loop angular rate sensing system with square wave driving signal AGC loop

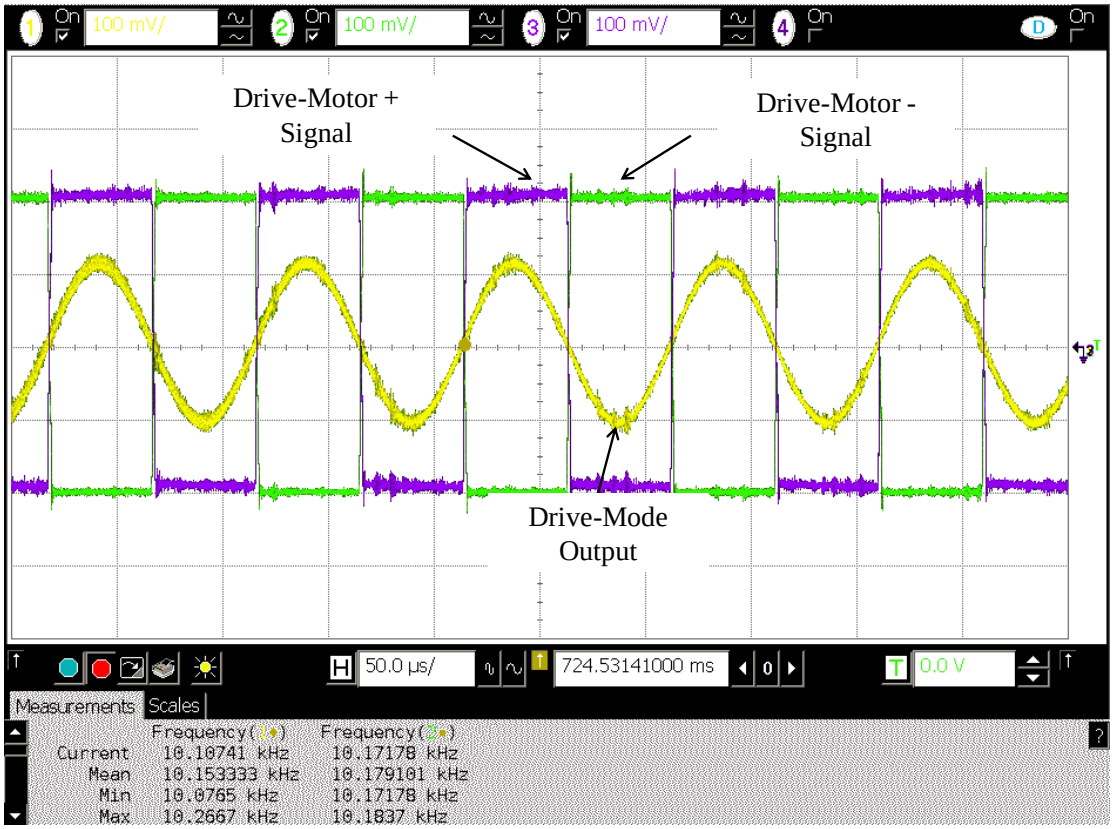

Figure 4.13: Waveform of the square-wave drive-motor (driving) signals generated by the automatic gain control loop and drive-mode output of HSOGSNW#9-L10 SOG gyroscope when 25 V is applied to the proof mass and amplitude set voltage is adjusted to 250 mV

The response of the system after the start-up is also critical. Figure 4.14 shows the measured drive-mode output signal after start-up of the system when 25 V is applied to the proof mass and when the amplitude set voltage is adjusted to 250 mV corresponding to 5.43 µm drive-mode displacement amplitude. The vibration amplitude starts to increase, and the designed controller allows an overshoot less than 10 % of the desired oscillation amplitude. Then, the vibration settles to its desired value and automatic gain control loop provides sustained oscillation that is consistent with the simulation results of the proposed controller design approach. Thus, Figure 4.13 and Figure 4.14 verify that the designed square wave driving AGC loop provides an automatically controlled self-triggered drive-mode oscillation.

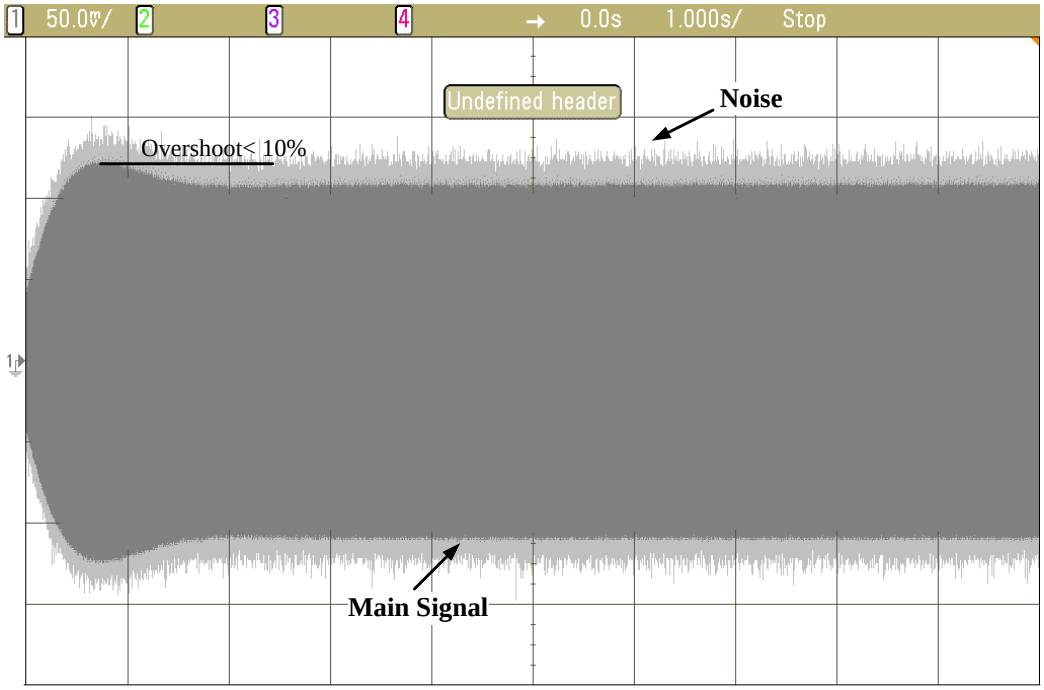

Figure 4.14: Drive-mode output signal after the start-up of the system when 25 V is applied to the proof mass and amplitude set voltage is adjusted to 250 mV

After verifying that the proposed automatic gain control loop provides a sustained oscillation, the scale factor and bias drift tests are performed to assess the performance of the complete angular rate sensing system with the HSOGSNW#9-L10 SOG gyroscope for three different applied proof mass voltages: 15 V, 25 V and 28 V. In this section, the scale factor test results are visually provided only for the case where 25 V is applied to the proof mass, and the test results of the other cases are mentioned numerically. Figure 4.15 illustrates the scale factor test result of the open-loop angular rate sensing system with square wave driving signal AGC loop when 25 V is applied to the proof mass and when the set voltage is adjusted to 350 mV. The test results are used to construct the gyroscope output versus applied rate characteristics, and a line is fitted to determine the scale factor, scale factor nonlinearity, and zero-rate output of the complete system. Figure 4.16 gives the constructed characteristic plot of the complete angular rate sensing system. The system has a scale factor of -49.8 mV/°/sec, and R^2-nonlinearity of the plot is calculated less than ±0.001 % in the range of ±100 °/sec. Moreover, the zero rate output is measured to be 322.5 mV which corresponds to 6.47 °/sec. The reason of

the zero-rate output is mainly due to the demodulation of the quadrature error output to the baseband due to the phase error introduced by the readout electronics.

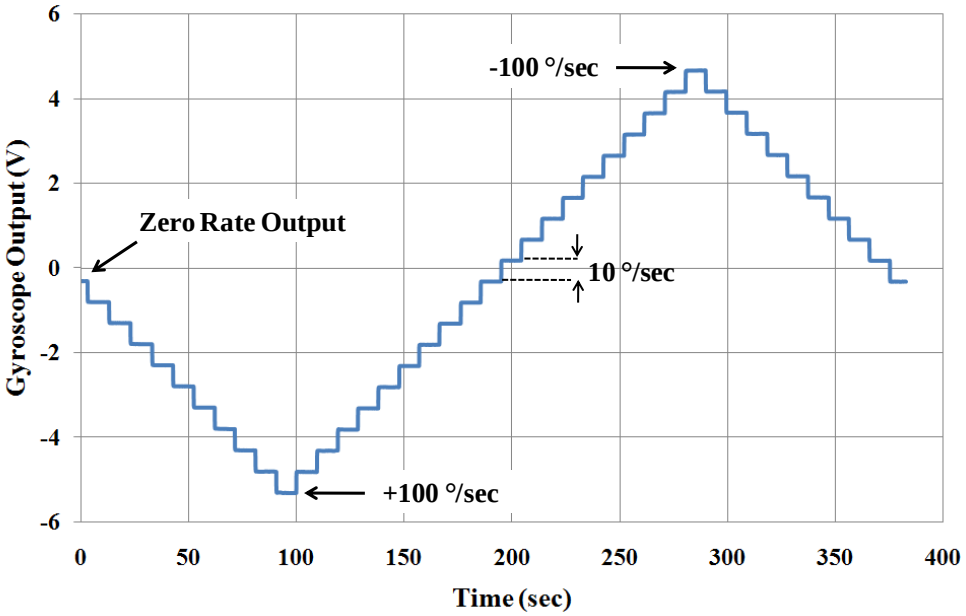

Figure 4.15: Scale factor test result of the open-loop angular rate sensing system with square wave driving signal AGC loop when 25 V is applied to the proofmass and the set voltage is adjusted to 350 mV

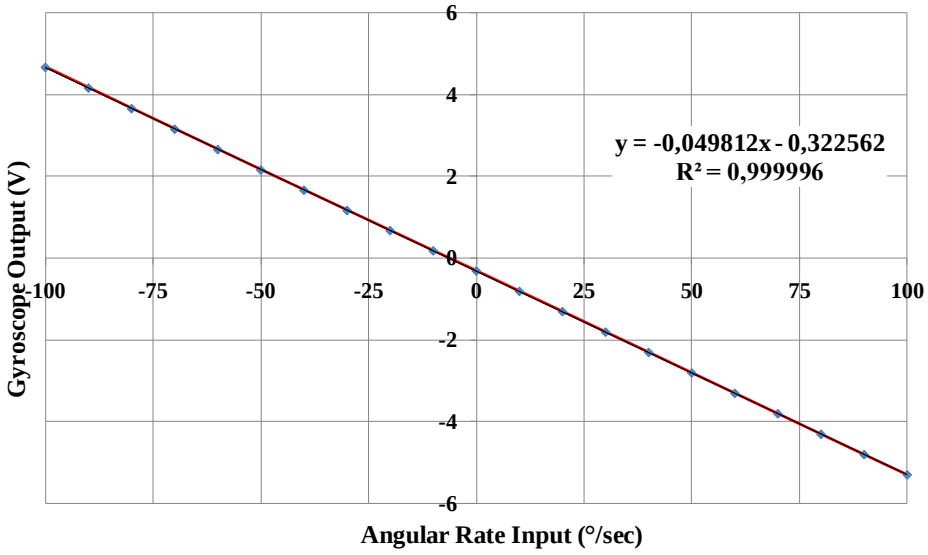

Figure 4.16: Gyroscope output versus angular rate input characteristics to determine the scale factor, scale factor nonlinearity and zero-rate output of the gyroscope

After the scale factor test, the bias drift data is collected for 2.5 hours period to determine the bias instability and angle random walk of the complete angular rate sensing system. Figure 4.17 illustrates the collected bias drift data of the proposed system after start up while the system is kept stationary and a zero rate input is applied. Following the power up, the output value of the gyroscope starts to changes rapidly and the change in the gyroscope output slows down as the time proceeds. To determine the source of the measured rapid change in the gyroscope output, HSOGSNW#9-L10 is disconnected from PCB, and by using the same setup, another bias drift test is performed while a 200 mV sinusoidal signal is applied to the corresponding drive-mode output and sense-mode output pins on the PCB. Figure 4.18 shows the bias drift data collected from the angular rate sensing system. The gyroscope output presents similar characteristics with the complete system output illustrated in Figure 4.15. Since, in this test, only the response of the sense-mode demodulation circuitry is tested, it can be concluded that the sense-mode demodulation dominates the rapid change in the gyroscope bias and this occurs due to the heat-up after start up, hence due to the temperature drift of the demodulation circuitry.

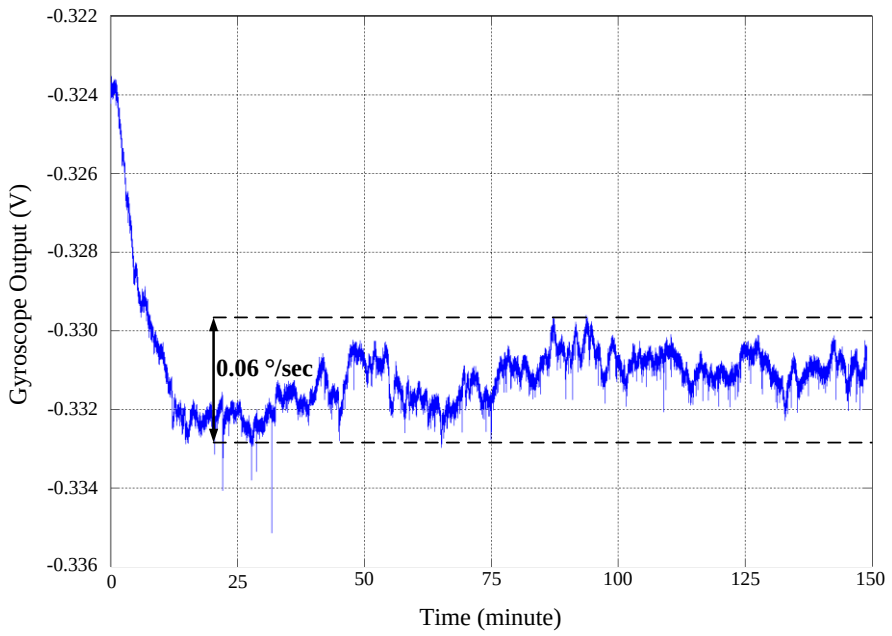

Figure 4.17: Bias drift data collected from the angular rate sensing system after the system starts-up when 25 V is applied to the proof mass

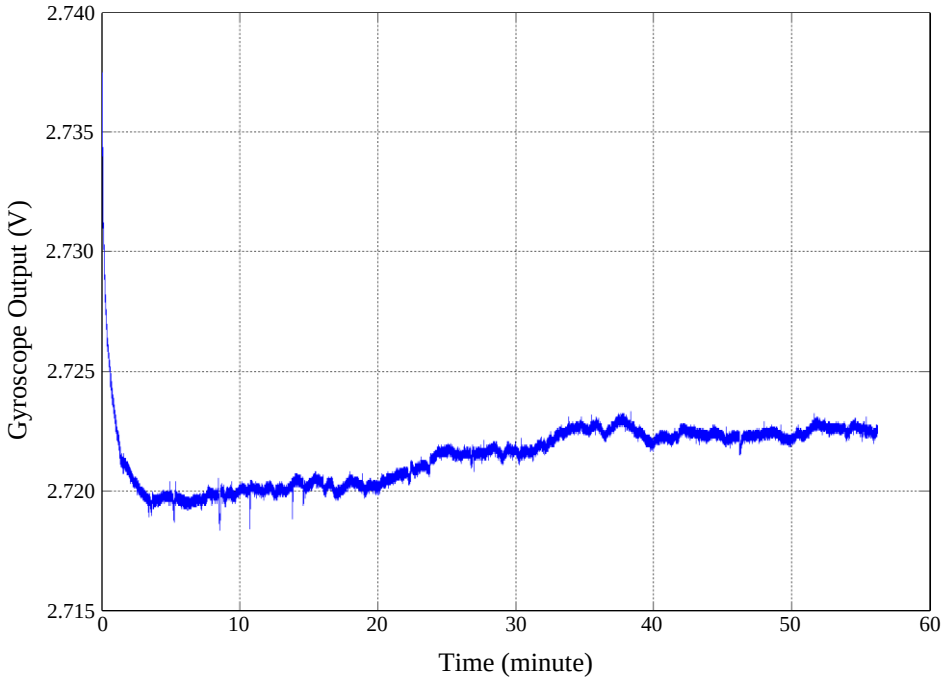

Figure 4.18: Bias drift data collected from the angular rate system after start up while 200 mV sinusoidal signal is applied to the corresponding gyroscope drive-mode output and sense-mode output pins on the PCB

Figure 4.19 demonstrates the Allan variance plot generated by the bias drift data given in Figure 4.17. The bias instability of the angular rate sensing system is calculated to be 5.12 °/hr which is sufficient for tactical-grade applications. As described in Section 4.1, the resolution of the system is found by fitting a line having -1/2 slope to the Allan Variance plot. Unfortunately, the generated plot doesn't have a section having -1/2 slope. Referring to the general Allan Variance plot given in Figure 4.11 it can be claimed that the section should reside in the left of the generated plot. However, the data acquisition speed of the test setup system is limited by the Agilent 34401 multimeter to 16 Hz; hence the resolution of the system for the adjusted operation conditions cannot be found by the present test setup. Nevertheless, the resolution of the system can be estimated by putting a line with -1/2 slope to the edge of the Allan variance plot and assuming the exact fitted line resides towards the left of this line. The proposed line intersects $\tau=1$ at $\sigma(\tau)=1.01$ °/hr, thus noise equivalent rate and angle random walk of the system is estimated to be better than 1.01 (°/hr)/√Hz and 0.017 °/√hr. It should be noted here that these results are comparable to the best results in the literature.

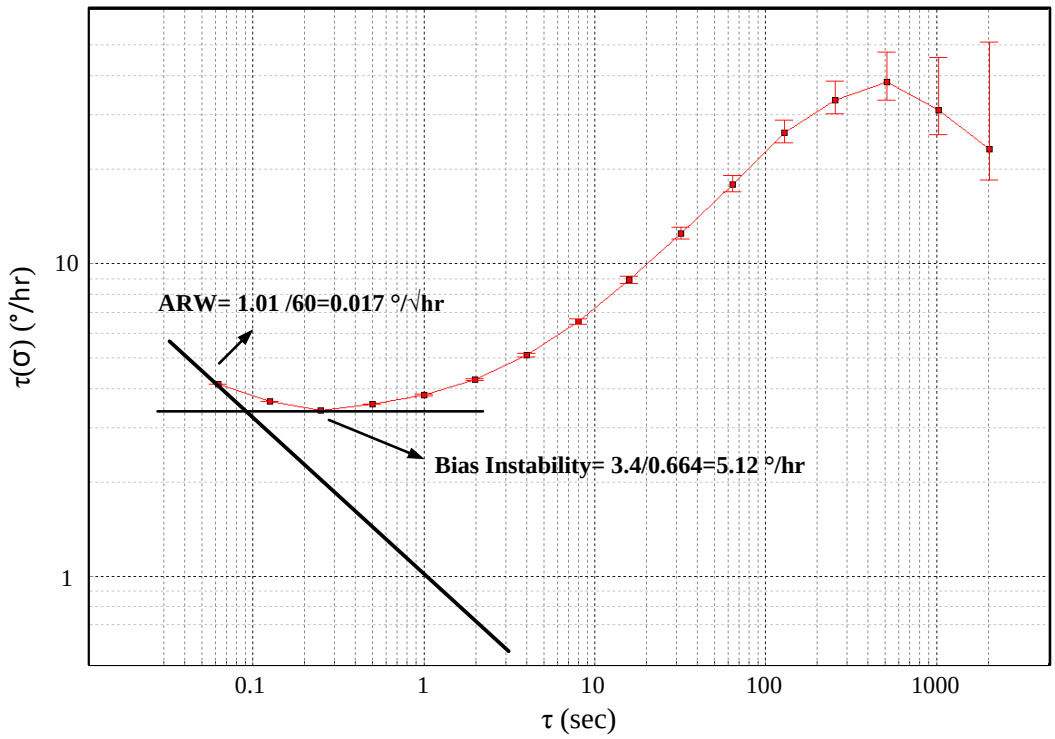

Figure 4.19: Allan Variance Plot generated by the drift data given in Figure 4.15

The scale factor and bias drift tests are also performed for the cases when 15 V and 28 V are applied to the proof mass. Figure 4.20 and Figure 4.21 give the Allan Variance plot of the angular rate sensing system with square wave driving signal AGC loop for different cases, and Table 4.1 summarizes the results of the scale factor and bias drift tests for all cases. The test results verify that the proposed angular rate sensing system achieve tactical-grade angle random walk and bias instability performance for all operation cases. Moreover, Case 1 and Case 3 also satisfy the bandwidth requirements and scale factor linearity of the tactical grade applications.

Although implemented with discrete components the open-loop angular rate sensing system with the square wave driving signal AGC loop provides impressive performance, and the performance can be improved even further with lower noise and lower drift components and better test setup. It should be noted here that, the proposed AGC loop satisfies sustained oscillation without requiring an external trigger to start oscillation.

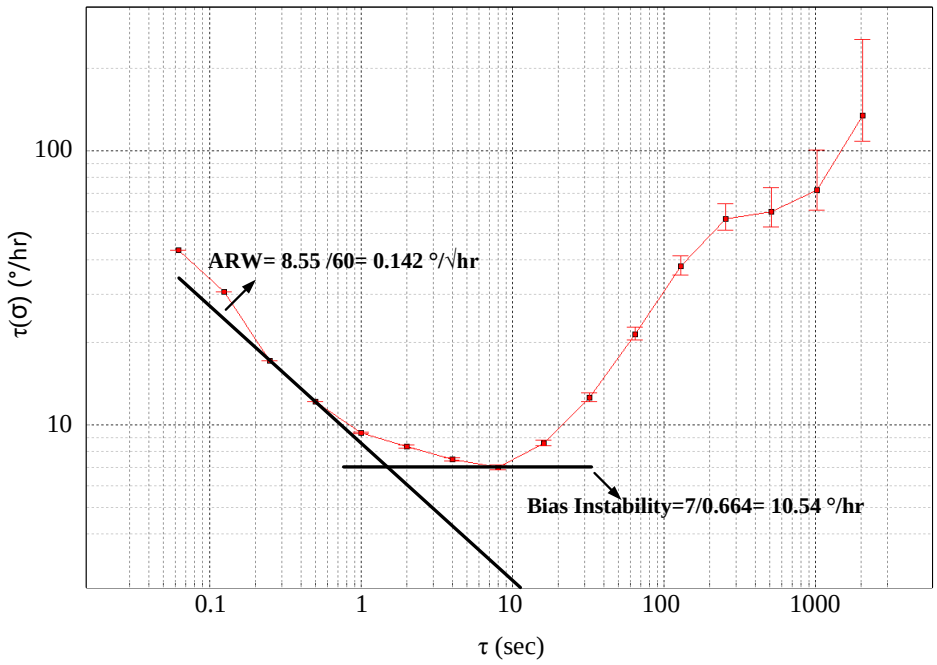

Figure 4.20: Allan Variance plot generated by collected bias drift data of angular rate sensing system with square wave driving signal AGC loop when 15 V is applied to the proofmass and the set voltage is adjusted to 200 mV

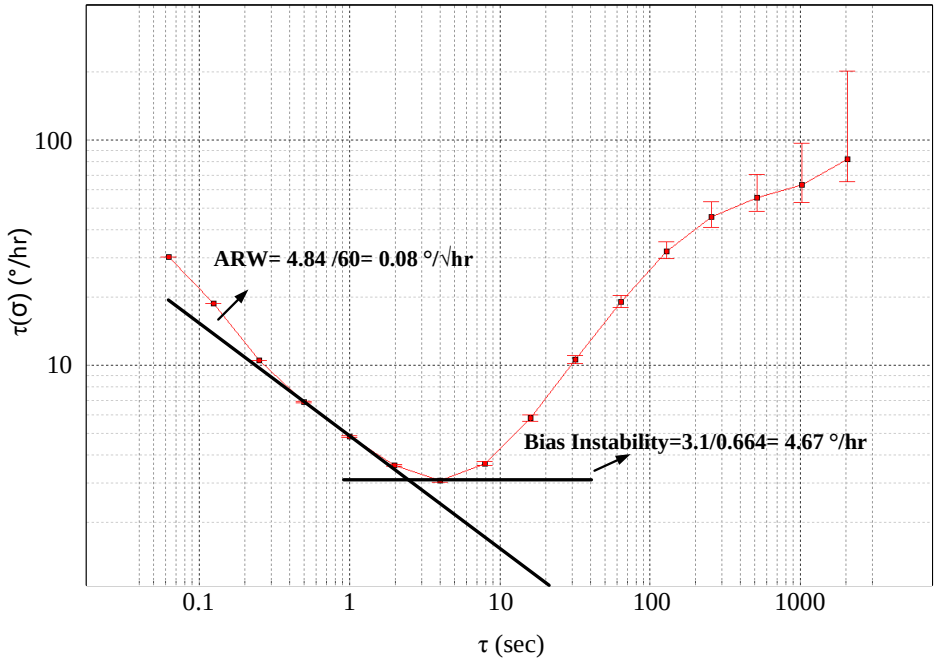

Figure 4.21: Allan Variance plot generated by collected bias drift data of angular rate sensing system with square wave driving signal AGC loop when 28 V is applied to the proof mass and the set voltage is adjusted to 400 mV

Table 4.1: Performance test results of the open-loop rate sensing system with square wave driving signal AGC loop for different cases using the HSOGSNW#9-L10 gyroscope

	Case 1	Case 2	Case 3
Proof mass Voltage (V)	15	25	28
Amplitude Set Voltage (mV)	200	350	400
Drive-Mode Displacement (μm)	7.24	7.6	7.76
Scale Factor (mV/°/sec)	9.86	-49.8	-22.6
R^2-Nonlinearity (%)	$3x10^{-4}$	$0.4x10^{-4}$	$1x10^{-4}$
Zero-Rate Output (mV)	-10.75	-322.2	-56.15
ARW (°/√hr)	0.142	< 0.017	0.080
Bias Instability (°/hr)	10.54	5.12	4.67
Mechanical Bandwidth (Hz)	100	30	100
Angular Input Range (°/sec)	100	100	100

4.2.3 Test Results of the Open-Loop Angular Rate Sensing System with Sinusoidal Wave Driving Signal AGC Loop

This section presents the test results of open-loop rate sensing system with sinusoidal wave driving AGC loop. The design details of the proposed system are given in Sections 3.2.1.2 and 3.2.2. The measurements are again performed for the hermetically vacuum sealed HSOGSNW9-L10 SOG gyroscope which was used in the tests provided in Section 4.2.2. Figure 4.22 shows the general view of the PCB of the proposed angular rate sensing system, and Figure 4.23 gives the measured waveforms of the sinusoidal wave driving signals generated by the automatic gain control loop and drive-mode output of HSOSNW#9-L10 when 25 V is applied to the proof mass and the amplitude set voltage is adjusted to 250 mV. The differential sinusoidal wave signals applied to the drive-motors vibrate the drive-mode of the gyroscope at 10186.3, Hz which is 15 Hz larger than the oscillation frequency of the previous AGC loop. The main reason of this discrepancy is the inaccuracy of oscilloscope frequency reading, since the sinusoidal wave signal's zero transition

point is not explicit due to the amplified noise. Besides, the magnitude gain of the oscillating gyroscope is calculated to be -8.54 dB that is closed to the measured magnitude gain at the oscillation frequency of the square-wave driving signal AGC loop.

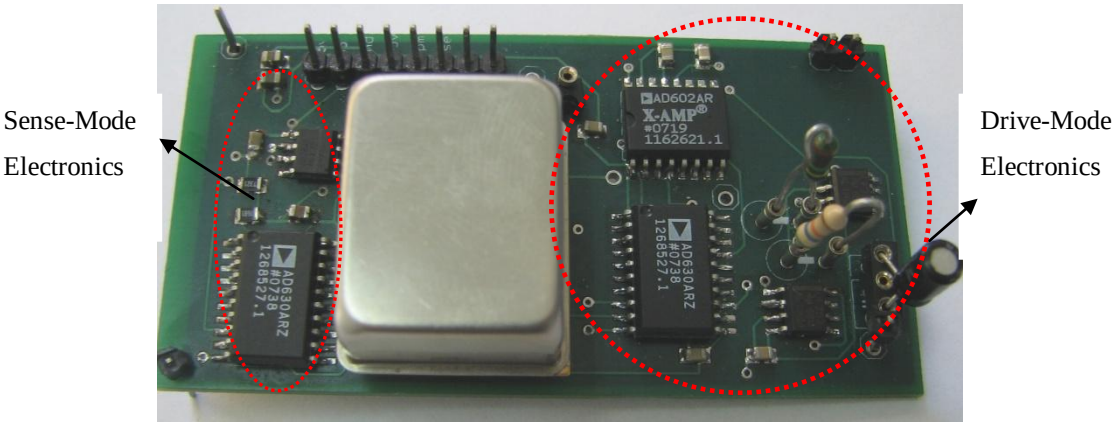

Figure 4.22: General view of the PCB of the open-loop angular rate sensing system with sinusoidal wave driving signal AGC loop

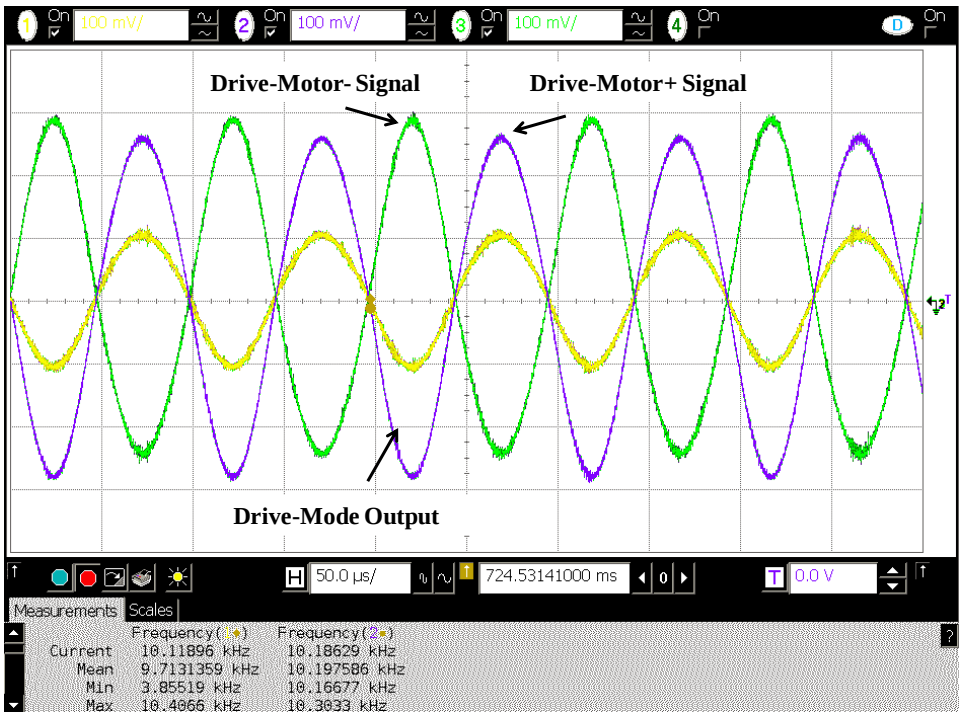

Figure 4.23: Measured waveforms of the sinusoidal-wave drive-motor (driving) signals generated by the automatic gain control loop and drive-mode output of HSOGSNW#9-L10 SOG gyroscope while 25 V is applied to the proof mass and the amplitude set voltage is adjusted to 250 mV

The designed controller described in Section 3.2.1.2 allows the magnitude of the closed-loop system to increase exponentially after power up and limits the overshoot of the oscillation. Then, the magnitude of the oscillation decays to the value determined by the amplitude set voltage. Figure 4.24 illustrates the drive-mode output signal after start up of the system when 25 V is applied to the proofmass and the amplitude set voltage is adjusted to 250 mV. The measured waveform demonstrates similar characteristics to the assumption used in the design of the controller, except that the tested closed-loop system goes undershoot after overshooting and subsequently settles to the desired value. In addition, the maximum overshoot is measured to be 13 % which is larger than the designed value (5 %). Hence the controller designed with the proposed approach provides sustained oscillation in the drive mode, but requires comprehensive analysis to control the system parameters much accurately.

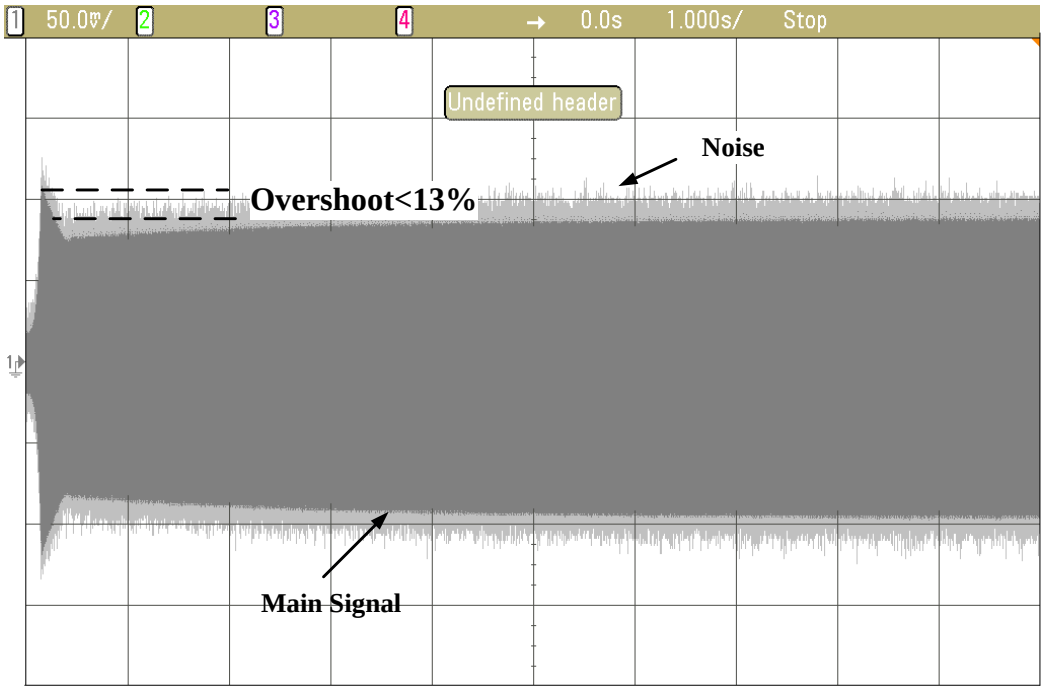

Figure 4.24: Measured drive-mode output signal after the start-up of the system while 25 V is applied to the proof mass and the amplitude set voltage is adjusted to 250 mV

Similar to the rate sensing system with the square-wave driving signal AGC loop, the performance tests are done for the open-loop rate sensing system with sinusoidal wave driving signal AGC loop by adjusting the identical operation conditions. Figure 4.25 demonstrates the scale factor test of the proposed angular rate sensing system when 25 V is applied to the proof mass and the amplitude set voltage is adjusted to 350 mV. Since the LF 353 opamp used in low-pass filter of the demodulation circuit doesn't operate rail-to-rail and since the AD602 limits the maximum supply voltages to ±5 V, for the ±5 V supply voltages the full scale range of the proposed system is limited to -100 °/s- +80 °/sec in this test configuration. Figure 4.26 gives the gyroscope output versus angular rate input characteristics between -100 °/s and +80 °/sec generated by the data collected in this scale factor test. The scale factor, R^2 nonlinearity, and zero-rate offset of the angular rate sensing system are calculated as 43.25 mV/(˚/sec) , 0.004 %, and 354.20 mV, respectively.

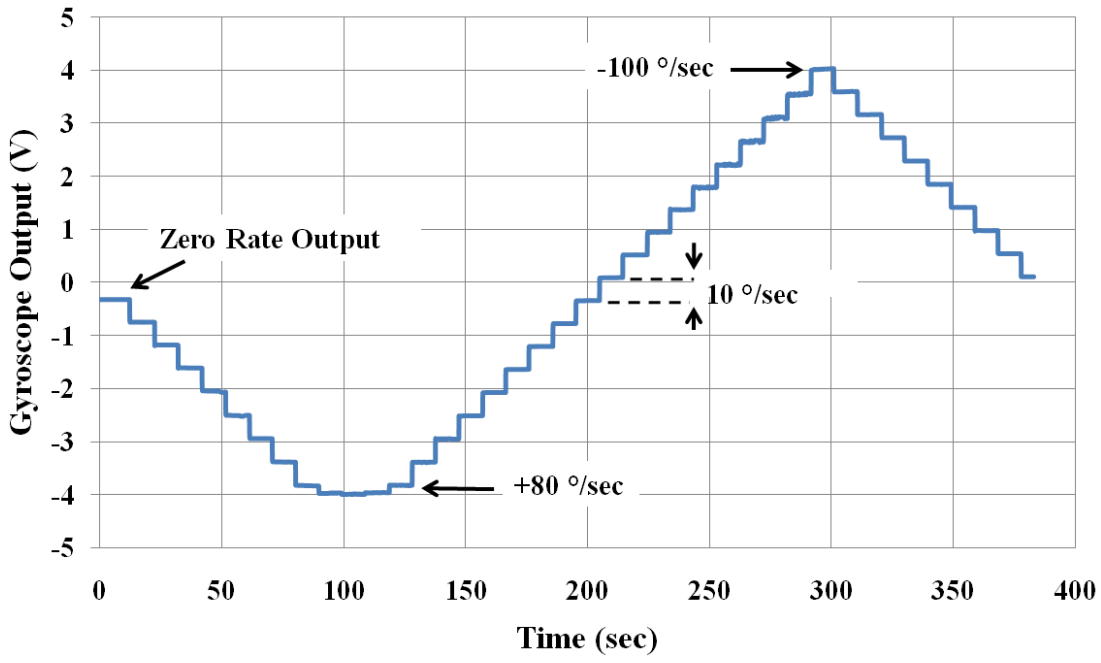

Figure 4.25: Scale factor measurement results of the open-loop angular rate sensing system with the sinusoidal wave driving signal AGC loop while 25 V is applied to the proof mass and the amplitude set voltage is adjusted to 350 mV

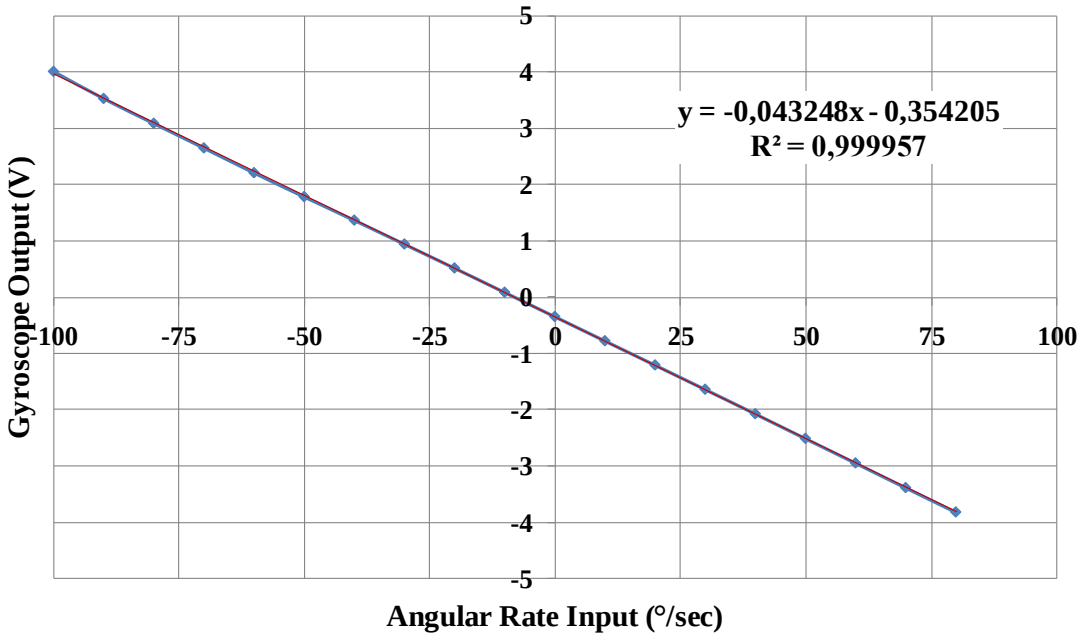

Figure 4.26: Gyroscope output versus angular rate input characteristics to determine the scale factor, scale factor nonlinearity and zero-rate output of the gyroscope

Figure 4.27 presents the bias drift data collected from the open-loop angular rate sensing system with the sinusoidal wave driving signal AGC loop after the system starts up, while 25 V is applied to the proof mass. The bias change of the proposed system exhibits similar characteristics with the bias drift data in Figure 4.17 in 2.5 hours period; the bias changes rapidly following start up and fluctuates slowly after tenth minute of the bias drift test. The fluctuation of the bias is measured to be less than 0.1 °/sec in 125 minutes test period. Following the bias drift test, the collected bias data is processed to obtain Allan variance plot of the angular rate sensing system. Figure 4.28 gives the Allan variance plot generated by the drift data given is Figure 4.24. The bias instability and noise equivalent rate of the angular rate sensing system are measured as 4.51 °/hr and 1.8 (°/hr)/√Hz, respectively while 25 V is applied to the proof mass and the amplitude set voltage is adjusted to 350 mV.

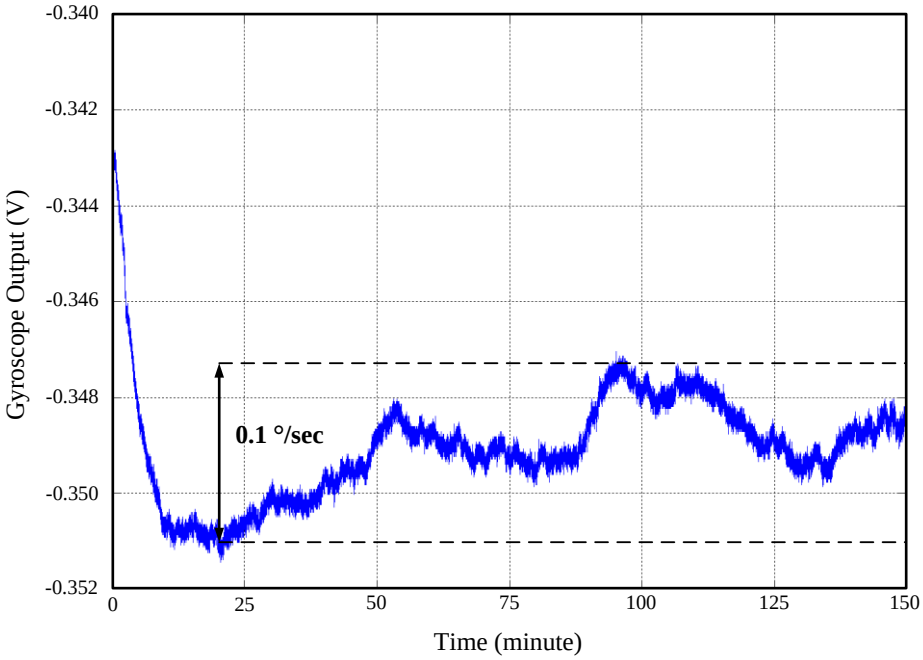

Figure 4.27: Bias drift data collected from the proposed angular rate sensing system after the system starts-up while 25 V is applied to the proof mass

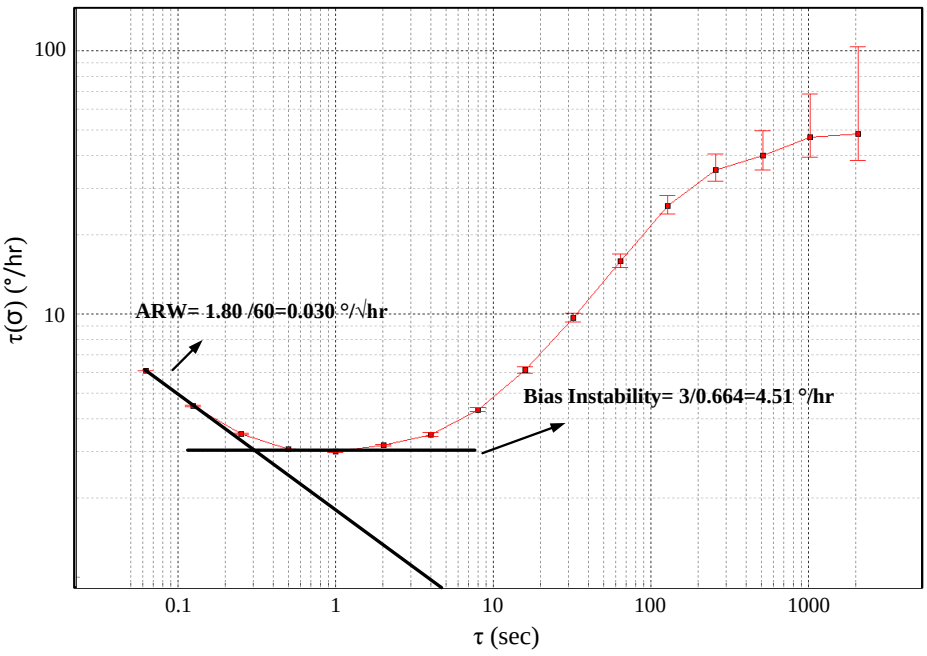

Figure 4.28: Allan Variance Plot generated by the drift data given in Figure 4.24

The same test procedure is followed for the cases when 15 V and 28 V are applied to the proof mass and the amplitude set voltage is adjusted to 200 mV and 400 mV,

respectively. Figure 4.29 and Figure 4.30 give the Allan variance plots generated by the drift data collected for two cases. In addition, Table 4.2 summarizes all the performance test results performed for the open-loop angular rate sensing system with sinusoidal wave driving signal AGC loop. The open loop angular rate sensing system with sinusoidal wave driving signal AGC loop exhibits a 6.92˚/hr bias instability and a 0.049 ˚/√hr ARW for the case when 28 V is applied to the proof mass and the amplitude set voltage is adjusted to 400 mV. Together with the test results given above it is also verified that the proposed angular rate sensing system can be classified as a tactical grade angular rate sensing system regarding their bias instability and ARW. However, the system operation degrades when the system operation shifted to 15 V proof mass voltage and 200 mV set voltage. The main reason of this degradation is probably the problems in the test setup; however,this could not be verified and better measurement results could not be obtained as the gyroscope HSGOSNW#9-L10 stopped functioning properly due to an unknown problem. As this gyroscope was in vacuumed package, it was not possible to identify the problem.

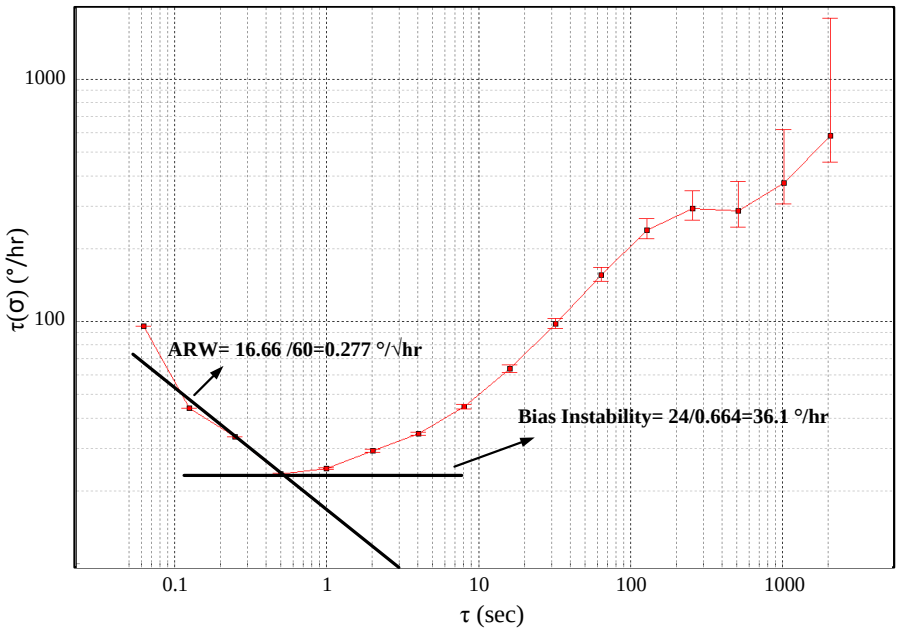

Figure 4.29: Allan Variance plot generated by collected bias drift data of angular rate sensing system with sinusoidal wave driving signal AGC loop when 15 V is applied to the proof mass and the amplitude set voltage is adjusted to 200 mV

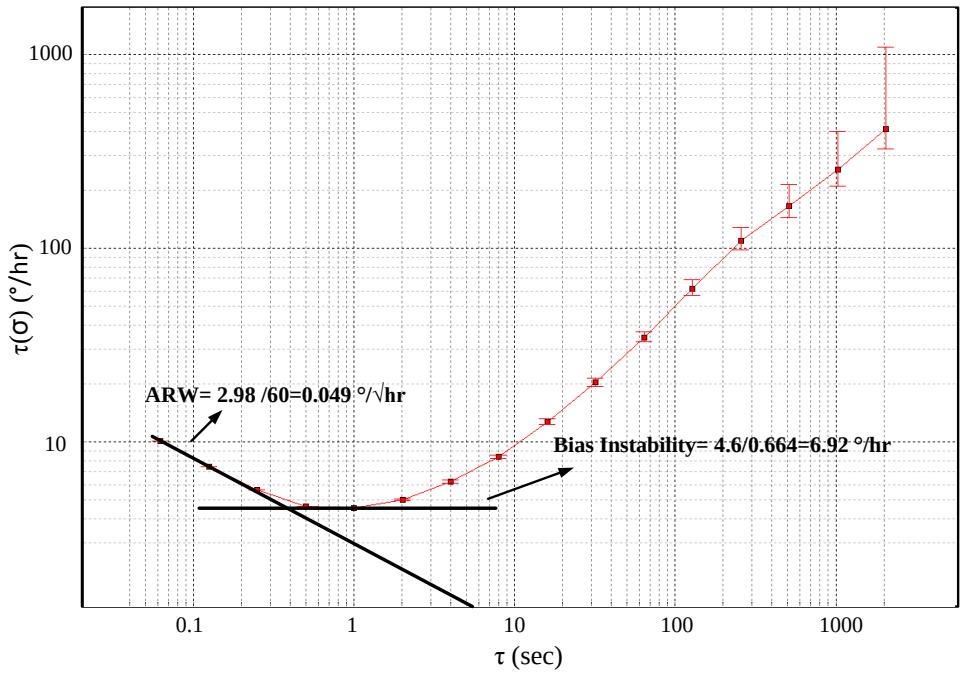

Figure 4.30: Allan Variance plot generated by collected bias drift data of angular rate sensing system with sinusoidal wave driving signal AGC loop when 28 V is applied to the proof mass and the amplitude set voltage is adjusted to 400 mV

Table 4.2: Performance test results of the open-loop rate sensing system with sinusoidal wave driving signal AGC loop for different cases using the HSOGSNW#9-L10 gyroscope

	Case 1	Case 2	Case 3
Proof Mass Voltage (V)	15	25	28
Amplitude Set Voltage (mV)	200	350	400
Drive-Mode Displacement (μm)	7.24	7.6	7.76
Scale Factor (mV/°/sec)	8.47	-43.24	-17.97
R^2-Nonlinearity (%)	$1.8x10^{-4}$	$4.3x10^{-3}$	$3x10^{-4}$
Zero-Rate Output (mV)	-110.5	-354.2	-100.4
ARW (°/√hr)	0.277	0.030	0.049
Bias Instability (°/hr)	36.1	4.51	6.92
Mechanical Bandwidth (Hz)	100	30	100
Angular Input Range (°/sec)	±100	-100 to +80	±100

In summary, it is verified that the sinusoidal wave driving signal AGC loop can be employed to obtain a sustained oscillation in the drive-mode. Moreover, the proposed controller design approach for AGC loop provides the ability of controlling the overshoot of the oscillation at the start up, and the test results shows similar performance with simulations. However, it is observed that the controller approach should be analyzed in detailed and should be improved for a better control of the system dynamics. Nevertheless, the system achieves tactical grade level performance and shows the lowest bias instability performance obtained in SOG gyroscopes developed at METU.

4.2.4 Test Results of the Open-Loop Angular Rate Sensing System with Off-Resonance Frequency Driving Signal AGC Loop

This section presents the test results of the open-loop rate sensing system with off-resonance frequency driving signal AGC loop. The design details of the off-resonance frequency driving signal AGC loop is given in Section 3.2.1.3. As mentioned previously, the off resonance driving signal is generated by modulating the sum of a DC signal and a sinusoidal signal at the resonance frequency by a carrier frequency at the half of the mechanical resonance frequency. As a result of two inherited signals, the AGC loop can be constructed by controlling either the magnitude of the sinusoidal part or the DC part of the modulated signal. In this section, the operations of two methods are verified and the performance tests of the off-resonance frequency AGC loop employing the control of the sinusoidal signal part are performed. The former method controls the gain of the VGA connected to the output of the transresistance amplifier, and this amplified signal is converted to two differential signals, while a constant 5 V is added to the differential signals. Then, the sinusoidal signal with a DC offset is modulated by two AD630 (modulator/demodulator) having gain of 2 and -2 configurations. Finally, the modulated signals are coupled to proof mass voltage and applied to the drive-motor inputs. Figure 4.31 shows the general view of the PCB designed for the proposed open-loop angular rate sensing system and Figure 4.32 gives the measured

demodulator outputs of the corresponding drive-motor signals and drive-mode output signal of the off-resonance driving signal AGC loop with VGA when 25 V is applied to the proof mass and the amplitude set voltage is adjusted to 250 mV. The measured frequency of the demodulator output is 5084.6 Hz; hence, the oscillation frequency of the closed loop system is approximately 10169.2 Hz, which is close to the frequency given in Figure 4.6.

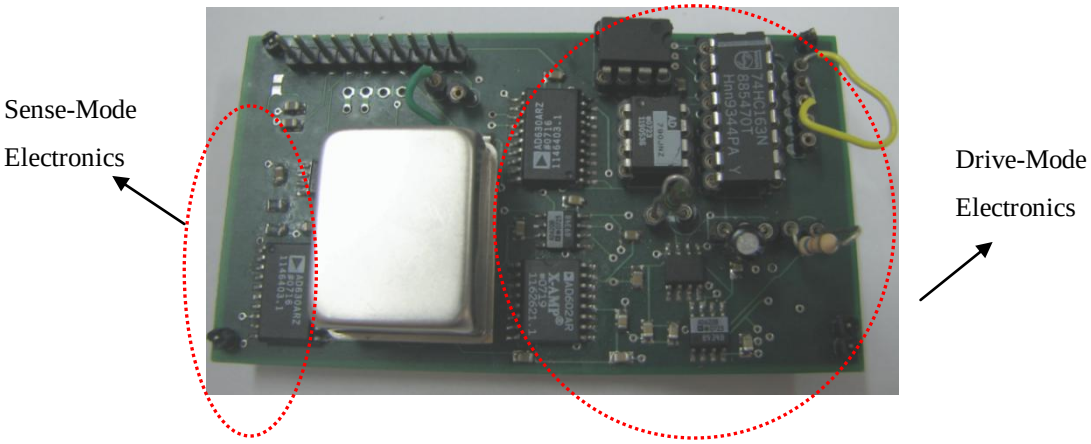

Figure 4.31: General view of the PCB of the open-loop angular rate sensing system with off-resonance frequency driving signal AGC loop with VGA control

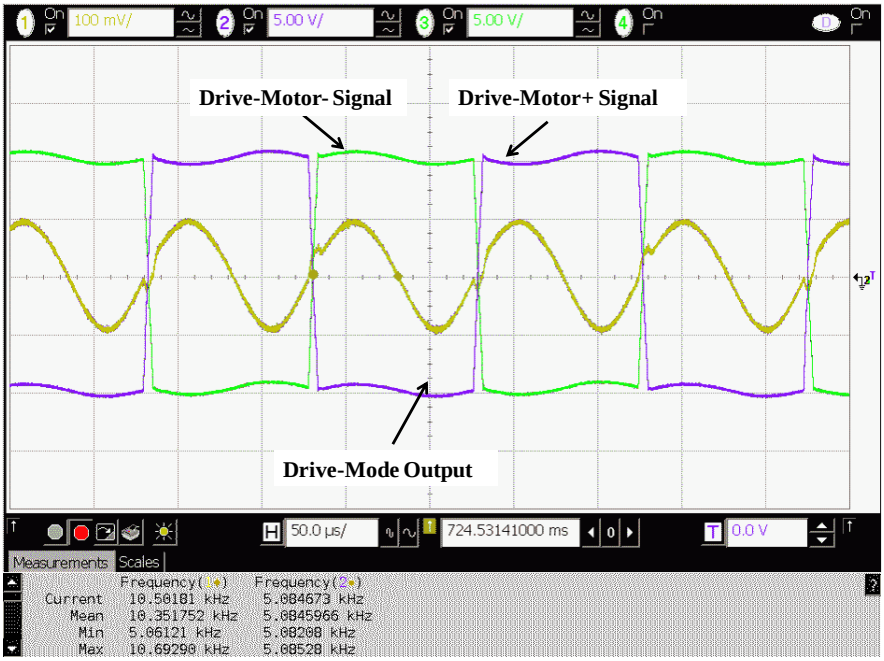

Figure 4.32: Measured demodulator outputs of the corresponding drive-motor signals and drive-mode output signal of the off-resonance driving signal AGC loop with VGA when 25 V is applied to the proof mass and the amplitude set voltage is adjusted to 250 mV.

The start up of the proposed system is also tested. The system cannot automatically start self-oscillation and it requires triggering. By applying a sinusoidal signal to the drive-mode output, the driving signals of the system are generated, and then the trigger signal is disconnected. Figure 4.33 illustrates the drive-mode output signal after the start-up of the system when 25 V is applied to the proof mass and the amplitude set voltage is adjusted to 200 mV. The controller of the AGC loop is designed by using the same approach with the sinusoidal wave driving signal AGC loop; hence, the magnitude of the oscillation grows exponentially after power up. Since the open loop gain of the proposed system is not high, the system doesn't overshoot and settles its desired value behaving as an overdamped system.

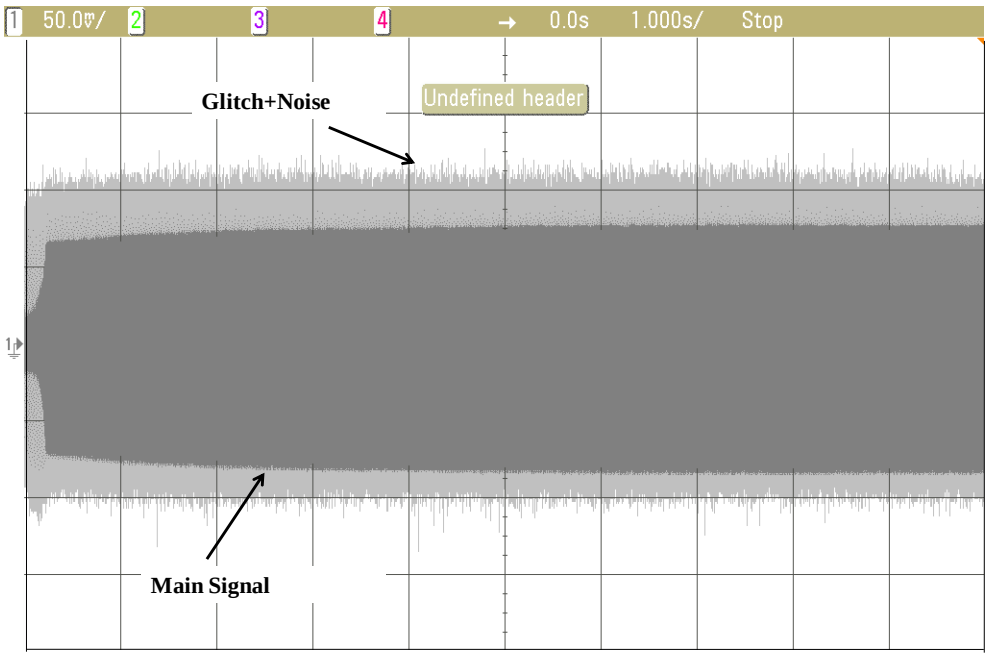

Figure 4.33: Drive-mode output signal after the start-up of the system when 25 V is applied to the proof mass and the amplitude set voltage is adjusted to 200 mV.

The scale factor and bias drift tests are performed to determine scale factor, scale factor nonlinearity, zero-rate output, bias instability, and resolution of the open-loop rate sensing system with off-resonance frequency driving signal AGC loop. Figure 4.34 gives the scale factor test result when 25 V is applied to the proof mass and the amplitude set voltage is adjusted to 350 mV, and, Figure 4.35 shows the measured

gyroscope output versus angular rate input characteristics constructed from the scale factor test. The sensor has a scale factor of 47.26 mV with a R^2 nonlinearity of 0.006 % in the -100 °/sec to +90 °/sec angular input range. In addition, the calculated zero rate offset is 327.53 mV corresponding to 6.93 °/sec.

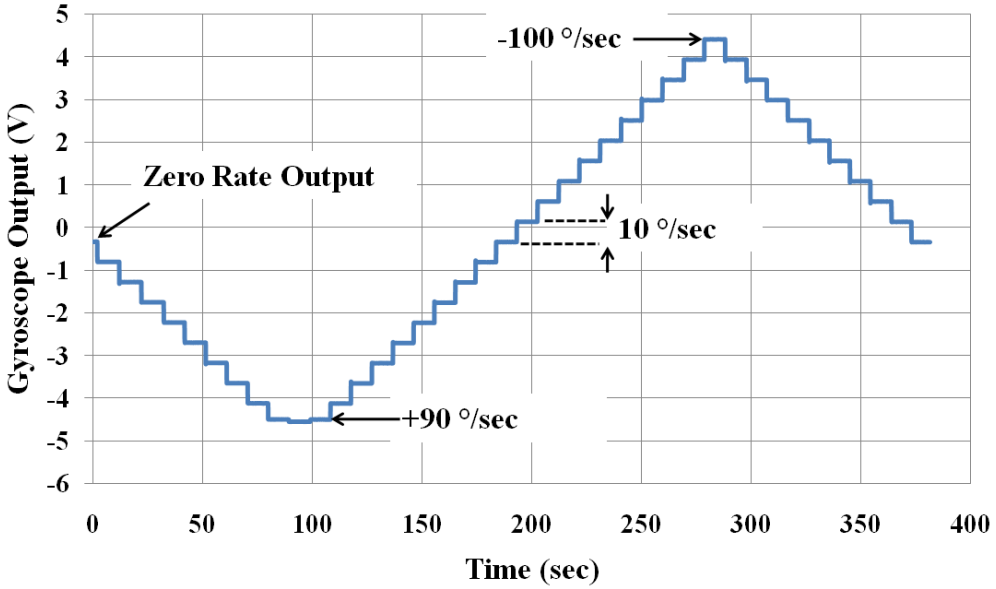

Figure 4.34: Scale factor test result of the open-loop angular rate sensing system with off-resonance frequency driving signal AGC loop when 25 V is applied to the proof mass and the amplitude set voltage is adjusted to 350 mV.

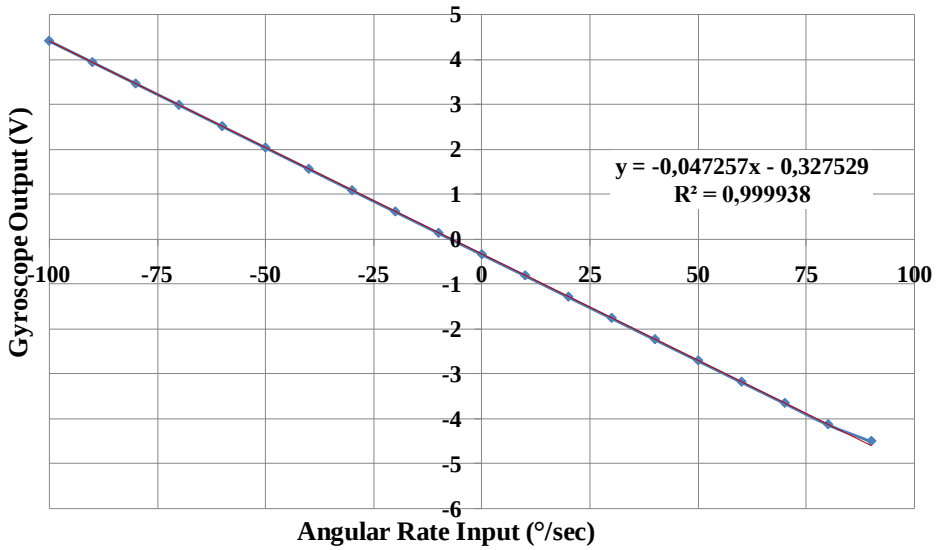

Figure 4.35: Measured gyroscope output versus angular rate input characteristics to determine the scale factor, scale factor nonlinearity, and zero-rate output of the gyroscope.

Figure 4.36 illustrates the bias drift data collected from the proposed angular rate sensing system after start up, when 25 V is applied to the proof mass during around 130 minutes. The measured gyroscope output change in time is similar to the bias drift data plots given in Figure 4.17 and Figure 4.27; the output changes rapidly in short time and the variation slows down in long time. It is measured that the bias drift corresponds to 0.14 °/sec between 20 and 135 minutes. Figure 4.37 demonstrates Allan Variance plot generated by the bias drift data given in Figure 4.36. The bias instability of the proposed system is found to be 5.72 °/hr, while the resolution and angle random walk are measured to be 2.76 °/hr, and 0.046 °/√hr, respectively.

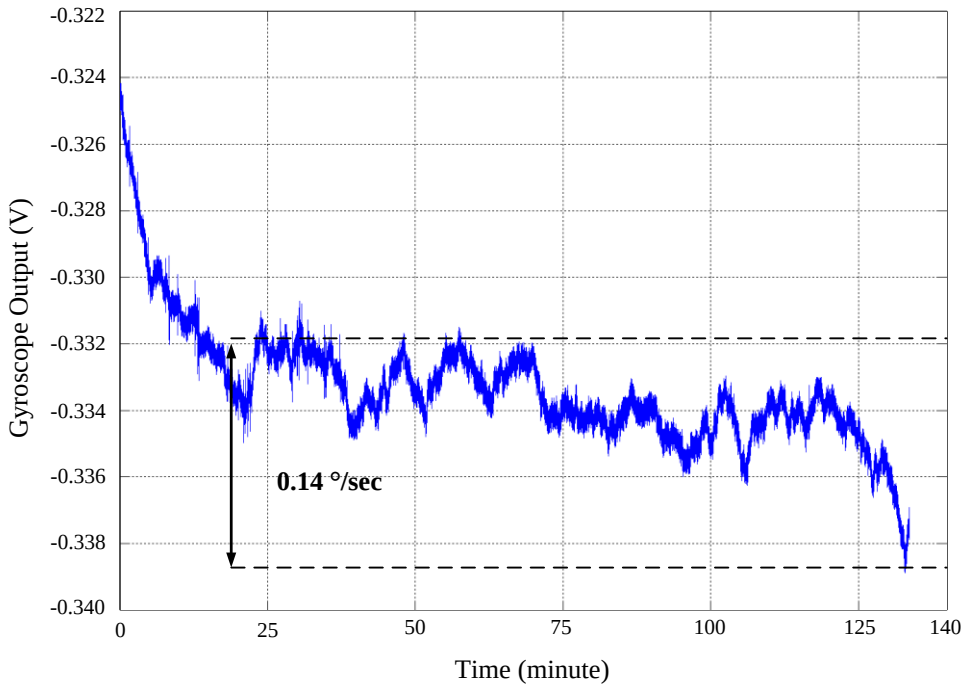

Figure 4.36: Bias drift data collected from the proposed angular rate sensing system after the system starts-up when 25 V is applied to the proof mass

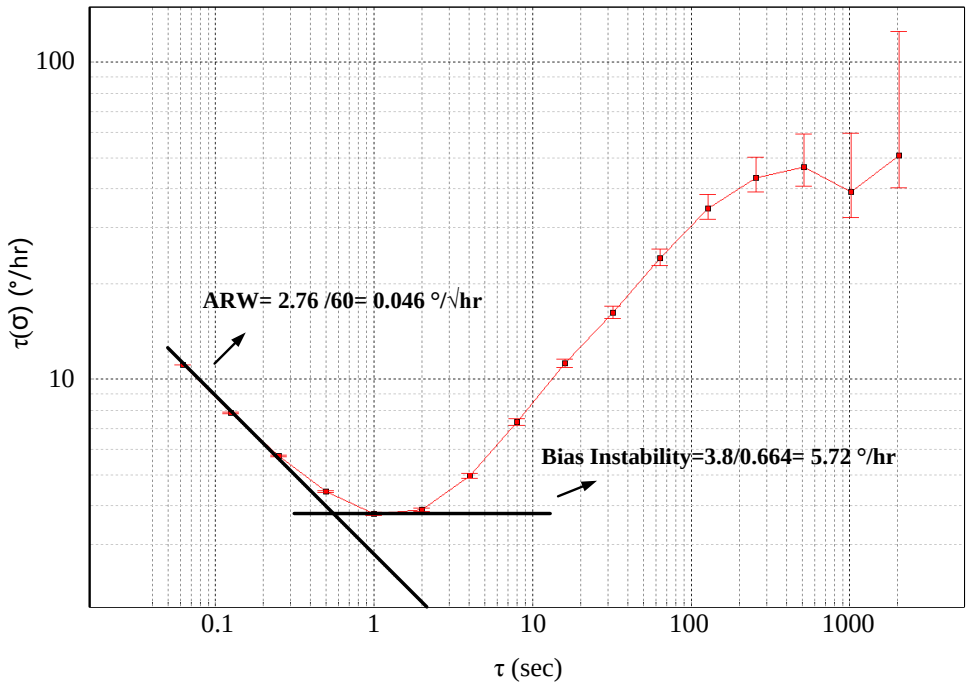

Figure 4.37: Allan Variance Plot generated by the drift data given in Figure 4.33

The performance test results for other operation conditions are also important to determine the effective noise and bias instability sources in the system. Hence, the performance tests are also performed for the cases when 28 V and 15 V are applied to the proofmass. Figure 4.38 and Figure 4.39 give the Allan Variance plot generated by the bias drift and scale factor tests for the mentioned cases. Moreover,

Table 4.3 gives the summary of the all test performed with the open-loop rate sensing system with the off-resonance frequency driving signal AGC loop. The test results shows that the proposed angular rate system has a bias instability of 16.56 °/hr with an ARW of 0.274 °/√hr when the proof mass voltage and the set voltage are 15 V and 200 mV, respectively. Furthermore, when the proof mass voltage is increased to 28 V and the amplitude set voltage is adjusted to 400 mV in order to provide similar drive-mode vibration amplitude, the bias instability improves to 8.43 °/hr with 0.086 °/√hr ARW. In both cases, the angular rate system shows low R^2-nonlinearities in the ±100 °/sec angular rate input range.

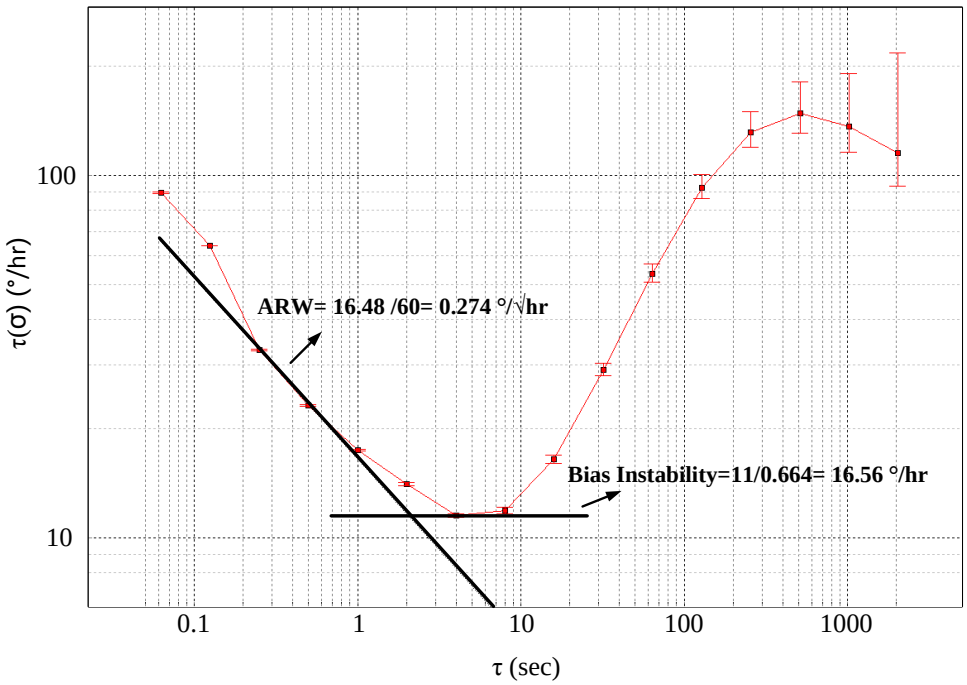

Figure 4.38: Allan Variance plot generated by collected bias drift data of angular rate sensing system with off-resonance frequency driving signal AGC loop when 15 V is applied to the proof mass and the amplitude set voltage is adjusted to 200 mV

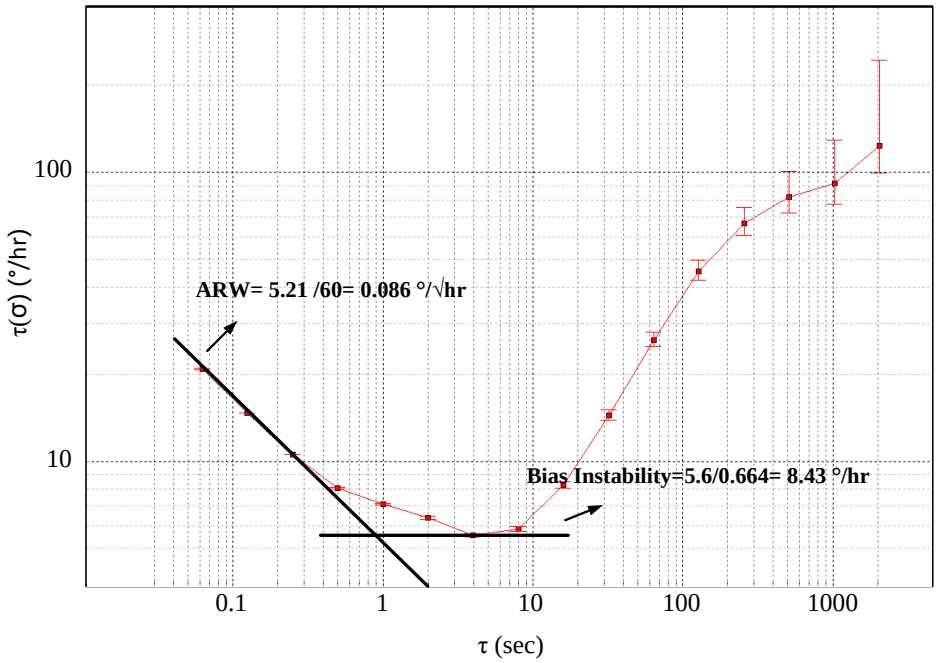

Figure 4.39: Allan Variance plot generated by collected bias drift data of angular rate sensing system with off-resonance frequency driving signal AGC loop when 28 V is applied to the proof mass and the set voltage is adjusted to 400 mV

Table 4.3: Performance test results of the open-loop rate sensing system with off-resonance frequency driving signal AGC loop for different cases with HSOGSNW#9-L10 gyroscope

	Case 1	Case 2	Case 3
Proof Mass Voltage(V)	15	25	28
Amplitude Set Voltage (mV)	200	350	400
Drive-Mode Displacement (μm)	7.24	7.6	7.76
Scale Factor (mV/°/sec)	8.17	-47.26	-20.97
R^2-Nonlinearity (%)	$1x10^{-4}$	$6.2x10^{-3}$	$1x10^{-4}$
Zero-Rate Output (mV)	-81.6	-327.5	-101.2
ARW (°/√hr)	0.274	0.046	0.086
Bias Instability (°/hr)	16.56	5.72	8.43
Mechanical Bandwidth (Hz)	100	30	100
Angular Input Range (°/sec)	±100	-100 to +90	±100

The carrier frequency of the off-resonance driving signal AGC loop is generated by a 4-bit counter whose clock frequency is the oscillation frequency of the AGC loop. The carrier signal input of the modulator can be switched to any output of the 4-bit counter which has a frequency of 1/2, 1/4, 1/8, or 1/16 of the clock frequency. Hence, the proposed AGC loop with HSOGSNW#13-M01 gyroscope, whose resonance frequency is 9676 Hz, is tested for four different carrier signals. Figure 4.40 illustrates the demodulator output of the drive-motor + signal and drive-mode output of the HSOGSNW#13-M01 gyroscope, when the carrier signal has 1/2, 1/4, 1/8 or 1/16 of the oscillation frequency. The frequencies of the driving signals are measured to be 4838.7 Hz, 2419.7 Hz, 12097.5 Hz and 604.9 Hz respectively. Hence, it can be concluded that the proposed AGC loop oscillates the drive-mode at frequency close to the drive-mode resonance frequency even though the driving signals are at 2^{-n} of the oscillation frequency and do not have any frequency component close to the resonance frequency.

The bias drift tests of the angular rate sensing system with the off-resonance driving signal AGC loop with DC amplitude control are also performed for similar operation conditions. However, the full scale factor tests were not performed, since the HSOGSNW#9-L10 stopped functioning properly due to an unknown problem.

Therefore, the exact values of the bias instability and angle random walk could not be measured. However, assuming the scale factor of the system is between the lowest and highest scale factor measured for the previous open-loop angular rate sensing systems, the worst case, and the best case bias instability, and ARW values can be estimated. Table 4.4 gives the estimated performance test results of the proposed system.

Table 4.4: Estimated test results of the open-loop rate sensing system with off-resonance frequency driving signal AGC loop with DC amplitude control for different cases with HSOGSNW#9-L10 gyroscope

	Case 1	Case 2	Case 3
Proof Mass Voltage(V)	15	25	28
Amplitude Set Voltage (mV)	200	350	400
Drive-Mode Displacement (μm)	7.24	7.6	7.76
Best ARW (°/√hr)	0.427	0.035	0.095
Worst ARW (°/√hr)	0.515	0.040	0.118
Best Bias Instability (°/hr)	30.12	4.97	6.32
Worst Bias Instability (°/hr)	37.65	5.72	7.83
Bias Instability (°/hr)	16.56	5.72	8.43

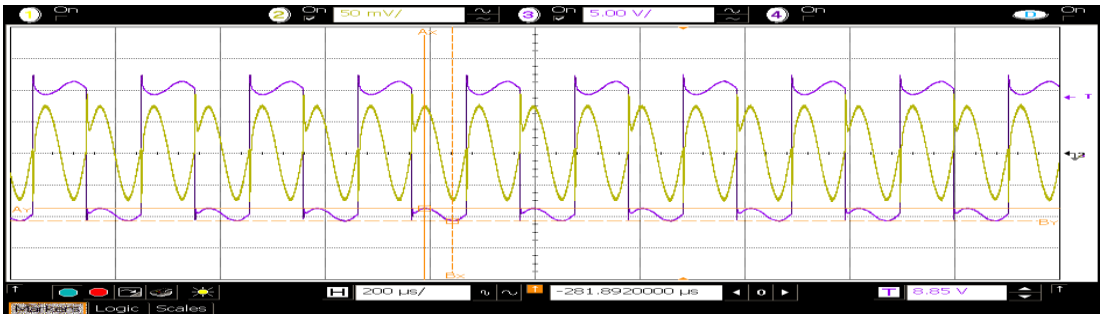

(a)

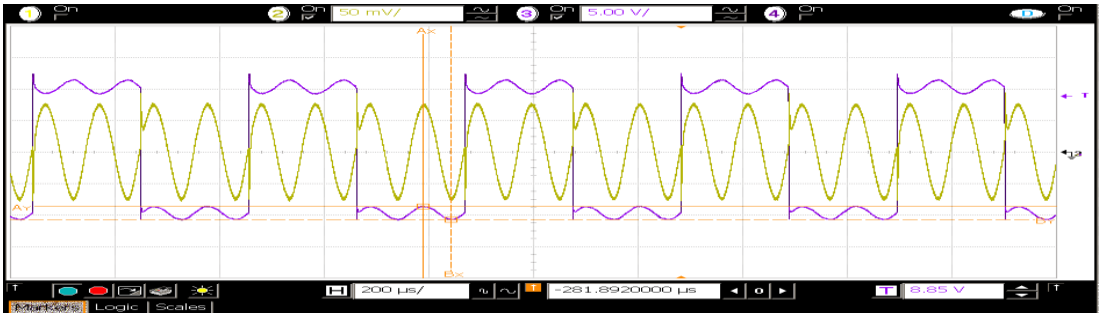

(b)

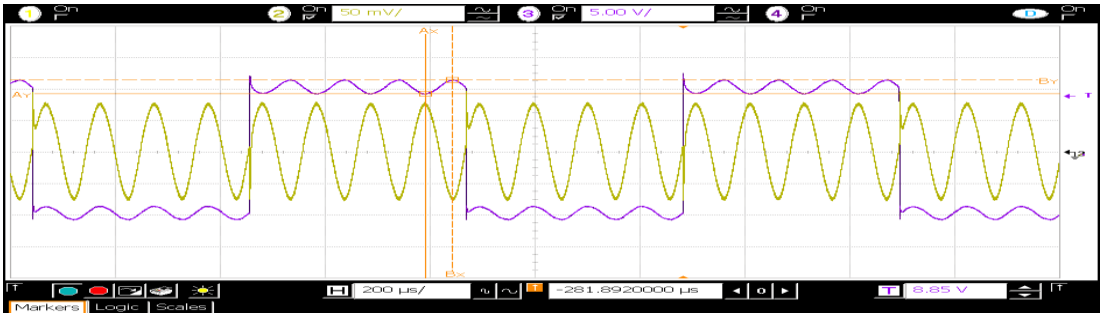

(c)

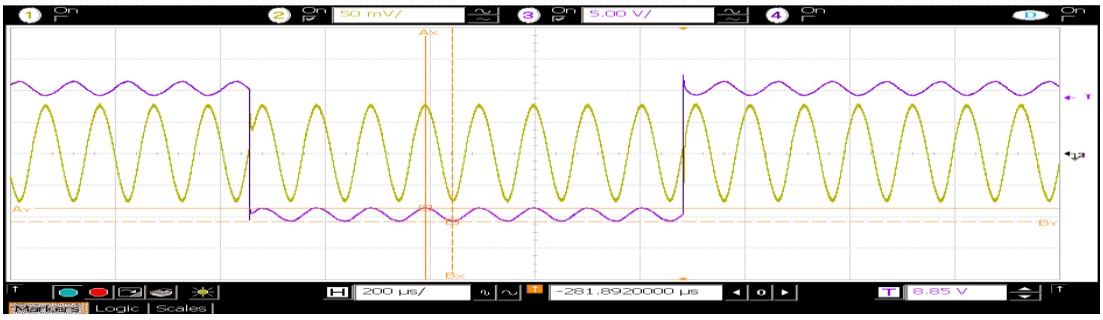

(d)

Figure 4.40: Demodulator output of the (drive-motor +) signal and drive-mode output of the HSOGSNW#13-M01 gyroscope, when the carrier signal has (a) 1/2, (b) 1/4, (c) 1/8 and (d) 1/16 of the oscillation frequency

4.2.5 Test Results of the Closed-Loop Angular Rate Sensing System with Square Wave Driving Signal AGC Loop

The circuit presented in this section is composed of the closed-loop sense-mode electronics and square wave driving signal AGC loop discussed in Section 3.1.2.1, 2.4.2.2.2, and Section 3.2.2. The verification of the drive-mode closed-loop operation is provided in Section 4.2.2. Therefore, this section focuses on the operation of the close-loop sense-mode and gives the test results of the complete angular rate sensing system. The aim of the closed-loop rate sensing is to increase the bandwidth of the rate sensing system and provide an output response less susceptible to the variations of the sense-mode frequency response which are process and ambient condition dependent. Equation 2.74 and 2.76 state that if the open-loop gain of the closed-loop angular rate sensing system is large enough in the vicinity of the mechanical resonance frequency of the drive-mode, the force generated by the voltage applied to the force feedback electrodes is very close to the induced Coriolis force. For this condition, Equation 2.73 defines the applied force feedback voltage, thus gyroscope output, is a function of the drive-mode displacement, proof mass voltage, angular rate input and gyroscope drive-mode and force feedback parameters which are not related to the frequency response of the gyroscope sense-mode. Hence, if the other parameters excluding the angular rate input are kept constant during gyroscope operation, the gyroscope output is a linear function of angular rate input, and closed-loop angular rate sensing is provided. In a closed-loop rate sensing mechnism, the scale factor of the angular rate sensing system should be linearly dependent to the amplitude set voltage and be inversely related to the square of the applied proof mass voltage, since the drive-mode amplitude is inversely proportional to the proof mass voltage and directly proportional to the amplitude set voltage. Consequently, in order to verify the operation of the closed-loop angular rate sensing, either the proof mass voltage or the amplitude set voltage is varied, and the scale factor change is observed. Figure 4.41 shows the PCB view of the proposed closed-loop angular rate sensing system with square-wave driving signal AGC loop. Table 4.5 gives the test results of the angular rate sensing system with HSOGSNW#9-L10 gyroscope for different amplitude set voltages in the

mismatched-mode operation, and when 21 V is applied to the proof mass. In addition, Figure 4.42 illustrates the scale factor versus the amplitude set voltage plot generated by the test data given in Table 4.5. As expected, the scale factor of the closed-loop rate sensing system has a linear relation to the amplitude set voltage, thus the drive-mode displacement with a R^2-nonlinearity error less than 0.0015 %. The offset of the fitted curve to the scale factor versus amplitude set voltage plot is due to the DC offset error of the drive-mode vibration amplitude detection circuit. Besides, it is observed that the zero rate output of the closed-loop system increases as the amplitude set voltage increases, since the quadrature error is directly proportional to the drive-mode displacement and the closed-loop system drives the sense-mode to null the DC level of the output signal at the demodulator of the sense-mode.

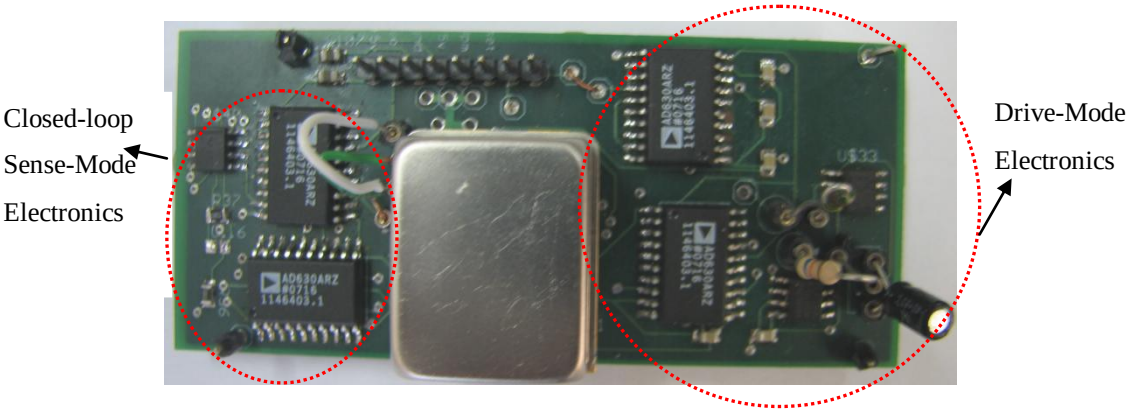

Figure 4.41: General view of the PCB of the closed-loop angular rate sensing system with square wqave driving signal AGC loop

Table 4.5: Test results of the closed-loop angular rate sensing system with HSOGSNW#9-L10 gyroscope for different amplitude set voltages when 21 V is applied to the proof mass

V_{set} (mV)	Scale Factor (mV)	R^2-Nonlinearity (%)	Zero-Rate Output (mV)
50	0.333	$4x10^{-4}$	-3.99
100	0.752	$1x10^{-4}$	-9.30
150	1.180	$2x10^{-4}$	-14.59
200	1.604	$1x10^{-4}$	-19.73
250	2.021	$3x10^{-4}$	-24.72
300	2.441	$3x10^{-4}$	-30.16

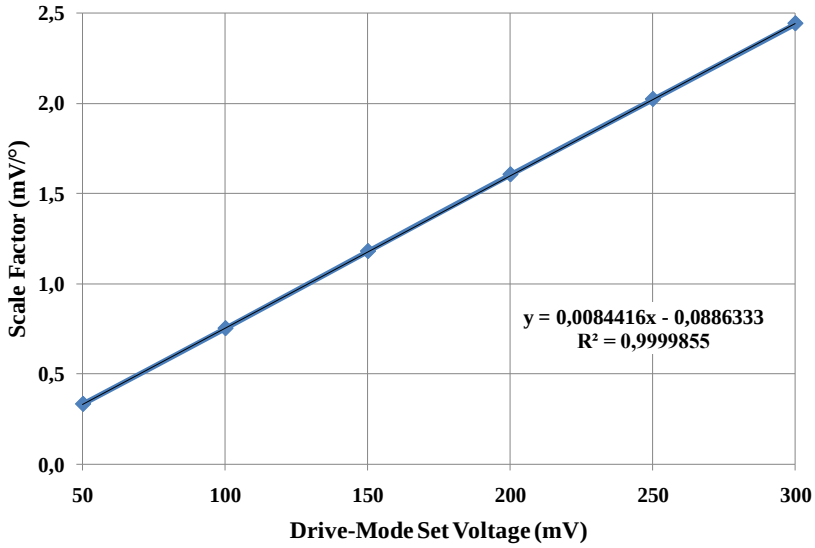

Figure 4.42: Scale factor versus drive-mode amplitude set voltage plot generated by the test data given in Table 4.4

The scale factor test of the closed-loop angular rate sensing system is also performed for different proof mass voltages while the amplitude set voltage is constant at 200 mV. When the set voltage is kept constant, the scale factor is expected to be inversely proportional to the square of the applied proof mass voltage for proper closed loop rate sensing. It should be noted that the closed-loop angular rate sensing system is designed for mismatched-mode operation and assuming the drive-mode resonance frequency is smaller than the sense-mode resonance frequency. Therefore, the proposed circuit cannot operate properly for matched-mode and nearly matched-mode conditions, i.e., between 23 V and 24 V for HSOGSNW#9-L10. As the system approaches the matched-mode the phase difference of the angular rate output and drive-mode output becomes around 90°, hence the phase sensitive demodulator cannot obtain the angular rate input and it requires addition phase shifter for proper operation. Moreover, if the proof mass voltage is increased sufficient enough to alter the sense-mode resonance frequency to be less than drive-mode resonance frequency, i.e., 23.5 V for HSOGSNW#9-L10, the phase shift between the voltage applied to the force feedback electrode (+) and sense-mode output changes 180 ° to 0 ° for the mismatched-mode, that makes the closed-loop rate sensing system be astable. Hence, during the tests, the signals applied to the force feedback electrodes are

swapped to provide stable closed-loop rate sensing for the proof mass voltages larger than 23.5 V. As a result, the polarity of the scale factor is reversed when the applied signals are swapped, since the phase of the induced Coriolis force is not affected by the phase change in the sense-mode response. Table 4.6 shows the scale factor test results for various proof mass voltages, and Figure 4.43 illustrates the plot generated by the test data in Table 4.5. In this plot, the absolute value of the scale factors is used. Then, the plotted data is fitted to a power curve, and the scale factor is calculated to be inversely proportional with the proof mass voltage to the power of 2.118. The obtained result is slightly different from the theoretical calculations since for low proof mass voltages, the 200 mV amplitude set voltage generates a large drive-mode displacement that increases the nonlinearity in the drive-mode, degrading the linear relationship between proof mass voltage and displacement. Thus, if the plot is generated for the conditions for which the proof mass voltage is larger than 19 V, the scale factor becomes related to the power of 2.013, representing closer value to the theoretical calculations. Hereby, the scale factor tests performed for the cases when one of the amplitude set voltage and proof mass voltage is varied and the other is kept constant verify, that in mismatched-mode operation the proposed closed-loop angular rate sensing system provides the gyroscope output in a value which is independent of the frequency response characteristics of the sense-mode.

Table 4.6: Test results of the closed-loop angular rate sensing system with HSOGSNW#9-L10 gyroscope for different proof mass voltages when the amplitude of the drive-mode is set to 200 mV

V_{PM} (V)	Scale Factor (mV)	R^2-Nonlinearity (%)	Zero-Rate Output (mV)
15	3.338	$4x10^{-4}$	-52.58
17	2.548	$2x10^{-4}$	-34.65
19	1.993	$1x10^{-4}$	-24.41
21	1.604	$1x10^{-4}$	-19.73
25	-1.134	$1x10^{-4}$	-7.542
28	-0.897	$2x10^{-4}$	-4.264

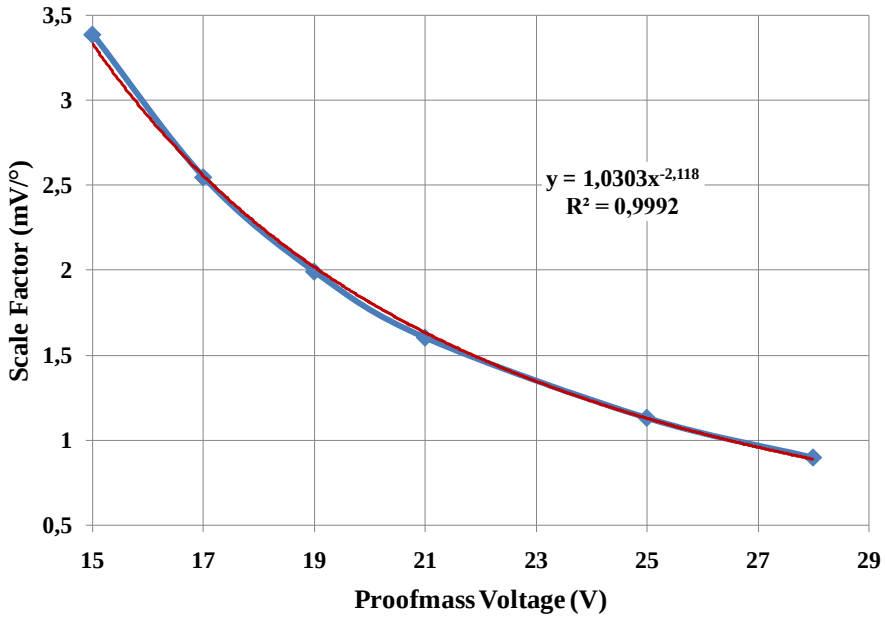

Figure 4.43: Scale factor versus proof mass voltage plot generated by the test data given in Table 4.5

After it is verified that the proposed system provides closed-loop angular rate sensing in the mismatched operation, the performance tests are performed for the proposed system by adjusting the similar operation cases for which the previous open-loop angular rate sensing systems are tested. Figure 4.44 shows the scale factor test result of the closed-loop angular rate sensing system when 25 V is applied to the proof mass and the amplitude set voltage is adjusted to 350 mV, and Figure 4.45 gives the gyroscope output versus angular rate input characteristics generated by the data obtained in the scale factor test. The scale factor of the closed loop angular rate sensing system is found to be 1.98 mV/(°/sec) with 0.01 % R^2 nonlinearity in the ±100 °/sec measurement range. After the scale factor test, the bias drift data of the system is collected. Figure 4.46illustrates the bias change of the gyroscope output in 160 minutes time interval. The bias change in time is measured to be similar to the previous tests performed with the open-loop angular rate systems. Meanwhile, in the long term, the change in bias is lower than 0.4 mV that is less compared to the measured value in previous tests, although the bias change is mentioned to be related to the sense-mode electronics in Section 4.2.2. The main reason of this difference is that the gain of LPF (low pass filter) used in the open-loop rate sensing system is 20, whereas the gain of the closed-loop rate sensing is 2. Hence, the bias change in the

open-loop rate sensing system is amplified more. The collected bias data is processed to generate the Allan Variance plot of the close-loop angular rate sensing system. Figure 4.47 presents the generated Allan Variance plot. The bias instability is measured to be 5.42 °/hr with an ARW of 0.057 °/√hr. It should be noted here that the bandwidth of the system cannot be determined easily, like in open-loop angular rate sensing system, and it should be measured using a rate table setup. This test has not been done yet.

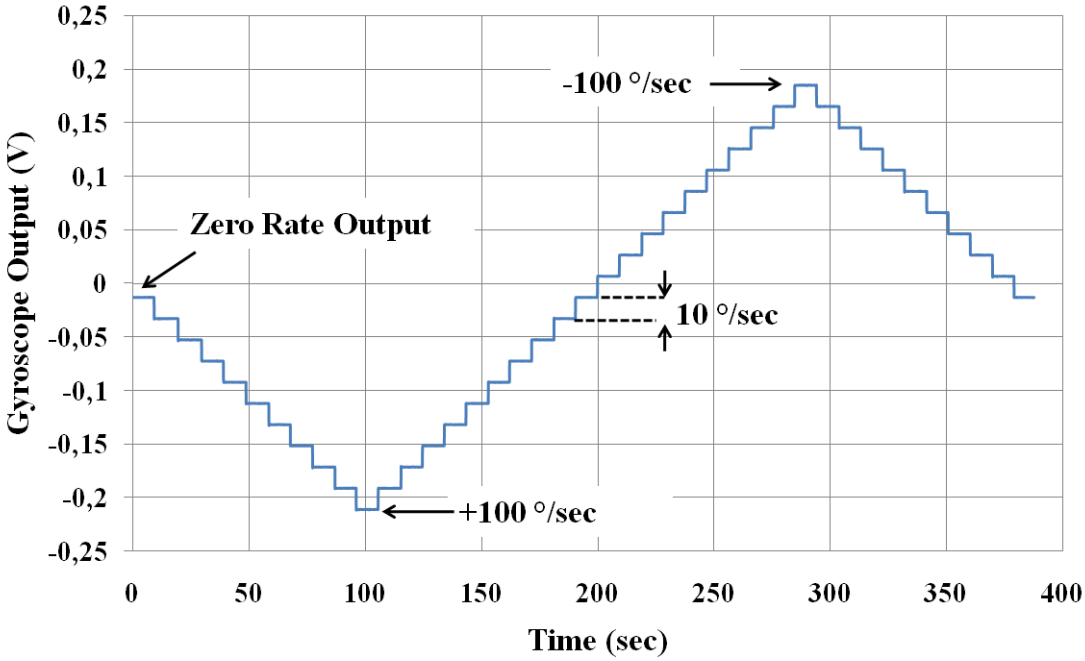

Figure 4.44: Scale factor test result of the closed-loop angular rate sensing system with square wave frequency driving signal AGC loop when 25 V is applied to the proof mass and the set voltage is adjusted to 350 mV

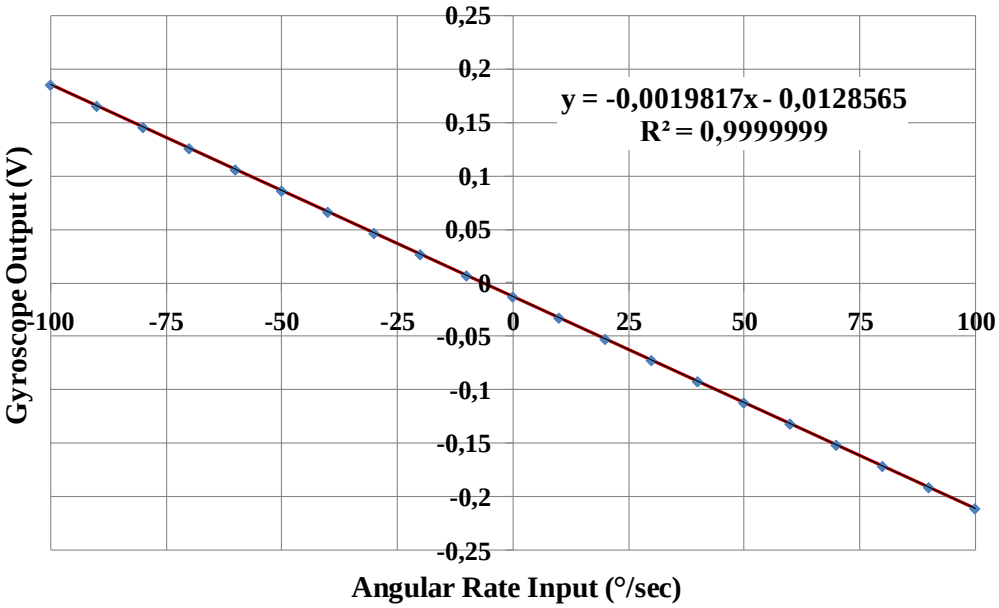

Figure 4.45: Gyroscope output versus angular rate input characteristics to determine the scale factor, scale factor nonlinearity, and zero-rate output of the gyroscope

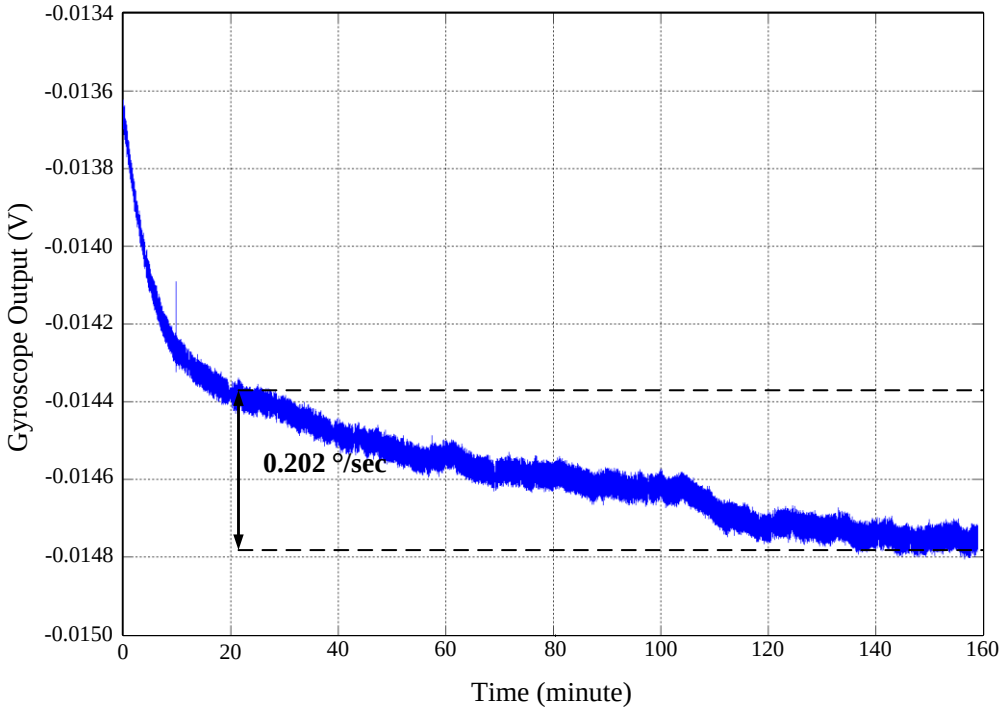

Figure 4.46: Bias drift data collected from the closed-loop angular rate sensing system after the system starts-up when 25 V is applied to the proof mass

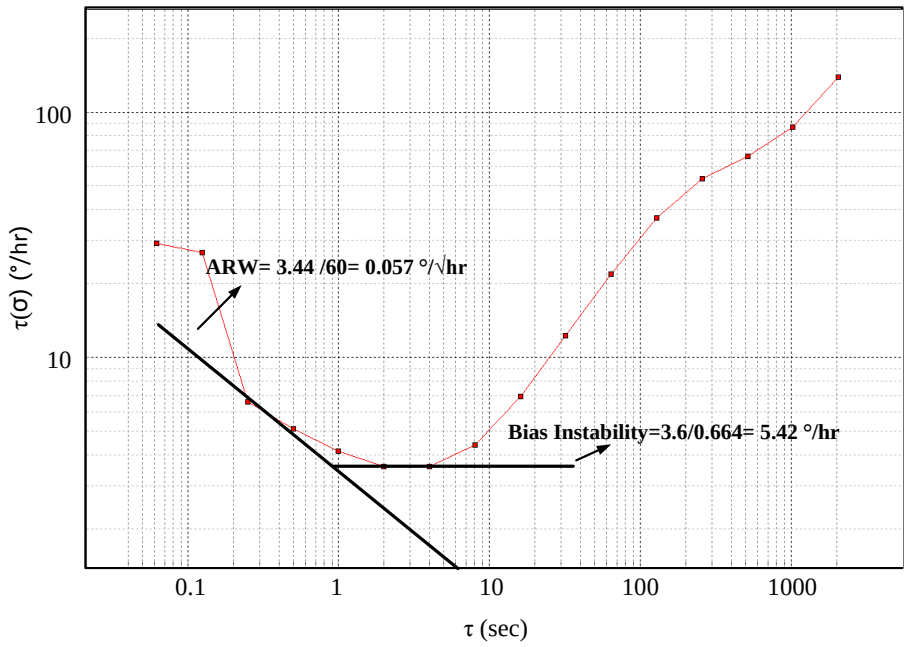

Figure 4.47: Allan Variance Plot generated by the drift data given in Figure 4.42

Figure 4.48, Figure 4.49, and Figure 4.50 give Allan Variance plots generated by the drift data collected for cases which 15 V, 21 V, and 28 V are applied to the proof mass and the amplitude set voltage is adjusted to 200 mV, 250 mV and 400 mV respectively. In addition, summarizes the all results of the scale factor and bias drift tests. The bias instabilities and ARWs of the all cases exhibits tactical-grade level performance. Different from the previous tests, the mechanical bandwidth of the closed-loop systems cannot be estimated by the sense-mode frequency response, since the system bandwidth is determined by the PI controller and the sense-mode parameters in the closed-loop system, as described in Section 3.2.2. The proportional and integral gains are designed as 0.25 and 100 in order to provide 20 Hz sense-mode bandwidth theoretically when the applied proof mass voltage to HSOGSNW#9-L10 gyroscope is 25 V. It should be noted that bandwidths of the closed-loop angular system for other cases are narrower as open-loop gains of these systems are less than the case when 25 V is applied to the proof mass. To increase the integral gain is an option in order to widen the bandwidth by increasing the open-loop gain. However, the high integral gain may be impractical to be implemented, i.e., 100 Hz bandwidth requires 2500 integral gain, and hence the gain of the other

stages in the closed-loop system should also be increased to implement the closed-loop angular rate sensing system with reasonable integral parameter.

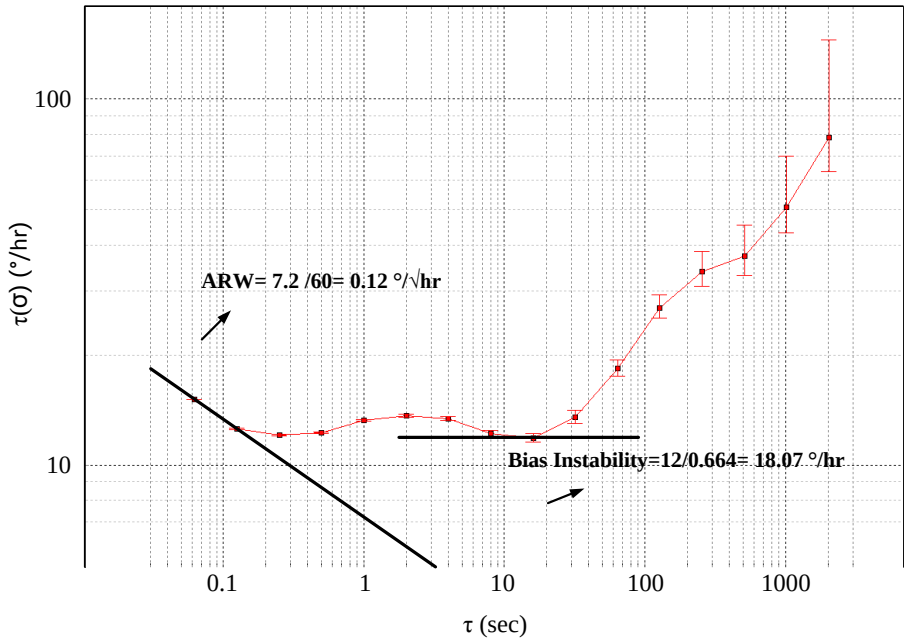

Figure 4.48: Allan Variance plot generated by collected bias drift data of closed-loop angular rate sensing system with square wave driving signal AGC loop when 15 V is applied to the proof mass and the amplitude set voltage is adjusted to 200 mV

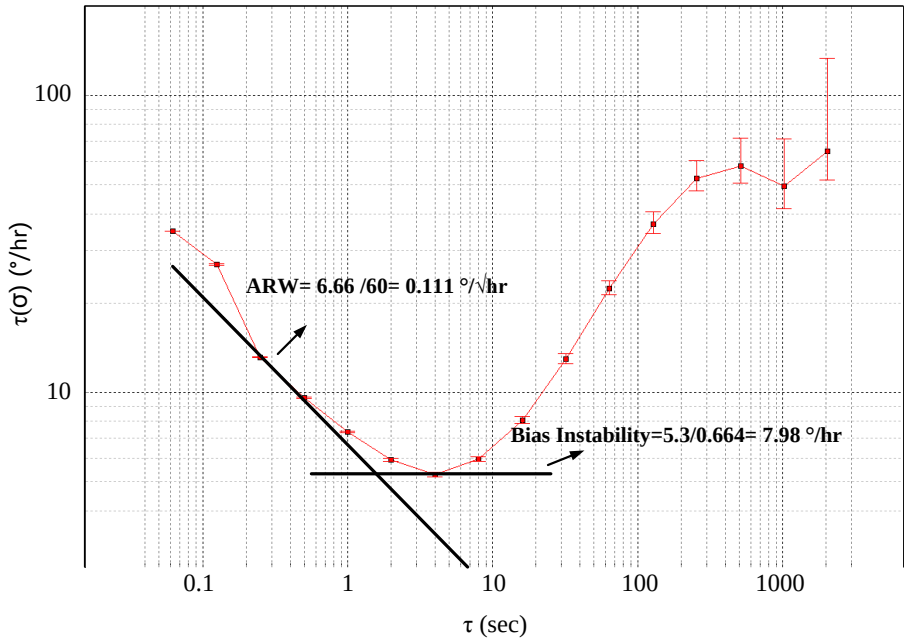

Figure 4.49: Allan Variance plot generated by collected bias drift data of closed-loop angular rate sensing system with square wave driving signal AGC loop when 21 V is applied to the proof mass and the amplitude set voltage is adjusted to 250 mV

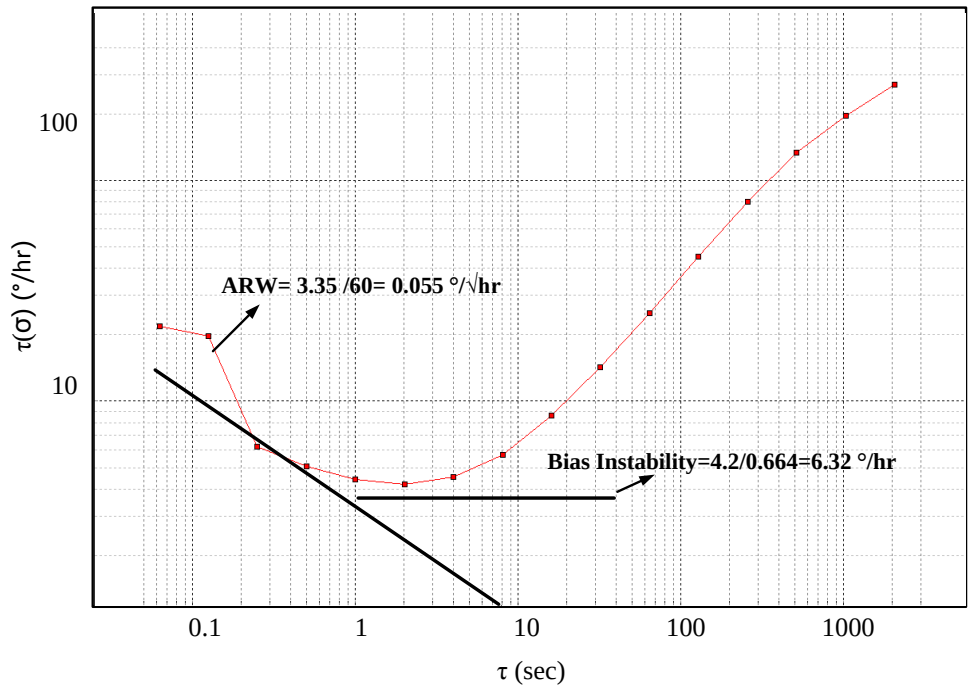

Figure 4.50: Allan Variance plot generated by collected bias drift data of closed-loop angular rate sensing system with square wave driving signal AGC loop when 28 V is applied to the proof mass and the amplitude set voltage is adjusted to 400 mV

Table 4.7: Performance test results of the closed-loop rate sensing system with square wave driving signal AGC loop for different cases

	Case 1	Case 2	Case 3	Case 4
Proof Mass Voltage(V)	15	21	25	28
Amplitude Set Voltage (mV)	200	250	350	400
Drive-Mode Displacement (μm)	7.24	6.4	7.6	7.76
Scale Factor (mV/°/sec)	3.388	2.02	-1.98	-1.79
R^2-Nonlinearity (%)	$4x10^{-4}$	$3x10^{-4}$	$1x10^{-4}$	$2x10^{-4}$
Zero-Rate Output (mV)	-52.58	-24.7	-12.85	-8.61
ARW (°/√hr)	0.120	0.111	0.057	0.055
Bias Instability (°/hr)	18.07	7.98	5.42	6.32
Angular Input Range (°/sec)	±100	±100	±100	±100

4.3 Summary of the Tests

This chapter presented the test results performed with four different angular rate sensing systems: 1) open-loop angular rate sensing system with the square wave driving signal AGC loop named as OLS_SquD, 2) open-loop angular rate sensing system with the sinusoidal wave driving signal AGC loop named as OLS_SineD 3) open-loop angular rate sensing system with the off-resonance frequency driving signal AGC loop OLS_OffD and 4) closed-loop angular rate sensing system with the square wave driving signal AGC loop named as CLS_SquD. It is verified that the drive-mode of the gyroscope can be oscillated with applying different signals and the amplitude of the oscillation can be controlled by different AGC loop approaches. In addition, it is shown that the closed-loop angular rate sensing system response is not dependent to the sense-mode frequency response characteristics thus lessens the dependency of the gyroscope output response to the process variation. Moreover, performance tests of the three open-loop angular rate sensing systems with HSOGSNW#9-L10 hermetically sealed SOG gyroscope were performed for three different proof mass voltages: (i) 15 V, (ii) 25 V, and (iii) 28 V. In addition, the amplitude set voltages are adjusted to 200 mV, 350 m V, and 400 mV, respectively, in order to provide similar drive-mode displacement. 15 V and 28 V proof mass voltages provide 100 Hz mechanical bandwidth, which is the requirement of tactical-grade applications; hence the performance tests of the open-loop angular rate sensing are performed in order to determine whether the performance of proposed systems satisfy the tactical grade-application requirements. On the other hand, for 25 V proof mass voltage, the mechanical structure has 30 Hz bandwidth with a larger mechanical gain, since the system is closer to the matched-mode operation. Therefore, when the test results of case (i) and case (iii) are compared, the effect of approaching to the matched-mode operation on system performance is investigated. As three test conditions have similar drive-mode displacement, their expected rate equivalent Brownian noise is same [61], hence the electrical noise of the angular rate sensing system is detected by comparing the test results, and the source of the noise is investigated. In addition, the test results provide data to compare the effect of the drive-mode driving approach on system performance. Similarly, the closed-loop

angular rate sensing system with the square wave driving signal AGC loop is tested for the same three conditions, and the results compared to the open-loop angular rate sensing system with square wave driving signal AGC loop in order to determine the effect of closed-loop rate sensing system on the system performance.

Table 4.8, Table 4.9, and Table 4.10 gives the measured and calculated tests results of four different angular rate systems for three operation conditions respectively. All angular rate sensing systems exhibits tactical-grade level performance for operation conditions 2 and 3 when their bias instabilities and ARWs are considered. Besides, for condition 3, the open-loop angular rate sensing systems provide bandwidth requirements of tactical-grade level. In addition, the angular rate sensing systems have quite linear relationship between the angular rate input and the gyroscope output. Hereby, the proposed angular rate sensing systems give promising results although they are implemented with commercial discrete components.

Table 4.8: Performance test results of the angular rate sensing systems with HSOGSNW#9-L10 hermetically sealed SOG gyroscope package when 15 V is applied to the proof mass and the amplitude set voltage is adjusted to 200 mV

Angular Rate Sensing System	OLS_SquD	OLS_SineD	OLS_OffD	CLS_SquD
Scale Factor (mV/°/sec)	9.86	8.47	8.17	3.388
R^2-Nonlinearity (%)	$3x10^{-4}$	$1.8x10^{-4}$	$1x10^{-4}$	$4x10^{-4}$
Zero-Rate Output (mV)	-10.75	-110.5	-81.6	-52.58
ARW (°/√hr)	0.142	0.277	0.274	0.120
Bias Instability (°/hr)	10.54	36.1	16.56	18.07
Angular Input Range (°/sec)	±100	±100	±100	±100
Mechanical Bandwidth (Hz)	100	100	100	-

Table 4.9: Performance test results of the angular rate sensing systems with HSOGSNW#9-L10 hermetically sealed SOG gyroscope package when 25 V is applied to the proof mass and the amplitude set voltage is adjusted to 350 mV

Angular Rate Sensing System	OLS_SquD	OLS_SineD	OLS_OffD	CLS_SquD
Scale Factor (mV/°/sec)	-49.8	-43.24	-47.26	-1.98
R^2-Nonlinearity (%)	$0.4x10^{-4}$	$4.3x10^{-3}$	$6.2x10^{-3}$	$1x10^{-4}$
Zero-Rate Output (mV)	-322.2	-354.2	-327.5	-12.85
ARW (°/√hr)	< 0.017	0.030	0.046	0.057
Bias Instability (°/hr)	5.12	4.51	5.72	5.42
Angular Input Range (°/sec)	100	-100 to +80	-100 to +90	±100
Mechanical Bandwidth (Hz)	30	30	30	-

Table 4.10: Performance test results of the angular rate sensing systems with HSOGSNW#9-L10 hermetically sealed SOG gyroscope package when 28 V is applied to the proof mass and the amplitude set voltage is adjusted to 400 mV

Angular Rate Sensing System	OLS_SquD	OLS_SineD	OLS_OffD	CLS_SquD
Scale Factor (mV/°/sec)	-22.6	-17.97	-20.97	-1.79
R^2-Nonlinearity (%)	$1x10^{-4}$	$3x10^{-4}$	$1x10^{-4}$	$2x10^{-4}$
Zero-Rate Output (mV)	-56.15	-100.4	-101.2	-8.61
ARW (°/√hr)	0.080	0.049	0.086	0.055
Bias Instability (°/hr)	4.67	6.92	8.43	6.32
Angular Input Range (°/sec)	±100	±100	±100	±100
Mechanical Bandwidth (Hz)	100	100	100	-

When the ARWs of the open-loop rate sensing systems are investigated, it is observed that the increase in the scale factor decreases the ARW of the system. Since the scale factor tests are performed for nearly same drive-mode displacement, the angular rate equivalent Brownian noise of the mechanical structure is approximately similar. Hence, the dominant source of measured ARW, thus white noise, is electrical. Moreover, when the output referred current noise is calculated for the given transimpedance interface values in Section 3.1, it is theoretically found as 22.76 μV/√Hz for the open loop rate sensing system. If the rate equivalent output

referred noise is calculated, the measured resolution values are very close to the theoretical calculations. Hence, the interface electronics dominates the output referred voltage noise of the angular rate sensing system. Since the interface noise is mainly contributed by the current noise of the interface opamp, replacing the opamp with components having a lower current noise will improve the ARW of the system. While the bias instabilities are compared in same manner, the similar relationship is observed between scale factors and the bias instabilities in operation conditions (i) and (iii). However, in condition (ii), the bias instability improvement is not parallel to increase in the scale factor, even for the angular rate sensing system with the square-wave driving signal, AGC loop the bias instability in condition (iii) is larger than the bias instability in condition (ii). Thus, it can be concluded that the bias instability of the angular rate system can be improved by using low-drift electrical components and that the stability of the mechanical structure degrades as the system approaches to matched-mode. Since the bias stability performance of the tested angular rate systems is not limited by the mechanical structure for operation conditions, the scale factor of the system increases as the system approaches to the matched-mode operation, and the bias instability, which is mainly due to the electrical components, decreases.

Another important result, which the performance tests reveal, is that the closed-loop angular rate sensing doesn't improve the bias instability of the angular rate sensing system in the mismatched-mode operation. Moreover, as discussed in Section 2.4.2.2.2, the closed-loop rate sensing doesn't affect the noise performance of the angular rate sensing system, hence the ARWs of the closed-loop rate sensing system and the open-loop rate sensing system with the square-wave driving signal AGC loop should be close to each other since same interface electronics and discrete components are employed. As expected, the ARWs of these systems are measured to differ less than 0.04 $^\circ/\sqrt{hr}$, and this difference is mainly due to imperfection in the test setup conditions.

The test results also show that neither of the proposed AGC loops have significant superiority compared to the others in performance aspects. However, the controller design of square wave driving signal AGC loop is the easiest. In addition, the

simulation and test results are very close to the hand calculations. On the other hand, although the test results of the proposed controller design for the sinusoidal wave driving signal and the off-resonance frequency driving signal AGC loops show similar characteristics to the simulations, their design is more complicated and should be improved for more accurate controllability. Besides, the square wave and sinusoidal wave driving signal AGC loops start self-oscillation after the power up whereas the off-resonance frequency driving signal AGC loop requires triggering to start the oscillation.

In conclusion, four different open-loop angular rate sensing systems and one closed-loop rate sensing system designed in this research are successfully implemented and their performance tests are performed with the double-mass micromachined SOG vibratory gyroscopes developed at METU. It is the first time at METU that the double-mass micromachined SOG gyroscopes developed at METU are tested and the closed-loop angular rate sensing is implemented. The performance results are the best results obtained at METU, satisfying the tactical-grade performances. Table 4.11 gives the best results in the literature and in this work, and it can be concluded that the measured results in this work are comparable to the best results in literature for silicon micromachined vibratory gyroscopes.

Table 4.11: Best performance results in literature and in this work

	ARW (°/√hr)	Bias Instability (°/hr)	Bandwidth (Hz)	Full Scale Range (°/sec)	System
Tactical-grade	0.5-0.05	0.1-10	100	>500	-
Georgia I.T.	0.003	0.1	1	20	OL
Bosch Sensortec	0.147	3-8	60	187	CL
Litef Gmbh	0.200	2-5	~500	1000	CL
Sensonor AS	0.180	3.2	-	10	CL
OLS_SquD	0.080	4.7	100	>100	OL
OLS_SineD	0.030	4.5	30	80	OL
CLS_SquD	0.057	5.4	-	>100	CL

CHAPTER 5

CONCLUSIONS AND FUTURE WORK

The research presented in this thesis includes the development of the readout and control electronics for realizing high performance angular rate sensing systems employing double-mass SOG (Silicon-on-Glass) vibratory gyroscopes developed at METU. High performance readout and control electronics developed in this thesis involves the transresistance and transimpadence type interfaces, four different AGC (automatics gain control) loops for self-triggered sustained oscillation in the drive-mode, and open-loop and closed-loop angular rate sensing mechanisms. Firstly, the SOG vibratory gyroscopes with interfaces are characterized and mathematically modeled for the controller parameter calculations and the system-level simulations. Then, the designed circuits are implemented with commercial discrete components on PCBs (printed circuit boards). The functionality of the proposed AGC loops and controller design approaches are verified by monitoring the drive-motor and output signals and the change of the drive-output signal after power-up. Finally, the performances of the complete open-loop and closed-loop angular rate systems are evaluated in terms of scale factor, scale factor linearity, zero-rate output, angle random walk, and bias instability.

Based on the results of this study, following conclusions can be made:

1. The transduction mechanism of the capacitive actuators used in the gyroscope drive-mode is investigated and the force generated by the capacitive actuators is analyzed when different waveforms are applied. It is shown that when either a sinusoidal or a square wave signal with a DC offset at resonance frequency is applied to the capacitive actuators; the generated time-varying force has a harmonic part at resonance frequency. Moreover, it is verified

that if a particular off-resonance frequency, which has no frequency component at the resonance frequency, is applied to the capacitive actuators, the applied signal generated an electrostatic force similar to the force generate by a sinusoidal signal at resonance frequency with DC offset. Thus the generated force has a harmonic at the resonance frequency although the applied signal does not have any electrical component at the resonance frequency. The off-resonance frequency signal is generated by modulating a sinusoidal signal at the resonance frequency with a DC offset by a carrier frequency at 2^{-n} of the resonance frequency where n is positive integer. Finally, the all transduction mechanisms and mechanical dynamics of the gyroscopes are analyzed, and the gyroscopes are mathematically modeled as second order systems for different actuating signals in order to use the models in the system-level simulations of the proposed circuits.

2. Transresistance and transimpedance type interfaces are analyzed in terms of their noise performance, stability, phase error, and parasitic capacitance effects, and they are implemented with discrete components. The analysis gives that these interface types reduces the phase error due to the parasitic capacitance between the high impedance node of the gyroscope and ground level. Moreover, it is shown that the minimum detectable signal level from the gyroscope can be improved by having an opamp with low current and voltage noises and by decreasing the parasitic capacitance at high impedance node of the gyroscope and the stationary capacitance of sensing mechanism should be decreased. Parasitic capacitances are decreased by placing the interfaces and the mechanical structure very close on a one-sided PCB-like glass substrate which has thin gold routes. Furthermore, high impedance in the feedback path of the opamp decreases the input referred noise of the interface. However, high resistance in the transresistance amplifier introduces a zero which leads stability problem; hence, a capacitor whose value is equal to the input capacitance of the opamp should be connected parallel to the resistor for compensation. In addition, the feedback capacitor of the transimpedance amplifier cannot bias the output of the interface to a

DC level, thus a resistor should be connected parallel to the capacitor to bias the interface output. Hereby, the same topology is used to implement the transresistance and transimpedance amplifiers, and the interface is determined by the equivalent impedance. In the drive-mode, transresistance amplifier providing -180˚ phase difference between the induced current and interface output is used, since the phase differences between the drive-motor electrodes and drive-mode interface become integer multiple of 180˚ at resonance frequency, and the self-oscillation loop of the drive-mode can be constructed by introducing just a controllable gain stage in order to satisfy the Barkhausen criteria. In the sense-mode, the transimpedance amplifier, which should provide 90˚ phase difference between the induced current and interface output, is employed. As in the mismatched operation, the sense-mode output is in-phase with the drive-mode output, and the phase sensitive demodulation of the sense-mode output is achieved without using any phase shifter. After determining the interface types, the optimum resistor and capacitor values are chosen to provide low noise and small phase error at the interface outputs.

3. Four different self-oscillation loops with automatic amplitude controls are developed for double-mass SOG gyroscopes. All loops are designed to satisfy the phase and gain conditions of the oscillation criteria, and they generate differential driving signals by processing the single-ended output of the drive-mode. The first oscillation loop controls the driving signal amplitude which is a square-wave signal at the oscillation frequency, whereas the second loop controls the gain of a VGA (variable gain amplifier) which amplifies the drive-mode output to produce the sinusoidal-wave driving signals. The last two loops employ the off-resonance frequency signal to oscillate the drive-mode at resonance. One of these two loops controls the amplitude of the sinusoidal signal to be modulated with a VGA, and the other adjusts the DC offset of the sinusoidal signal for proper operation. The linearized models of the all loops are constructed. Besides, the controller parameters design approaches enabling the estimation and control of the closed-loop system dynamics after start-up are discussed for all designed

loops. The theoretical analysis is verified by the system-level simulations performed in SIMULINK.

4. Together with the drive-mode self-oscillation control loops and the sense-mode demodulation circuitry, the open-loop angular rate sensing systems are constructed on PCBs with discrete components. According to the test results, all proposed self-oscillation loops provide sustained constant amplitude oscillations at a frequency close to the resonance frequency of the drive-mode, which are consistent with the simulation results. Then, a series of tests are performed for three main operation conditions in order to determine the scale factor, scale factor linearity, zero-rate offset, angle random walk, and bias instability of the proposed open-loop angular rate sensing systems. First, 15 V is applied to the proof mass, and the amplitude set voltage of the drive-mode is adjusted to 200 mV to achieve mechanical bandwidth around 100 Hz, then the proof mass is increased to 25 V which decrease the bandwidth around 30 Hz and the amplitude set voltage is increased to 350 mV to satisfy same drive-mode displacement amplitude. Finally, all systems are tested for 28 V proofmass voltage and 400 mV amplitude set voltage, where the mechanical bandwidth is around 100 Hz. The open-loop rate sensing system with the square-wave driving signal AGC loop demonstrates bias instabilities of 10.54 ˚/hr, 5.12 ˚/hr, and 4.67 ˚/hr and angle random walks of 0.142˚/√hr, 0.017˚/√hr, and 0.080˚/√hr for three different operation conditions, respectively. The performance tests with the open-loop rate sensing system with the sinusoidal wave driving signal AGC loop shows that the system has bias instabilities of 36.1˚/hr, 4.51˚/hr, and 6.92˚/hr with 0.277˚/√hr, 0.030˚/√hr, and 0.049˚/√hr angle random walks. Further measurements show that the open-loop angular rate sensing system with off-resonance frequency has bias instabilities of 16.56˚/hr, 5.72˚/hr, and 8.43˚/hr and angle random walks of 0.274˚/√hr, 0.046˚/√hr, and 0.086˚/√hr, respectively. Moreover, the R^2 nonlinearity of the scale factor is calculated to be less than 0.43% for all angular rate sensing systems in the angular rate input range of -100˚/sec and +80˚/sec. The angular rate input is limited by supply voltages in some test

conditions. The test results show that the proposed angular rate sensing systems demonstrates tactical-grade level performance in terms of scale factor linearity, bias instability, and angle random walk for second and third operation conditions. Besides, the systems provide 100 Hz bandwidth required for tactical-grade applications for third operation condition. It is concluded that any angular rate sensing system doesn't have superiority among others. But further tests need to be performed to verify that the performance is not limited by the measurement set up. Furthermore, it is measured that the electrical noise is dominant on the system performance, and the most of the electrical noise is generated by the transimpedance interface, especially the current noise of the used opamp. As a result, the performance of the systems can be improved by improving the test setup and using discrete components having lower noise and with low bias drift.

5. Closed-loop rate sensing is designed and implemented on a PCB together with the square wave driving signal AGC loop. The closed-loop angular rate sensing system is tested for the mismatched condition, and it is verified that the system provides gyroscope output voltages independent of the frequency response of the sense-mode, that provide robustness against temperature and ambient vacuum level changes. Furthermore, the gyroscope output is linearly proportional to the applied angular rate input. The system is tested for same operation conditions described above. The bias instabilities are measured as 18.07˚/hr, 5.42˚/hr, and 6.32˚/hr with angle random walks of 0.120˚/√hr, 0.057˚/√hr, and 0.055˚/√hr, respectively. The scale factor has R^2 linearity less than 0.04 % in ±100 ˚/sec measurement for all test conditions. Theoretical calculations imply that the closed-loop rate sensing doesn't affect the contribution of electrical components on noise and bias instability performance of the overall system. Provided that the noise and bias instability of the systems are dominated by electrical components, the measured performance values of the closed loop system should be close to the open-loop rate sensing system with the square wave driving AGC loop. The test results demonstrate that the two systems have close performance values

with little difference, and the discrepancies are mainly due to the setup conditions. It should be noted here that the bandwidth is expected but this could not be shown due to the limitations of the test set up.

Although major research objectives are accomplished by realizing high performance open-loop and closed-loop angular rate sensing systems, there is still need for further research for improving the performance of MEMS gyroscopes developed at METU. Some of the possible future research issues can be listed as follows:

1. Although the proposed angular rate systems demonstrate impressive performance, the test results reveal that the angular rate sensing systems should be implemented with electrical components having less noise and low bias drift, especially using opamps having lower current noise in order to improve the performance further.

2. Throughout the tests performed with different double-mass SOG gyroscopes, it is observed that the performance of the angular rate system degrades as the quadrature error and the frequency difference between the sense-mode resonance frequencies of the double masses increase due to the process imperfection. Hence, the effects of these errors should be analyzed in detail, and the process of the double-mass gyroscopes should be improved to minimize these errors.

3. The quadrature cancellation loops should be integrated to the closed-loop angular rate sensing systems. It is shown that the performance of the rate sensing systems will improve as the system gets closer to the matched-mode operation, thus the closed-loop angular rate sensing system should be designed and implemented for the matched-mode operation. In addition, control loops adjusting proof mass voltage providing the matched-mode operation should be researched.

4. For future research, the monolithic gyroscope should be developed by implementing CMOS interfaces and control electronics integrated with the

mechanical structure on a single chip. The monolithic solution will improve the performance of the rate sensing system since the parasitics due to interconnections are eliminated.

5. The control electronics designs with analog electronics for self-oscillation in the drive-mode, closed-loop rate sensing, mode-matching and quadrature cancellation are fixed and limited. Therefore, the future research should consider the digitally controlled and digital output gyroscopes to implement new algorithms and parameter optimizations. These gyroscopes can be realized by using high resolution ΣΔ-modulated A/D converters, which have been designed and used for MEMS accelerometers developed at METU.

In conclusion, the major achievement of this research is the development of high performance readout and control electronics for MEMS gyroscopes developed at METU. The double-mass SOG gyroscopes are tested in a fully-functional angular rate sensing system for the first time, and the designed open-loop and closed-loop angular rate sensing systems demonstrates performance satisfying the requirements of the tactical-grade applications. It is believed that the theoretical background and test results provided in this study would be helpful to the development of even higher performance MEMS gyroscopes for military and industrial applications.

REFERENCES

[1] T. Lee, "The Design of CMOS Radio-Frequency Integrated Circuits," Cambridge University Press, 1998.

[2] N. Yazdi, F. Ayazi, and K. Nacafi, "Micromachined Inertial Sensors," *Proc. of the IEEE*, Vol. 86, No.8 , pp. 1640-1659, August 1998.

[3] J. Marek, "Microsystems for Automotive Applications," *Proc. 13th Eur. Conf. Solid State Transducers (Eurosesnsors XIII)*, pp. 1-8, Hague, Netherlands, September 1999.

[4] H. Kuisma, "Inertial Sensors for Automotive Applications," *Tech. Dig. 11th Int. Conf. Solid-State Sensors and Actuators (Transducers'01)*, pp. 430-433, Munich, Germany, June 2001.

[5] R. Neul, U. Gómez, K. Kehr, W. Bauer, J. Classen, C. Döring, E. Esch, S. Götz, J. Hauer, B. Kuhlmann, C. Lang, M. Veith, and R. Willig, "Micromachined Angular Rate Sensors for Automotive Applications," *IEEE Sensors Journal*, Vol. 7, No. 2, pp. 302-309, February 2007.

[6] Research and Markets, "MEMS Gyro Markets- New Players and Business Models Give Momentum to Defence, Automative&Consumer Applications," www.researchandmarkets.com/reportinfo.asp?report_id=342965, September 2008.

[7] IEEE Standard for Inertial Sensors Terminology, Std 528-2001, November 2001.

[8] P. Greiff, B. Boxenhorn, T. King, and L. Niles, "Silicon Monolithic Micromechanical Gyroscope," *Tech. Dig. 6th Int. Conf. Solid-State Sensors and Actuators (Transducers'91)*, San Francisco, CA, pp. 966-968, June 1991.

[9] M. W. Putty, "A Micromachined Vibrating Ring Gyroscope," *Ph.D. Dissertation*, The University of Michigan, 1995.

[10] D. Fang and H. Xie, "A Low-Noise Low-Power Preamplifier for Capacitive CMOS-MEMS Gyroscopes," *49th IEEE Int. Midwest Symposium on Circuits and Systems (MWSCAS'06)*, San Juan, Puerto Rico, Vol. 1, pp. 270-274, August 2006.

[11] M. Saukoski, L. Aaltonen, K. Halonen, and T. Salo, "Fully Integrated Charge Sensitive Amplifier for Readout of Micromechanical Capacitive Sensors," *Proc. IEEE Int. Symp. on Circuits and Systems 2005 (ISCAS'05)*, Vol. 6, pp. 5377-5380, May 2005.

[12] A. Sharma, M. F. Zaman, and F. Ayazi, "A 104-dB Dynamic Range Transimpedance-Based CMOS ASIC for Tuning Fork Microgyroscopes," *IEEE J. of Solid-State Circuits*, Vol. 42, No.8, August 2007.

[13] J. A. Geen, S. J. Sherman, J. F. Chang, and S. R. Lewis, "Single-Chip Surface Micromachined Integrated Gyroscope with 50 °/hr Allan Deviation," *J. Solid State Cct.*, Vol. 37, No. 12, pp. 1860-1866, December 2002.

[14] N. Yazdi, H. Kulah, and K. Najafi, "Precision Readout Circuits for Capacitive Microaccelerometers," *Proc. IEEE Sensors 2004*, Vol. 1, pp. 28-31, October 2004.

[15] T. Singh and T. Ytterdal, "A Single-Ended to Differential Capacitive Sensor Interface Circuit Designed in CMOS Technology," *Proc. IEEE Int. Symp. on Circuits and Systems 2004 (ISCAS'04)*, Vol. 1, pp. 948-951, May 2004.

[16] N. Wongkomet and B. E. Boser, "Correlated Double Sampling in Capacitive Position Sensing Circuits for Micromachined Applications," *IEEE Asia-Pasific Conf. on Circuits and Systems*, pp. 723-726, November 1998.

[17] R. Oboe, R. Antonello, E. Lasalandra, G. S. Durante, and L. Prandi, "Control of Z-Axis MEMS Vibrational Gyroscope," *IEEE/ASME Transactions on Mechactronics, Vol. 10, No. 4*, August 2005.

[18] M. F. Zaman, A. Sharma, and F. Ayazi, "High Performance Matched-Mode Tuning Fork Gyroscope," *The 19th IEEE International Conference on Micro Electro Mechanical Systems (MEMS'06)*, Istanbul, Turkey, pp. 66-69, January 2006.

[19] J. Jiwei, H. Ming, W. Xiangli, C. Yong, and W. Yuelin, " A Digital Demodulation Solution to Achieve Stable Driving for Micro-Machined Gyroscope with an AGC Mechanism," *Proc. of IEEE Sensors 2004*, vol.1, pp. 429-432, October 2004.

[20] H. Rödjegard, D. Sandström, P. Pelin, M, Carlsson, M. Bohman, N. Hedenstierna, and I. Andersson, "A Novel Architecture for Digital Control of MEMS," *Proc. of IEEE,* Vol.3, pp. 1403-1406, October 2004.

[21] H. Rödjegard, D. Sandström, P. Pelin, N. Hedenstierna, and I. Andersson," A Digitally Controlled MEMS Gyroscope with 3.2 Deg/Hr Stability," *The 13th International Conference on Solid-State Sensors, Actuators and Microsystems (Transducer'05),* Seoul, Korea, Vol.1, pp. 535-538, June 2005.

[22] W. Geiger, J. Bartholomeyczik, U. Breng, W. Gutmann, M. Hafen, E. Handrich, M. Huber, A. Jäckle, U. Kempfer, H. Kopmann, J. Kunz, P. Leinfelder, R. Ohmberger, U. Probst, M. Ruf, G. Spahlinger, A. Rasch, J. Straub-Kalthoff, M. Stroda, K. Stumpf, C. Weber, M. Zimmermann, and S. Zimmermann, "MEMS IMU for AHRS Applications," *IEEE/ION PLANS'* 08, Monterey, CA, pp. 225-231, May 2008.

[23] A. Sharma, M. F. Zaman, M. Zucher, and F. Ayazi, "A 0. 1°/HR Bias Drift Electronically Matched Tuning Fork Microgyroscope," *Technical Digest of the 21th International Conference on Micro Electro Mechanical Systems (MEMS' 0*8), Tucson, Arizona, USA pp. 6-9, 2008.

[24] S. E. Alper, "MEMS Gyroscopes for Tactical-Grade Inertial Measurement Applications," *Ph.D. Dissertation*, Middle East Technical University, September 2005.

[25] S. E. Alper and T. Akin, "A Single-Crystal Silicon Symmetrical and Decoupled MEMS Gyroscope on an Insulating Substrate," *J. of Microelectromechanical Systems*, Vol. 14, No. 4, pp. 707-717, August 2005.

[26] S. E. Alper, K. Azgin, and T. Akin, "High-Performance SOI-MEMS Gyroscope with Decoupled Oscillation Modes," *19th IEEE Int. Conf. on Micro Electro Mechanical Systems (MEMS' 06)*, Istanbul, Turkey, pp. 70-73, January 2006.

[27] K. Azgin, Y. Temiz, and T. Akin, "An SOI-MEMS Tuning Fork Gyroscope with Linearly Coupled Drive Mechanism," *20th IEEE Int. Conf. on Micro Electro Mechanical Systems (MEMS' 07)*, Kobe, Japan, pp. 607-610, January 2007.

[28] S. E. Alper and T. Akin, "A Symmetrical and Decoupled Nickel Microgyroscope on Insulating Substrate," *Sensors Actuators A*, Vol. 115/2-3, pp. 336-350, September 2004.

[29] S. E. Alper, K. M. Silay, and T. Akin, "A Low-Cost Rate-Grade Nickel Microgyroscope," *Sensors Actuators A*, Vol. 132, Issue 1, pp. 171-181, November 2006.

[30] S. E. Alper, K. M. Silay, and T. Akin, "Tactical-Grade Silicon-on-Glass Gyroscope with Very-Small Quadrature Coupling," *Proc. of the 20th European Conf. on Solid-State Transducers (Eurosensors XX)*, Gothenburg, Sweden, September 2006.

[31] K. Sahin, "A Wide Bandwidth High-Sensitivity MEMS Gyroscope", *Msc. Thesis*, Middle East Technical University, July 2008.

[32] K.Sahin, E. Sahin, S. E. Alper, and T. Akin, "A Wide-Bandwidth and High-Sensitivity Robust Microgyroscope," *19th MicroMechanics Europe Workshop (MME 2008)*, pp. 97-100, Aachen, Germany, September 2008.

[33] S. E. Alper, "Silicon Surface Micromachined Gyroscopes Using MEMS Technology," *M.Sc. Thesis*, Middle East Technical University, September 2000.

[34] K. Azgin, "High Performance MEMS Gyrocsopes.," *M. Sc. Thesis*, Middle East Technical University, February 2007.

[35] M. K. Silay, " High Performance CMOC Capacitive Interface Circuits for MEMS Gyroscopes," *Msc. Thesis*, Middle East Technical University, September 2006.

[36] Y. Temiz, "Advanced Readout and Control Electronics for MEMS Gyroscopes," *M. Sc. Thesis*, Middle East Technical University, August 2007.

[37] B. E. Boser, "Electronics for Micromachined Inertial Sensors," *Tech. Dig. 9th Int. Conf. Solid-State Sensors and Actuators (Transducers'97)*, Chicago, IL, pp. 1169-1172, June 1997.

[38] J. Bernstein, S. Cho, A. T. King, A. Kourepenis, P. Maciel, and M. Weinberg, "A Micromachined Comb-Drive Tuning Fork Rate Gyroscope," *Proc. IEEE Micro Electro Mechanical Systems Workshop (MEMS'93)*, Fort Lauderdale, FL, pp. 143-148, February 1993.

[39] G. He and K. Najafi, "A Single-Crystal Silicon Vibrating Ring Gyroscope," *Proc. IEEE Micro Electro Mechanical Systems Workshop (MEMS'02)*, Las Vegas, CA, January 2002, pp. 718-721.

[40] M. Lutz, W. Golderer, J. Gerstenmeier, J. Marek, B. Maihofer, S. Mahler, H.Munzel and U. Bischof, "A Precision Yaw Rate Sensor in Silicon Micromachining," *Tech. Dig. 9th Int. Conf. Solid-State Sensors and Actuators (Transducers'97)*, Chicago, IL, pp. 847-850, June 1997.

[41] A. R. Schofield, A. A. Trusov, C. Acar, and A. M. Shkel, "Anti-Phase Driven Rate Gyroscope with Multi-Degree of Freedom Sense Mode," *Proceedings of the Solid-State Sensors, Actuators and Microsystems Conference (Transducers'07)*, Lyon, France, pp. 1199-1202, 2007.

[42] X. Huikai and G. K. Fedder, "A CMOS-MEMS Lateral-Axis Gyroscope," *Proc. IEEE Micro Electro Mechanical Systems Workshop (MEMS'01)*, Interlaken, Switzerland, January 2001, pp. 162-165.

[43] H. Luo, X. Zhu, H. Lakdawala, L. R. Carley, and G. Fedder, "A Copper CMOS-MEMS Z-Axis Gyroscope," *Proc. IEEE Micro Electro Mechanical Systems Workshop (MEMS'02)*, Las Vegas, CA, January 2002, pp. 631-634.

[44] T. Juneau, A. P. Pisano, and J. H. Smith, "Dual Axis Operation of a Micromachined Rate Gyroscope," *Tech. Dig. 9th Int. Conf. Solid-State Sensors and Actuators (Transducers'97)*, Chicago, IL, pp. 887-890, June 1997.

[45] G. K. Fedder, "Simulation of Microelectromechanical Systems," *Ph.D. Dissertation*, University of Michigan, 1995.

[46] J. Wu, G. K. Fedder, and L. R. Carley, "A Low-Noise Low-Offset Capacitive Sensing Amplifier for a 50 μg/√Hz Monolithic CMOS MEMS Accelerometers," *Tech. Dig. IEEE Int. Solid-State Circuits Conf.*, Vol. 1, February 2002.

[47] H. Kulah, J. Chae, N. Yazdi, and K. Najafi, "A Multi-Step Electromechanical Sigma-Delta Converter for Micro-g Capacitive Accelerometers," *IEEE Int. Solid-State Circuits Conf.*, pp. 202-203, February 2003.

[48] H. Kulah, J. Chae, N. Yazdi, and K. Najafi, "Noise Analysis and Characterization of a Sigma-Delta Capacitive Microaccelerometer," *IEEE J. Solid-State Circuits*, Vol. 41, No. 2, pp. 352-361, February 2006.

[49] Z. Wang, Z. Li, and W. Lu, "A New Self-Oscillation Loop for MEMS Vibratory Gyroscopes," *ASICON'07*, Guilin, China, Vol.1, pp. 1046-4049, October 2007.

[50] C. Acar, S. Eler, and M. Shkel, "Concept, Implementation, and Control of Wide Bandwidth MEMS Gyroscopes," *Proc. Of the American Control Conference*, Vol.2, pp. 1229-1234, June 2001.

[51] P. Ward, "Electronics for Coriolis Force and Other Sensors," U. S. Patent 5 481 914, January 4, 1996.

[52] D.Xia, B. Zhou, and S. Wang, "Double Matched Microgyro Resonant System in Drive and Sense Modes," *The 1st Nano/Microengineered and Molecular Systems (NEMS'06)*, Zhuhai, China, pp, 919-922, January 2006.

[53] J. Raman, E. Cretu, P. Rombouts, and L. Weyten, "A Digitally Controlled MEMS Gyroscope with Unconstrained Sigma-Delta Force-Feedback Architecture," *The 19th IEEE International Conference on Micro Electro Mechanical Systems (MEMS 2006)*, Istanbul, Turkey, pp. 710-713, January 2006.

[54] W.-T. Sung, S. Sung, J. G. Lee, and T. Kang, "Design and Performance Test of a MEMS Vibratory Gyroscope with a Novel AGC Force Rebalance Control," *J. of Micromechanics and Microengineering*, Vol. 17, pp. 1939-1948, August 2007.

[55] R. P. Leland, "Adaptive Control of a MEMS Gyroscope Using Lyapunov Methods," *IEEE Transactions on Control Systems Technology*, Vol.10, No. 2, pp.278-283, March 2006.

[56] M. Salah, M. McIntyre, D. Dawson, and J. Wagner, "Time-Varying Angular Rate Sensing for a MEMS Z-Axis Gyroscope," *Proc. of the 45th IEEE Conference on Decision&Control*, pp. 2165-2170, December 2006.

[57] W.-T. Sung, and J. G. Lee, "H∞ Controller Design of MEMS Gyroscope and Its Performance Test," *Position, Location and Navigation Symposium*, pp. 63-69, April 2004

[58] R. F. Yazicioglu, "Surface Micromachined Capacitive Accelerometers Using MEMS Technology," *M.Sc. Thesis*, Middle East Technical University, August 2003.

[59] Analog Devices, "OPAMP Application Handbook," 2006.

[60] National Semiconductor, "LF353 Wide Bandwidth Dual JFET Input Operational Amplifier," *Datasheet*, 1995.

[61] Analog Devices, "AD8609 Quad, Zero Drift, Single-Supply, Rail-to-Rail Operational Amplifier," *Datasheet,* 2008.

[62] K. Ogata, "Modern Control Engineering," Prentice Hall, 1990.

[63] Analog Devices, "AD620 Low Drift, Low Power Instrumentation Amplifier with Set Gains of 1 to 10000," *Datasheet,* 2004.

[64] Analog Devices, "AD630, Balanced Modulator/Demodulator," *Datasheet,* 2004.

[65] Analog Devices, "AD600/AD602, Dual, Low-Noise, Wideband Variable Gain Amplifiers," *Datasheet,* 2006.

[66] B. Linares-Barranco, T. Serrano-Gotarredona, "A Loss Control Feedback Loop for VCO Stable Amplitude Tuning of RF Integrated Filters," *IEEE Int. Symposium on Circuits and Systems (ISCAS'02),* Vol. 1, pp. 521-524, May 2002.

[67] IEEE Standard Specification Format Guide and Test Procedure for Single-Axis Interferometric Fiber Optic Gyros, *IEEE Std 952-1997,* pp. 65, September 1997.